High temperature forearc metamorphism and consequences for sulfide stability in the Pacific Rim Terrane, British Columbia

by

Alexander C. Geen

B.Sc., McGill University, 2017

A Thesis Submitted in Partial Fulfillment of the Requirements for the Degree of

MASTER OF SCIENCE

in the School of Earth and Ocean Sciences

University of Victoria

Supervisory Committee

High temperature forearc metamorphism and consequences for sulfide stability in the Pacific Rim Terrane, British Columbia

by

Alexander C. Geen

B.Sc., McGill University, 2017

Supervisory Committee

Dr. Dante Canil, Supervisor
School of Earth and Ocean Sciences

Dr. Laurence Coogan, Departmental Member
School of Earth and Ocean Sciences

Dr. Ruohong Jiao, Departmental Member
School of Earth and Ocean Sciences

Abstract

The Pacific Rim Terrane in British Columbia is a group of fault-bound forearc metasedimentary and metaigneous rocks subcreted to Wrangellia, comprising three lithological units: the Leech River Complex (LRC), the Pandora Peak Unit (PPU), and the Pacific Rim Complex. Of these three, the LRC and PPU were subject to an elevated thermal metamorphic event which locally overprinted typical low temperature, medium pressure forearc assemblages with low greenschist through amphibolite facies assemblages. The field study shows that biotite, garnet and staurolite isograds occur concentrically in the LRC, centered on the Leech River fault, which separates the Pacific Rim Terrane from the underlying Metchosin Igneous Complex of the Crescent terrane. Local thermal overprint in the PPU is sub-biotitic and is characterized by local replacement of prehnite-pumpellyite and lawsonite-bearing assemblages with muscovite ± chlorite. Multi-method geothermobarometry shows peak metamorphic temperatures from ~230 °C in the northern PPU to ~600 °C near the Leech River fault at ~4 kbar, and isotherms are continuous across the LRC-PPU boundary. The interfoliated Tripp Creek metabasites and Eocene Walker Creek intrusions do not control the distribution of isotherms, and syn-metamorphic felsic sills rarely have contact aureoles. Intercalated metabasites show two distinct rare earth element (REE) patterns, including NMORB-like light REE depletion among most Tripp Creek metabasites, and light REE enrichment in PPU metabasites. The lack of thermal aureoles associated with metabasites, and interlayered garnetite bands with negative Ce-anomalies attributed to seafloor hydrothermal processes, suggest the Tripp Creek metabasites are not syn-metamorphic sills and formed prior to accretion. The subcretion of then recently formed oceanic crust belonging to the Crescent terrane is identified as the probable cause of anomalously high temperature forearc conditions, as well as possible proximity to an Eocene mid ocean ridge.

The high temperature metamorphic rocks in the Pacific Rim Terrane document the conversion of inherited primary pyrite to pyrrhotite in carbonaceous metasediments. S-inclusive pseudosections for LRC protoliths predict a low temperature (<420 °C) narrow pyrite desulfidation window that produces pyrrhotite and releases negligible S to the fluid phase. Conversely, sulfide petrography in the LRC shows pyrite can persist up to ~550 °C as inclusions in andalusite and staurolite porphyroblasts, as well as possibly in the rock matrix. S contents in carbonaceous pelites show a marked reduction at medium grade, associated with a dearth of visible sulfide in LRC phyllites. Sluggish pyrite desulfidation, pyrrhotite desulfidation, and terrane-scale S mobility are interpreted as the driver for mobility of intra-terrane sourced Au, leading to the formation of a hypozonal orogenic Au deposit in the central LRC.

Table of Contents

List of Tables

List of Appendix Tables

List of Figures

Appendix Figures

Acknowledgements

First, I must express my gratitude to my supervisor Dante Canil for the opportunity to study the wonderfully complex geology of southern Vancouver Island, and for the enthusiasm, encouragement, and feedback he provided throughout my degree. Furthermore, I am grateful for his openness to allow the project to evolve, and for the imparted wisdom in maintaining project scope, without which I would surely still be glued to the petrographic microscope. Secondly, thank you to Dominic Fode for his assistance in an ambitious week of field work, during which he provided keen observations and insight. Thank you to Rebecca Morris, who provided sage advice in the field, on petrography, and on sustainably pursuing an MSc. I am grateful for the assistance of Rebecca Scholtysik and Alex Wlasenko, who both provided invaluable advice while I learned to use the Raman microscope. Thank you to Andrew Locock at the University of Alberta's Electron Microprobe Laboratory, and to Jody Spence (UVic) for their time and guidance in using the EMP and LA-ICP-MS respectively. For the opportunities to be a TA and to learn via teaching in labs and the field, I am grateful to Kathy Gillis, David Nelles, Dante Canil, Jon Husson, and Duncan Johannessen. I would also like to gratefully acknowledge the feedback and advice of my supervisory committee, Laurence Coogan, Ruohong Jiao, and Dante Canil.

Special thanks also to all those who offered support, kindness, and balance to my academics, including Emily and Yuri, who allowed me to be the fun 'uncle' to their corgi, Quigley. I would like to thank my mother Laura, who always encouraged me to follow my passions, including that first momentous leap to go study geology in Montréal. Thank you to my father David, who taught me the merit of hard work, and spurred my interest in geoscience through a taught admiration for nature. Finally, thank you to my partner Erin, who inspires me with her own passion and prowess for science. I owe her an immeasurable debt for all the times I have stopped us to, "take a quick look at the rocks."

This thesis was supported by a Natural Sciences and Engineering Research Council of Canada (NSERC) CGS-M (A.C. Geen), the Society of Economic Geology's Canada Foundation (SEGCF) Student Research Grant (A.C. Geen), and an NSERC Discovery grant (D. Canil).

Dedication

For my partner Erin,

Without whom this would not have been possible.

Chapter 1. Introduction

1.1 The forearc environment

Records of subduction and continental growth are preserved in forearc metamorphic terranes. The rocks which comprise these terranes are diverse in provenance, composition, and metamorphic evolution. As oceanic lithosphere subducts, it delivers an ongoing but variable veneer of sediments to the forearc (von Huene & Scholl, 1991). Some fraction of these sediments, as well as fragments of the upper basaltic crust, can be mechanically abraded from the downgoing plate and accumulate landward of the trench in an accretionary mélange (von Huene & Scholl, 1991; Tsukada et al., 2013). In tandem to this frontal accretion, sediments may also be accreted to the bottom of the overriding plate via underplating, growing the forearc from below (Ruh, 2020). The balance of sediments bypass forearc accretion entirely, and traverse into the shallow mantle wedge (von Huene & Scholl, 1991), as evidenced by sedimentary isotopic signatures in arc melts (Plank & Langmuir, 1993; Plank, 2005). In addition to marine sediments, accreted and subcreted sediments may also comprise detritus and volcanogenic material from the hinterland, that accumulated in the wedge or in associated forearc basins (Simpson, 2010; Festa et al., 2016). Consequently, protoliths in forearc terranes are highly heterogeneous, including lithologies like cherts, marine mudstones, coarse siliciclastic sediments, basalts, arc-derived volcanic tuffs, and other material juxtaposed by both sedimentary and tectonic processes (Cowan, 1985; Festa et al., 2016).

Accreted forearc sediments, including those in the prism and subcreted to the overriding plate, generally experience low temperature – medium pressure to low temperature – high pressure metamorphic conditions (e.g., Dumitru, 1991; Wakabayashi, 2015; forearc accretion and underplating models of Ruh, 2020). Decades of work has been spent examining the genesis of forearc terranes and their petrology globally (e.g., Cowan, 1985; Cawood et al., 2009; Riel et al., 2013; Wakabayashi, 2015). The archetypal case of forearc metamorphic conditions is the ‘fossil’ subduction interface of the Franciscan Complex in California, which records a partial record of >100 Ma of subduction in complex metasedimentary mélanges hosting blueschist blocks (Wakabayashi, 2015). Recent data confirm that accreted early Cretaceous members of the eastern Franciscan Complex attained metamorphic temperatures of 280 to 377 °C at depths of ~30 to 40 km (Schmidt & Platt, 2020). However, thermal models suggest temperature gradients in forearc environments can vary significantly between subduction zones, and vary with time in the same subduction zone (Dumitru, 1991; Harris et al., 2014; van Keken et al., 2019; Peacock, 2020).

Forearc thermal structure is subject to significant variability arising from subduction zone parameters, including the dip, buoyancy, age, sediment cover and subduction rate of the downgoing slab, and whether the margin is accretionary or erosive (Dumitru, 1991; Molnar & England, 1994; Harris et al., 2014). For example, the Franciscan accretionary complex experienced dominantly zeolite through blueschist facies conditions consistent with low temperature, high pressure metamorphism, and blueschist clasts retrieved from serpentinite seamounts in the Mariana subduction zone record conditions of 150 to 250 °C at depths of 16 to 20 km (Maekawa et al., 1993). In contrast, the exhumed El Oro forearc along the Andean margin experienced a thermal gradient of 30 °C km^{-1} during peak metamorphism, causing migmatization and significant S-Type magmatism (Riel et al., 2013). Thus, while preserved accretionary complexes are known as typical low temperature, high pressure terranes, they are not restricted to this P-T space.

1.2 Eocene forearc of the Canadian Cordillera

The Canadian Cordillera comprises a ‘terrane collage’ (term borrowed from Pavlis et al., 2019) of broadly north-south oriented terranes aligned from the margin of the North American Craton in the Foreland belt to the Insular belt (Figure 1.1) along the continental margin (Monger & Price, 2002). Contentious debate over the manner of Cordillera assembly continues, between a standard accretionary model invoking long-term east-dipping subduction delivering successive exotic terranes (e.g., Cook et al., 2012; review of competing models in Chen et al., 2019; McMechan et al., 2020) and collisional models proposing suture of preassembled terranes or archipelagos to the craton via west-dipping subduction (e.g., Sigloch & Mihalynuk, 2017; Chen et al., 2019). The manner of accretion for the Insular superterrane (e.g., Wrangellia and Alexander terranes) is debated, including models of Andean-style eastward subduction, and closure of an ocean basin via westward subduction (Sigloch & Mihalynuk, 2017, Figure 7 therein; Pavlis et al., 2019). Nonetheless, there is strong evidence for east-dipping subduction by the earliest Cretaceous, recorded in east-adjacent forearc complexes such as the Chugach Complex in Alaska and the Franciscan Complex in California (Clennett et al., 2020), even if it did coincide with collision of the Insular superterrane against the edge of North America via west-dipping subduction (Sigloch & Mihalynuk, 2017).

In British Columbia, the record of Cretaceous through Eocene eastward subduction is less distinct than the long-lived Chugach and Franciscan accretionary complexes. Outboard of Wrangellia on southern Vancouver Island, the Pacific Rim Terrane is a package of E-W striking metasedimentary and subsidiary metavolcanic rocks (Fairchild & Cowan, 1982) with as young as Jurassic-Cretaceous detrital zircon ages (Dlugosz et al., 2020). Unlike the accretionary complexes to the south and north, there is less consensus as to the precise tectonic affinity of the Pacific Rim Terrane. Early workers (e.g., Muller 1977; Muller 1983) classed the terrane as an accretionary complex, but it has subsequently interpreted as an accreted allochthonous terrane (Fairchild & Cowan, 1982), or a correlative unit of blueschist facies rocks in the San Juan-Cascades thrust system, emplaced by post-Cretaceous lateral translation (Brandon, 1989a). The Pacific Rim Terrane underlies Wrangellia along a set of poorly exposed faults, at least one of which is interpreted as a thrust (Fairchild & Cowan, 1982; Clowes et al., 1987), and itself is underpinned by the Eocene basalts of the Metchosin Igneous Complex—part of the Crescent terrane—along the steeply dipping Leech River fault (Clowes et al., 1987). Sense of motion along the Leech River fault has been reinterpreted numerous times, including as a left-lateral transform (Fairchild & Cowan, 1982), a thrust (Clowes et al., 1987), and most recently recognized as a paleo-subduction interface (Seyler et al., 2020).

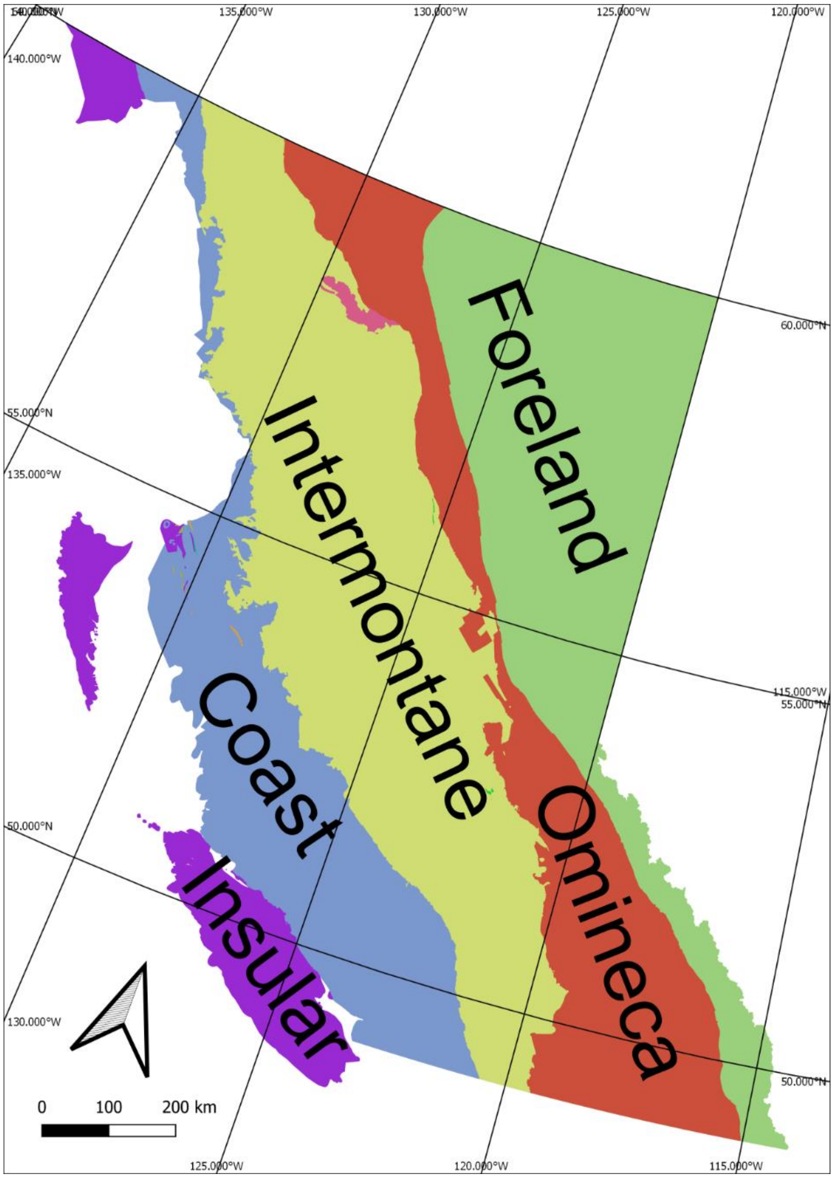

Figure 1.1 Simplified map of the morphogeological belts comprising the Cordillera in British Columbia. From Cui et al. (2017), BC Digital Geology. The Pacific Rim Terrane is exposed at the southwest margin of the Insular belt on southern Vancouver Island.

Unlike the Franciscan Complex to the south, the Pacific Rim Terrane experienced anomalously high forearc metamorphic temperatures, with recent estimates ranging up to 550 °C in andalusite stability conditions (Groome et al., 2003; Jakob et al., 2016). The cause of this thermal metamorphism has been a longstanding subject of research, and explanations usually involve a series of felsic intrusions that resulted from the influence of either a subducting mid ocean ridge, interaction with a hotspot, or both (Groome et al., 2003; Jakob et al., 2016). Elevated forearc metamorphic temperatures and magmatism are also detected farther north in the Chugach accretionary complex, including the schists on Baranof Island (Sisson et al., 2003; Cowan, 2003). This extensive pattern of elevated forearc temperatures has spurred numerous hypotheses and tectonic reconstructions. The Baranof-Leech River hypothesis (Cowan, 2003) postulates that the Baranof schists experienced some 1100 km of northward displacement after being subject to the same ridge-trench thermal metamorphism as the LRC at 48 °N. This has more recently been formulated as the 'Mobilist' model (summarized in Fuston & Wu, 2020), where the mobile Chugach terrane transits across the 'fixed' subducting Kula-Farallon Ridge. Other workers contend the pattern of widespread hotter-than-average forearc metamorphism is a consequence of oblique subduction of the hypothesized Resurrection plate in Eocene time, wherein Kula-Resurrection and Farallon-Resurrection ridges could have swept the Alaskan and British Columbian forearcs respectively (Haeussler et al., 2003; Bradley et al., 2003; Fuston & Wu, 2020).

In the context of elevated temperatures along the northern Cordillera forearc, this thesis provides a detailed account of the metamorphic evolution of the Pacific Rim Terrane and seeks to provide insight about how the terrane relates to assembly of the Eocene Cordilleran forearc. This includes re-examining the likely cause of metamorphism, and whether the comprising units of the Pacific Rim Terrane were subject to the same metamorphic event. This will be accomplished using recent and established methods of geothermobarometry and pseudosection modelling. New whole rock geochemical data are acquired to provide insight into the origin of the numerous intercalated metabasic lithologies in the terrane, and indications of provenance for the Pacific Rim Terrane.

1.3 Metamorphism of sulfide minerals and links to orogenic Au

Carbonaceous marine siliciclastic rocks like black shales and argillites may host significant (>1 wt%) S, usually in the form of the sulfide pyrite (Goldhaber, 2003). As these rocks are metamorphosed, the sulfide and silicate mineral assemblages shift in tandem to attain equilibrium. Changes in sulfide assemblages with increasing metamorphic grade are widely studied and often motivated by a link between the transport of Au and sulfide stability (e.g., Carpenter, 1974; Ferry, 1981; Pitcairn et al., 2010; Tomkins, 2010; Pitcairn et al., 2015; Zhong et al., 2015; Finch & Tomkins, 2017). Chiefly, the breakdown of pyrite (Py) to pyrrhotite (Po) is associated with the release of S (Ferry, 1981) and numerous economically important elements, including Au, are bound in biogenic and diagenetic Py (Large et al., 2011; Large et al., 2012; Zhong et al., 2015). Sulfide metamorphism also bears on the Earth’s S cycle, particularly in forearc rocks where the relative stability of sulfide and sulfate minerals can differentially affect the fO_2 of the subduction system and overlying mantle wedge (Walters et al., 2020). Despite growing recognition of their importance, sulfide assemblages remain less well understood compared to their silicate counterparts, partly because sulfides are thought to be easily overprinted or otherwise perturbed by retrograde and post-metamorphic alteration (Barton, 1970). Furthermore, many S-bearing minerals lack compiled thermodynamic data and activity-composition (a-x) models that that allow their incorporation into models like pseudosections. However, the addition of internally consistent thermodynamic data for some S minerals (e.g., Evans et al., 2010) in the widely applied HP databases (Holland & Powell, 2011) has enabled modelling of metamorphic systems including S.

This thesis utilizes the S-inclusive internally consistent datasets (Holland & Powell, 2011) in the PerpleX Gibbs free energy minimization suite (Connolly, 2005) to model changes to the sulfide mineral assemblage during anomalously high temperature forearc metamorphism in the Pacific Rim Terrane. The results of the models are then contrasted with observations from the rock record in conjunction with this study’s thermometry results. This analysis seeks to inform the genesis of a regional orogenic Au deposit, and how it relates to other orogenic Au deposits associated with elevated forearc metamorphism along the North American margin (e.g., Haeussler et al., 1995; Bradley et al., 2003) and globally (e.g., Pitcairn et al., 2010).

1.4 Thesis format

This thesis is subdivided into two standalone papers which comprise Chapters 2 and 3. Chapter 2 examines the conditions of metamorphism in the southern contiguous Pacific Rim Terrane, including the Leech River Complex (LRC) and Pandora Peak Unit (PPU), utilizing Raman Spectroscopy of Carbonaceous Materials (RSCM) geothermometry, garnet-biotite geothermometry, allied geobarometry, and pseudosection models. Furthermore, whole rock geochemical data are utilized to interpret the provenance of the Pacific Rim Terrane metasediments and the intercalated metabasic rocks. The thermometry results from Chapter 2 are then utilized in Chapter 3 to investigate the behavior of sulfides during prograde metamorphism in natural rocks, and how this compares to recent thermodynamic models in the literature, and new pseudosection models presented here. Both chapters seek to inform the metamorphic history of the Pacific Rim Terrane, including likely causes of high temperature forearc metamorphism, and the genesis of an orogenic Au deposit in the region. These findings are summarized in Chapter 4.

Chapter 2. Evaluation of high temperature forearc metamorphism in the Pacific Rim Terrane, British Columbia by geothermobarometry

2.1 Introduction: Forearc metamorphism and the Pacific Rim Terrane

Forearc sedimentary protoliths can include sediments of both continental and oceanic affinity accumulated in forearc basins (e.g., Laursen et al., 2002; Maravelis et al., 2016), or accretionary mélanges, comprising the fraction of sediments scraped off the subducting oceanic crust while the balance is recycled into the mantle (von Huene & Scholl, 1991). The forearc of a subduction zone is ordinarily associated with low temperature – medium pressure metamorphic conditions. Thus, metasediments preserved in the accretionary complex or subcreted to the overriding plate typically preserve a record of prehnite-pumpellyite through blueschist facies metamorphism. In the Insular Belt of the Canadian Cordillera, a package of highly deformed forearc metasediments, the Pacific Rim Terrane (Figure 2.1) instead reach up to amphibolite facies conditions incongruous with typical forearc conditions. The cause and tectonic significance of the anomalously high temperature forearc metamorphism has been used in tectonic reconstructions to argue for positions of a slab window or hotspot and thus bears on interpretations of the recent tectonic assembly of the Insular belt (Groome et al., 2003; McCrory & Wilson, 2013; Wells et al., 2014; Jakob et al., 2016).

The Pacific Rim Terrane comprises the Leech River Complex (LRC), Pandora Peak Unit (PPU), and Pacific Rim Complex (PRC). In the LRC, Fairchild & Cowan (1982) argued for two periods of deformation, with initial isoclinal folding of sedimentary strata into parallelism (D_1), and subsequent large-scale open folding of the earlier foliation (D_2), with a single metamorphic event that overlapped both phases. The adjacent PPU, however, shows variable pervasive internal deformation and evidence of sub-blueschist facies metamorphism manifested as local assemblages of prehnite, pumpellyite and lawsonite (Rusmore & Cowan, 1985). Fairchild & Cowan (1982) argue the absence of remnant blueschist assemblages in the LRC precludes it from being an *in-situ* subduction complex, and that it instead represents an allochthonous terrane emplaced against the PPU along high-angle strike-slip faults.

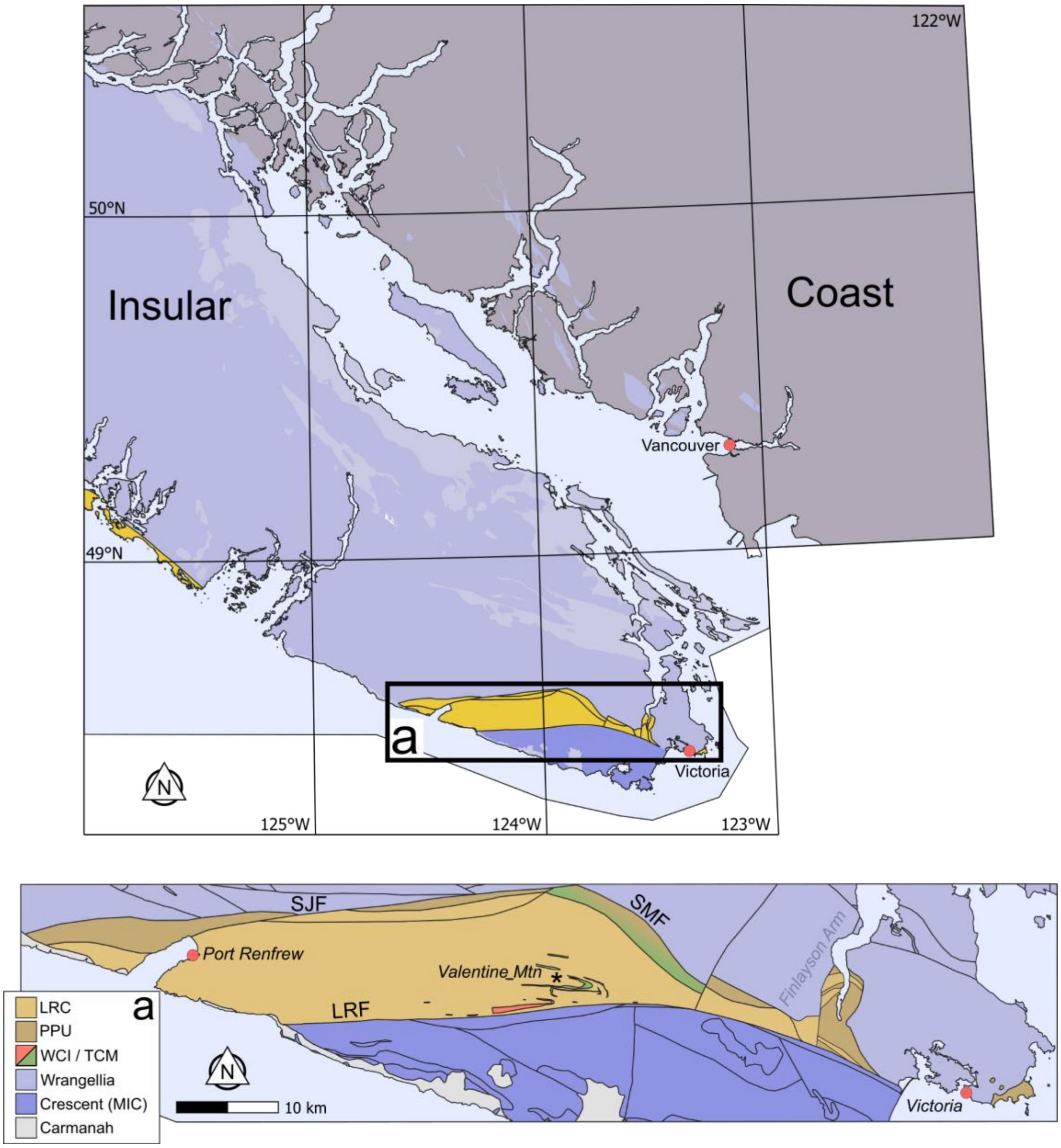

Figure 2.1 Simplified terrane map of southwestern British Columbia, showing the Coast and Insular Cordilleran belts. The Pacific Rim Terrane (PRT), including the Pacific Rim Complex at and above the 49th parallel, is indicated in yellow. *Inset a:* Simplified geologic map of the southern contiguous PRT, including Leech River Complex (LRC) and Pandora Peak Unit (PPU) and Walker Creek intrusions (WCI), modified after Massey et al. (2005) with elements of the Victoria PPU after Pope (2006), Finlayson Arm geology after Muller (1983) and Rusmore & Cowan (1985), Tripp Creek Metabasite (TCM) after Grove (1984) and field observations. Gradational unit near SMF indicates the metavolcanic-rich unit after Fairchild & Cowan (1982). SJF = San Juan Fault, SMF = Survey Mountain Fault, LRF = Leech River Fault. Asterisk * indicates location of Valentine Mountain.

The mutual proximity of high-grade rocks with syn-deformation felsic intrusions has been indicated as a causational relationship for amphibolite-grade metamorphism in the LRC. Groome et al. (2003) and Jakob et al. (2016) favor a two-phase metamorphic history comprising both a mid-Cretaceous and Eocene period of heating, each associated with pulses of felsic magmatism. However, neither Groome et al. (2003) nor Jakob et al. (2016) explicitly address the volume of intrusions required to induce upper greenschist through amphibolite facies conditions in the whole LRC, and how these estimates compare to the exposed area of intrusions. Estimates from mapped surface area suggest the ratio of metamorphosed host rock to intrusions is on the order of 20:1 (estimated from map of Massey et al., 2005). Further uncertainty arises over the identity of one of the larger quartzofeldspathic bodies, the “Jordan River metagranodiorite” at Valentine Mountain (Groome et al., 2003; see location in Figure 2.1a), which is interpreted by earlier workers as a large metapsammitic body (Fairchild & Cowan, 1982; Grove, 1984). Furthermore, the timing of the proposed mid-Cretaceous heating event relies upon one zircon retrieved from thin sills near Port Renfrew (Jakob et al., 2016), and two analyses within the LRC at Valentine Mountain (Groome et al., 2003).

Given the body of work, there still exists considerable uncertainty in the metamorphic history of the Pacific Rim Terrane. This study builds a more detailed dataset of metamorphic conditions for the terrane over a broader area than previous studies using Raman Spectroscopy of Carbonaceous Material (RSCM) geothermometry, a method applicable to a wide range of carbon-bearing rock types, in parallel with garnet-biotite geothermobarometry. Additionally, pseudosection results for a set of typical LRC metasediment compositions are used to further assess the most likely metamorphic P-T history. Major and trace element bulk rock analyses and detrital zircon geochronology are presented with detailed petrographic descriptions of the Pacific Rim Terrane metasediments and interfoliated meta-igneous rocks to assess protolith sources and ages in the context of regional setting in the Cordillera. Together with previous work on the LRC (Fairchild & Cowan, 1982; Groome et al., 2003; Jakob et al., 2016) and PPU (Rusmore & Cowan, 1985; Pope, 2006; McEwen, 2013), the new results lead to a more complete interpretation of the elevated thermal metamorphism in the forearc and how this relates to the Eocene tectonic framework of the Insular belt.

2.2 Geology and Petrography

This study considers two of the three sub-units of the Pacific Rim Terrane: The LRC, and the PPU. The third sub-unit, the Pacific Rim Complex, comprises olistostromal mélanges of pelitic, psammitic and pelagic metasediments with interbedded meta-tuffs and metabasalts, exposed along the West Coast fault in Ucluelet, BC (Brandon, 1989a; 1989b). The LRC and PPU otherwise outcrop as a semi-continuous ~630 km^2 body from west of Port Renfrew to Victoria, BC (Figure 2.1), bounded to the north along the San Juan Fault, and to the south by the high-angle Leech River fault. Within a few hundred meters of the Leech River fault, extreme deformation demarcates the Bear Creek Shear Zone (Figure 2.2), wherein there is a decrease in average grain size and the abundance of porphyroblasts. Within ~100 meters of the inferred Leech River fault trace, the rocks are characteristically mylonitized.

2.2.1 Leech River Complex

The LRC comprises predominantly metapelitic and metapsammitic rocks, with subsidiary inter-foliated tuffaceous, felsic, and basic metaigneous units. The latter include the Walker Creek intrusive suite and Tripp Creek metabasite (after Groome et al., 2003). Here, the mapped exposure of the Tripp Creek metabasite is modified after Grove (1984), and the largest sill of the Walker Creek intrusive suite is mapped after Massey et al. (2005) and Fairchild & Cowan (1982). Other sub-meter felsic and basic metaigneous rocks are below mappable scale.

Metamorphic grade in the LRC varies from low greenschist facies in the north and east margins of the unit, to amphibolite facies near the Leech River fault in the south. Metapelites dominate the terrane, including graphitic phyllites and schists (Figure 2.2) in which all sedimentary features are overprinted by penetrative deformation. The only exception occurs in Finlayson Arm (Figure 2.1), wherein successions of sub-greenschist interbedded metasandstone and black argillite of LRC affinity occur as a cryptic kilometer-wide, fault-bound blocks within PPU tectonites and cherts, as mapped by Muller (1983). In this location original sedimentary features including bedding, normal grading, and rip-up clasts are clearly preserved. The beds outcrop in large, open folds with ~E-W striking hinge lines and, limbs comparable to the foliation plane of the rest of the LRC. However, these blocks have not been subject to the same isoclinal folding and cataclasis that has otherwise obscured depositional features further west (Jakob et al., 2016).

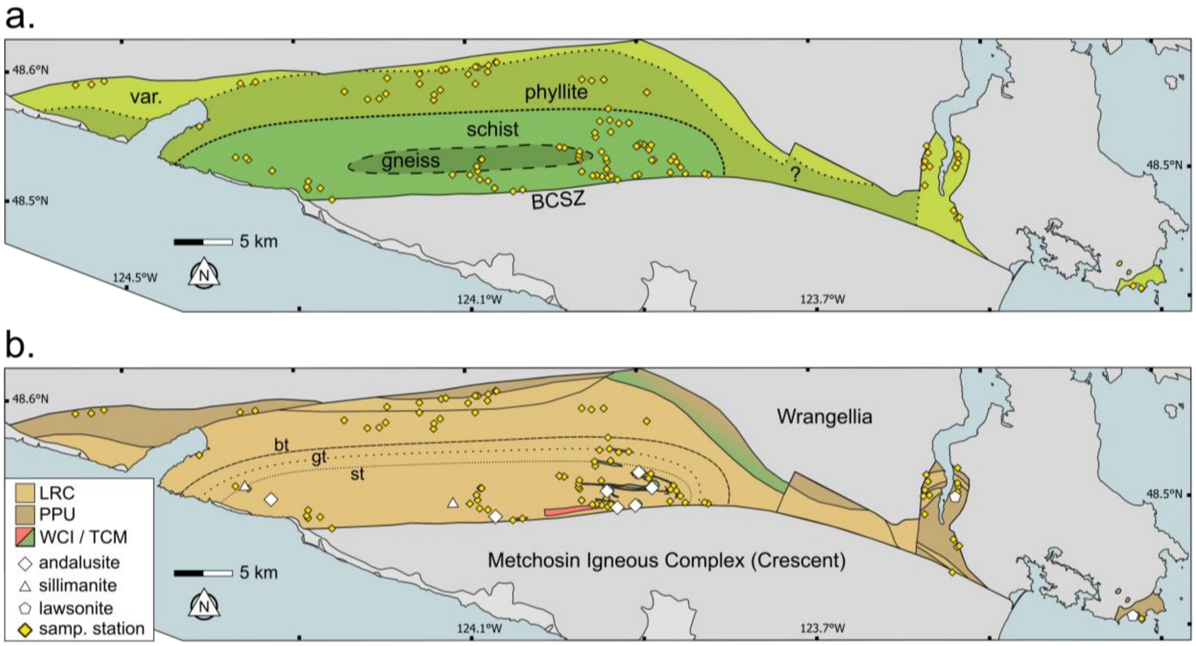

Figure 2.2 *Panel a:* A highly simplified map showing the dominant metamorphic rock type, including the paragneiss which occurs parallel to the E-W hinge line of a large-scale open fold. Sample stations are indicated in yellow. The variable (var.) field encompasses the PPU, which comprises numerous foliated, non-foliated and olistostromal units. Uncertain areas indicated by the '?' symbol. BCSZ = Bear Creek Shear Zone. *Panel b:* Simplified geologic map showing the approximate biotite, garnet and staurolite isograds. Other index mineral occurrences are indicated in key. Colour gradient in northeast segment indicative of gradational contact between metasediments and metavolcanics (see Fairchild & Cowan, 1982). Maps modified after Massey et al. (2005), as indicated in Figure 2.1.

Locally, metapsammites are present in successions of up to tens of meters with subsidiary pelitic rocks. Such metapsammitic lithologies are associated with elevated topographic relief and form E-W trending bluffs. The Valentine Mountain region comprises a large quartzose metasandstone body with an apparent thickness of up to ~1 km and lateral length of tens of kilometers. Field observations presented here favour the interpretation of earlier workers (Fairchild & Cowan, 1982; Grove, 1984) that the Valentine Mountain unit is indeed a metapsammite, as opposed to a mid-Cretaceous metagranodiorite (e.g., Groome et al., 2003). Similarly, an ~8 km long quartz-rich body presently mapped as a sill in the northwest LRC (Massey et al., 2005) is re-interpreted here as a package of grey metasandstone comparable to the Valentine Mountain unit and thus excluded from Figure 2.2 on the basis of petrography and new detrital zircon ages (e.g., Dlugosz et al., 2020) discussed hereafter.

Pelitic Protoliths

Pelitic protoliths in the LRC outcrop as phyllites and schists (Figure 2.2) from greenschist to amphibolite facies. The LRC phyllites are characterized by an assemblage of primarily quartz, muscovite, plagioclase, and organic matter, ± chlorite, calcite, epidote, tourmaline, titanite, Fe-Ti oxides, and sulfides. Most phyllites are fine-grained, carbon-rich and form continuous bodies that may be traced for several kilometers along strike. However, some samples taken from near the poorly resolved LRC-PPU boundary variably host porphyroclasts of plagioclase, quartz, and a high-relief inclusion-rich mineral interpreted as titanite. Porphyroclasts, irrespective of mineralogy, are typically rounded to subhedral oval grains with their long axis sub-aligned to the foliation plane. Muscovite is the foliation-defining mica, although chlorite is locally abundant. Organic matter is generally present as thin (<10 µm thick) opaque strands which run sub-parallel to the foliation and deform around porphyroclasts and polycrystalline quartz lenses, where present. Occasionally, in quartz-rich phyllites, organic matter is observed as small (<5 µm) discrete anhedral grains in quartz. Phyllites locally exhibit quartz-calcite veining that crosscuts the foliation. Heavily veined phyllites may develop a porous texture wherein the margins of void spaces (<2 cm) exhibit drusy quartz habits and are commonly associated with orange-yellow sulfidic staining.

In upper greenschist and amphibolite facies, biotite schists predominate, with a typical porphyroblast assemblage of garnet, ± staurolite and andalusite (locally *var*. chiastolite). The garnet and staurolite isograds occur in mutual proximity (Figure 2.2), but generally do not overlap as interpreted by Jakob et al. (2016). The matrix mineral assemblage includes quartz, plagioclase, biotite, muscovite, graphite, ilmenite, ± chlorite, sillimanite (*var.* fibrolite), epidote, calcite, sulfides, zircon, and tourmaline. The schists typically host annealed quartz-rich bands that are ≤2 cm wide, though may locally be wider. Most schists consist of a quartz- and organic-rich matrix, producing dark grey to black blocky outcrops that are not fissile.

Andalusite forms porphyroblasts commonly larger than either garnet or staurolite (Figure 2.3), and locally as megacrysts up to 8 cm in diameter (mean, $\mu = 0.5 – 1$ cm). Andalusite also locally forms in stretching lineations, where grain fragments occur as boudins in linear segments that extend up to 50 cm. While sometimes preserved as euhedral to subhedral grains, andalusite is commonly wholly or partially replaced by an assemblage of sericite, chlorite, and quartz. Andalusite porphyroblasts also host monomineralic inclusions of sulfides, ilmenite, and occasionally polymineralic fragments of matrix including quartz, feldspar, and biotite, suggesting rapid growth. Where grown in proximity, andalusite porphyroblasts are embayed by staurolite, and in one instance andalusite partially overgrows a euhedral garnet.

Garnet porphyroblasts occur as small, euhedral to subhedral grains up to 0.5 mm in diameter. Most garnets exhibit relatively few inclusions (e.g., Figure 2.3 a), although high grade samples such as those adjacent to the Bear Creek Shear Zone have poikiloblastic garnets up to 1 cm diameter, with inclusions of quartz, plagioclase, ilmenite and chlorite. Unlike andalusite, garnet porphyroblasts are observed to both be deformed within, and overprint, the foliation at different outcrops. Garnets are also commonly restricted to centimeter-scale layers in outcrop and are not homogenously distributed throughout the rock matrix. Euhedral to subhedral garnets are locally observed to grow on, or within the rims of anhedral staurolite (Figure 2.3 e).

Staurolite porphyroblasts are highly variable in size, up to approximately 1 cm in length, and are commonly anhedral to subhedral with a poikiloblastic texture (Figure 2.3 c, e). Staurolite penetration twins are common but generally fragmented or deformed, leaving a subhedral grain with the interface of the twins exposed, recognizable by differences in extinction in cross polarized light, and differential presence or paucity of inclusions. Unlike the garnet or andalusite porphyroblasts, staurolite commonly hosts partial or complete graphitic inclusion trails which may be parallel to, or rotated from, the foliation plane.

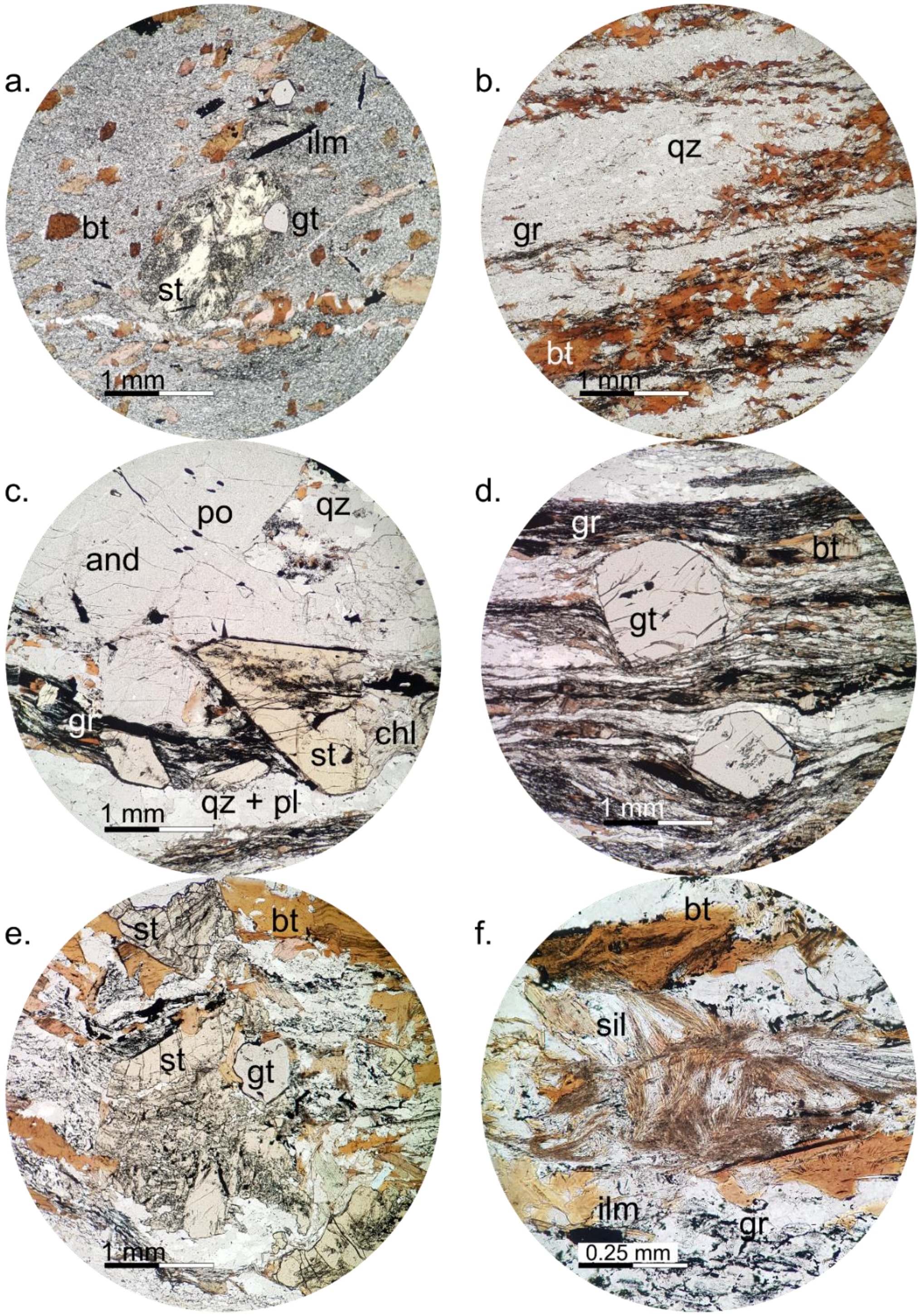

Figure 2.3 (*Previous Page):* Thin section photomicrographs with abbreviations after Whitney & Evans (2010). *a:* Spotted st-gt-bt hornfels (AG049-1), showing a rare non-foliated matrix with strongly anhedral staurolite and subhedral garnet in a fine-grained qz-graphite (gr) matrix. *b:* Quartz-rich paragneiss (AG121), showing subsidiary layers of gr and bt with minor Fe-oxides. *c:* A coarse and-schist (AG042) showing st embaying and. *d:* Same sample as *c*, showing gt porphyroblasts caught in the deformation in a qz-pl-gr-bt matrix. *e:* Strongly anhedral st with graphitic inclusion trails breaking down to form gt in the sillimanite schist AG041. *f:* Fibrolite nucleating on matrix bt and overgrowing matrix qz (AG041).

Biotite is the most modally abundant mica in the LRC schists. Biotite grains are generally intact and not significantly retrogressed, although a few samples locally are altered to chlorite and associated with acicular opaque needles that are likely Ti-oxides. In samples with significant modal carbonaceous matter, biotite commonly exhibits graphitic trails which may run parallel to, or are rotated from the foliation plane. Growth rims, and biotite precipitated in fractures of pre-existing biotite grains do not host these graphitic trails. Intergrowths of subhedral chlorite and biotite are observed in numerous samples, with intact graphitic trails that traverse both continuously. Biotite typically forms as anhedral grains or clots of grains and may partially overgrow porphyroblasts of garnet and staurolite.

Sillimanite (*var.* fibrolite) is observed in a minority of schists in the central LRC as knots of fibrous, elongate needles that nucleate on matrix biotite but commonly overprint matrix quartz grains (Figure 2.3 f). Sillimanite and andalusite are generally mutually exclusive, although some andalusite-bearing outcrops exhibit fine-grained needles in the rims of garnet porphyroblasts that might be sillimanite. Sillimanite schists are correlated with larger-than-average garnet porphyroblasts that exhibit poikiloblastic textures primarily comprising quartz and ilmenite, and anhedral morphologies.

The most common opaque phases in the LRC pelitic rocks include carbonaceous matter (graphite at high grade), sulfides, and ilmenite. Ilmenite generally forms ≤1 mm poikiloblastic laths (Figure 2.3 a,d,f) hosting primarily quartz inclusions. Ilmenite may be rotated and deformed in the direction of the foliation, and with pyrrhotite constitutes the most abundant inclusions observed in the staurolite and garnet. Zoned green-brown tourmaline crystals are common accessory phases in the matrix, and are generally <0.5 mm, though elongate grains can occasionally range up to 0.4 mm in maximum length. Lenses of tourmalinite schist occasionally occur in proximity to outcrops of the Tripp Creek metabasite.

While the majority of pelitic rocks have a clearly developed schistose foliation, two samples collected from disparate locations exhibit a spotted texture. Within the biotite zone in the central LRC, a black, fine-grained garnet staurolite spotted hornfels was identified in proximity to a fine-grained felsic sill (Figure 2.3 a). Therein, euhedral garnet, subhedral biotite, and anhedral staurolite overprint the quartz-plagioclase-graphite matrix. The second sample was collected in Port Renfrew adjacent to a large (~10 m wide) tonalitic sill. Between the pyrite-bearing carbonaceous phyllite and the metatonalite intrusive, a ~1 m contact zone exhibits a spotted texture that overprints the phyllitic foliation. The mineral assemblage, including the porphyroblasts, is entirely replaced by calcite, chlorite and siderite, and the pre-existing porphyroblast is unknown, but is speculated to be cordierite on the basis of grain morphology.

Psammitic Protoliths

Metapsammitic rocks occurring in the chlorite zone comprise mostly quartz (up to greater than 90 modal percent) with smaller proportions of plagioclase, muscovite, feldspar, carbonaceous matter, and Fe-Ti oxides (Figure 2.3 b). Metapsammitic rocks outcrop as dark grey, thermally annealed massive successions. In the biotite zone, there is little variation in mineral assemblage except for the appearance of biotite, and local horizons of garnet porphyroblasts. In the west central LRC, a thick metapsammite unit on strike with the Valentine Mountain unit outcrops as paragneiss exhibiting distinct compositional banding. The paragneiss assemblage includes quartz, plagioclase, potassium feldspar, biotite, graphite, ± garnet porphyroblasts. Where present, garnet porphyroblasts are larger than those in typical pelite schists (up to 1 mm diameter) and are sub-poikiloblastic with anhedral grain morphology. Inclusions of quartz are more common, as opposed to ilmenite and sulfides which dominate the inclusion assemblage in pelitic porphyroblasts.

Igneous Protoliths

The Tripp Creek metabasite outcrops as submeter to decameter scale sills inter-foliated with the pelitic and psammitic successions of the LRC, and are most abundant in the Valentine Mountain region.

The Tripp Creek metabasites outcrop less frequently in the chlorite zone (as defined in pelitic compositions), but where they do are characterized by an assemblage of epidote-clinozoisite, chlorite, plagioclase, quartz, and subsidiary Fe-oxides. One exceptional outcrop hosts large 50 μm to 1 mm (μ = 0.4 mm) euhedral poikiloblastic magnetite porphyroblasts that overprint the surrounding foliation. Locally, epidote forms large porphyroblastic clots of numerous grains (<0.5 mm) in quartz and plagioclase-rich layers. At the biotite isograd, an exposure of the Tripp Creek metabasite outcrops as an actinolite schist, with a mineral assemblage of fine to medium-grained actinolite, epidote-clinozoisite, plagioclase, chlorite, ilmenite, pyrrhotite, chalcopyrite, and biotite. Plagioclase-rich layers host clots of strongly zoned epidote-clinozoisite, as observed in lower grade samples. Samples collected from this locality (AG137) exhibit a bimodal size distribution, including very fine-grained ≤2 cm wide lenses of acicular amphibole and chlorite, imbricated within a medium-grained actinolite, plagioclase, epidote, and ilmenite assemblage.

Most of the Tripp Creek metabasite outcrops as medium to coarse-grained foliated amphibolites comprising zoned tremolite-hornblende amphibole, plagioclase, quartz, epidote, chlorite, biotite and ± garnet. Several outcrops of foliated metabasite near Valentine Mountain hosted microcrystalline pink-orange bands of garnetite, from ~1 mm to 5 cm thick (Figure 2.4). While garnet occasionally occurs in the interstitial matrix between amphibole laths, most is limited to the garnetite bands. Outcrops in which garnetite bands are present are characterized by an absence or significant reduction in the modal abundance of plagioclase feldspar, and comparatively more quartz. Banded amphibolites are locally interfoliated with, and occasionally boudins within, the psammitic paragneisses in the central LRC. As with other units in the LRC, no primary textures persist at any grade for the Tripp Creek metabasites, and all layers are transposed into parallelism with the hosting sedimentary protoliths. While the Tripp Creek metabasites frequently outcrop in proximity to the highest-grade rocks in the terrane, there is no obvious increase in porphyroblast abundance or size toward sill margins in the country rock.

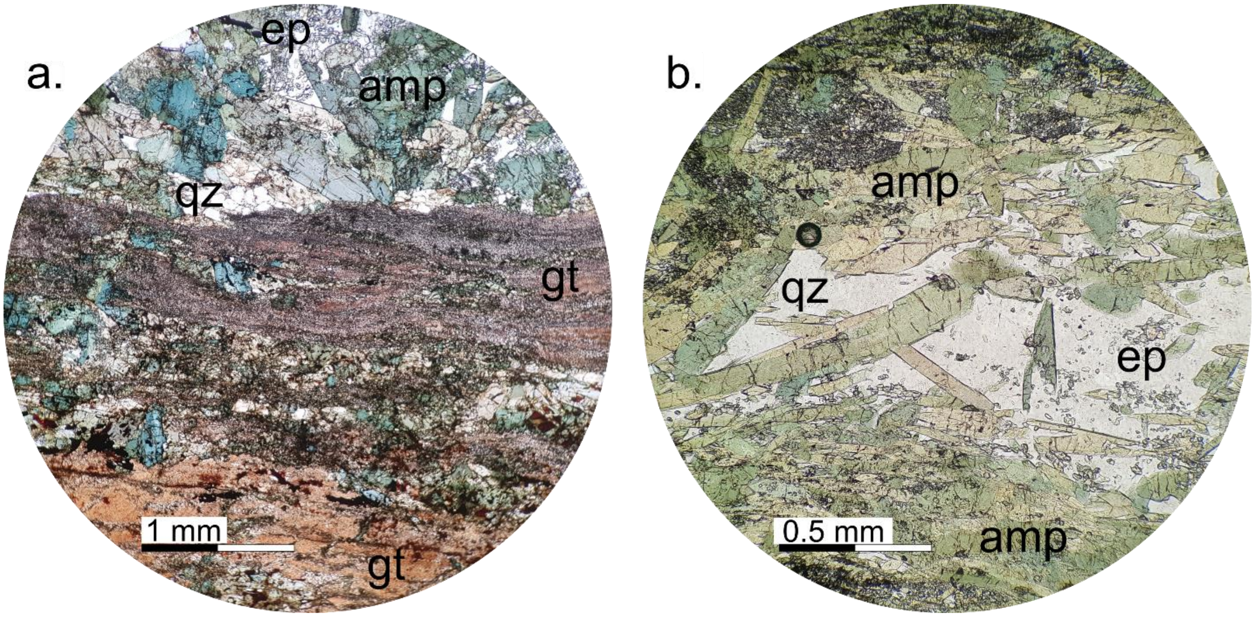

Figure 2.4 PPL photomicrographs of metabasite AG069-2. *a:* Foliated, fine-grained garnetite bands run parallel to the foliation defined by the coarse-grained amphibole laths. *b:* The typical mineral assemblage of AG069-2 distal to the garnetite banding. Note the conspicuous absence of plagioclase, and patchy epidote in the interstices between amp laths.

In the central LRC, weakly foliated felsic sills are interfoliated with the metasedimentary rocks. Sills range from <0.5 m up to tens of meters in width, and can occasionally be traced for hundreds of meters along strike. Most sills are tonalite and are distinguished from the psammitic rocks by a greater abundance of plagioclase feldspar and consequently a paler white colour in outcrop. Locally, the felsic intrusions may host trace quantities of small (<0.5 mm) diameter garnets. The felsic intrusions are generally not observed to outcrop in the chlorite zone and are exclusively observed interfoliated with the LRC and not the PPU. However, there is generally no observed increase in the abundance or size of any porphyroblasts in the meta-sedimentary units adjacent to the sills, bar the two exceptions outlined above. Within one sill near the Leech River fault, <10 cm long foliated fragments are hosted within the tonalite (Figure 2.5). Groome et al. (2003) identified these fragments as xenoliths of the surrounding schist, however the mineral assemblage comprises exclusively biotite and subsidiary quartz, which is not observed elsewhere in the field area.

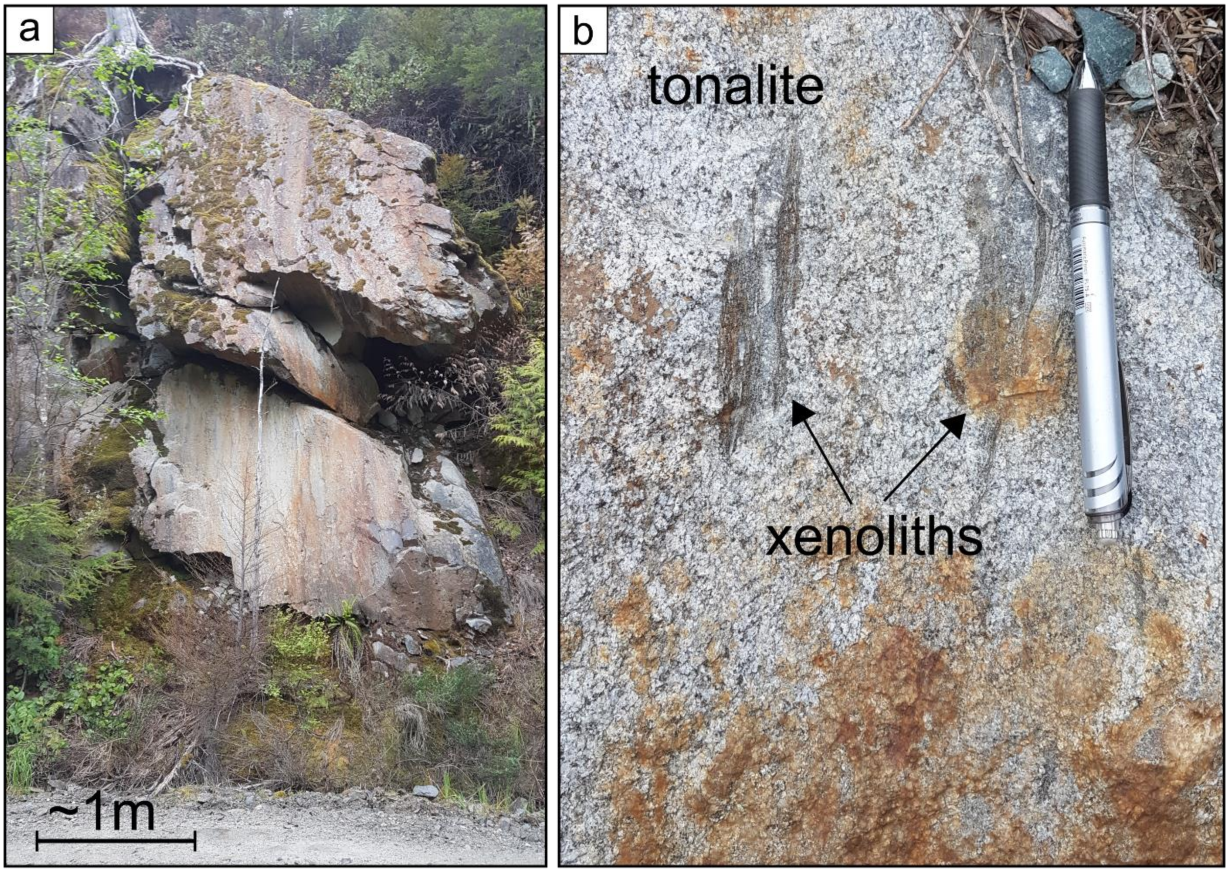

Figure 2.5 Field images of the Walker Creek intrusion suite. *a:* A large felsic sill in the south central LRC exposed by differential weathering of the surrounding schists. *b:* Foliated bt-rich xenoliths hosted in a ~tonalite sill located within 0.5 km of the Leech River Fault.

2.2.2 Pandora Peak Unit

The Pandora Peak Unit outcrops along the northern and eastern margins of the LRC, along an inferred fault boundary for which no clear exposure has been identified. The PPU comprises numerous lithologies such as clastic tectonites, argillites and metabasalts, as well as rocks that are not pervasively deformed, including banded green and blue cherts, radiolarian cherts, metaultramafics, and clastic metasediments, and carbonaceous phyllites. One outcrop in Victoria exhibits mylonitic deformation near an inferred fault contact with Wrangellia (Figure 2.6 f). Most clastic metasedimentary rocks primarily comprise clasts of quartz, sericitized plagioclase and potassium feldspar, epidote, and locally hornblende.

The metamorphic parageneses of the PPU metasediments is difficult to assess since equilibrium is only variably achieved (Rusmore & Cowan, 1985). Where identifiable, metamorphic minerals include zeolites, chlorite, muscovite, prehnite, ± pumpellyite, calcite, iron oxides and sulfides. One outcrop of a grey-blue clastic tectonite at Gonzalez Bay in Victoria hosts subhedral lawsonite that has grown in the matrix between quartzofeldspathic clasts (Figure 2.6 a), and another in Finlayson arm hosts prehnite + pumpellyite + lawsonite in veins within a radiolarian chert (Figure 2.6 e).

Metabasalts in the PPU outcrop as heavily deformed pale grey to mint green sub-greenschist rocks with cryptic mineralogy not discernable in hand sample. In Victoria, the metabasalt occurs as <1 m long boudins in a tectonized argillite matrix, but this study did not identify the interpreted metabasalt pillow structures identified by McEwen (2013). Northwest of Port Renfrew, a similar grey, altered metabasalt was observed interfoliated with a carbonaceous, pyritic metasediment.

Three outcrops of sandy tectonized phyllites along the northern margin of the PPU also host discontinuous blocks and lenses of serpentine-chlorite-spinel bearing rocks (Figure 2.6 c,d). The blocks range in diameter from less than a meter to several meters and have a distinct greasy facoidal appearance at the margins. The pelitic matrix deforms around the blocks, and hosts several other lithologies including psammites and white, chalky rocks. Thus, the blocks are interpreted as meta-ultramafic rocks that show pervasive alteration, including extensive replacement of an unknown mineral, possibly a pyroxene, by a carbonate (Figure 2.6 d). One block is entirely serpentinized after coarse, interlocking grains that were possibly olivine. Spinel euhedra and patchy carbonate pseudomorphs occur in the interstices between the serpentinized grains. The margins of the serpentinite blocks show no indication of thermal metamorphism and are tectonically interleaved with the host metasedimentary rock. The meta-ultramafics are only observed in close proximity to the San Juan fault, and were not identified elsewhere in either the PPU, or LRC.

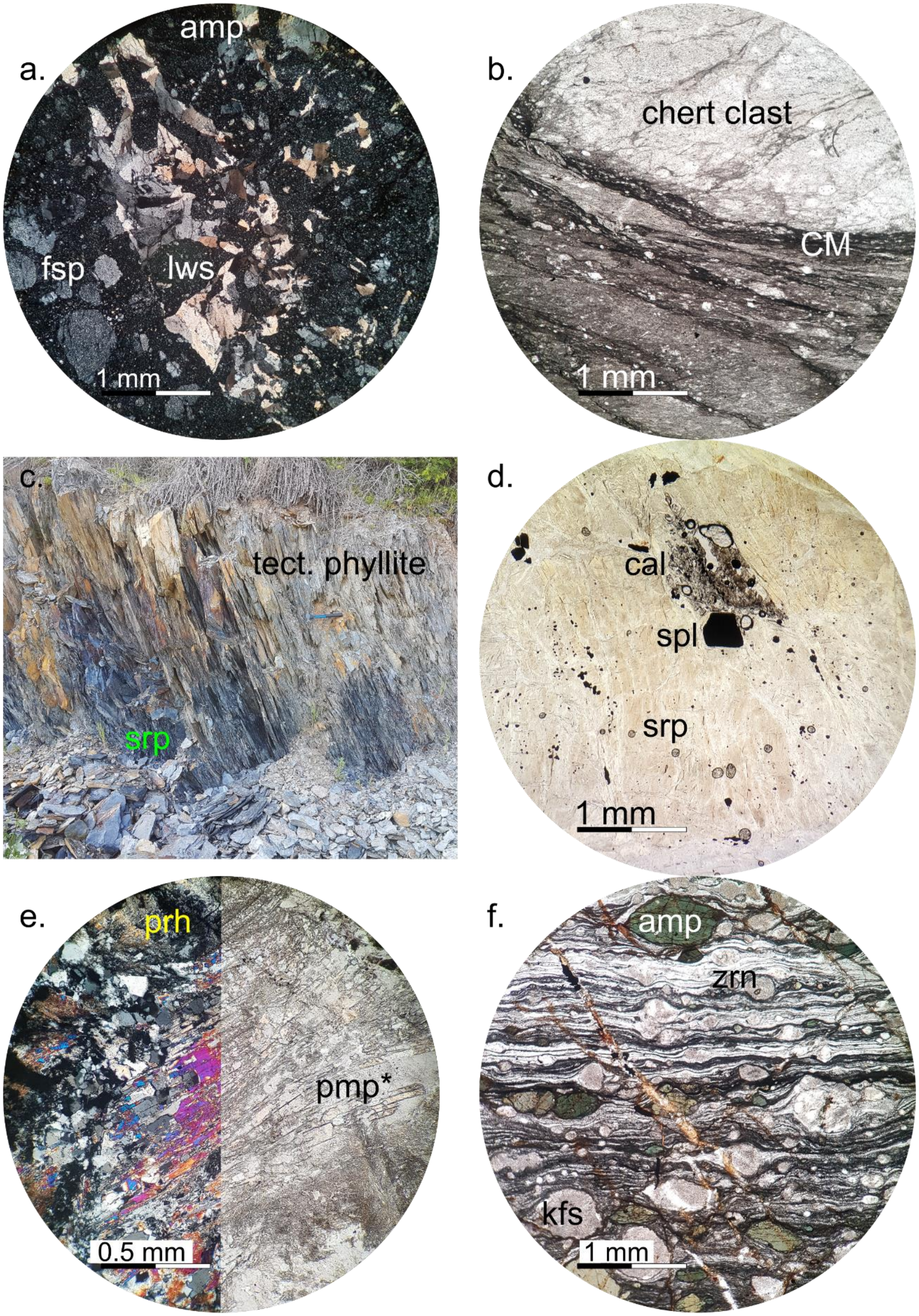
a.
amp
fsp
lws
1 mm
b.
chert clast
CM
1 mm
c.
tect. phyllite
srp
d.
cal
spl
srp
1 mm
e.
prh
pmp*
0.5 mm
f.
amp
zrn
kfs
1 mm

Figure 2.6 (*Previous page*) Photomicrographs and images of PPU rocks. *a:* Patchy lawsonite (lws) and qz assemblage in a low-grade clastic rock from Gonzalez Bay, Victoria (AG002). *b:* A pebbly tectonite with a CM-rich matrix deforming around a large chert clast (AG019). *c:* Image (hammer for scale) showing the blocks of facoidal serpentinite near the SJF, interfoliated with a tectonized sandy (CM-bearing) pelite matrix (AG097). *d:* Photomicrograph of a meta-ultramafic taken from the core of a serpentinite (srp) block at station AG097 (*image c)*, showing mesh vein textures and euhedral spinel. *e:* Prehnite-pumpellyite (± lws, not imaged) vein assemblage in a fractured radiolarian chert (AG013). *f:* Mylonitized clastic fault rock from the boundary of the PPU with the Westcoast Crystalline Complex in Victoria (MVDB09-33).

2.3 Methods

2.3.1 Sample collection and preparation

Rock samples were collected directly from outcrop with due care to select a representative sample size of the broader outcrop and to minimize weathering rinds or other alteration. At stations with substantial local compositional variation, multiple samples were collected. Carbonaceous metasedimentary rocks were collected where possible at each station for use in RSCM geothermometry (see below). Sample cutting and the polishing of puck mount samples was performed at the University of Victoria. Foliated samples were cut perpendicular to the foliation for consistency, and any weathering rinds were removed prior to further processing.

2.3.2 Bulk Rock Geochemistry

Samples selected for whole rock major and trace element analyses were cut into slabs at the University of Victoria and crushed using a steel jaw crusher at the British Columbia Geological Survey. Powdering was completed at either the University of Victoria using benchtop planetary agate ball mill, or at Activation Laboratories Ltd with mild steel to 95% passing a 105 µm filter. For samples processed at the University of Victoria, the mill was cleaned with a quartz sand wash between each sample set. Bulk rock analyses for major and trace element geochemistry were performed at Activation Laboratories Ltd in Ancaster, Ontario. Major oxide analyses were analyzed by lithium metaborate/tetraborate fusion, dissolved in 5% nitric acid, and analyzed by ICP-OES. For samples in which major oxide analyses were not performed, total Fe was also determined via INAA. Trace elements are also determined via lithium metaborate/tetraborate method and analyzed by ICP-MS, plus select elements including As and Sc were determined by INAA. Total C and S analyses were measured at Activation Laboratories Ltd via IR detection of SO_2 and CO_2 from 0.2 g of combusted sample material in a high oxygen environment.

2.3.3 Raman Spectroscopy

Carbonaceous Matter (CM) in metasedimentary rocks undergoes a unidirectional graphitization reaction with progressive metamorphism, and thus is a generally reliable recorder of peak metamorphic conditions (Beyssac et al., 2002a; Beyssac et al., 2002b). Raman Spectroscopy of Carbonaceous Materials (RSCM) thermometry interrogates the structural changes of CM during graphitization with a Raman spectrometer, yielding temperature-dependent spectra which have been calibrated against independently determined estimates of peak metamorphic temperature (Beyssac et al., 2002a; Aoya et al., 2010; Kouketsu et al., 2014; Lünsdorf et al., 2017). Empirical RSCM geothermometers are valid for rocks which have undergone metamorphism from <200 °C, up to approximately 600 °C, above which all CM is converted to graphite and the geothermometer is rendered inapplicable. In this study, the RSCM geothermometer was applied to argillites, phyllites, schists and CM-bearing metapsammitic rocks from wide areas of the LRC and the PPU. Once any weathering rind was removed, samples were cut perpendicular to the dominant foliation if developed, such that CM grains were likelier to be in the same orientation between samples. Samples were prepared as both 30 µm thick polished thin sections and puck mounts. Polishing on puck mounts proceeded to a minimum 1 µm diamond suspension grit.

RSCM was performed using the Renishaw inVia microRaman system at the University of Victoria’s Facility for Imaging, Photonics & Spectroscopy. At least ten CM grains per sample were analyzed where possible using a 532 nm laser, 50x objective and grating of 2400 l/mm at 1 to 5% power for at least 30 seconds, collected over a Raman Shift window of 700 cm^{-1} to at least 2000 cm^{-1} to provide a consistent baseline across all analyses. To minimize structural artefacts induced by polishing (Pasters, 1989), CM grains hosted within or below transparent minerals such as quartz and calcite were selected where possible, including all analyses of medium and high grade rocks (> 400 °C). Low grade samples lacking defined foliation or transparent minerals of sufficient grain size had their matrix CM analyzed directly, which recent workers suggest has little impact on the temperature estimate for low grade samples (Lünsdorf et al., 2017). If CM hosted below transparent minerals and at the surface were visible within the same sample, both were analyzed for comparison. Any Raman spectra where the maximum signal peak intensity was lower than the background fluorescence, or signal interference from other phases identified using CrystalSleuth (Laetsch & Downs, 2006) and comparison with expected CM signal peak positions (after Kouketsu et al., 2014).

Processing of Raman spectra for geothermometry was performed using the Iterative Fitting of Raman Spectra (IFORS) algorithm and calibration curve developed by Lünsdorf et al. (2017) to minimize operator bias introduced during the curve fit process. The operator sets the integration window, the number of repetitions, sensitivity factors for distinguishing noise and signal, polynomial type, and any Raman Shift (cm^{-1}) window to be ignored due to signal contamination from other phases. No information on the location or number of peaks to be fit is prescribed. The IFORS algorithm performs a polynomial baseline correction and calculates two Scaled Total Area (STA) parameters, scaled to the maximum intensity values of the D-Band and G-Band in the spectra. Resulting STA parameters are then run against a calibration curve to calculate an estimate of peak metamorphic temperature with a calibration uncertainty of ± ~37 °C (Lünsdorf et al., 2017).

As a test of the robustness of the IFORS geothermometer method, a selection of samples from across grade were also calibrated with the protocols of Kouketsu et al. (2014) and Aoya et al. (2010). Spectral baselines were removed by manually fitting a curve to subtract the fluorescence, with points set at specific Raman shift intervals to maintain consistency between analyses. Using the open-source software Fityk (Wojdyr, 2010), pseudo-voigt functions were assigned to each spectral peak area as prescribed in Kouketsu et al. (2014) and Aoya et al. (2010), and the pseudo-voigt shape parameters are adjusted to attain the best fit with the spectra by minimizing the chi-square parameter through Levenberg-

Marquardt curve-fitting. Samples with estimated metamorphic temperature below 400 °C were calibrated using the Full-Width-Half-Maximum (FWHM) calibration (Kouketsu et al., 2014), and the calibration by Aoya et al. (2010) for those greater than 400 °C.

2.3.4 EPMA & SEM

Electron microprobe analyses for major and select trace element concentrations of garnet, biotite, plagioclase, staurolite, chlorite, epidote, and amphibole were measured at the University of Alberta using the JEOL JXA-8900R using the wavelength dispersive spectrometer (WDS) at an accelerating voltage of 20 kV and current of 20 nA. Spot analyses were performed with beam diameter set at between the minimum (1 µm) and 2 µm spot size, with 20 seconds on peak and 10 seconds on background for each element analyzed.

Garnet-biotite pairs were selected to minimize samples with any chloritization of biotite, or numerous inclusions of silicate minerals or graphite. Nonetheless, the preponderance of graphitic biotite contributed to lower totals among some analyses. Garnet-biotite pairs were also selected to be in reasonable proximity and thus within probable equilibrium volume. Grains in mutual contact were included, with multiple biotite analyses in transects away from the boundary to assess any degree of retrograde equilibration.

The garnet-biotite geothermometer of Ferry & Spear (1978), henceforth FS78, and geothermobarometer of Wu (2017), henceforth Wu17, are applied to quantify variability from symmetric and asymmetric Margules interaction parameters and imposed estimates of Fe^{3+} content in garnet (Fe^{3+} / [Fe^{2+} + Fe^{3+}] = 0.03) and biotite (Fe^{3+} / [Fe^{2+} + Fe^{3+}] = 0.113) as proposed by Wu (2017). The temperature and pressure dependencies of the Margules parameters introduced by Holdaway (1997; 2000) and modified by Wu (2017), were solved iteratively with a MATLAB script adapted from the spreadsheet of Wu (2017), using the FS78 temperature as the initial guess. The Wu17 model utilizes an adapted version of the Holdaway (2000) (H2000) geothermometer but is only applicable to parageneses which include an aluminosilicate due to the integrated Garnet-Biotite-Aluminosilicate-Quartz (GBAQ) geobarometer based on the equilibria (Wu, 2017):

$$Fe_3Al_2Si_3O_{12} + 3K(Fe_2Al)(Si_2Al_2)O_{10}(OH)_2 + 4SiO_2 = 3KFe_3(AlSi_3)O_{10}(OH)_2 + 4Al_2SiO_5 \textbf{ [1]}$$

$$Mg_3Al_2Si_3O_{12} + 3K(Mg_2Al)(Si_2Al_2)O_{10}(OH)_2 + 4SiO_2 = 3KMg_3(AlSi_3)O_{10}(OH)_2 + 4Al_2SiO5 \textbf{ [2]}$$

Thus, two samples (AG116-1 and AG049-1) were iteratively calculated using model H2000 and a fixed estimated pressure of 4 kbar based on results for nearby stations and the occurrence of fibrolite and andalusite in proximity to one another.

Scanning electron microscopy was performed for mineral identification and backscatter imaging at the University of Victoria’s Advanced Microscopy Facility using a Hitachi S-48000 field emission scanning electron microscope equipped with a Bruker Quantax EDS system. Acceleration voltage was selected at 20 kV and current at 20 µA.

2.3.5 Pseudosection Models

Pressure-Temperature (P-T) and Temperature-Composition (T-X) pseudosections were prepared in the Perple_X Gibbs free energy minimization package (Connolly, 2005) using major element analyses from this study. P-T pseudosections were calculated between 2 – 6 kbar and 400 – 700°C. In all cases, the system Mn-Na-Ca-K-Fe-Mg-Al-Si-H-Ti-O (MnNCKFMASHTO) was used with C as a saturated component. Solution models after White et al. (2014) were used for garnet, biotite, staurolite, chlorite, epidote, white mica, ilmenite, and cordierite, and the ternary feldspar solution after Fuhrman & Lindsley (1988) was utilized. Fluid was not explicitly set as a saturated phase and was instead modelled using a generic COH-fluid model utilizing a hybridized equation of state from the pure components. Nitrogen, sulfur, and fluorine-based species were automatically excluded, leaving the fluid to vary between CO_2, CH_4, CO, H_2, and H_2O. Molar H and O were artificially inflated above LOI values in a ratio of 2:1 in the specified composition to ensure the fluid-present conditions. While no explicit redox buffers were imposed, the specified ratio of H:O was set with fractionally less O_2 to favour reduced conditions consistent with graphitic pelites. Importantly, solution models for melt are not compatible with the COH-fluid model, and thus melt phases were excluded, and supra-solidus pseudosection results may be less reliable in the very low-pressure (< ~2 kbar), high temperature (> ~650 °C) domain of the models.

2.3.6 Geochronology

One sample of banded blue chert interfoliated with a grey, sandy metapelite was submitted to the University of British Columbia's PCIGR for CA-TIMS analysis. After crushing and mineral separation, crack- and inclusion-free zircons were documented and annealed at 900 °C for 60 hours. Zircons were then treated successively by acetone, 6 N HCl, and finally a solution of 50 µL 50% HF and 5 µL 14 Normal HNO_3. Each solution is then spiked with EARTHTIME ET535, and dissolved in a 10:1 HF:HNO_3 solution for an additional 40 hours at 220 °C. Solutions were then dried, dissolved in HCl at high pressure, again dried, and then analyzed using a thermal ionization mass spectrometer.

2.4 Results

2.4.1 Bulk Rock Geochemistry

Major oxide analyses for three carbonaceous metapelitic samples taken from the LRC are compositionally similar from low greenschist to amphibolite facies (Table 2.1). LOI values show a decrease from 4.13 wt% in the argillite to 2.34 wt% in the fibrolite schist, while total C content among the three metapelitic samples does not show systematic variation with grade and remains within 0.6 – 1 wt% C. Total Fe for the full metasediment sample suite, shows more significant variation (1.8 to 8.2 wt% Fe). Excluding the quartz vein AG128 and the pyritic cataclasite AG089-2, the range is significantly reduced (2.6 to 6.6 wt% Fe).

Major oxide analyses of the Tripp Creek and Pandora Peak metabasites also show little systematic variation with metamorphic grade. The Total Alkali Silica (TAS) system classifies all metabasite samples as basalt, except AG089-1, which narrowly falls in the picro-basalt field. The garnet-banded amphibolite AG069-2 has an MnO value of 1.36 wt%, while the average for all other metabasite samples is 0.22 wt% (1σ = 0.05 wt%). The magnesium number (molar [Mg / Mg + $\mathrm{Fe_T}$] ×100) values for the metabasites vary from 37.3 to 64.3 (μ = 51.0, 1σ = 9.4). LOI data are negatively correlated with metamorphic grade, sub-greenschist and greenschist facies metabasites have 2 – 4 wt% LOI, compared to values of ~1 wt% LOI in amphibolite facies. Whole rock magnesium numbers for the three meta-peridotite samples collected from the PPU are all >90. AG136-2, the only other meta-igneous sample analyzed, is classified as an andesite by the TAS classification.

Normalized against the North American Shale Composite (NASC, Condie et al., 1993), most metasedimentary rock samples have flat REE profiles that fall marginally below 1. Three samples have significantly lower normalized concentrations than the other metasedimentary rocks, including a sample comprising a sulfidic coarse quartz-veined schist. All the REEs, Th, and U show no systematic variation with metamorphic grade. The large ion lithophile elements (LILE) generally exhibit greater variability across metamorphic grade. Despite similarities in major oxide chemistry, the metatuff AG136-2 exhibits an elevated REE concentrations relative to the metasedimentary samples and significantly higher Th and U values relative to NASC. The pyritic cataclasite AG089-2 is distinct from the rest of the metasediment suite due to a positive Eu anomaly and lower Th and U. Additionally, AG089-2 has total C content of 1.27 wt%, double the metasediment suite average (μ = 0.59 wt% 1σ = 0.29 wt%).

In the metabasite suite (n = 9), multi-element plots show two groups distinguished by light REE values. Group 1, which comprises solely samples from the Tripp Creek metabasite, exhibits light REE depletion relative to the heavy REE (Figure 2.7). The Group 2 metabasites, which comprises the two samples from the PPU and two from the Tripp Creek unit, show significant light REE enrichment relative to heavy REE and relative to the Group 1 metabasites. All REE and high field strength elements shows no systematic variation with estimated metamorphic temperature, as observed in the metasediment suite.

Table 2.1 Whole rock geochemical data determined by ICP-OES.

		Detection Limit (%)	0.01	0.01	0.01	0.001	0.01	0.01	0.01	0.01	0.001	0.01		0.01
Sample	**Name**	**Rock Type**	**SiO_2**	**Al_2O_3**	**Fe_2O_3 (T)**	**MnO**	**MgO**	**CaO**	**Na_2O**	**K_2O**	**TiO_2**	**P_2O_5**	**LOI**	**Total**
LC 12	Chl Phyllite	Metabasite	49.06	16.01	10.35	0.17	7.61	11.31	2.52	0.13	1.11	0.09	2.46	100.8
AG 055-1	Chl Mt Schist	Metabasite	49.33	17.36	10.93	0.17	4.35	7.66	3.45	0.51	1.43	0.16	3.09	98.44
AG 059	Amphibolite	Metabasite	45.83	18.98	13.09	0.20	4.07	9.39	3.52	0.69	2.51	0.39	0.77	99.44
AG 069-2	Gt Amph.	Metabasite	45.64	15.61	12.49	1.36	6.32	12.56	2.07	0.22	1.57	0.25	1.09	99.19
AG 069-3	Amphibolite	Metabasite	49.74	15.2	10.3	0.33	8.22	10.55	3.04	0.53	1.58	0.15	1.03	100.7
AG 070-2	Amphibolite	Metabasite	48.74	17.21	9.78	0.26	6.99	12.52	2.17	0.16	1.13	0.19	1.00	100.2
AG 121-2	Amphibolite	Metabasite	47.68	15.88	12.11	0.27	6.6	13.51	1.49	0.32	1.63	0.15	0.95	100.6
AG 137	Act Schist	Metabasite	46.95	17.29	9.68	0.17	8.81	11.42	2.63	0.18	1.38	0.12	2.16	100.8
AG 089-1	Metabasalt	Metabasite	44.4	20.78	11.13	0.27	3.34	12.57	1.49	0.28	1.46	0.2	4.82	100.7
AG 105-4	Metabasalt	Metabasite	49.34	18.61	11.57	0.21	4.34	9.34	3.1	b.d.l.	0.83	0.13	3.32	100.8
AG 095-2	Metabasalt	Metabasite	46.86	12.81	13.16	0.20	7.46	8.86	2.8	0.42	2.10	0.28	4.04	98.99
AG 136-2	Metatuff	Metavolcanic	61.25	16.54	6.82	0.23	2.72	2.05	6.2	0.04	0.75	0.34	2.59	99.53
AG 029-4	Argillite	Metasediment	61.58	17.34	6.62	0.08	2.72	1.08	2.36	2.74	0.81	0.19	4.13	99.65
AG 101-1	Phyllite	Metasediment	61.49	17.68	5.71	0.07	2.36	3.01	1.83	2.87	0.83	0.16	4.03	100
AG 080	Sil Gt St Schist	Metasediment	61.24	18.03	7.73	0.14	3.15	2.27	2.08	2.59	0.89	0.22	2.34	100.7
AG 093-1	Metaperidotite	MetaUM	37.02	0.58	7.96	0.12	37.68	0.17	b.d.l.	b.d.l.	0.01	b.d.l.	16.63	100.2
AG 093-4	Metaperidotite	MetaUM	42.95	0.64	5.93	0.07	38.12	0.02	b.d.l.	b.d.l.	0.00	b.d.l.	12.03	99.77
AG 097-1	Metaperidotite	MetaUM	43.27	0.19	4.84	0.06	38.7	0.38	b.d.l.	b.d.l.	0.00	b.d.l.	12.76	100.2

Table 2.2 Select trace element data for the *n* = 25 metasedimentary, metabasic and metavolcanic samples.

	Group	LRC	LRC	LRC	LRC	LRC	LRC	LRC	LRC	LRC	LRC	LRC	LRC	LRC
	Protolith	metased	metased	metased	metased	metased	metased	metased	metased	metased	metased	metased	metased	metased
DL*	Analyte	AG 029-4	AG 101-1	AG 080	AG140	AG046-3	AG127	AG118	AG049-1	AG054	AG128	AG105-1	AG103-2	AG056
5	V	181	160	194	209	154	178	156	147	136	51	183	147	61
5	Cr	91	77	127	116	96	111	96	68	71	30	104	98	48
1	Co	10	10	19	12	16	19	14	17	6	3	18	8	25
1	Ni	38	21	58	56	55	62	41	42	14	15	63	24	36
1	Cu	23	71	14	50	59	52	39	67	14	13	46	12	38
1	Zn	92	92	104	156	88	118	115	94	99	34	139	105	78
1	Rb	80	83	89	75	86	82	79	96	89	21	84	63	19
2	Sr	185	607	263	134	297	218	250	407	377	114	247	272	114
0.5	Y	23.9	19.6	23.1	34.8	21.3	26.3	21.1	23.2	13.5	8.4	20.9	18.1	11.7
1	Zr	113	113	145	122	120	147	117	118	89	31	99	118	67
0.2	Nb	7.3	8.5	8.8	6.7	7.3	8.5	7.5	8.3	5.8	1.8	6	6.1	3.6
0.1	Cs	3.7	2.7	5	3.4	4.2	3.8	4.1	3.7	4.3	1.1	4.4	2	0.8
3	Ba	931	938	899	770	877	1020	890	961	820	150	770	602	174
0.05	La	19.6	22.3	20.8	32.8	21.2	28.7	20	23.1	13.6	5.77	20.9	19.1	8.77
0.05	Ce	40.8	45.3	42.3	43.5	41.5	55.4	39.4	45.9	27.2	11.9	42	37.3	17.3
0.01	Pr	5.02	5.36	5.07	8.33	5.1	6.64	4.78	5.56	3.23	1.47	4.78	4.34	2.08
0.05	Nd	20.9	21.7	20.9	37.5	20.9	26.7	19.3	22.7	12.9	6.21	18.8	16.9	9.08
0.01	Sm	4.51	4.49	4.49	8.91	4.46	5.57	4.18	4.89	2.67	1.41	3.84	3.67	2.15
0.005	Eu	1.03	1.31	1.17	2.28	1.1	1.25	0.965	1.2	0.727	0.485	0.992	0.88	0.445
0.01	Gd	4.46	4.09	4.19	8.51	4.16	5.07	3.83	4.36	2.42	1.54	3.58	3.15	1.98
0.01	Tb	0.72	0.63	0.67	1.18	0.69	0.79	0.63	0.68	0.36	0.25	0.56	0.5	0.35
0.01	Dy	4.28	3.66	3.97	6.28	3.65	4.38	3.58	3.87	2.17	1.41	3.42	2.88	1.91
0.01	Ho	0.86	0.69	0.77	1.18	0.73	0.9	0.75	0.79	0.45	0.29	0.73	0.6	0.39
0.01	Er	2.47	2.05	2.33	3.22	2.05	2.53	2.06	2.24	1.31	0.75	2.13	1.85	1.06
0.005	Tm	0.375	0.319	0.34	0.484	0.308	0.387	0.31	0.346	0.211	0.119	0.318	0.303	0.167
0.01	Yb	2.55	2	2.23	3.12	2.08	2.52	1.96	2.31	1.41	0.8	2.18	2	1.08
0.002	Lu	0.403	0.311	0.341	0.51	0.313	0.388	0.357	0.332	0.235	0.12	0.36	0.316	0.171
0.1	Hf	3	3.1	3.8	3.3	3.2	3.9	3.1	3.3	2.3	0.8	2.7	2.9	1.7
0.01	Ta	0.55	0.62	0.67	0.43	0.53	0.64	0.56	0.59	0.43	0.14	0.54	0.5	0.31

0.05	Tl	0.39	0.29	0.35	0.31	0.41	0.32	0.32	0.4	0.41	0.09	0.33	0.27	0.06
5	Pb	5	13	13	9	15	11	11	11	12	5	10	15	16
0.05	Th	5.51	6.78	6.58	4.61	6.83	7.92	6.3	6.99	5.47	1.7	7.84	6.2	3.65
0.01	U	1.98	2.29	2.4	1.79	2.08	2.7	2.1	2.72	1.78	0.6	2.66	2.08	1.21
0.01%	Total C	0.62	0.92	0.71	0.53	0.59	0.5	0.65	0.46	0.32	0.2	0.88	0.62	0.15
0.01%	Fe	4.78	4.25	5.53	6.64	4.99	4.95	4.7	4.67	3.82	1.8	8.2	4.66	2.57
0.1	Sc	21.1	17.1	21.7	23.6	16.4	17.5	15.7	14.6	12.4	5.5	16.1	16.9	7

Table 2.2 continued

	Group	LRC	PPU	TCM	TCM	TCM	TCM	TCM	TCM	TCM	PPU	PPU	LRC
	Protolith	metased	metased	metabas	metabas	metabas	metabas	metabas	metabas	metabas	metabas	metabas	metavolc
DL*	Analyte	AG135	AG006-1	LC 12	AG 055-1	AG 059	AG 069-2	AG 070-2	AG 137	AG 105-4	AG 089-1	AG 095-2	AG 136-2
5	V	195	133	273	260	329	377	240	249	251	284	232	141
5	Cr	103	44	297	504	355	318	227	320	13	36	362	108
1	Co	14	16	45	60	66	45	41	45	27	25	51	9
1	Ni	38	28	100	231	183	156	113	126	6	12	241	22
1	Cu	70	56	111	57	45	64	2	69	94	85	59	110
1	Zn	159	103	61	102	106	84	75	64	72	115	116	94
1	Rb	87	60	2	10	22	2	2	1	b.d.l.	5	15	b.d.l.
2	Sr	167	118	186	485	504	364	319	257	329	200	400	226
0.5	Y	28.2	19.5	20.1	30.8	38	34.7	23.6	25.3	19.3	42.1	29.1	34
1	Zr	117	106	57	98	211	109	62	73	24	113	161	167
0.2	Nb	9	4.8	2.5	1.2	14.3	4.7	1.5	1.6	0.3	4.4	13.5	9.2
0.1	Cs	3.7	1.1	0.1	0.4	1.2	0.2	0.4	0.1	0.2	0.6	1.4	b.d.l.
3	Ba	875	465	52	38	130	75	75	8	18	100	341	8
0.05	La	29.1	13.9	3.39	3.39	15.5	9.39	3	2.67	2.8	10.7	16.4	32.6
0.05	Ce	54.7	29.5	8.97	11.3	37.5	14.6	6.88	8.16	7.47	27.3	35.1	53
0.01	Pr	6.68	3.66	1.39	1.93	4.91	3.11	1.45	1.41	1.25	4.24	4.48	8.11
0.05	Nd	27.4	15.1	7.47	10.6	22.3	15.2	7.91	7.85	7.08	21.3	19.8	33.1
0.01	Sm	6.19	3.62	2.51	3.44	6.24	4.33	2.69	2.91	2.24	6.07	5.27	7.17
0.005	Eu	1.24	0.984	1.02	1.35	2.3	1.73	0.952	1.11	0.868	1.74	1.77	1.74
0.01	Gd	5.74	3.62	3.26	4.66	6.85	5.58	3.98	3.87	3.01	6.88	6.03	7.05
0.01	Tb	0.87	0.59	0.56	0.8	1.15	0.94	0.68	0.71	0.5	1.14	0.98	1.07

0.01	Dy	4.88	3.29	3.68	5.36	6.97	6.03	4.36	4.51	3.29	7.22	5.62	6.37
0.01	Ho	1	0.7	0.76	1.13	1.4	1.26	0.9	0.95	0.68	1.51	1.06	1.26
0.01	Er	2.77	2.02	2.16	3.36	3.77	3.63	2.59	2.74	2.08	4.43	2.83	3.51
0.005	Tm	0.414	0.286	0.31	0.511	0.54	0.499	0.372	0.409	0.31	0.655	0.394	0.481
0.01	Yb	2.63	1.86	1.99	3.35	3.57	3.32	2.41	2.66	2.11	4.12	2.46	3.25
0.002	Lu	0.406	0.315	0.317	0.532	0.574	0.534	0.395	0.405	0.325	0.621	0.365	0.528
0.1	Hf	3.3	2.8	1.6	2.3	4.8	2.7	1.8	2.1	0.8	3.2	4	4.5
0.01	Ta	0.65	0.3	0.2	0.07	1.01	0.34	0.21	0.11	b.d.l.	0.24	0.9	0.72
0.05	Tl	0.28	0.27	b.d.l.	0.06	0.11	b.d.l.	b.d.l.	b.d.l.	b.d.l.	b.d.l.	0.08	b.d.l.
5	Pb	10	7	b.d.l.	b.d.l.	b.d.l.	13	b.d.l.	b.d.l.	b.d.l.	b.d.l.	b.d.l.	b.d.l.
0.05	Th	8.88	3.25	0.21	0.09	0.98	0.27	0.07	0.13	0.15	1.34	1.56	9
0.01	U	3.13	1.46	0.07	0.11	0.61	0.35	0.17	0.04	0.06	0.56	0.43	2.64
0.01%	Total C	0.83	0.26	b.d.l.	b.d.l.	b.d.l.	b.d.l.	0.04	0.04	0.17	b.d.l.	0.35	b.d.l.
0.01%	Fe	5.3	4.71	7.34	8.05	9.7	9.28	7.24	7.12	8.42	8.18	9.72	4.96
0.1	Sc	17.4	15.7	37.8	46.7	47.4	37.4	37.3	37	39.6	41.3	24	19

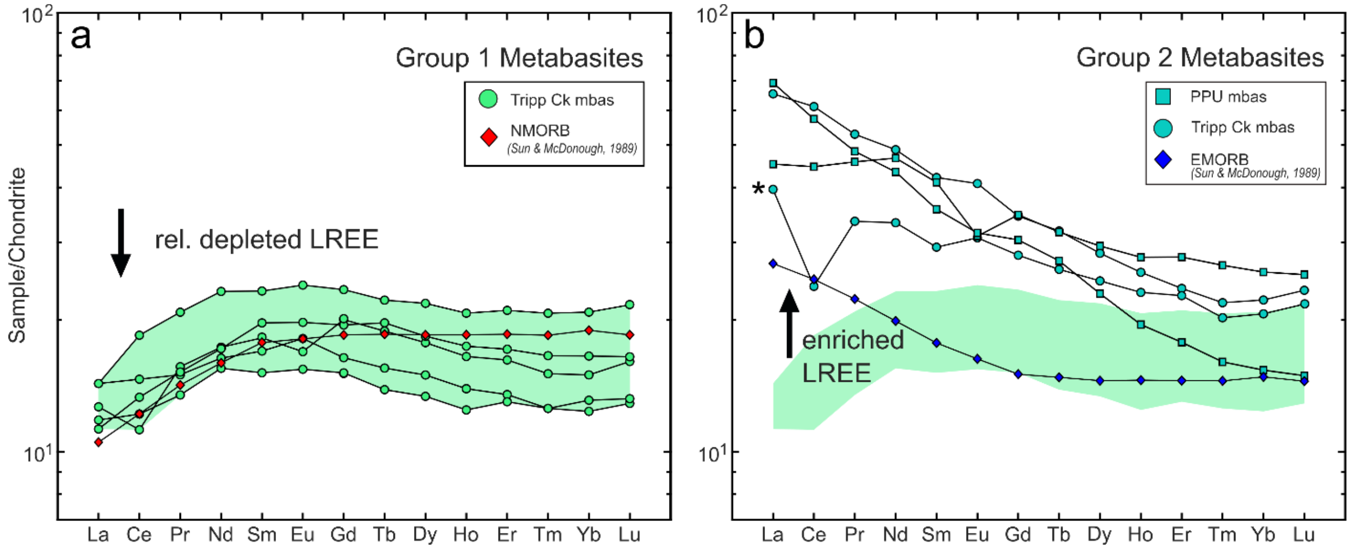

Figure 2.7 REE multi-element plots normalized to chondrite values (GERM). *a:* The Group 1 metabasites, comprising Tripp Creek Metabasites with significant LREE depletion relative to HREE. *b:* The Group 2 metabasites (overlain on Group 1 trace from *a* in green), comprising two TCM samples, and two PPU metabasalts which show significant LREE enrichment above EMORB values. Asterisk indicates sample with interfoliated garnetite bands.

2.4.2 Raman Geothermometry

RSCM analysis of 16 samples yielded a minimum metamorphic temperature of 229 ± 37 °C in the carbonaceous tectonite from the PPU west of Port Renfrew BC, to 584 ± 37 °C in the sillimanite schist AG080 from the central LRC. RSCM temperatures are taken as the simple mean of the temperature estimate for each individual spectrum collected per station (Table 2.3). In all stations, the standard deviation (1σ) is less than the uncertainty of ~37 °C on the calibration using IFORS, and typically 1σ < 20 °C. The data for low-grade (<400 °C) samples, wherein both subsurface and surface carbonaceous matter were analyzed, show no statistical difference, as reported by Lünsdorf et al. (2017). Samples with confirmation analyses performed using the Kouketsu et al. (2014) FWHM method show compatible results. For example, AG006-1 has a T-IFORS of 290 ± 36 °C, while the same spectra yield T-Kouketsu of 301 °C (1σ = 11°C) to 313 °C (1σ = 12°C) depending on baseline selection and subtraction. Similarly, AG030-2 has a T-IFORS of 319 ± 36 °C and a T-Kouketsu of 315 °C (1σ = 12°C). At higher temperatures, AG116-1 has a T-IFORS of 562 ± 37 °C, whereas T-Aoya for the same spectra was 567 °C ($1\sigma = 36$°C). Thus, the IFORS results are consistent with commonly cited RSCM geothermometers.

There exists a broadly monotonic increase in T-RSCM estimates from north to south, with maximum temperatures recorded near the Leech River fault (Figure 2.12). The RSCM temperature of an andalusite schist in the Bear Creek Shear Zone 563 ± 37 °C. The east and western margins of the LRC exhibit a systematic decrease in RSCM temperatures. Near Port Renfrew, RSCM temperature estimates drop from ~540 to 400 ± 36 °C in Port Renfrew over ~4 km. RSCM temperatures of metasediments near sills and metabasites do not show a significant increase relative stations distal from the meta-igneous rocks. Instead, the RSCM thermometry results show remarkable consistency on a kilometer-scale.

Table 2.3 RSCM temperature estimates and locations

Sample	**Lat (N)**	**Lon (W)**	**Mean T (°C)**	**1σ**	**Spectra *n* =**	**Calib. Uncert.***
DC0514	48.5888399	124.554442	229	9	22	37
AG006-1	48.4057333	123.322267	290	10	17	36
AG027	48.447417	123.539955	303	12	18	36
AG138	48.507647	123.56333	309	12	7	36
AG030-2	48.511950	123.568563	319	22	21	36
AG097-3	48.59555801	124.088323	370	20	12	36
AG105-1	48.554828	124.411361	399	8	21	36
AG056	48.58234797	123.953458	458	18	27	36
AG103-2	48.57082704	124.137924	474	15	24	36
AG101-1[a]	48.57912303	124.241639	475	14	3	36
AG067	48.532523	123.899356	544	28	16	37
AG116-1	48.512232	123.96795	562	18	27	37
AG042	48.505130	123.926822	563	14	31	37
AG109-1	48.52372502	124.083864	578	12	7	37
AG080	48.51258002	124.118506	584	19	29	37

[a] Sample performed as a spot check of nearby T

*Calibration uncertainty calculated using empirical calibration array from Lunsdorf et al. (2017)

The systematic T-RSCM trends in the LRC are not replicated in all of the PPU. In the Finlayson Arm corridor surrounding Saanich Inlet, no significant gradient in temperatures is observed between AG030-2 at 319 ± 36 °C, and AG027 from adjacent the Leech River fault boundary at 303 ± 36 °C. The argillite AG006-1 sampled in Victoria attained 290 ± 36 °C, within uncertainty of AG030-2. The RSCM temperature for a sandy metapelite inter-foliated with blocks of metaperidotite near the San Juan Fault is

370 ± 36 °C, notably higher than other samples of the PPU, and comparable to the nearby LRC metasediments.

2.4.3 Conventional Geothermobarometry

Garnet-biotite analyses were acquired for eight samples including all of fibrolite-bearing, andalusite-bearing, and aluminosilicate-free parageneses. Transects of garnet porphyroblasts variably exhibit weak zoning profiles (Figure 2.8) wherein the magnitude of core-to-rim change is small, typically only a few percent in endmember composition. However, rare coarse anhedral poikiloblastic garnets do show more variation in calculated temperatures (e.g., AG074-2). Nevertheless, calculated temperatures between core and rim vary by significantly less than the uncertainty (1σ) for the samples considered here.

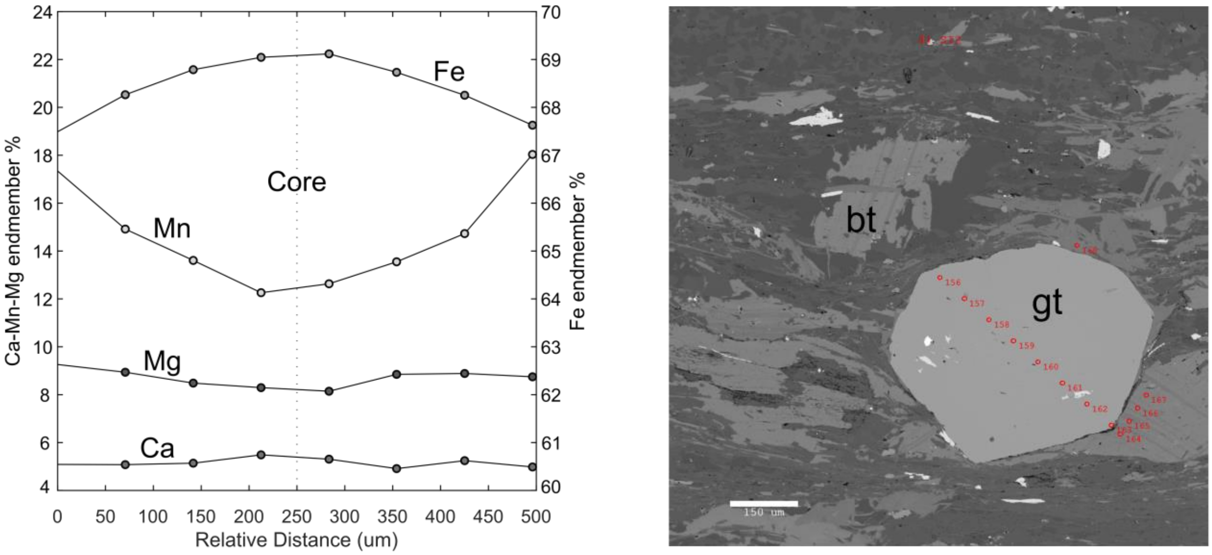

Figure 2.8 Representative profile across a small subhedral garnet from a high-grade sillimanite garnet staurolite schist (AG041). BSE image of the EPMA transect for the data presented in left panel. Almandine endmember plotted on separate axis for clarity.

The range of garnet-biotite calculated temperatures (Table 2.4) for FS78 are 485 °C – 591 °C, and for Wu17 are 572 – 600 °C. Model FS78 produces significantly lower temperature estimates compared to Wu17 for lower KD values but estimates converge at higher temperatures in garnet analyses with less Mn (Figure 2.9). The Wu17 model consistently estimates highest temperatures and predicts a smaller total range among the eight samples. Model H2000 produces comparable temperatures to Wu17, and the imposed pressure only has an effect of approximately ~2.5 °C $kbar^{-1}$. Thus, the H2000 model temperatures are taken for samples with aluminosilicate-free parageneses.

Table 2.4 Computed Gt-Bt equilibria temperature and GBAQ pressure estimates.

					°C				kbar		
Sample	**Als**	**Gt Mg/Fe**	**KD**	**KD Fe^{3+}**	**T-FS78**	**1σ**	**T-Wu17**	**1σ**	**P-Wu17**	**1σ**	**P_{Fixed}**
AG067	And	0.125	0.135	0.123	485	16	572	9	4.4	0.1	-
AG042	And	0.130	0.142	0.129	498	10	575	5	4.4	0.2	-
AG041	Sill	0.136	0.149	0.136	512	13	579	7	3.7	0.1	-
AG047	And	0.152	0.158	0.144	529	18	586	8	4.1	0.2	-
AG049-1	*	0.146	0.156	0.142	526	13	596	7	-	-	4
AG080	Sill	0.178	0.173	0.158	559	19	597	9	3.9	0.2	-
AG116-1	*	0.150	0.160	0.146	534	20	600	9	-	-	4
AG074-2	And	0.212	0.190	0.174	591	38	596	22	4.0	0.1	-

*assemblages without aluminosilicate computed using H2000 (fixed pressure estimate)

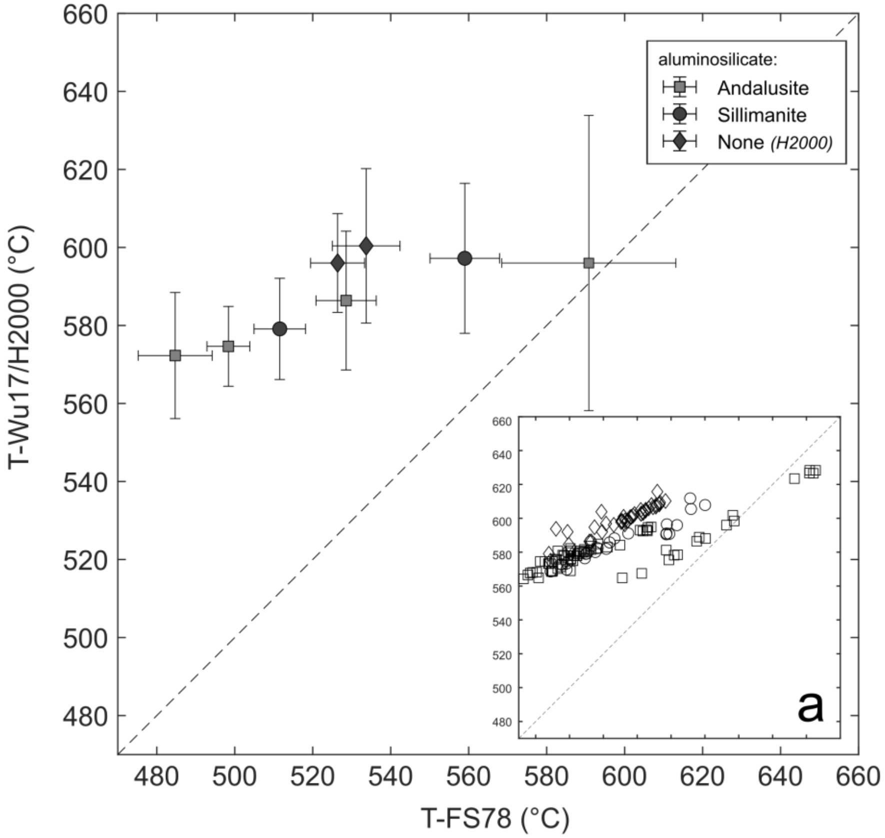

Figure 2.9 (*Previous Page*) Comparison of the thermometry results using the two applied models after Ferry & Spear (1978) and Wu (2017). Error bars are taken as 1σ. *Inset a:* showing all data used in calculating the mean temperatures on identical axes. Several analyses for the highest temperature sample (AG074-2) have a subset of temperatures significantly higher than the mean, corresponding to analyses of

large fractured and anhedral garnets. The large discrepancy in values highlights the influence of non-ideality due to Mn.

The Garnet-Biotite-Aluminosilicate-Quartz (GBAQ) geobarometer applied within model Wu17 to aluminosilicate-bearing samples (AG047, AG041, AG080, AG067, AG042) produced estimates pressure estimates ranging from 3.7 – 4.4 kbar ($\mu = 4.1$ kbar, $1\sigma = 0.3$ kbar), and thus all samples are mutually within the method uncertainty of ±1.8 kbar. The barometry results are generally consistent with the aluminosilicate parageneses which suggest andalusite stability is locally overstepped into the sillimanite stability field.

2.4.4 Geochronology

Results for sample DC13 BMTN, collected from the PPU near Bear Mountain, show two detrital zircon age populations (Table 2.5). One population (n = 4) of $^{206}Pb/^{238}U$ ages ranges from 116.71 ± 0.17 Ma to 117.74 ± 0.17 Ma, and the other comprises one detrital zircon with an age of 72.46 ± 0.78 Ma, taken to represent the revised maximum depositional age of the metasedimentary protolith.

Table 2.5 U-Pb data table for sample DC13 BMTN from Finlayson Arm. ID corresponds to grain and fractions thereof. All errors presented as 2σ.

	Radiogenic Isotope Ratios								Isotopic Age	
ID	$^{208}Pb/^{206}Pb$	$^{207}Pb/^{206}Pb$	% err	$^{207}Pb/^{235}U$	% err	$^{206}Pb/^{238}U$	% err	cor. coef.	$^{206}Pb/^{238}U$	±
4-1	0.064	0.04550	20.389	0.07092	21.369	0.01130	1.083	0.909	72.46	0.78
2-1	0.262	0.04823	1.292	0.12149	1.382	0.01827	0.143	0.658	116.71	0.17
2-5	0.193	0.04825	1.479	0.12206	1.579	0.01835	0.146	0.706	117.19	0.17
5-4	0.193	0.04799	4.132	0.12123	4.384	0.01832	0.285	0.892	117.03	0.33
5-3	0.195	0.04826	1.185	0.12265	1.271	0.01843	0.142	0.637	117.74	0.17

2.5 Discussion

2.5.1 Pseudosections

Pseudosections produced with PerpleX (Connolly, 2005) in the chemical system MnNCKFMASHTO for the composition of an average LRC metapelite (simple mean of the pelites in Table 2.1), generally model the peak temperature mineral parageneses inferred from petrography at conditions comparable to the model results of T-RSCM, T-Wu17 and GBAQ geobarometry for applicable assemblages (Figure 2.10). For example, the sillimanite schist AG080 is predicted at conditions in agreement with T-RSCM (584 ± 37 °C) and T-Wu17 (597 ± 1σ = 9 °C) model results, and P-GBAQ (3.9 ± 1.8 kbar) results (Figure 2.10). In this example, the field comprises gt + bt + st + sill + ilm + qz + pl + fluid, and ranges from ~575 – 640 °C and ~3.7 to >6 kbar. Notably, chlorite and muscovite both occur in the rock sample for AG080. However, chlorite generally occurs as trace localized replacements of biotite and is often associated with cleavage-parallel Fe-Ti oxides, inferred to be from exsolution during cooling. Small amounts of muscovite also form tabular laths throughout the rock volume; however, it is undetermined if these grains occur via a modest overstep of their predicted stability corresponding to sluggishness in the muscovite-out reaction that immediately precedes the peak metamorphic assemblage, or if they are retrograde growths.

Greenschist facies parageneses also compare favorably with T-RSCM for biotite schists, but the fields are generally stable over large domains and offer little constraint on pressure. For example, the carbonaceous phyllite AG103-2 has a T-RSCM of 474 ± 37 °C, and the inferred peak metamorphic assemblage is indicated at comparable temperatures (Figure 2.10, in green). However, there are several notable discrepancies between predicted and observed parageneses, particularly at low greenschist conditions. For example, garnet is stabilized in the models to lower pressures and temperatures than observed in equivalent greenschist facies rocks. The stability of garnet is highly dependent on specified MnO content (Symmes & Ferry, 1992; Mahar et al., 1997). In the average metapelite pseudosection with

0.11 mol% MnO, garnet is stabilized to pressures as low as ~2.5 kbar and temperatures as low as 480 °C. Additionally, a garnet-free ‘window’ occurs at pressures between ~3 – 6 kbar and ~530 – 620 °C. However, pseudosection field topology in principle a rock which equilibrates at conditions of ~540 °C and ~4 kbar could have garnet, but not staurolite, as part of its peak temperature paragenesis (Field 1, Figure 2.10). Only a few samples collected show this assemblage, but nonetheless mapping of the garnet isograd at lower temperatures than the staurolite isograd (e.g., in Figure 2.2) is consistent with pseudosection results. At higher grades, the proposed porphyroblast assemblage of st + gt + sill in AG080, or st + gt + and in AG042, likely represent a continuous reaction wherein staurolite is consumed and garnet produced, which corresponds to the appearance of strongly anhedral staurolite—which may be an indication of consumption in a reaction—and comparatively euhedral garnet which may form near and within staurolite. A prediction of the pseudosection results is that a rock which equilibrated along a clockwise P-T path could stabilize garnet twice if it attained a peak temperature >580 °C. However, if the principle of ‘continuous equilibration’ is inapplicable and the rock volume did not have sufficient time to nucleate and grow during prograde metamorphism, then the first appearance of garnet for high grade rocks may be restricted to higher temperatures, as implied by the T-Wu17 values. Conversely, for samples which reach peak temperature in greenschist facies conditions (Figure 2.10, field 1), garnet could form at lower temperatures and thereby satisfy the field relations that the garnet isograd occurs down-grade of the staurolite isograd.

Figure 2.10 *(Next Page)*: Pseudosection for an average LRC pelite produced in PerpleX with C as a saturated component. Some field labels are omitted for clarity, and the full list of assemblages is included in appendices. Field shading corresponds to calculated variance by the phase rule (F = C – P + 2). Highlighted fields correspond examples of samples collected in the field, and to the colour-matched lines indicating T-RSCM constraints. The garnet-biotite P-T estimate for AG080 is overlain (yellow circle), with uncertainty taken as 1σ on T and calibration uncertainty on P. Mineral-in contours are represented by dashed lines. Cordierite is not observed in any samples, and thus provides a minimum pressure estimate for high grade rocks. Garnet-in is highly sensitive to specified MnO content. Note that T-RSCM estimates are associated with a ± ~37 °C uncertainty envelope omitted here for clarity.

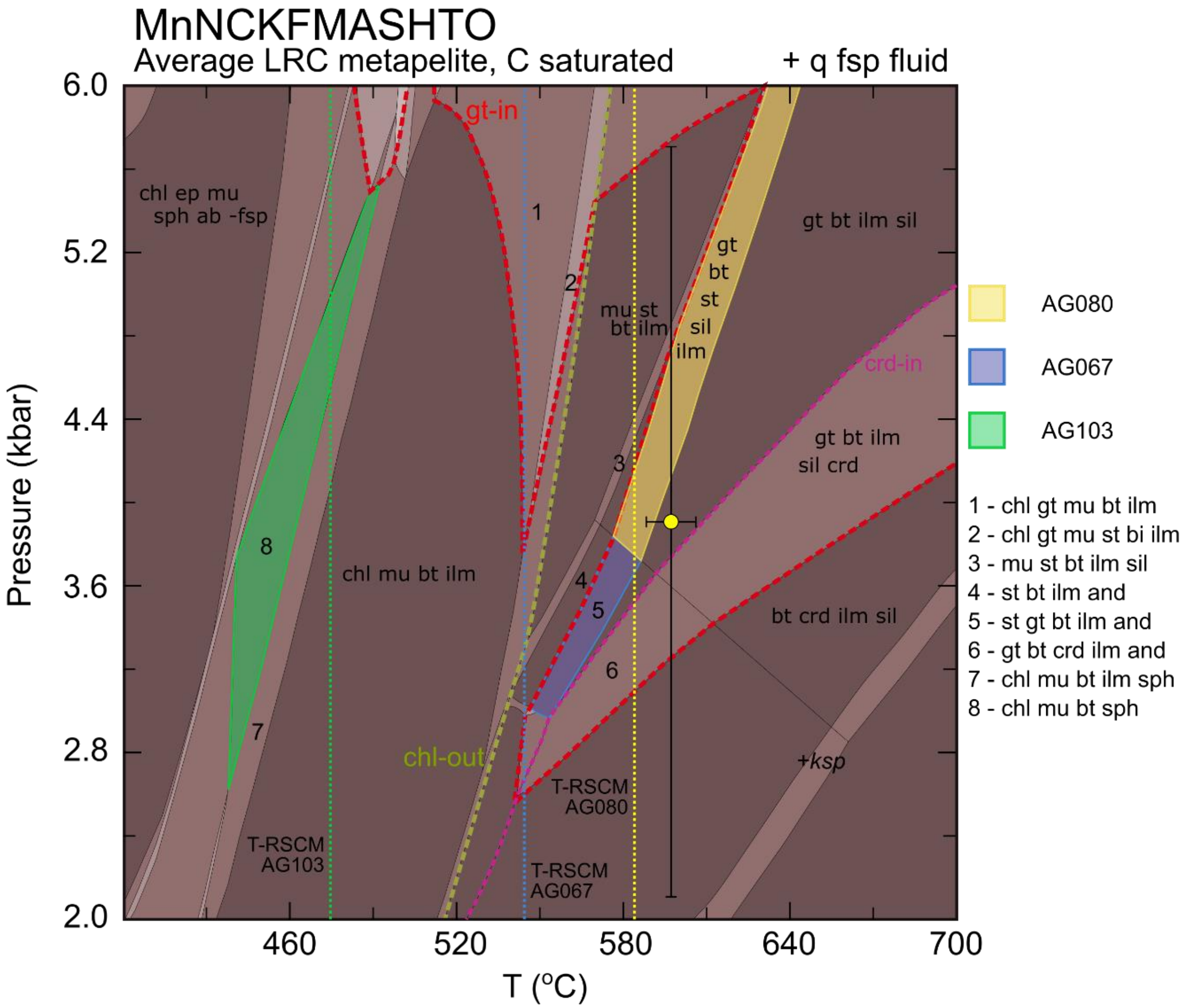

The stability of ilmenite, and the proportion of the component $MnTiO_3$ (pyrophanite) also bears on the stability of garnet. If ilmenite sequesters significant amounts of Mn before garnet nucleation at high temperature, then the reactive bulk chemistry (after Lanari & Engi, 2017) may have less Mn than specified in the models (McCarron et al., 2019). Ilmenite analyses in LRC schists have ~0.3 to 0.9 mol% MnO, whereas the predicted composition of ilmenite retrieved from the pseudosections is only ~0.05 mol% MnO at T_{peak} for high grade schists, and ranges between 0 and 0.1 mol% MnO over the full domain. Thus, the real composition 'seen' during garnet growth may contain slightly less Mn, further restricting garnet stability at lower pressures and temperatures for some protoliths (McCarron et al., 2019). Therefore, the preponderance of small, euhedral, and scarcely zoned high-temperature garnets in LRC rocks are likely the result of their formation at near T_{peak}, and not via a prior reaction such as the decomposition of chlorite and muscovite, which is only accountable for the presence of garnet in greenschist facies rocks. This reaction is taken as the equilibria (after Spear & Pattison, 2017):

$$\text{chl} + \text{mu} + \text{pl} + \text{q} = \text{gt} + \text{bt} + H_2O_{\text{fluid}} \; \textbf{[3]}$$

Andalusite and sillimanite are the two aluminosilicates which occur in the LRC and are typically mutually exclusive. Andalusite zone rocks occur in discontinuous and disparate zones throughout the terrane and are not strictly proximal to sills. Rather, the occurrence of andalusite can vary on the scale of tens meters (Grove, 1984), suggesting a compositional control. Importantly, select andalusite-bearing samples have T-RSCM and P-Wu17 estimates which exceed the andalusite stability field, implying andalusite may be metastable in some assemblages. No textural evidence exists for the polymorphic conversion of andalusite to sillimanite. For example, sample AG042 hosts up to 10 modal percent andalusite as coarse subhedral to euhedral porphyroblasts, but T-RSCM (563 ± 36 °C), T-Wu17 (574 ± 5 °C) and P-Wu17 (4.4 ± 1.8 kbar) values are above or near the andalusite-sillimanite transition (e.g., Pattison, 1992). Large uncertainties in P-Wu17 precludes further analysis.

To evaluate andalusite stability among the metapelitic samples, a T-X section is presented wherein Al_2O_3 is varied between the composition of a psammitic LRC rock, and a synthetic Al_2O_3-rich composition (Figure 2.11). The figures demonstrate that a typical LRC metapelite will not ‘see’ the appearance of andalusite, whereas a more aluminous composition will. Therefore, the appearance of andalusite in the LRC is not a reliable indicator of higher metamorphic grades or contact metamorphism, and is instead a consequence of compositional variation among the sedimentary protoliths. To this end, Groome et al. (2003) report greenschist facies rocks within a kilometer of the Leech River fault (Figure 2 therein), but andalusite-bearing schists nearer the sill margins, which was interpreted as a contact aureole. However, T-RSCM and T-Wu17 results do not substantiate these sub-kilometer scale changes in grade in the region adjacent to the sills. Furthermore, the regular occurrence of andalusite distal to any felsic granitoid outcrops (e.g., AG012 in the eastern LRC) further implies a protolith-, not thermal-control on the distribution of andalusite-bearing rocks. Furthermore, in the 3.75 kbar case, it is demonstrated how some LRC schists develop sillimanite (*var*. fibrolite) without any pre-existing andalusite, as inferred from petrography. Sufficiently low alumina compositions (e.g., AG080, AG041) can bypass andalusite stability, and have sillimanite produced via the rapid breakdown of staurolite that is observed near T_{peak}. Alternatively, the 4 kbar case shows that even a pressure increase of 0.25 kbar could yield aluminous rocks which do not form andalusite prior to sillimanite (yellow field, Figure 2.11).

Cordierite, although a common high temperature – low pressure pelite mineral, is conspicuously absent from the LRC rocks examined in this study. The only possible exception is the spotted phyllite abutting the tonalite sill in Port Renfrew, which may have developed cordierite, but the anhedral, round porphyroblasts are entirely pseudomorphed by carbonate minerals. Nevertheless, cordierite-absent conditions in the pseudosection framework demarcates the lowest possible pressures attained in the LRC. Field six (Figure 2.10) contains cordierite, providing a more robust minimum pressure for LRC rocks than attained via GBAQ barometry. Thus, amphibolite facies andalusite-bearing schists formed at pressures greater than ~2.8 kbar, and sillimanite-bearing schists formed at pressures greater than ~3.6 kbar. Cordierite stability, like garnet, is also influenced by protolith Mn content (Mahar et al., 1997), but trials with LRC compositions show the effect is limited to shifting the first appearance of cordierite or andalusite at low pressures (<3 kbar).

Figure 2.11 *(Next Page)*: Simplified Temperature-Composition (T-X) pseudosections between a psammitic and highly aluminous composition at 3.75 kbar (top) and 4.0 kbar (bottom), indicating two cases to explain the occurrence of mutually exclusive sil- versus and-bearing assemblages by X and P controls. Grey fields indicated where garnet is absent. *Top:* Shaded blue field corresponds to the assemblage of gt-st-and schist AG042. Approximate composition of a typical LRC schist will not ‘see’ andalusite in its prograde assemblage. *Bottom:* At pressures above andalusite stability, a rock like gt-st-sil schist AG080 could also form sillimanite via staurolite breakdown without first developing andalusite in its prograde assemblage.

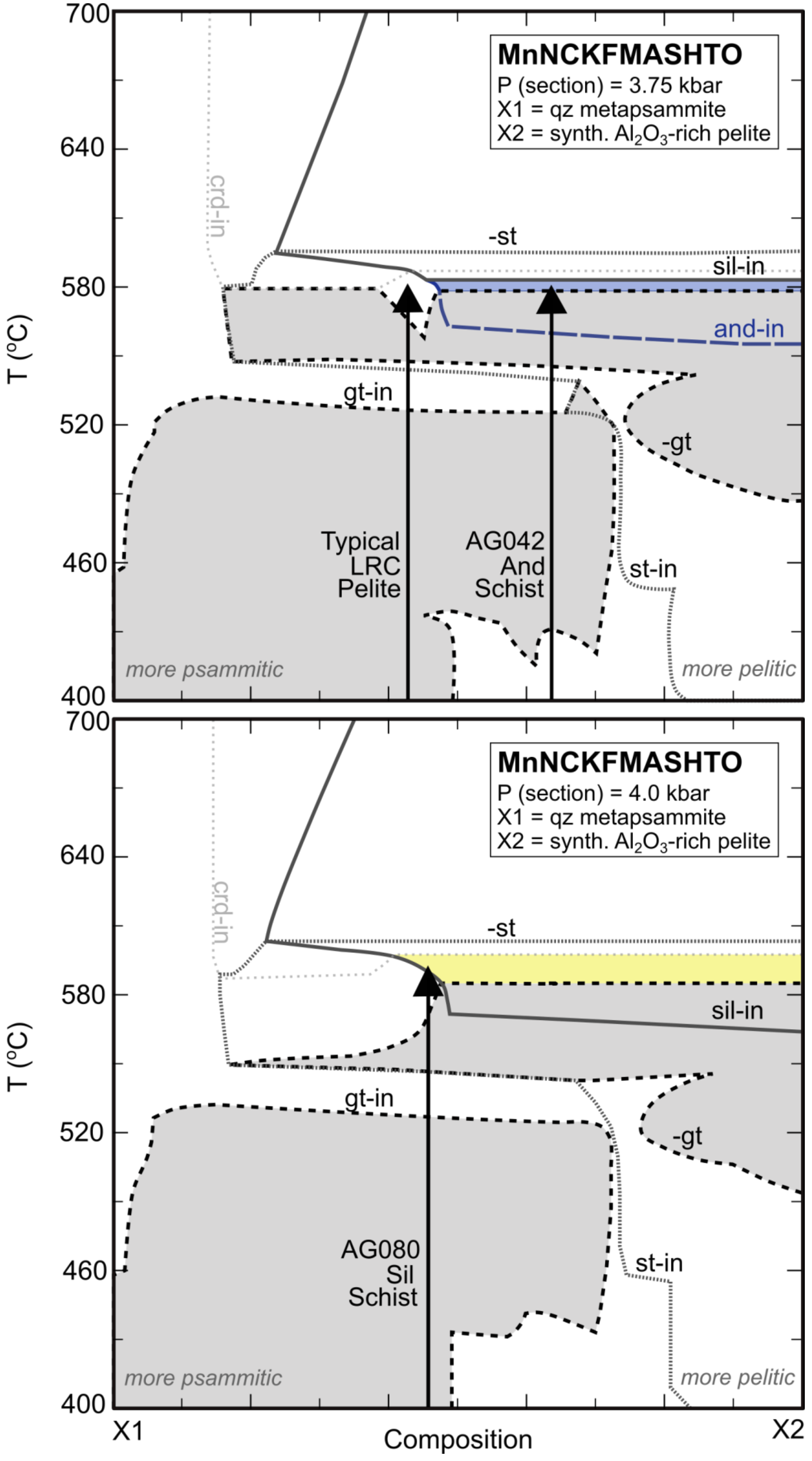
MnNCKFMASHTO
P (section) = 3.75 kbar
X1 = qz metapsammite
X2 = synth. Al_2O_3-rich pelite
700
640
580
520
460
400
T (°C)
crd-in
-st
sil-in
and-in
gt-in
-gt
st-in
Typical LRC Pelite
AG042 And Schist
more psammitic
more pelitic
MnNCKFMASHTO
P (section) = 4.0 kbar
X1 = qz metapsammite
X2 = synth. Al_2O_3-rich pelite
700
640
580
520
460
400
T (°C)
crd-in
-st
sil-in
gt-in
-gt
st-in
AG080 Sil Schist
more psammitic
more pelitic
X1
Composition
X2

Most LRC and PPU samples have only minor retrograde replacement of peak assemblage minerals, consistent with rapid uplift and denudation inferred from $^{40}Ar/^{39}Ar$ cooling ages on muscovite (Groome et al., 2003), and deposition of the overlying Carmanah Group by 35 Ma (Fairchild & Cowan, 1982). Similarly, garnet compositional profiles do not show any significant retrograde re-equilibration at rims, and only show either weak prograde heating zonation, or flat profiles which are fully equilibrated at T_{peak}. Nonetheless, locally staurolite and andalusite are replaced by white micas, quartz, and chlorite, and some samples show partial replacement of biotite by chlorite. These retrograde assemblages of mu + chl + q + pl may correspond to field assemblages at ~2 to 3 kbar and 400 to 430 °C, although there is no evidence for titanite as the Ti-bearing phase among retrograde assemblages. Since peak metamorphism is interpreted here to coincide with the 51 Ma felsic syn-metamorphic, syn-deformation intrusions (Groome et al., 2003), and was exhumed by 35 Ma (Fairchild & Cowan, 1982), amphibolite facies rocks cooled at a rate on the order of ~30 °C Ma^{-1}, which could facilitate relatively minor retrograde assemblages in most rocks examined in this study.

Integrating constraints from T-RSCM, T-Wu17, P-Wu17, and pseudosection topology, it is possible to partially reconstruct the P-T paths taken by samples within the LRC. Carbonaceous phyllites have poor pressure constraints (~2.6 to 5.4 kbar) but correspond to a temperature range ~430 to 500 °C, which is consistent with T-RSCM estimates (e.g., AG103-2). Rocks with 'typical' (i.e., less aluminous) LRC compositions and garnet-zone assemblages of gt + chl + bt, correspond to field 1 in Figure 2.10 which comprises chl + mu + gt + bt + ilm + q + fsp + fluid. Staurolite zone schists which lack either andalusite or sillimanite and have euhedral garnets may have formed staurolite via the reaction (after Pattison & Tinkham, 2009):

$$\text{Mu} + \text{Chl} + \text{Qtz} = \text{St} + \text{Bt} + \text{H}_2\text{O}_{\text{Fluid}} \quad \mathbf{[4]}$$

The highest-grade rocks with T_{peak} > 570 °C show the onset of staurolite breakdown, and the resulting production of fibrolite and high-temperature garnet porphyroblasts. The occurrence of andalusite-bearing schists is controlled primarily by protolith alumina content, and to a lesser degree by pressure. The resolution of GBAQ barometry is insufficient to demonstrate the influence of pressure on the stable aluminosilicate, but pseudosection topology permits a pressure differential as small as 0.25 kbar between a sample that develops no andalusite and ultimately sillimanite (e.g., AG041), versus a sample that develops andalusite and not sillimanite (e.g., AG012). Finally, the retrograde arm of the P-T path is poorly constrained, but transits through low temperature sub-biotitic assemblages comprising primarily chl + mu.

2.5.2 Metamorphic History

The LRC underwent high temperature forearc metamorphism up to ~600 °C under at pressures of 3.8 to 4.4 ± 1.8 kbar. T-RSCM values from this study and Jakob et al. (2016) show that peak metamorphic temperatures uniformly decrease to the northern and eastern extents of the Pacific Rim Terrane. To verify compatibility between the datasets, several stations were compared. One station from Jakob et al. (2016) was directly replicated in this study (AG006-1) using comparable collection methodology but analyzed using IFORS, producing a T-RSCM of 290 ± 36 °C, compared to 260 ± 50 °C (Jakob et al., 2016). An additional two datapoints from Jakob et al. (2016) were bracketed with stations from this study. In Finlayson Arm, Jakob et al. (2016) report a sample which attained 313 ± 50 °C, consistent with presented T-RSCM values of 324 ± 36 °C to the north (AG030-2), and 302 ± 36 °C (AG027) to the south. In Port Renfrew, the phyllite AG105-1 has a T-RSCM of 399 ± 36 °C, ~2 km from a Jakob et al. (2016) sample temperature of 409 ± 50 °C. The notable low temperature sample Jakob et al. (2016) report along the western Leech River fault could not be replicated with samples collected in this study, since all proximal samples lacked carbonaceous matter.

Given consistent results between the datasets, the geolocated T-RSCM data are compiled into a gridded map, onto which 50 °C increment isotherms were calculated using natural-neighbor interpolation in MATLAB (Figure 2.12). This map highlights the notable E-W continuity of metamorphic grade in the central LRC, and the high degree comparability with mineral isograds observed in the field (Figure 2.2). Caution should be used interpreting regions of the terrane that are poorly constrained (e.g., Survey

Mountain region adjacent the Survey Mountain fault), but generally the thermal map adequately estimates peak metamorphic temperature to within ~50 °C. This was evaluated qualitatively by comparison with porphyroblast assemblages, and spot checks of additional samples using the T-RSCM method. The isotherms do not account for any post-metamorphic faulting (e.g., Jakob et al., 2016), but no significant (>50 °C) discontinuities in grade were observed in the field. Additionally, no boundaries between the LRC and PPU were prescribed in the interpolation.

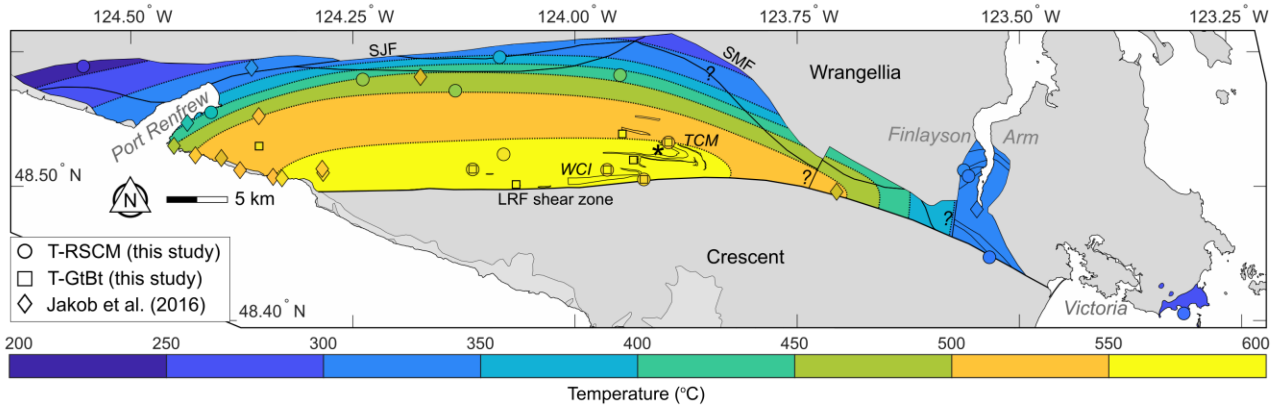

Figure 2.12 Schematic map of peak metamorphic isotherms from interpolation of T-RSCM data and field observations. Symbols are keyed to a gradient between 200 and 600 °C. Areas indicated with ‘*?*’ have poor RSCM data coverage and lack supplementary observations from the field study due to inaccessibility. Isotherms show E-W continuity in peak metamorphic temperature, high temperatures near the LRF in the central LRC, and continuity between T-RSCM values in the northwestern LRC-PPU boundary. One datapoint from Jakob et al. (2016) along the western LRF could not be replicated and was discarded. Asterisk indicates the location of the Valentine Mountain region. Other abbreviations as per Figure 2.1.

Crucially, calculated isotherms and mineral isograds are not controlled by the distribution of exposed metaigneous rocks, including both the Eocene Walker Creek intrusions and the Tripp Creek metabasite (Figure 2.12). Instead, T-RSCM isotherms suggest a regional heat source which more greatly affects rocks juxtaposed against the Leech River fault. While RSCM thermometry is susceptible to a ‘pre-texturing’ problem wherein carbonaceous matter is slow to structurally re-equilibrate to multiple phases of metamorphism (Beyssac et al., 2019), reasonable agreement between T-Wu17 (Figure 2.13), pseudosection topology, and T-RSCM indicates these results are robust and record the true T_{peak}. While there is a weak correlation between exposure of intrusions and higher grades in the Valentine Mountain region, the highest-grade rocks—including fibrolite schists and psammitic paragneisses—are distal to any exposed intrusions of significant volume. Thus, the felsic intrusions are not interpreted as the primary mechanism by which the LRC was heated. This study reports a conspicuous absence of distinct thermal aureoles around most syn-deformation Walker Creek intrusions, which is attributed to low thermal contrast between the intrusions and country rock, and the small volumes of magma involved, but this should be evaluated further using numerical thermal models.

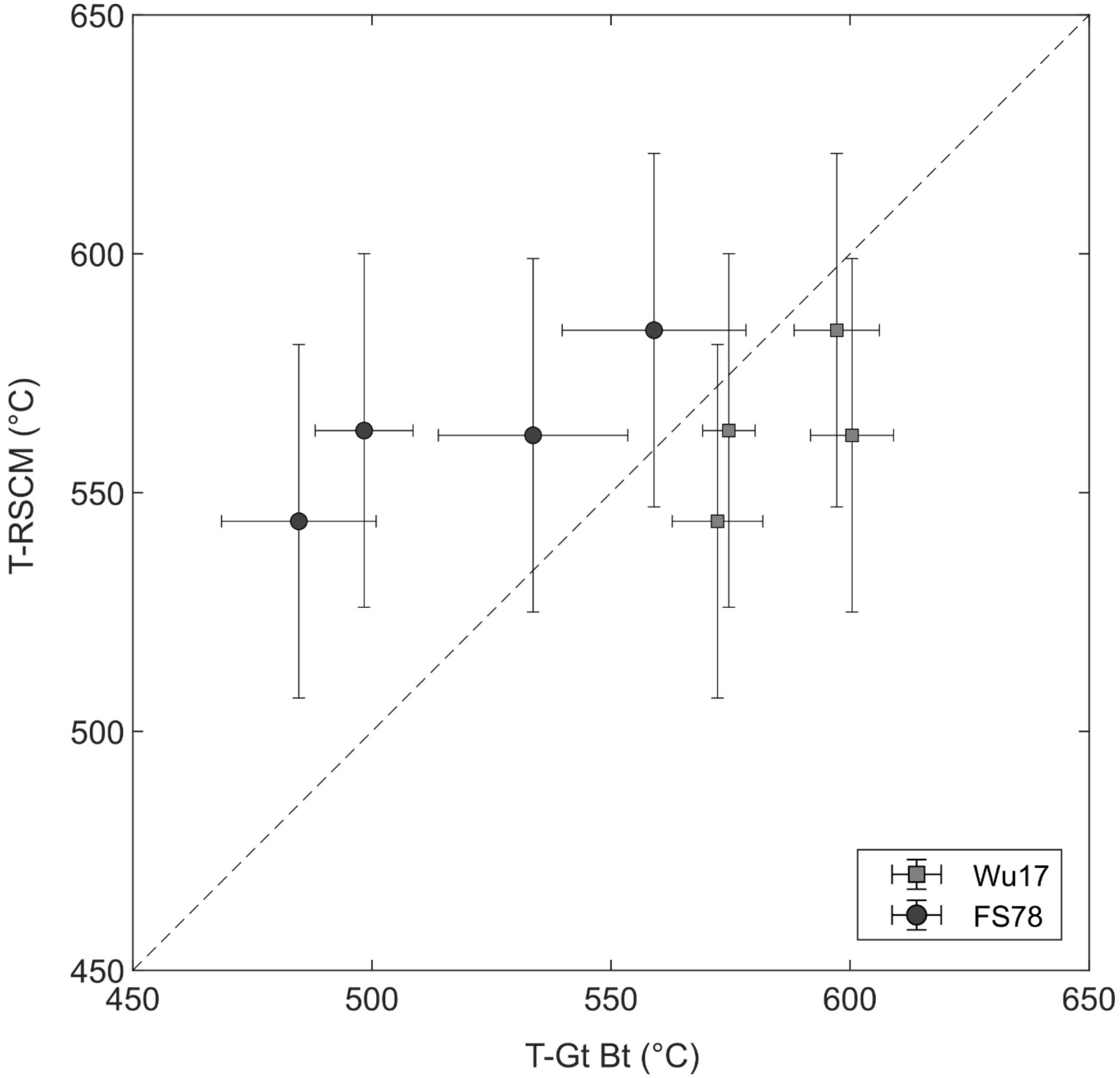

Figure 2.13 Comparison of 4 samples with T-RSCM and T-Gt Bt values, using both T-Gt Bt estimates (T-FS78 and T-Wu17) against T-RSCM values. Uncertainty on T-RSCM is that of the empirical calibration (~37 °C), while uncertainty on gt-bt thermometry is taken to be 1σ. Dashed line indicates a 1:1 relationship. T-FS78 underestimates T-RSCM, while T-Wu17 overestimates T-RSCM by a smaller magnitude.

Furthermore, the two-phase metamorphism model (e.g., Groome et al., 2003; Jakob et al., 2016) which proposes magmatism in the Mid-Cretaceous and Eocene causing greenschist and amphibolite facies metamorphism, respectively, is not adopted here. The first magmatism phase was invoked to explain three observations: (1) concordant titanite ^{206}Pb/^{238}U dates of 88.2 ± 0.8 Ma extracted from quartzofeldspathic bodies formerly identified as intrusions in the Valentine Mountain region which compare favorably with discordant zircon fractions (Groome et al., 2003), and a concordant zircon age of 91.62 ± 0.26 Ma from a narrow sill in Port Renfrew (Jakob et al., 2016), (2) the presence of foliated biotite-schist xenoliths within Eocene felsic sills (e.g., Figure 2.5), suggesting greenschist facies metamorphism prior to the Walker Creek magmatism, and (3) the spatial association of the large quartzofeldspathic bodies with high grade rocks.

The mid-Cretaceous timing of the purported magmatism is poorly constrained due to the exceptional dearth of zircons in the felsic intrusions. Indeed, recent age data for detrital zircons from the LRC yield pre-deposition rim ages as young as 65 Ma (Dlugosz et al., 2020), which precludes a mid-Cretaceous magmatic event. Similarly, the detrital zircon age of 72.5 ± 0.8 Ma from the chert and pelite sample collected in the PPU near Finlayson Arm conflicts with the proposed first phase of metamorphism. Therefore, the emplacement ages for the felsic intrusions (e.g., Groome et al., 2003; Jakob et al., 2016) must instead be ages of inherited detrital zircons. Furthermore, the large quartz-rich body previously mapped as the Valentine Mountain metagranodiorite is not associated with any marginal temperature increase or preponderance of porphyroblasts, particularly along its northern extent. Instead, here the unit is interpreted as a metapsammite with modal quartz locally greater than 90 % and generally very little plagioclase or potassium feldspar, and subsidiary interfoliated metapelite. The unit is comparable to grey subarkosic to quartz arenitic metasandstone beds identified within the fault-bounded blocks of LRC lithologies in Finlayson Arm, wherein T_{peak} is ~320 °C and interbedding with argillites is clearly identifiable.

Since the Eocene felsic intrusions are syn-deformation (Groome et al., 2003; Jakob et al., 2016; this study), the presence of schistose xenoliths rafted into the sills do not necessitate a prior metamorphic event. Rather, if the felsic intrusions are in-part a result of sediment melting at depth (e.g., Groome et al., 2003), the schistose foliation could be developed in the same metamorphic event at sub-solidus conditions and then rafted into an intruding melt. Since the xenoliths are dominated by biotite and have only subsidiary plagioclase, the xenoliths may represent fragments of restite from melting of the sediments, but this conjecture has not been investigated. Finally, since the RSCM thermometer is sensitive to pre-texturing of samples by prior metamorphism (Beyssac et al., 2019), it is possible the T-RSCM values could reflect the conditions attained in the first phase of metamorphism, causing discrepancies between garnet-biotite thermometry and T-RSCM. However, calculated isotherms are both independent of the Valentine Mountain unit, and consistent with T-Wu17 values, adding further evidence that the unit is unlikely to be a large intrusive body. Similarly, near Port Renfrew, a 6 km long E-W trending unit mapped as an Eocene intrusion (Massey et al., 2005 via BC MapPlace) has no thermal aureole overprinting the adjacent greenschist-facies carbonaceous phyllites and is instead another psammitic lithology. A sample of this psammitic lithology yielded detrital zircon ages that resemble populations for the Nanaimo Basin (Dlugosz et al., 2020).

Metabasic Lithologies

The Tripp Creek metabasite was also evaluated as a source of heat for metamorphosing LRC sediments. The destruction of primary textures obscures the identity of the unit as either intrusive sills occurring concomitantly to Eocene felsic magmatism (e.g., Groome et al., 2003), or as submarine lava flows that erupted in the cryptic LRC depositional environment (e.g., Fairchild & Cowan, 1982). If the unit is intrusive, like the Walker Creek intrusions, it must have intruded during the D_1 isoclinal folding event, as the unit is transposed into parallelism with the metasediments and subjected to the same D_2 open folding (Fairchild & Cowan, 1982; Grove, 1984). However, it could also be consistent with small submarine basalt pillows or sheet flows interbedded with LRC sediments, shallow dikes, or a combination of the above that formed prior to metamorphism and were tectonically interleaved during subcretion.

Some insight regarding the identity of the Tripp Creek metabasites may be garnered from observations in analogous terranes, like the Chugach accretionary complex on Baranof Island, Alaska. There, the Cretaceous accretionary complex was intruded by numerous anatectic granitic intrusions of age 53 to 47 Ma (Davidson, 2018), causing up to amphibolite facies metamorphism in a unit of metasediments and metabasalts (Nilsen & Zuffa, 1982; Zumsteg et al., 2003). Paleomagnetic data and the notable similarity in high-temperature forearc conditions led to the Baranof-Leech River hypothesis, which argues that the LRC and Baranof units were continuous at time of metamorphism, but the Baranof schist was subsequently displaced ~1100 km northward along the continental margin (Cowan, 2003). Copious other models have been developed to explain the similar HT-MP forearc conditions along western North America, such as oblique ridge subduction associated with the Resurrection plate (e.g., Farris & Paterson, 2009; Fuston & Wu 2020), and an exhaustive discussion is beyond the scope of this study. Nevertheless, numerous metamafic units are interfoliated with these forearc rocks, some of which preserve primary textural relationships, unlike in the Tripp Creek metabasites. Therein, metamafic rocks include pillow basalts and dikes interbedded with turbiditic sequences, which is used as evidence for deposition on the seafloor prior to being scraped into a forearc accretionary mélange (Nilsen & Zuffa, 1982). Irrespective of whether the Baranof accretionary complex is correlative with the LRC or simply analogous, it demonstrates that shallow seafloor mafic volcanics can be interfoliated with forearc sediments during accretion. In this context, the petrogenesis of the Tripp Creek metabasites is discussed further below.

Like the Walker Creek intrusions, there are numerous discontinuous metabasite bodies associated with amphibolite facies rocks in the Valentine Mountain region. However, near the high grade paragneisses further west, metabasite bodies are uncommon, and where present occur as meter-scale boudins. Additionally, below the biotite isograd, metamafic chlorite-actinolite schists and chlorite-magnetite phyllites occur in large (>10 m) wide bodies but are not associated with any thermal aureoles. Similarly, T-RSCM estimates are unaffected by proximity to the Tripp Creek metabasites. Therefore, there is conflicting evidence for interpreting the origin of the Tripp Creek metabasites: An argument exists for coeval MORB-like mafic magmatism and melting of LRC sediments to produce the Eocene intrusions (Groome et al., 2003), but if all the metamafic bodies are syn-deformation, syn-metamorphic sills, the lack of associated contact metamorphism in lower grade rocks is difficult to reconcile. This points to an origin as interbedded mafic volcanics (Fairchild & Cowan, 1982). It also bears noting that the low-greenschist facies blocks of the LRC fault-bound within the PPU in Finlayson Arm host neither intrusive lithologies nor interbedded basalt flows.

The Survey Mountain metavolcanics, if co-genetic with the Tripp Creek metabasites, could offer additional clues. Unlike in the Tripp Creek lithologies, primary plagioclase phenocrysts in metabasalts are reported among the greenschist facies rocks at Survey Mountain (Fairchild & Cowan, 1982). The Survey Mountain metavolcanic unit, which has been understudied since its early descriptions (e.g., Muller 1983) has a gradational contact with the LRC's pelitic lithologies, but still hosts subsidiary amounts of biotitic schists and phyllites (Fairchild & Cowan, 1982). The easternmost extent of the Survey Mountain metavolcanics reportedly hosts brecciated and massive basalt flows as well as sequences of pillow basalt, among intercalated ribbon cherts, biotitic-argillites, and bimodal tuffs (Malczak et al., 1982). Subsidiary felsic dikes are also reported to crosscut the volcanic units, and a single gabbroic to dioritic stock is reported in the vicinity of Survey Mountain (Malczak et al., 1982). Overall grade for this lithology was interpreted to range from greenschist to amphibolite facies (Fairchild & Cowan, 1982; Malczak et al., 1982), consistent with metamorphic grade in the LRC but not the PPU. Survey Mountain is also host to a modest, 4 m wide and 1 km long Besshi-type volcanic-hosted massive sulfide ore showing, comprising pyrite, pyrrhotite, chalcopyrite and sphalerite (Malczak et al., 1982; McIntyre & Wilson, 1989). Thus, if the Tripp Creek metabasites are correlative to or continuous with the Survey Mountain metavolcanics, then they are likely extrusive volcanics which were interfoliated with the LRC sediments either during deposition or accretion. Geochemical constraints for these hypotheses are evaluated in a subsequent section.

Pandora Peak Unit

The PPU did not universally experience the same degree of high temperature metamorphism as observed in the LRC, in-part since it is distal to the central LRC where the highest degrees of metamorphism occurred. In the western PPU near Port Renfrew, T-RSCM values increase towards the cryptic LRC boundary, but always remain <400 °C and lack porphyroblasts. Metamorphic parageneses are generally patchy and restricted to only some protoliths (Rusmore & Cowan, 1985), but coexisting lawsonite and quartz in lithic cataclasites (e.g., in Gonzalez Bay, Victoria) are consistent with a shallow subduction environment and the nearby T-RSCM estimate of 290 ± 36 °C. The field study here noted green-grey altered metamafic rocks locally host anhedral plagioclase interpreted as surviving primary phenocrysts. Previous workers (e.g., Rusmore & Cowan, 1985; McEwen, 2013) have interpreted these mafic rocks as volcanics, as either pillows or ‘green tuffs’, and there is no evidence to suggest any elevated thermal metamorphism associated with metamafic rocks in the PPU. In Victoria, the metamafic rocks outcrop as meter-long boudins in a tectonized argillite matrix. Thus, the metamafic rocks in the PPU are not agents of metamorphism, and are instead metavolcanics, either as deposited in the depositional environment, or via a sedimentary olistostromal origin, stoping into either a forearc basin or accretionary melange (e.g., Brandon, 1989b; Festa et al., 2016).

Direct comparison of the metamorphic conditions in the LRC and PPU is hindered by difficulty identifying the boundary in the field. Nonetheless, T-RSCM estimates from either side of the cryptic LRC-PPU boundary in the western Pacific Rim Terrane suggest the metamorphic gradient is continuous, with higher temperatures in the PPU recorded nearer the LRC boundary. A continuous thermal gradient implies that the LRC and PPU were juxtaposed prior to high temperature metamorphism, and that the PPU was spared significant thermal overprint since it was distal to the heat source. However, the relationship in the eastern Pacific Rim Terrane near Finlayson Arm is less clear. Jakob et al. (2016) report a sample from Leechtown (eastern LRC) at ~500 °C, but a green meta-mudstone ten kilometers east along the Leech River Fault has a T-RSCM of 303 ± 36 °C. North of this mudstone, T_{peak} estimates increase northward but are within uncertainty (<340 °C), unlike the characteristic northward decreasing T_{peak} gradient in the LRC.

The structure of the Finlayson Arm corridor bears on this discrepancy: Rusmore & Cowan (1985) argued the region represents a half-window through overlying Wrangellia to subcreted blocks of the PPU. A shallowly north-dipping subcreted unit unaffected by a high-temperature overprint could conceivably explain the Finlayson Arm T-RSCM values. Furthermore, along the northeastern extent of the corridor, a massive radiolarian chert hosts a vein assemblage comprising lawsonite, chlorite, quartz and pumpellyite, plus minor amounts of prehnite (Figure 2.6, AG013), consistent with a pre-blueschist facies rock. However, the field relations are not indicative of an erosive fenster, since the PPU in this region is bounded by sub-vertical discrete faults with no obvious fault cataclasis or indications of slip (Rusmore & Cowan, 1985). Notably, in contrast the boundary between the PPU and Westcoast Crystalline Complex in Victoria locally comprises ultramylonites along more shallowly dipping faults. Nevertheless, the PPU records at least a partial record of prehnite-pumpellyite through lawsonite zone conditions typical of a shallow forearc accretionary complex, with only local evidence for the thermal overprint in sections closer the elevated thermal conditions in the central and east LRC.

2.5.3 Tectonic affinity for metasedimentary and metaigneous rock in the Pacific Rim Terrane

Some limited insight regarding the depositional setting of the LRC and PPU may be gleaned from field observations. For example, the presence of large serpentinized peridotite blocks in a sandy pelitic matrix along the San Juan Fault, and argillite-hosted blocks of laminated soft-sediment deformation textures in Victoria suggests the PPU is in-part an olistostromal unit. In contrast, the few LRC outcrops with preserved bedding show flysch-like sequences of argillite and sandstone. However, since penetrative deformation has obscured primary textures and field relations for most rocks in the LRC, geochemical

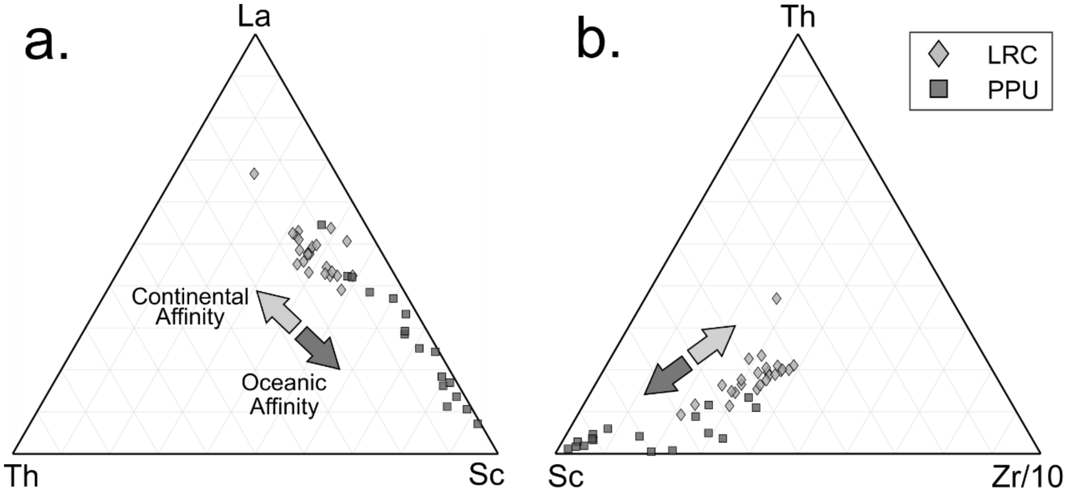

Figure 2.14 Sediment provenance discrimination diagrams after the ternaries calibrated for greywackes by Bhatia & Crook (1986), using data compiled from this study, Jakob et al. (2016); McEwen, (2013); Groome et al. (2003); Johnston, (2000); Canham, (2000). Specific tectonic fields omitted here because of significant 'protolith mixing' via deformation in the LRC and PPU. Here, 'continental affinity' refers to a greater contribution of felsic plutonic and recycled sedimentary detritus from the hinterland, whereas 'oceanic affinity' is adapted from 'oceanic arc affinity', implying less evolved volcanic units in the source lithology.

analyses provide some clues into the depositional environment and evolution of the Pacific Rim Terrane. Geochemical provenance discrimination plots (e.g., Bhatia & Crook, 1986; Roser & Korsch, 1988) have only variable success in classifying the tectonic environments for sedimentary rocks (Ryan & Williams, 2007). Nonetheless, some trace elements (e.g., Zr, Sc, Th) can provide qualitative distinction of tectonic character for sediment suites. Applying these discriminants to metasediments further assumes immobility among trace and major elements. For the greenschist to amphibolite facies LRC rocks, most high field strength elements and REE are unlikely to be mobilized (Hammerli et al., 2016), which is corroborated by no systematic trends in bulk rock data plotted against T-RSCM estimates.

Ternary sedimentary discrimination diagrams after Bhatia & Crook (1986), which were calibrated for a suite of deep sea and marginal basin turbiditic rocks liberally classified as greywackes, are applied here to bulk rock data from the LRC and PPU. Assuming that the fault-bound blocks of LRC metasediments in Finlayson Arm are representative of the western LRC, then the terrane protoliths comprise mainly quartz arenites, subarkose arenites, mudstones, and subsidiary lithic arenites, although even among sub-greenschist facies rocks, recrystallization precludes straightforward estimates of matrix fractions. Chemical sediment classification systems (after Herron, 1988) applied for LRC and PPU metasediments classify them mostly as Fe-sands, likely because deformation has disrupted and interleaved protoliths on a centimeter-scale. However, metapsammitic samples from thicker lithologies are consistent with wacke and quartz arenite classifications. Thus, these sedimentary discrimination diagrams are applied cautiously to delineate differences between the LRC and PPU, using compiled data from the terranes (this study; Jakob et al., 2016; McEwen, 2013; Groome et al., 2003; Johnston, 2000). The ternary diagrams Th-La-Sc and Sc-Th-(0.1×Zr) (Figure 2.14) successfully demarcate the LRC and PPU: The LRC population has proportionally greater Th, Zr, and La than the PPU, which conversely has greater Sc. Qualitatively, there is greater 'continental arc affinity' among LRC metasediments, and greater 'oceanic arc affinity' among PPU metasediments. Sc values for the PPU range significantly higher than LRC, suggesting a greater volcanic component. However, most discrimination power arises from higher Th, Zr, and La in the LRC (Figure 2.15), consistent with a greater proportion of felsic plutonic or recycled detritus in the source terrane (Bhatia & Crook, 1986). However, the potential for a significant degree of 'source mixing' along an active continental margin, especially if it has undergone significant margin-parallel translation (e.g., Cowan, 2003), limits further interpretation of terrane provenance from bulk geochemistry alone.

Figure 2.15 *(Next Page)*: Histograms of trace element discriminants used in the adapted Bhatia & Crook (1986) ternary discrimination diagrams, with summary statistics of mean (μ), one standard deviation (1σ) and computed two-tailed *p* values (p2t). The means of all populations are significantly different: $\mu_{PPU} < \mu_{LRC}$ for La, Th, and Zr, while $\mu_{PPU} > \mu_{LRC}$ for Sc. These data corroborate greater contribution of evolved components (e.g., felsic plutonics and recycled detritus) to the LRC protolith.

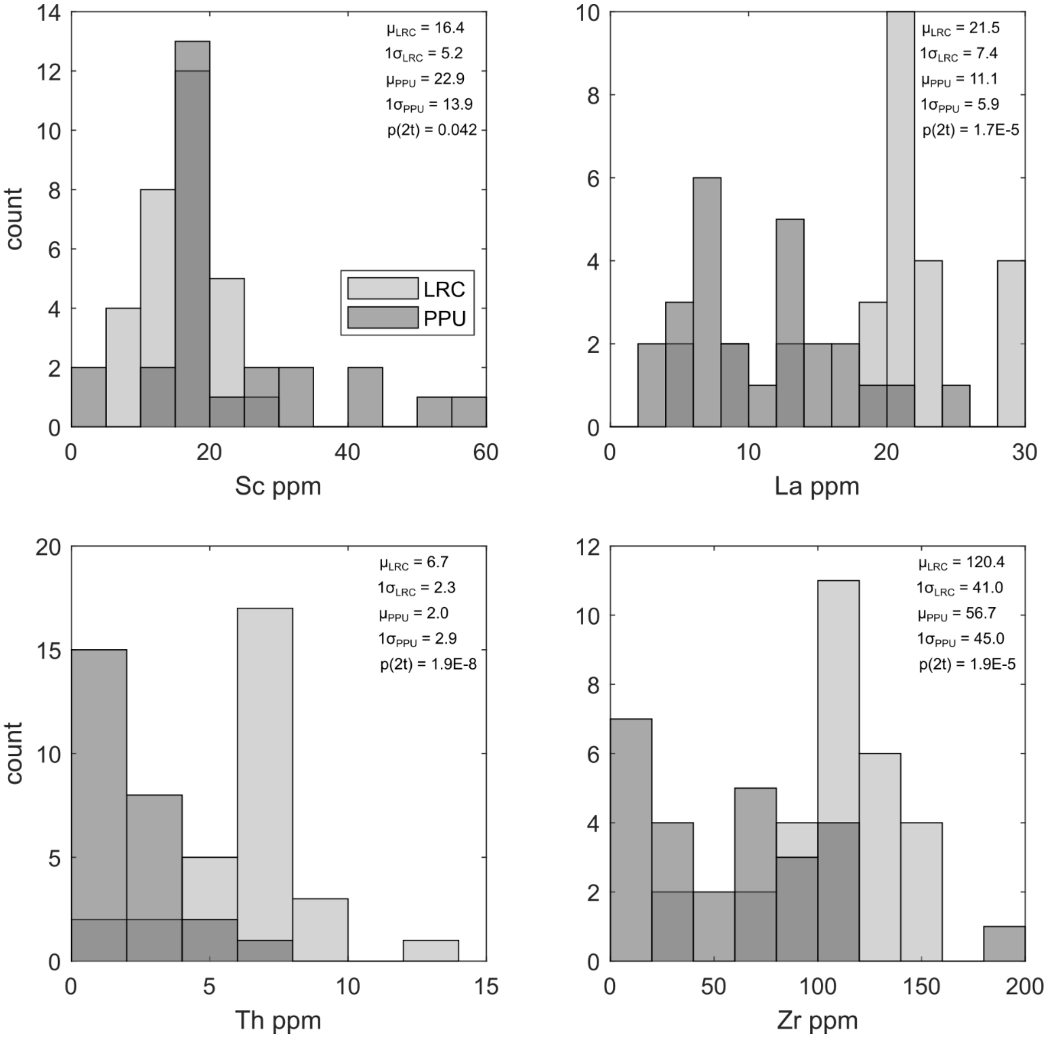

Recent work has established that the Crescent terrane, including the subcreted Metchosin Igneous Complex on Vancouver Island, and numerous basalt units in the regional forearc are members of a cogenetic accreted oceanic plateau (Wells et al., 2014; Phillips et al., 2017). The proximity of the Tripp Creek metabasites to the Metchosin Igneous Complex and their comparable chemistry merits examining the relationship between the Siletz terrane and the metabasites identified in the Pacific Rim Terrane. As outlined in the results, Group 1 metabasites comprise exclusively the Tripp Creek metabasite. In contrast, ‘Group 2’ comprises the two PPU metabasites, as well as a garnetite-bearing amphibolite and coarse-grained banded amphibolite from the Tripp Creek metabasite suite. Trace element data reported by Groome et al. (2003) for the Tripp Creek metabasites show similar patterns of high- and low-light REE profiles reported here. Among the Group 2 light REE-enriched samples have an approximately ‘E-

MORB' composition (after Sun & McDonough, 1989). Plotting the Group 1 and Group 2 metabasites in Nb/Yb – Th/Yb space (Figure 2.16, after Pearce, 2008) shows that most plot along the N-MORB to E-MORB array, and most of the Tripp Creek samples plot closely with data from the Metchosin Igneous Complex. From this study's dataset, there are two exceptions: AG105-4, which is offset the trend by low Nb values, and the PPU metabasalt AG089-1, which is offset by higher Th values as deduced from comparison of the elemental data (Table 2.2). Since the immobile trace elements are unlikely to have been widely disturbed during low amphibolite facies metamorphism (Hammerli et al., 2016), the trace element data are still likely reflective of inherited protolith chemistry. In the context of discrimination diagram accuracy (i.e., generally poorly resolved: Li et al., 2015), the results are broadly consistent with MORB-like chemistries, ranging from NMORB to EMORB.

Similar compositional groupings in metabasites have been identified in other forearc accretionary environments, such as within the Ivrea Zone in the Italian Alps (Sills & Tarney, 1984). Therein, Sills & Tarney (1984) attributed the difference to heterogeneities in the seafloor volcanic rocks, such as the presence of seamounts, that were tectonically interlayered with the sediments via erosion from the subducting plate. That model is relevant to the Tripp Creek metabasites, where Group 1 and 2 metabasites are exposed in proximity, sometimes only a few tens of meters apart. If LRC sediments were deposited in a near-ridge environment, Group 2 metabasites could imply a nearby EMORB-like source or differentiation to account for elevated light REE contents. Similar N-MORB to E-MORB groupings are also observed among basalts in accretionary complexes in Japan (Safonova et al., 2016). In these forearc terranes Safonova et al. (2016) derived a set of key geochemical features to class the origin of basaltic lithologies, including $Nb/La_{PUM} \leq 1$ and $Al_2O_3/TiO_2 = 8 – 17$ for MORBs. The Tripp Creek metabasites satisfy these criteria but lacks the correlative primary igneous textures for definitive identification.

Figure 2.16 *(Next Page):* Th/Yb versus Nb/Yb after Pearce (2008) for PRT metabasites and regional Eocene basalts. Metabasites split into their groups (see results) by colour. Most of the Tripp Creek data plot along the basalt array and are comparable to data from the Metchosin Igneous Complex (Phillips et al., 2017).

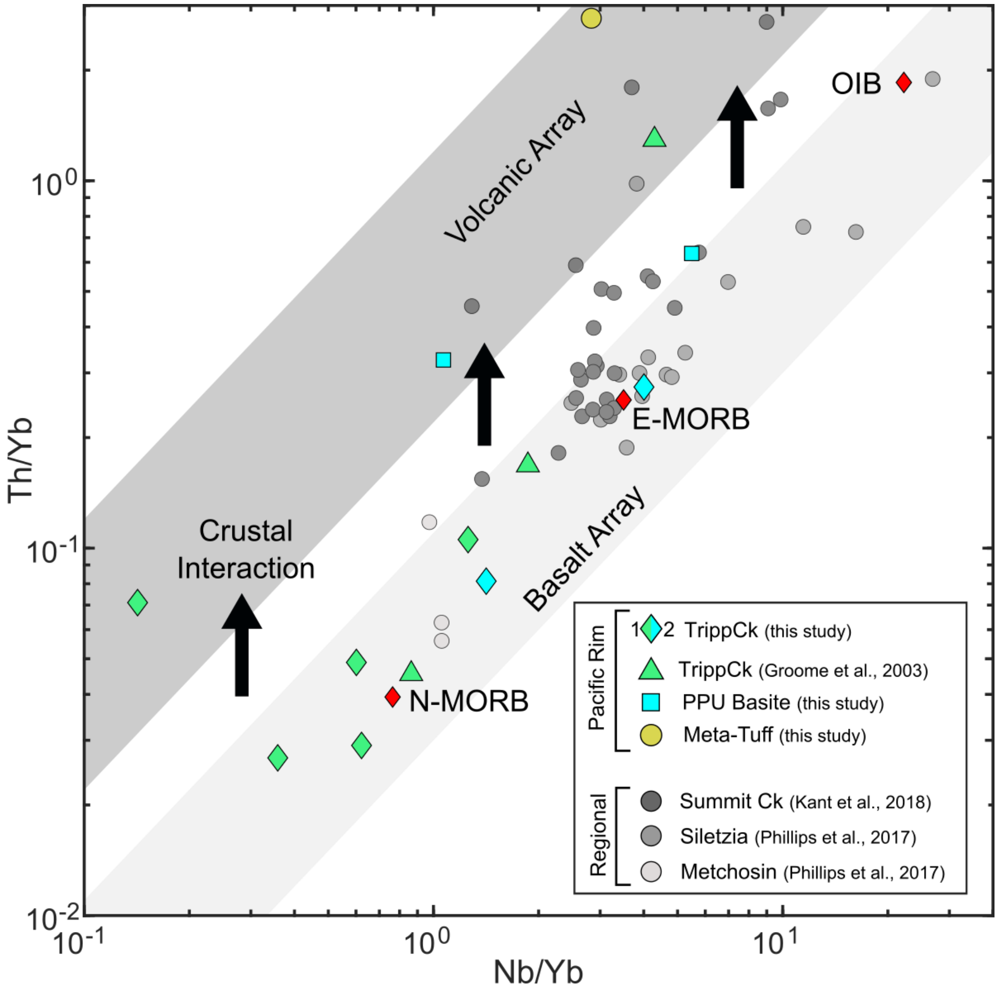

Nevertheless, the majority of the Tripp Creek metabasites have N-MORB-like REE contents (after Sun & McDonough, 1989). This is consistent with the Metchosin Igneous Complex (e.g., Timpa et al., 2005; Phillips et al., 2017) and more broadly, the northward trend of relative depletion among the Siletz basalts, consistent with a MOR setting (Phillips et al., 2017). Dy/Yb data are also consistent with northward decreasing trends in Phillips et al. (2017), with Group 1 metabasites averaging ~1.70, comparable to the Metchosin Igneous Complex, and Group 2 averages ~1.95, similar to the central Crescent formation. Further analysis of the source and affinity of the Tripp Creek metabasites requires additional isotopic analyses. However, the Group 1 metabasites were likely produced at a spreading center, and there is no evidence for arc-like affinities, such as higher Th.

Finally, one sample from Group 2 (AG069-2) shows a distinct negative Ce-anomaly (Figure 2.7), which is attributed here to the centimeter-scale layering of fine-grained, Mn-rich garnetite within the sample. Since primary textures are overprinted by metamorphism, the petrogenesis of the garnetite bands is indistinct. However, negative Ce anomalies may be associated with hydrothermal alteration of seafloor sediments, by imparting the negative Ce anomaly associated with seawater (e.g., Barrett & Jarvis, 1988). If the garnetite bands are derived from hydrothermally altered sediments, it would further imply the intercalated metabasites in the LRC formed in the shallow oceanic crust prior to subcretion.

2.5.3 Implications for the Eocene Cordilleran Forearc

The above discussion has highlighted several revisions regarding the metamorphic history of the Pacific Rim Terrane, specifically that: (1) Large, quartz-rich lithologies recently interpreted as felsic intrusions are instead metapsammitic units, (2) Felsic magmatism in the Pacific Rim Terrane occurred in the Eocene, but mid-Cretaceous magmatism is precluded by new detrital zircon ages (this study; Dlugosz et al., 2020; Seyler et al., 2020), (3) Intercalated metabasic rocks are likely not syn-metamorphic sills, but instead seafloor mafic rocks juxtaposed during either deposition or accretion, (4) Metamorphic isotherms are indifferent to the distribution of mafic lithologies and felsic sills, which are rarely associated with contact aureoles, (5) Peak metamorphism attained conditions up to ~600 °C and ~4.4 kbar in the LRC, and up to ~370 °C in the PPU (6) The metamorphic temperature gradient decreases monotonically from south to north, and current data suggest the gradient is continuous across the cryptic LRC-PPU boundary. This work otherwise confirms the presence of sub-blueschist assemblages locally preserved in the PPU (Rusmore & Cowan, 1985), and that the anomalously high-temperature metamorphic event coincided with isoclinal folding of the original strata into parallelism, followed by kilometer-scale open folding and top-to-the-east shear (Fairchild & Cowan, 1982; Jakob et al., 2016).

The metamorphic gradient presented here offers additional constraints on the cause of the elevated forearc temperatures. Since the calculated T-RSCM isotherms are broadly concentric and centered upon the Leech River fault, the, heating of the overlying metasediments appears to have been uniform and lacks heating the subcreted sediments nearest the Leech River Fault greater than structurally distal sediments. This is unlikely to be explained by the felsic Walker Creek intrusive suite, which barring a few coarse sills near the Leech River fault, are sparse and restricted to <2 m wide discontinuous bodies, and lack contact aureoles in all but two localities observed in greenschist facies rocks. The simplest explanation for this pattern is the subduction of hot, recently formed oceanic crust belonging to the Crescent terrane. To this end, Seyler et al. (2020) argue that the Leech River fault and the associated Bear Creek Shear Zone represent a palaeo-subduction interface based on near-fault microstructural and petrographic observations in both the LRC and Metchosin Igneous Complex (Crescent terrane). Notably, Seyler et al. (2020) retrieved geothermobarometric constraints of ~8 kbar and ~550 °C from within the shear zone, almost double the pressure estimate retrieved in this study via GBAQ barometry from an andalusite schist (T-RSCM = 563 °C, T-Wu17 = 574 °C, P = 4.4 ± 1.8 kbar, $1\sigma_P$ = 0.2 kbar) adjacent to the mylonitized shear zone. These results are not necessarily discrepant, as a preserved subduction interface may show significant variability in P-T conditions on short length scales (e.g., Penniston-Dorland et al., 2018), and numerous blocks of mylonitized metasediments and metabasites were observed along the Leech River fault during the field study. For example, the coarse garnet schist AG074-2 (T-Wu17 = 596 ± 22 °C) shows considerably more variation in estimated temperature as compared to typical LRC garnets distal to the shear zone, possibly suggesting a more protracted heating path.

Strong evidence exists for the formation of young oceanic crust in the Eocene forearc. Basalts in northern Siletzia were erupted between ~53 and ~44 Ma, including three emplacement ages from intrusive rocks in the Metchosin Igneous Complex at 51.176 ± 0.023, 51.115 ± 0.070 and 50.986 ± 0.023 Ma (Eddy et al., 2017). This coincides with the age of the syn-metamorphic Walker Creek tonalite sills, which are dated to 50.7 ± 1.9 Ma (Groome et al., 2003). This is compatible with the subduction of the Crescent terrane, comprising recently formed oceanic crust at approximately ~51 Ma, further implying proximity to a mid ocean ridge, either or both of which could have provided the heat necessary to cause a terrane-wide thermal anomaly at forearc depths of 12 to 15 km. The Metchosin Igneous Complex also shows an internal metamorphic gradient from prehnite-pumpellyite facies in the east, to low amphibolite facies grade in the west along the Leech River fault, which exceeds ‘typical’ seafloor metamorphic temperatures (Timpa et al., 2005). In addition to driving metamorphism in the Pacific Rim Terrane, the arrival of Siletzia also choked the Eocene subduction interface, shifting it westward to the present Cascadia subduction zone (e.g., Stern & Dumitru, 2019). This sequence of metamorphism followed by cessation of subduction and uplift shortly thereafter is consistent with the presently available constraints which include the ~51 Ma syn-metamorphic sills which likely accompanied T_{peak}, and muscovite cooling ages of 45.2 ± 0.2 Ma (Groome et al., 2003).

Subcretion of young oceanic crust has historically been considered to explain other hot forearcs (e.g. Chugach accretionary complex, Barnett et al., 1994). Molnar & England (1995) argue on the basis of numerical models that subcretion of lithosphere <1 Ma could produce T_{peak} of 400 °C at 10 km depth, and that higher slip-rates (~100 mm yr^{-1}) could contribute up to 200 °C via shear heating. The subduction rate of the Farallon plate has been estimated to be at least 160 mm yr^{-1} (Usui et al., 2003), so shear heating could be a viable contributing factor to metamorphism in the LRC. For example, simple thermal models incorporating shear heating during oceanic lithosphere subcretion are invoked explain conditions of ~600 °C at 3 to 7 kbar for ~15 Ma in the Chugach complex (Barnett et al., 1994). Whether heating of the overriding LRC was predominantly via conduction, advection of fluids or both (e.g., James et al., 1989), is unclear. Nevertheless, the T-RSCM results presented here do suggest that the felsic intrusions were not an effective vector for heating the forearc metasediments since they are infrequent and lack contact aureoles.

Ridge-trench intersection has been another proposed cause of elevated thermal metamorphism in the Pacific Rim Terrane (e.g., Groome et al., 2003; Groome & Thorkelson, 2009), and for other forearc terranes along the north Pacific margin (e.g., Bradley et al., 2003; Zumsteg et al., 2003, Farris & Paterson, 2009), as well as other Paleogene subduction zones like the Eurasian margin in East Asia (e.g., Wu & Wu, 2019). Definitively distinguishing subcretion of young oceanic crust from a ridge system is difficult using geology of the forearc alone, partly since the former implies proximity to the latter, blurring the distinction (Bradley et al., 2003). Nevertheless, high temperature forearc metamorphism along the Pacific margin has been an impetus for numerous models of plate boundaries and motions in Cretaceous to Paleogene time, such as the hypothesized Resurrection plate (Bradley et al., 2003; Fuston & Wu, 2020), or the Baranof-Leech River hypothesis (Cowan, 2003). The results presented here are not suitable to test the validity of such plate reconstructions but can be compared with expected ridge-trench characteristics (after Sisson et al., 2003). The Eocene forearc magmatism in the Pacific Rim Terrane is consistent with limited anatexis at depth, permitting emplacement of syn-metamorphic sills (Groome et al., 2003). However, the number and size of these felsic sills is significantly smaller than isograd-defining plutons in analogous forearc terranes, such as the Crawfish Inlet and Redfish Bay plutons at southern Baranof Island (Zumsteg et al., 2003). A possible explanation of this could be that the Pacific Rim Terrane was affected by off-axis ridge metamorphism and did not directly intersect the subducted Kula-, or Resurrection-Farallon Ridge, such that there were only limited degrees of partial melting at depth. Finally, the Pacific Rim Terrane is also host to quartz-sulfide-Au veins (Houle, 2011), and a stratiform volcanic-hosted massive sulfide deposit in the Survey Mountain metavolcanics (Malczak et al., 1982), which are indicative factors, but not definitive proof of ridge-trench intersection (Sisson et al., 2003).

2.6 Summary

The preferred model of elevated forearc metamorphism in the Pacific Rim Terrane presented here is the subcretion of then recently produced oceanic crust belonging to the Crescent terrane, and possibly proximity to a ridge system. The juxtaposition of the Crescent terrane against the LRC induced an elevated regional thermal gradient with the highest-grade rocks justified along the Leech River fault. RSCM geothermometry, garnet-biotite geothermobarometry and pseudosection modelling show rocks near the Leech River fault straddle and locally exceed the andalusite-sillimanite transition, with conditions up to ~600 °C and ~4.4 kbar. The metamorphic gradient delineated by T-RSCM values decreases monotonically from south to north, conforming to neither the distribution of felsic nor mafic protoliths within the LRC. Nonetheless, anatexis at ~51 Ma (Groome et al., 2003) produced a suite of volumetrically small felsic sills concentrated near the Leech River fault, but the proposed mid-Cretaceous intrusions are re-interpreted here as metapsammitic schists and paragneisses. The Eocene syn-metamorphic, syn-deformation sills did not produce identifiable contact aureoles except among rare intrusions into greenschist facies rocks at biotite or sub-biotite conditions. This observation, taken with the limited surface exposure of the felsic intrusions relative to the exposed area of rock metamorphosed, the absence of intrusions near the highest-grade rocks in the terrane including sillimanite schists and paragneisses, and indifference of isotherms to the distribution of sills challenges the proposal that contact metamorphism caused amphibolite facies metamorphism in the Pacific Rim Terrane.

Instead, this study proposes the necessary heat is derived from the subcretion of the underlying Crescent terrane. This metamorphic gradient is continuous across the LRC-PPU boundary, evidenced by chlorite-zone greenschist facies overprint in the north and western PPU, which otherwise has sub-blueschist facies, lawsonite-zone metamorphism in patchy vein and matrix assemblages. In addition to heat conduction from the then recently formed Crescent terrane, shear heating could play a role in elevating temperatures during subduction, as has been suggested elsewhere (e.g. Molnar & England, 1995), and more generally to reconcile higher temperatures in exhumed more deeply subducted rocks than predicted by thermal models (e.g., Kohn et al., 2018). However, the magnitude of shear heating remains contentious (e.g., van Keken et al., 2019). For this reason, future work should examine the proposal presented here, including the generation of supra-solidus conditions for a wet pelite via shear heating at relatively shallow forearc depths with numerical thermal models.

A 72.5 ± 0.8 Ma detrital zircon age in the PPU revises the maximum depositional age of the Pacific Rim Terrane to younger than the prior proposed age of ~88 to 92 Ma felsic magmatism, in line with other recent work (e.g., Dlugosz et al., 2020; Seyler et al., 2020). Geochemical discriminants suggest distinct provenance for the LRC and PPU metasediments, including more recycled detritus or continental felsic plutonics in the LRC source terrane, and a less evolved volcanic component in the PPU. The units were juxtaposed prior to Eocene thermal metamorphism such that isotherms are continuous across the boundary. Intercalated metabasites in the LRC have primarily NMORB affinity, although two samples show E-MORB-like chemistries, as do metabasalts interfoliated in the PPU. Nevertheless, the metabasic suite matches regional trace element trends observed in the accreted Siletz regional terrane to which the Crescent terrane belongs (Phillips et al., 2017). Multiple lines of evidence suggest the Tripp Creek metabasites pre-date metamorphism, but their interpretation as magmatic sills coeval to the Eocene felsic magmatism (Groome et al., 2003) cannot yet be definitively ruled out. Rapid uplift of the Pacific Rim Terrane constrained by ^{40}Ar/^{39}Ar muscovite cooling ages at 45.2 ± 0.2 Ma and a nonconformity with the ~35 Ma Carmanah group (Groome et al., 2003) is likely due to the arrival of the Siletz terrane, including the Crescent terrane, thickened by interaction with the Yellowstone plume, which served to clog the Eocene subduction system (Phillips et al., 2017; Stern & Dumitru, 2019). This rapid uplift is reflected in a lack of retrograde equilibration rims in garnet, and sparse retrograde replacements of the otherwise well preserved high-temperature LRC assemblages evaluated in this study.

Chapter 3. Sulfide stability during high temperature forearc metamorphism: Insights from the Pacific Rim Terrane, British Columbia

3.1 Sulfur in forearc metasediments

S is a minor component of most of the Earth's crust, but by virtue of its wide range of oxidation states (-II to +VI) and affinity for economically valuable elements, it is of significant interest in metamorphic systems. In marine siliciclastic sedimentary protoliths, S is typically bound in sulfides derived from biogenic, diagenetic, and hydrothermal processes (Goldhaber, 2003). Among carbonaceous marine sediments, pyrite (Py, mineral abbreviations hereafter from Whitney & Evans, 2010) is the most abundant sulfide phase and may occur in a vast array of habits, including as disseminated anhedral grains, laminae and bands, framboids, spherulites, and cubic euhedra (Goldhaber, 2003). Since sedimentary and diagenetic Py is commonly enriched in elements like Zn, Cu, Mo, Pb, Au and Ag (Thomas et al., 2011; Large et al., 2012), the stability of Py during prograde metamorphism bears on the mobility of these economically important elements. For example, models for the genesis of sedimentary-hosted 'orogenic Au' deposits commonly invoke Py and organic matter as the intra-terrane source from which Au may be mobilized and concentrated (e.g., Large et al., 2012; Pitcairn et al., 2015).

Furthermore, since S is exported to the mantle via subduction of oceanic lithosphere, sulfide stability bears on the global S cycle and mantle fO_2 (Evans & Tomkins, 2011; Canil & Fellows, 2017). S is a potentially important redox agent in the arc mantle, and its influence as a net oxidizing or reducing agent is contingent upon the P-T stability fields of sulfide and sulfate, and the P-T paths taken by subducted slabs (Tomkins & Evans, 2015; Walters et al., 2020). However, the behavior of sulfides in the shallow forearc environment of the subduction zone (<80 km depth, after van Keken et al., 2019) necessitates consideration given the possibility for significant S mobility and transformation of the sulfide assemblage at comparatively low-grade metamorphic conditions (Pitcairn et al., 2010).

During low pressure prograde metamorphism of carbonaceous sediments, the most significant reaction involving sulfide is a desulfidation reaction, in which Py (FeS_2) is converted to pyrrhotite, (Po, $Fe_{1-x}S$)

(Ferry, 1981; Tomkins, 2010). The reaction may be simplified as the pyrite-pyrrhotite buffer (Tomkins, 2010):

$$FeS_2 = FeS + 0.5S_2 \ \mathbf{[1]}$$

where for every mol of Py consumed, one mol of S is liberated. In more practical petrologic terms, a devolatilizing carbonaceous metapelite could also drive the production of reduced S species, such as in the desulfidation reaction (Ferry, 1981):

$$2FeS_2 + 2H_2O_{(fluid)} + C_{(gr)} = 2FeS + 2H_2S_{\ (fluid)} + CO_{2\ (fluid)} \ \mathbf{[2]}$$

In this manner, S could be mobilized and transported in a metamorphic fluid (Tomkins, 2010). However, this still neglects reactivity between liberated sulfide and the silicate mineral assemblage. Nonetheless, the breakdown of Py enables the redistribution of trace elements previously hosted therein (Large et al., 2012). There is significant variability in the degree of mobilization of base metals such as Cu, As, Zn, and Pb (Hammerli et al., 2016; Stepanov, 2021), but a growing body of evidence suggests liberated Au is efficiently transported as complexes with S ligands in metamorphic fluids (Pokrovski et al., 2009). This mechanism is favorable for justifying the ‘Au-only’ nature of many sediment-hosted orogenic Au deposits, since Au complexes with S ligands, such as $Au(HS)_2^-$, are stable for typical metamorphic fluid compositions, whereas base metals that complex with chloride ligands are unfavored at low salinities (Zhong et al., 2015).

Delineating the conditions of Py stability, and hence Py desulfidation, is chiefly important for understanding mechanisms of S and Au mobility during prograde metamorphism. The development of internally consistent thermodynamic data for common sulfides like Py and Po (Evans et al., 2010) has enabled advances in models of sulfide-silicate phase relations. Such models, however, show contrasting results. When reactions between sulfides and Fe-silicates are precluded, then models show Py stability can persist until conditions approximating terminal chlorite breakdown and the associated fluid production via devolatilization (Tomkins, 2010). Conversely, recent models including sulfide-silicate phase relations show that the Py-Po transition is a narrow, low-temperature threshold that may be influenced by bulk rock chemistry (Zhong et al., 2015). Thus, sulfide phase relations are variable in dimensions of pressure, temperature and composition (P-T-X), necessitating careful consideration of both protolith and the trajectory of P-T paths when interpreting conditions of S release.

This study seeks to test sulfide stability under variable T-X parameters by examining major and trace element changes from sub-greenschist to amphibolite facies metamorphic conditions using natural rocks, and pseudosections produced using the PerpleX suite of Gibbs free energy minimization programs (Connolly, 2005). The Pacific Rim Terrane on southern Vancouver Island, British Columbia, provides a suitable environment in which to pursue this question: The sulfide-bearing carbonaceous forearc metasediments have been variably metamorphosed up to amphibolite facies at ~4 kbar and ~600 °C (Chapter 2). These anomalously high metamorphic temperatures in the forearc were likely induced by subcretion of young, hot oceanic crust during Eocene time (Chapter 2; Groome et al., 2003). The Pacific Rim Terrane is the probable source for placer gold in regional catchments, which spurred a nineteenth century goldrush (Grove, 1984). In more recent decades, quartz-sulfide-Au veins in greenschist-amphibolite grade rocks in the terrane have been the subject of periodic economic interest with indicated reserves of more than ~50 kton Au (Houle, 2011). Thus, the Pacific Rim Terrane is uniquely suited to evaluate temperature and compositional controls on prograde desulfidation, and consequences for the genesis of an orogenic Au deposit. The occurrence of Py, Po, and chlorite in the terrane are compared with representative pseudosections and whole rock geochemistry to test proposed models of desulfidation.

3.2 Regional geology and metamorphism

3.2.1 The Pacific Rim Terrane

The Pacific Rim Terrane is a package of metasedimentary and subsidiary metaigneous rocks subcreted to Wrangellia in Eocene time and metamorphosed to amphibolite grade (Fairchild & Cowan, 1982; Groome et al., 2003; Chapter 2). Metamorphism coincided with two periods of deformation: (1) isoclinal folding that transposed depositional fabrics into parallelism, obscuring regional stratigraphy, and

(2) subsequent top-to-east shear and large-scale open folding of the foliation (Fairchild & Cowan, 1982; Jakob et al., 2016). The terrane comprises three sub-units, two of which are in mutual contact and considered by this study: The volumetrically larger Leech River Complex (LRC) and the smaller Pandora Peak Unit (PPU). The LRC comprises mostly interfoliated metapelitic and metapsammitic lithologies, including carbonaceous argillites through schists, and recrystallized arkoses and greywackes, which occur as quartz-rich paragneisses at highest grades (Chapter 2). Subsidiary but common horizons of metabasic rocks are also found intercalated with the metasediments at all grades, ranging in width from submeter to tens of meters. Within the LRC, volumetrically minor felsic sills are interfoliated with the metasediments but generally lack contact aureoles (Chapter 2). The metaigneous sills may have been generated by supra-solidus conditions of the LRC at depth (Groome et al., 2003), leading to melting and their emplacement as syn-deformation intrusions among independently heated metasediments.

The PPU comprises diverse lithologies including clastic argillites, tectonites, disrupted and intact radiolarian ribbon cherts, metabasalts, and meta-ultramafic olistostromes. Peak metamorphic temperatures within the PPU range from 230 to 370 °C (Chapter 2). Patchy and vein-restricted metamorphic assemblages of lawsonite and prehnite-pumpellyite suggest the PPU attained sub-to-low blueschist facies conditions. Nonetheless, the LRC and PPU were likely subjected to the same thermal metamorphic event, as the temperature gradient between the two units is continuous (Chapter 2). However, the PPU is distal to the subcreted Crescent terrane that initiated thermal metamorphism, and therefore the conventional forearc metamorphic assemblages are locally preserved.

Metamorphic isotherms have been delineated by RSCM geothermometry (Figure 3.1). Individual temperatures estimates were geospatially oriented and semi-quantitative estimates of metamorphic temperature for the terrane were made by natural neighbor interpolation in MATLAB. A detailed discussion of the metamorphism was covered in Chapter 2. While the model is simple and does not account for discontinuities such as post-metamorphic faults, the constructed isotherms are consistent with petrographic observations.

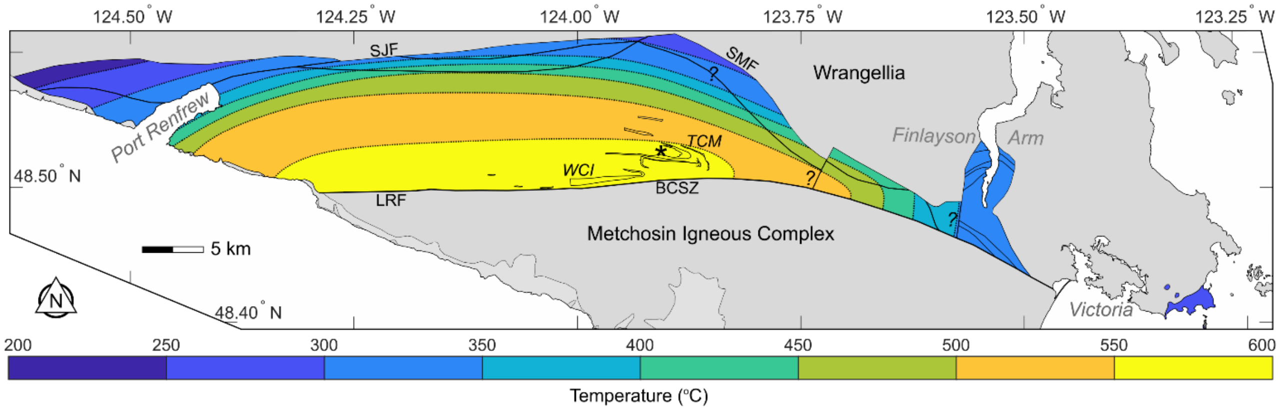

Figure 3.1 Simplified isotherm map modified after Chapter 2 to integrate T-RSCM (Chapter 2; Jakob et al., 2016), T-Gt-Bt, petrography and field observations. Base map modified after Massey et al. (2005) with elements from Grove (1984), Fairchild & Cowan (1982), Pope (2006), and Chapter 2. The southern contiguous Pacific Rim Terrane (LRC and PPU), contoured, is thrust beneath Wrangellia, and in turn underthrust by the Metchosin Igneous Complex. Isotherms are continuous across the western LRC-PPU boundary in the vicinity of Port Renfrew. Peak metamorphic temperatures (up to ~600 °C) are in the vicinity of the Leech River Fault (LRF). Placenames in grey. WCI = Walker Creek Intrusions, TCM = Tripp Creek Metabasite, BCSZ = Bear Creek Shear Zone, SJF = San Juan Fault, SMF = Survey Mountain Fault. Asterisk indicates approximate location of the Valentine Mountain Au prospect. Areas with '?' symbol have poor data density and lack corroborating field observations.

3.2.2 Sulfide Petrography

The sulfide assemblages among the LRC and PPU are variable but can be generalized by a greater frequency of Po and chalcopyrite (Ccp) among high grade rocks (>500 °C), and Py occurring across grade (Figure 3.2). This study does not explicitly consider the sulfide assemblages associated with the Valentine Mountain orebody, which has been detailed in resource reports (e.g., Grove, 1984; Houle, 2011). Sulfides associated with the Au-bearing quartz veins reportedly include Py, Po, Ccp, and coarse arsenopyrite (Apy) which hosts inclusions of the other common sulfides, as well as native Au. Auriferous quartz veins do occur among metabasic rocks but are generally hosted in the thick psammitic (± pelitic) succession in the Valentine Mountain region, historically called the Valentine Mountain metasandstone (after Fairchild & Cowan, 1982). This study focuses on the sulfides hosted in the matrix and porphyroblasts of the surrounding metasedimentary and metaigneous lithologies across grade in the

Pacific Rim Terrane. While the depositional character of the LRC and PPU are distinct (Chapter 2), the low-grade carbonaceous argillites and metabasalts of the PPU are taken as a proxy for assemblages among sub-greenschist LRC metasediments, which were largely overprinted by the Eocene thermal metamorphic event.

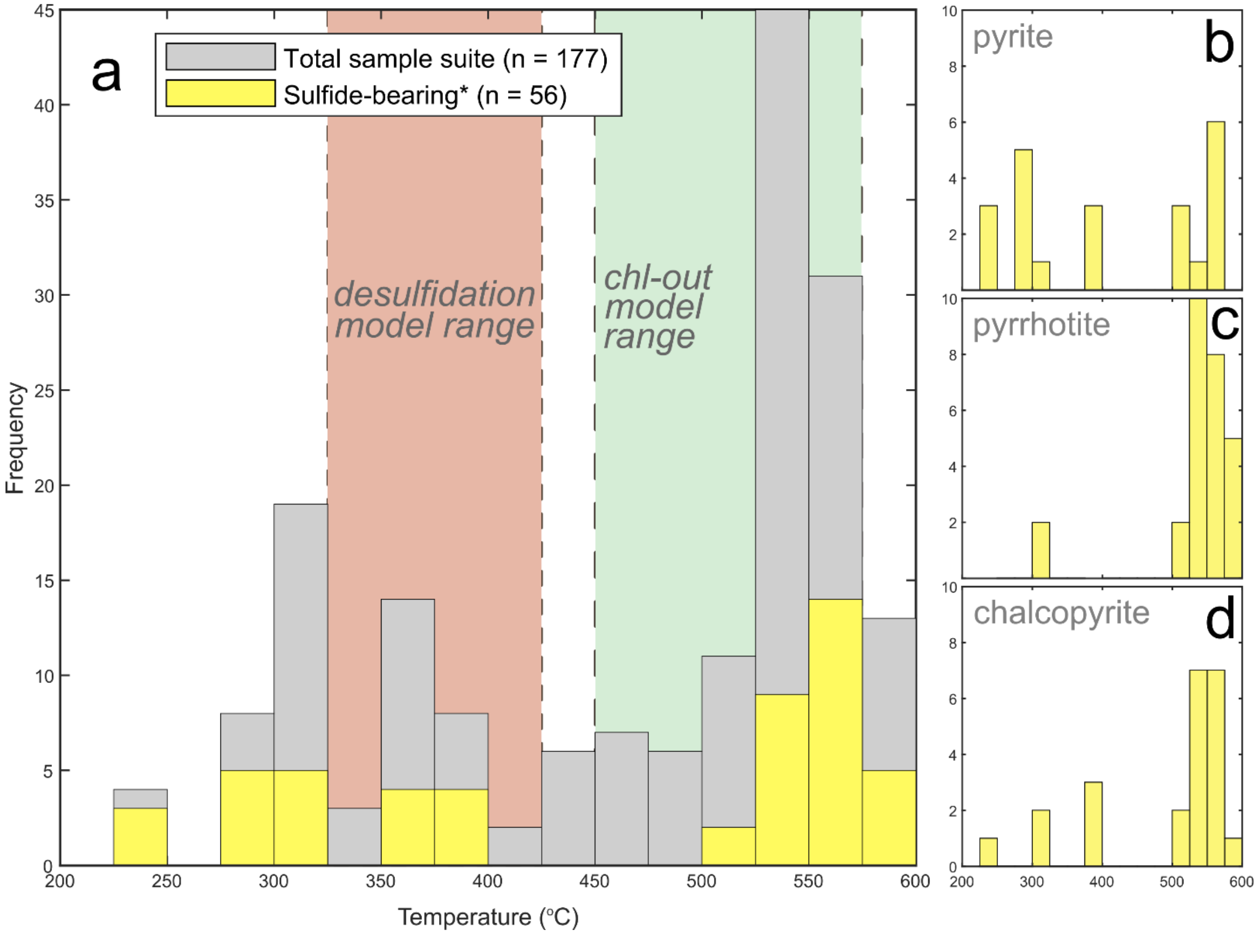

Figure 3.2 Histogram plot showing the distribution of the sample suite at their estimated peak metamorphic temperature from the interpolated gridded dataset. *a:* *Sulfide-bearing samples are defined as those which show appreciable sulfide identified in hand sample, polished mount and thin section. Samples with trace disseminated sulfide not readily identifiable with petrographic microscope are not included (see, bulk rock S content data). Fields of 'desulfidation' and 'chl-out' indicate locations of where each continuous reaction can occur, integrative of variation in protolith and pressure conditions *b:* Occurrences of pyrite (Py), *c:* pyrrhotite (Po), and *d:* chalcopyrite (Ccp) across metamorphic temperature. Note that samples may host one or all of the identified sulfides. Rare sulfide phases (e.g., sphalerite, bornite) are included in *a*.

Among low grade argillites and clastic tectonites, Py commonly occurs as singular or aggregate spheroidal grains, interpreted as framboidal Py. Framboidal morphologies persist even in rocks which experienced substantial cataclastic deformation, and in samples which attained temperatures up to ~350 °C. Other common morphologies include euhedral to subhedral Py cubes, often hosted within laminated to thinly banded ribbon cherts, and anhedral, ‘porous’ Py grains which chiefly occur within psammitic protoliths. Less commonly, Po, sphalerite (Sp), and Ccp are observed in low grade sediments associated with deformed lenses of calcite and quartz. For example, within the clastic argillite AG010-2, the carbonaceous argillite matrix hosts fine-grained fractured spheroids replaced by Po and Fe-oxides, whereas adjacent deformed calcite lenses host coarse-grained Po with intergrowths of Ccp and Sp (Figure 3.3). Low grade samples of interbedded argillite and sandstone retrieved from fault-bound blocks of LRC strata hosted within the PPU show exclusively anhedral, porous Py. At comparable metamorphic temperatures along strike, a disrupted banded chert from the PPU hosts exclusively anhedral grains of Po with subsidiary Ccp and rare grains of native Au. In the lowest grade sample analyzed (DC0514, 230 °C), Py is the dominant sulfide, occurring as euhedra and framboids (Figure 3.4). Low-grade basic protoliths generally do not bear sulfides, but where observed, both Py and Po occur.

Among the low-grade suite there is significant variation in the sulfide mineral assemblages. Textural equilibrium is not attained in most samples, amplifying difficulty in assigning sulfide minerals to specific parageneses. Nonetheless, the following generalizations are made: (1) the primary sulfide for low-grade metasedimentary rocks is Py, commonly exhibiting framboidal and cubic morphologies consistent with expected primary textures for a near-margin marine depositional environment; (2) Po locally pseudomorphs primary Py grains, including framboidal morphologies; (3) coarse-grained Po and intergrown sulfides are hosted within distinct lenses that may suggest they belong to a late or retrograde metamorphic paragenesis.

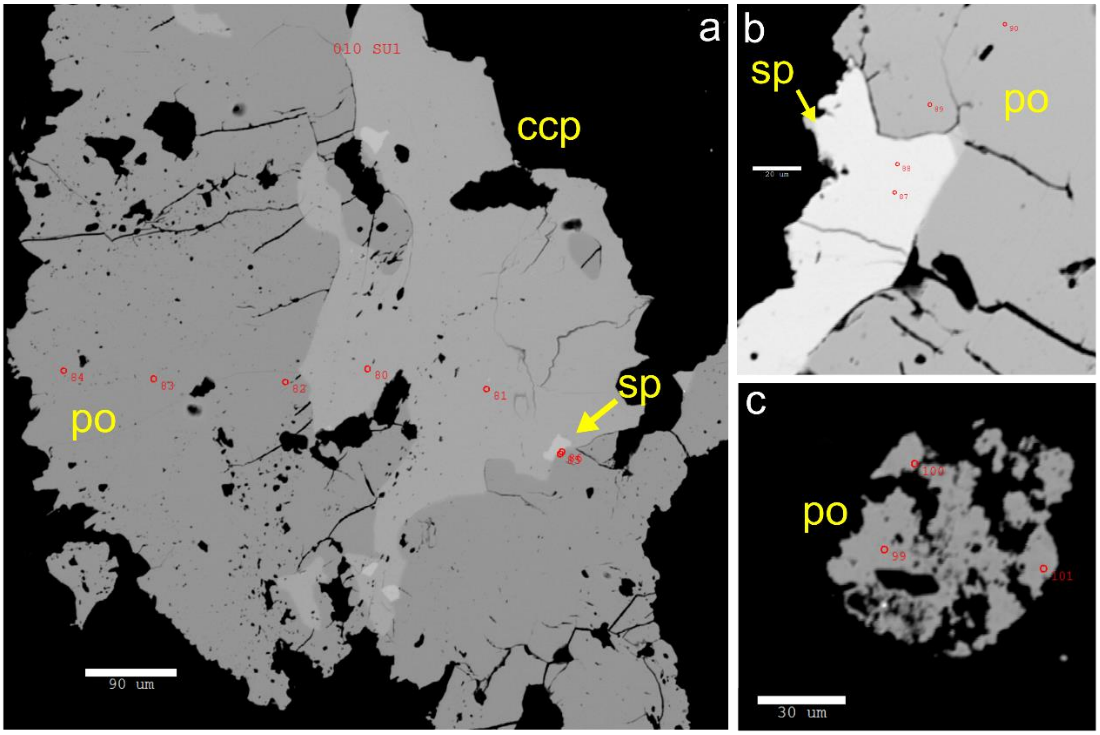

Figure 3.3 Backscatter EPMA images (*University of Alberta EML*) showing the complex sulfide morphology in the low-grade sample AG010-2 from the PPU. *a:* Coarse sulfide intergrowths of Po, Ccp and blebby Sp, hosted in a deformed calcite lens. Note blebs of Po within Ccp host fractures which are not continuous in Ccp and thus predate Ccp formation. *b:* Intergrowth of Sp and Po in another calcite-hosted grain. *c:* Spheroidal Po (after Py) grain hosted in the tectonized clastic-argillite matrix.

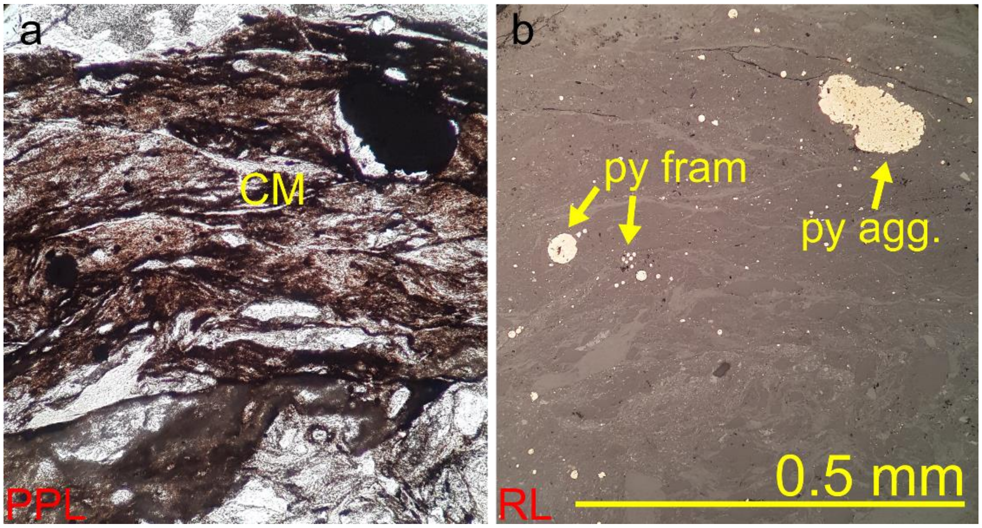

Figure 3.4 Plane polarized transmitted light (*a*) and reflected light (*b*) of disaggregated Py framboids and coarser Py aggregates in a CM-rich tectonized metasediment from the PPU (DC0514).

Samples which attained moderate metamorphic grades (i.e., 350 to 450 °C), exhibit a dearth of visible sulfide grains (Figure 3.2). However, among the sub-biotitic phyllites found at these grades, small lenticular foliation-parallel porosities are common. While the cause of these porosities is unclear, some are lined with granular brown Fe-oxides which could be a result of leaching and oxidation of sulfides via late fluid alteration or supergene processes. For example, replacement of Po by goethite is noted in forearc metasediments in New Zealand (Pitcairn et al., 2010). However, it is unclear why this textural feature is only observed among phyllites and not common in the argillites or schists elsewhere in the terrane. Where sulfides do occur among moderate grade phyllites, Py is dominant in pelitic protoliths, while Po is observed in basic protoliths. In one sample (AG105-1, 399 °C), thin 'stringers' of Py occur parallel to the phyllitic foliation. The Py stringers have a smooth to porous texture, an internal foliation-parallel fabric, and locally host small blebs of Ccp (Figure 3.5).

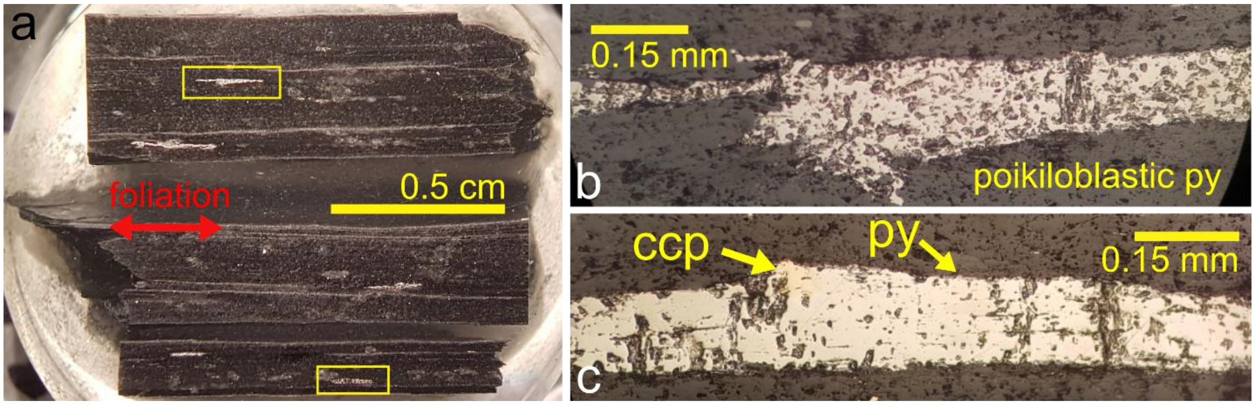

Figure 3.5 *(a)* Image of the carbonaceous phyllite AG105-1 in a polished mount, with (*b*) and (*c*) corresponding to inset boxes. Deformed pyrite stringers have variable pitting textures, and can show foliation-parallel internal fabrics defined by microcrystalline inclusions. Large vertical fractures are indicative of brittle extension, suggesting deformation locally outlasted T_{peak} at this station.

At higher grades (i.e., 450 to 600 °C) the sulfide assemblages are described based on their textural context in either the rock matrix, or as inclusions within porphyroblasts. In the matrix, all of Py, Po, and Ccp occur. Sulfide morphology is highly variable, including deformed cubic Py, and elongated anhedral grains that are deformed in the foliation. Grain morphology indicates that sulfides in the matrix may both predate and postdate deformation, consistent with multiple generations of sulfide growth. The highest grade metapelites (575 to 600 °C) typically do not host any matrix sulfide.

Porphyroblasts of garnet, staurolite and andalusite occasionally encapsulate inclusions of the same sulfide phases observed in the matrix, but Po inclusions occur with much greater frequency than Py, and Ccp typically occurs as small blebs within or near the grain boundaries of Po. Staurolite and andalusite host all of Po, Ccp, and subsidiary Py inclusions, whereas garnet only hosts Po and subsidiary Ccp. Fewer sulfide inclusions occur in all porphyroblasts at temperatures greater than ~575 °C.

The relative timing of porphyroblast formation can be partially deduced from petrography. While the initiation of andalusite porphyroblast growth is unconstrained, its growth must coincide with the appearance of staurolite, which locally embays the rims of andalusite. One case shows garnet partially encapsulated by coarse andalusite which has partially been replaced by chlorite that pseudomorphs the grain boundary (Figure 3.6). Thus, andalusite growth also overlaps with garnet growth. Locally, large anhedral staurolite porphyroblasts are intergrown with euhedral garnet, possibly indicating the incomplete reaction of staurolite to produce garnet (Chapter 2). Thus, garnet and staurolite also co-existed near peak temperature conditions, although not necessarily stably, and staurolite may overstep its nominal stability. While garnet is normally subhedral to euhedral, staurolite in the sillimanite zone exhibits strong disequilibrium textures, including anhedral patchy grains and partial replacement by biotite. Additionally, garnet locally overprints the matrix foliation, suggesting that its growth, and peak metamorphism, at least locally outlasted deformation.

Therefore, the following generalized sequence best describes porphyroblast appearance: (1) in sufficiently aluminous protoliths, the andalusite porphyroblasts nucleate first; (2) staurolite porphyroblasts form second and co-exist stably with andalusite such that staurolite laths embay into the mid-rim of andalusite; (3) garnet likely joins the assemblage last in the highest temperature rocks, although may also nucleate in staurolite-absent rocks in greenschist facies (Chapter 2). These generalizations do not exhaustively describe phase textural relationships, as variation in protolith composition bears on the phase equilibria that produce the porphyroblasts. Nonetheless, andalusite sulfide inclusions are likely the earliest glimpse of sulfide phase stability in high temperature rocks, then staurolite, and finally garnet.

Garnet porphyroblasts, which are typically euhedral and ≤0.5 mm diameter among most of the schists in the LRC, only occasionally host small anhedral Po ± Ccp. Garnet porphyroblasts may locally exceed 1 cm in diameter among biotitic paragneisses and sillimanite schists but are often barren of sulfide. Staurolite porphyroblast morphology includes euhedral cruciform cross-penetrative twins, elongate tabular grains, and rounded anhedral porphyroblasts. Staurolite grain size is variable, but laths may range to greater than 1 cm in length. Staurolite porphyroblasts are highly poikiloblastic, often comprising inclusions of quartz, plagioclase, graphite, Po and occasionally Py (Figure 3.7). Inclusion morphology within staurolite is comparable to those within garnet, comprising rounded anhedral and non-porous blebs.

Andalusite forms the largest porphyroblasts, ranging from 0.5 cm to megacrystic grains with diameters >5 cm. Inclusion abundance in andalusite is variable between outcrops, ranging from completely barren to numerable sulfides, at identical metamorphic temperatures. In one coarse andalusite porphyroblast, inclusions of coexisting Py and Po are observed (Figure 3.6). Therein, the adjacent sulfide grains have contrasting textures: both are angular and anhedral, but the Py hosts numerous small silicates and Ccp inclusions distributed throughout the grain. In contrast, the adjacent Po hosts few silicate inclusions, and Ccp persists as larger round blebs at the margin of the grain (Figure 3.6). Po inclusions elsewhere within the same porphyroblast do host rounded silicate blebs, but Ccp always occurs either as rounded lamellae propagating from grain margins or independent adjacent grains (Figure 3.6). Sulfide inclusions are commonly elongated on an axis parallel to the cleavage planes in andalusite. Py grains do not occur clustered in the grain core, as anticipated if the andalusite porphyroblasts faithfully recorded the desulfidation reaction, and instead occur in the mid-rim.

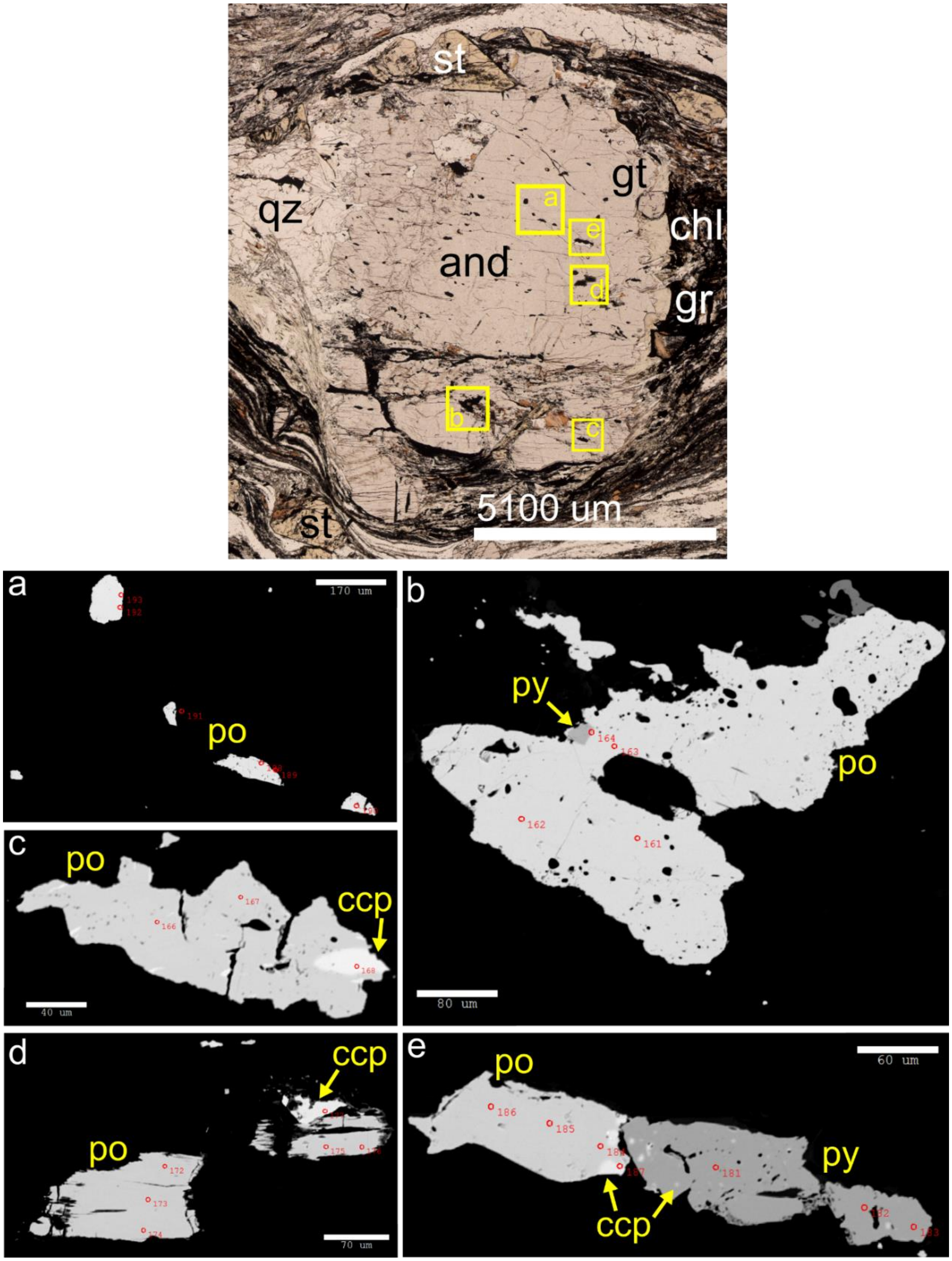

Figure 3.6 Map of inclusions within a coarse andalusite porphyroblast in sample AG042. *(a)* Small, anhedral Po inclusions with few silicate inclusions. *(b)* Large Po-Py composite grain, where Py forms as blebby grains in Po margins. *(c)* Po grain with elongate Ccp lamellae possibly from exsolution. *(d)* Coarse, fractured Po with ragged margins (rimmed by f.g. micas). *(e)* Coexisting Py and Po in mutual contact. In Po, Ccp occurs as blebs arranged at the grain margin. In Py, Ccp occurs as small point grains throughout along with small silicate inclusions.

Metabasic and metapsammitic units are also observed across all metamorphic grades in the LRC and PPU. However, in all but the lowest grade metapsammitic lithologies no sulfide is observed, and even narrow centimeter-scale layers of psammitic compositions within the pelites have a marked reduction in total sulfide content. Thus, it is impractical to track the stable sulfide assemblage across grade in psammitic protoliths. Metabasic lithologies do host sulfides, especially at low grade where irregular Py and Po occur as discrete grains and disseminated in deformed veins. In metabasite units Po is more abundant than Py at comparable metamorphic temperatures as compared to metasedimentary lithologies, although Py does locally occur as blebs within Po at moderate metamorphic grades (~400 °C). High grade amphibolites are often sulfide-poor, or host trace amounts of Po and Ccp as inclusions within amphibole or grown in the interstices between laths. However, metabasite lithologies which also bear pink garnetite banding are associated with a greater modal abundance of interstitial Po, locally replaced at the margins by fingers of bornite and an Fe-oxide.

Figure 3.7 *(Next Page)*: EPMA (University of Alberta EML) and SEM (University of Victoria AMF) backscatter images of low- and high-grade sulfides in the matrix and as inclusions. (*a)* Framboidal Py in a tectonized argillite from the PPU (~290 °C), including disaggregated grains distributed in the fine-grained matrix. *(b)* Aggregate Py from the same sample as *a*. *(c)* A complex inclusion assemblage of Po + Py + Ccp + anhedral andalusite hosted in a coarse grained staurolite porphyroblast (~550 °C). Anhedral andalusite intergrowths may imply production by staurolite breakdown. Ccp occurs as distinct blebs at Po grain margins. *(d)* Composite Po + Cp and ilmenite inclusion assemblage in staurolite (~550 °C). *(e)* Isolated Py inclusion in coarse grained staurolite (~550 °C). *(f)* A long Py stringer contours the margin of a garnet and staurolite porphyroblasts and has been caught up in the foliation-defining deformation.

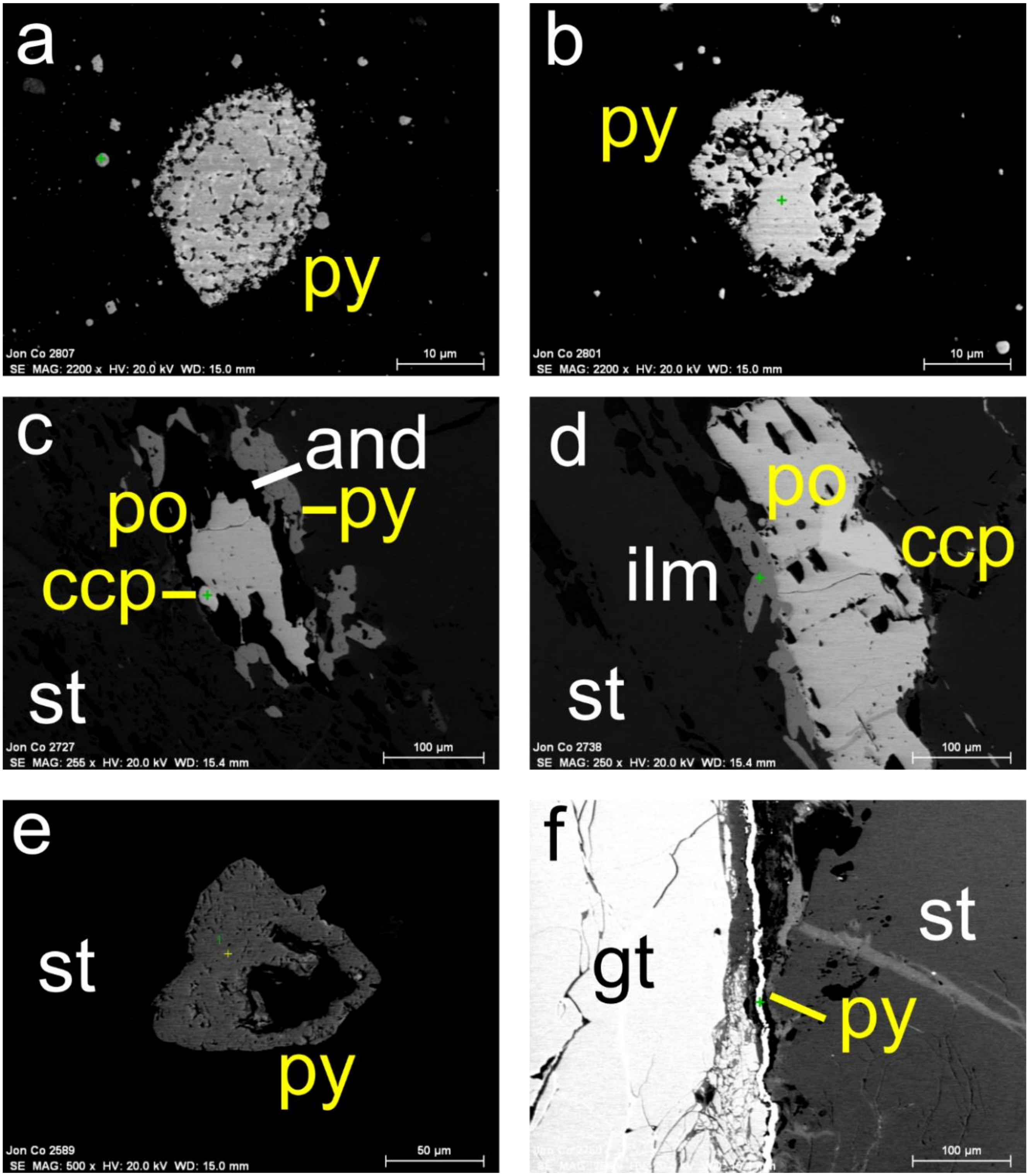
a
py
Jon Co 2807
SE MAG: 2200 x HV: 20.0 kV WD: 15.0 mm
10 µm
b
py
Jon Co 2801
SE MAG: 2200 x HV: 20.0 kV WD: 15.0 mm
10 µm
c
and
po
py
ccp
st
Jon Co 2727
SE MAG: 255 x HV: 20.0 kV WD: 15.4 mm
100 µm
d
po
ccp
ilm
st
Jon Co 2738
SE MAG: 250 x HV: 20.0 kV WD: 15.4 mm
100 µm
e
st
py
Jon Co 2589
SE MAG: 500 x HV: 20.0 kV WD: 15.0 mm
50 µm
f
gt
st
py
100 µm

3.3 Methods

3.3.1 Thermometry

Metamorphic temperatures were assessed using Raman Spectroscopy of Carbonaceous Materials (RSCM) geothermometry in Chapter 2, and details of the procedure and results are outlined therein. Gridded RSCM results were interpolated in MATLAB, from which approximate estimates of metamorphic temperature for sulfide-bearing samples were extracted for this study.

3.3.2 Whole Rock Geochemistry

Rock samples were selected to assess S, C, and trace element content between protoliths and across metamorphic grade. Bulk rock major and trace element geochemistry were performed as outlined in Chapter 2, and total S and C analyses, were performed for a suite of 28 samples. Total C and S analyses were measured at Activation Laboratories Ltd via IR detection of SO_2 and CO_2 from 0.2 g of combusted sample material in a high oxygen environment.

3.3.3 EPMA & SEM

Electron microprobe analyses for major and select trace elements in sulfides were performed at the University of Alberta using a JEOL JXA-8900R microprobe with the wavelength dispersive spectrometer (WDS) at an accelerating voltage of 20 kV and current of 20 nA. Due to small sulfide grain diameters and uncertain morphology at depth within slides, spot analysis diameter was set to the minimum (<1 µm) with 20 seconds on peak collection and 10 seconds on background collection for each analyte. Scanning electron microscopy was performed at the University of Victoria’s Advanced Microscopy Facility with the Hitachi S-48000 to collect backscatter imagery of sulfide minerals and qualitative mineral chemistry data was retrieved using the Bruker Quantax EDS system with an accelerating voltage of 20 kV and current of 20 nA.

3.3.4 Pseudosection Models

Pseudosection models for the metasedimentary units were generated by Gibbs free energy minimization in the PerpleX program suite (Connolly, 2005). Bulk rock major element data for modelled samples were recast in the same manner as Chapter 2 except including S. Given the significant variation in total S content among the carbonaceous sedimentary protoliths (Goldhaber, 2003), each standard model run is prescribed 0.5 mol% S_2 as an upper estimate of protolith total S content, unless otherwise specified. Pressure-Temperature (P-T) pseudosections were calculated in the domain of one to six kilobars and 300 – 700 °C, and Temperature-Composition (T-X) pseudosections were calculated over specified compositional domains at fixed pressures of 2 and 4 kbar, and temperatures of 300 – 700 °C. The solution models of White et al. (2014) were used for garnet, biotite, staurolite, chlorite, epidote, white mica, ilmenite, and cordierite. The ternary feldspar solution model after Fuhrman & Lindsley (1988) was utilized. The ideal stilpnomelane, Stlp, and four component non-ideal carbonate, Carb(M), solution models were also utilized. The selected chemical system excludes many components relevant to sulfide phases (e.g., Cu, As, Ni) since solution models for many sulfides are not yet available, and base metal speciation is not addressed in this study. Thus, the only sulfide solution model included is that of Po (Evans et al., 2010), comprising the solid solution between troilite (FeS) and trov ($Fe_{0.875}S$). The fluid phase was treated explicitly as a solution using a COHS fluid model, which relies upon hybridized equations of state for the pure comprising species H_2O, CO_2, CO, H_2, and H_2S (e.g., after Connolly & Cesare, 1993). To produce fluid-present conditions in the low-temperature domain, molar H:O is artificially raised relative to LOI values at a ratio of two to one, while the ratios of other components are unchanged.

3.4 Results

3.4.1 Bulk Rock Geochemistry

Bulk rock major element analyses are presented in Chapter 2. LOI values decrease with increasing temperature, but total C does not, exhibiting scatter between 0.1 and 1 wt% in the sample suite

(Table 3.1). Bulk S content shows a distinct decrease between 200 to 500 °C, and an increase at temperatures higher than 500 °C. The initial bulk S decrease is reflected in both metasedimentary and metabasic lithologies, but the high-grade increase is more definitively reflected in metasedimentary samples.

Chalcophile trace elements (Table 3.2), including Cu, Pb, and Ga do not exhibit systematic variation with metamorphic grade (Figure 3.8). Data for Zn in metabasites show a slight decrease with increasing temperature, but this effect is not observed for the metasedimentary suite. Similarly, bulk Co is approximately unchanged for metasedimentary units, but exhibits a small increase at higher temperatures for the metabasic samples. Ni exhibits a modest increase with metamorphic grade among metasedimentary samples, but there is significant scatter among the metabasites. Bulk As data are highly variable across grade, but samples in the range of 500 – 550 °C exhibit the highest values, albeit with the largest total range. Most analyses for Au are <2 ppb detection limit. However, of the four samples with detectable Au, the highest values are recorded at low and high grade respectively (Figure 3.8). The highest Au value of 77 ppb was detected in an otherwise nondescript fine-grained biotite schist, while the other high-grade sample above detection limit are associated with a greater prevalence of late quartz veining in andalusite-bearing schists from the Valentine mountain region.

Table 3.1 Bulk rock major element data determined by ICP-OES and peak T from Chapter 2.

			Det Limit (%)	0.01	0.01	0.01	0.001	0.01	0.01	0.01	0.01	0.001	0.01		0.01
Sample	Unit	T (°C)	Rock Type	SiO_2	Al_2O_3	Fe_2O_3*	MnO	MgO	CaO	Na_2O	K_2O	TiO_2	P_2O_5	LOI	Tot
LC 12	TCM	555	Basite	49.06	16.01	10.35	0.17	7.61	11.31	2.52	0.13	1.11	0.09	2.46	100.8
AG 055-1	TCM	449	Basite	49.33	17.36	10.93	0.17	4.35	7.66	3.45	0.51	1.43	0.16	3.09	98.44
AG 059	TCM	554	Basite	45.83	18.98	13.09	0.20	4.07	9.39	3.52	0.69	2.51	0.39	0.77	99.44
AG 069-2	TCM	544	Basite	45.64	15.61	12.49	1.36	6.32	12.56	2.07	0.22	1.57	0.25	1.09	99.19
AG 069-3	TCM	544	Basite	49.74	15.2	10.3	0.33	8.22	10.55	3.04	0.53	1.58	0.15	1.03	100.7
AG 070-2	TCM	542	Basite	48.74	17.21	9.78	0.26	6.99	12.52	2.17	0.16	1.13	0.19	1.00	100.2
AG 121-2	TCM	537	Basite	47.68	15.88	12.11	0.27	6.6	13.51	1.49	0.32	1.63	0.15	0.95	100.6
AG 137	TCM	511	Basite	46.95	17.29	9.68	0.17	8.81	11.42	2.63	0.18	1.38	0.12	2.16	100.8
AG 089-1	PPU	235	Basite	44.4	20.78	11.13	0.27	3.34	12.57	1.49	0.28	1.46	0.2	4.82	100.7
AG 105-4	TCM	399	Basite	49.34	18.61	11.57	0.21	4.34	9.34	3.1	b.d.l.	0.83	0.13	3.32	100.8
AG 095-2	PPU	370	Basite	46.86	12.81	13.16	0.20	7.46	8.86	2.8	0.42	2.10	0.28	4.04	98.99
AG 029-4	LRC	313	Pelite	61.58	17.34	6.62	0.08	2.72	1.08	2.36	2.74	0.81	0.19	4.13	99.65
AG 101-1	LRC	475	Pelite	61.49	17.68	5.71	0.07	2.36	3.01	1.83	2.87	0.83	0.16	4.03	100
AG 080	LRC	584	Pelite	61.24	18.03	7.73	0.14	3.15	2.27	2.08	2.59	0.89	0.22	2.34	100.7

b.d.l. = below detection limit

*Total Fe tabulated as Fe_2O_3

Table 3.2 Select trace element data determined by ICP-MS, ICP-OES, INAA and IR

	Group	LRC	LRC	LRC	LRC	LRC	LRC	LRC	LRC	LRC	LRC	LRC	LRC	LRC
	Protolith	metased	metased	metased	metased	metased	metased	metased	metased	metased	metased	metased	metased	metased
	T (°C)	313	475	584	372	556	545	548	596	495	545	399	474	458
DL*	**Analyte**	AG 029-4	AG 101-1	AG 080	AG140	AG046-3	AG127	AG118	AG049-1	AG054	AG128	AG105-1	AG103-2	AG056
0.01%	**C**	0.62	0.92	0.71	0.53	0.59	0.5	0.65	0.46	0.32	0.2	0.88	0.62	0.15
0.001%	**S**	0.033	0.027	0.004	0.009	0.233	0.168	0.203	0.345	0.069	0.015	0.224	0.065	0.007
0.01%	**Fe**	4.78	4.25	5.53	6.64	4.99	4.95	4.7	4.67	3.82	1.8	8.2	4.66	2.57
0.01%	**Na**	1.7	1.36	1.57	1.22	1.84	1.39	1.67	1.83	1.72	0.79	1.08	1.42	2.82
5	**V**	181	160	194	209	154	178	156	147	136	51	183	147	61
5	**Cr**	91	77	127	116	96	111	96	68	71	30	104	98	48
1	**Co**	10	10	19	12	16	19	14	17	6	3	18	8	25
1	**Ni**	38	21	58	56	55	62	41	42	14	15	63	24	36
1	**Cu**	23	71	14	50	59	52	39	67	14	13	46	12	38
1	**Zn**	92	92	104	156	88	118	115	94	99	34	139	105	78
1	**Ga**	20	22	22	24	18	23	20	22	16	7	19	18	8
0.5	**Ge**	1.3	1.9	1.8	1.8	1.4	1.1	1	1.2	1.2	0.8	0.8	1.4	1
0.5	**As**	1.5	7.9	b.d.l.	16.2	2.9	45.9	1.8	b.d.l.	12.7	22.6	19.6	9	13.4
1	**Rb**	80	83	89	75	86	82	79	96	89	21	84	63	19
2	**Sr**	185	607	263	134	297	218	250	407	377	114	247	272	114
2	**Mo**	b.d.l.	b.d.l.	b.d.l.	b.d.l.	b.d.l.	b.d.l.	b.d.l.	2	2	b.d.l.	b.d.l.	b.d.l.	b.d.l.
0.3	**Ag**	b.d.l.	b.d.l.	b.d.l.	b.d.l.	b.d.l.	b.d.l.	b.d.l.	b.d.l.	b.d.l.	b.d.l.	b.d.l.	b.d.l.	b.d.l.
1	**Sn**	1	1	2	5	5	4	8	3	1	1	1	1	1
0.2	**Sb**	0.4	1.5	b.d.l.	2.1	0.7	0.2	0.2	0.4	0.3	b.d.l.	0.9	0.5	0.5
0.1	**Cs**	3.7	2.7	5	3.4	4.2	3.8	4.1	3.7	4.3	1.1	4.4	2	0.8
3	**Ba**	931	938	899	770	877	1020	890	961	820	150	770	602	174
0.5	**W**	0.6	0.7	b.d.l.	b.d.l.	b.d.l.	b.d.l.	b.d.l.	0.8	1.5	b.d.l.	0.9	b.d.l.	b.d.l.
0.05	**Tl**	0.39	0.29	0.35	0.31	0.41	0.32	0.32	0.4	0.41	0.09	0.33	0.27	0.06
5	**Pb**	5	13	13	9	15	11	11	11	12	5	10	15	16
2	**Au**	b.d.l.	b.d.l.	b.d.l.	b.d.l.	b.d.l.	14	b.d.l.	b.d.l.	b.d.l.	12	5	b.d.l.	b.d.l.
0.1	**Sc**	21.1	17.1	21.7	23.6	16.4	17.5	15.7	14.6	12.4	5.5	16.1	16.9	7

Table 3.2 continued

	Group	LRC	PPU	TCM	TCM	TCM	TCM	TCM	TCM	TCM	PPU	PPU
	Protolith	metased	metased	metabas	metabas	metabas	metabas	metabas	metabas	metabas	metabas	metabas
	T (°C)	514	290	555	449	554	544	542	511	399	235	370
DL*	**Analyte**	AG135	AG006-1	LC 12	AG 055-1	AG 059	AG 069-2	AG 070-2	AG 137	AG 105-4	AG 089-1	AG 095-2
0.01%	**C**	0.83	0.26	b.d.l.	b.d.l.	b.d.l.	b.d.l.	0.04	0.04	0.17	b.d.l.	0.35
0.001%	**S**	0.231	0.702	0.004	0.002	0.008	0.005	0.004	0.104	0.349	0.166	0.017
0.01%	**Fe**	5.3	4.71	7.34	8.05	9.7	9.28	7.24	7.12	8.42	8.18	9.72
0.01%	**Na**	1.56	2.61	1.8	2.64	2.63	1.52	1.66	1.87	2.34	1.09	2.05
5	**V**	195	133	273	260	329	377	240	249	251	284	232
5	**Cr**	103	44	297	504	355	318	227	320	13	36	362
1	**Co**	14	16	45	60	66	45	41	45	27	25	51
1	**Ni**	38	28	100	231	183	156	113	126	6	12	241
1	**Cu**	70	56	111	57	45	64	2	69	94	85	59
1	**Zn**	159	103	61	102	106	84	75	64	72	115	116
1	**Ga**	22	18	17	15	22	19	17	17	16	23	20
0.5	**Ge**	1.1	0.8	1.7	2.2	2.7	2	2	1.4	2	3	1.9
0.5	**As**	2.7	11.9	3	b.d.l.	3.7	5	1.7	b.d.l.	b.d.l.	b.d.l.	b.d.l.
1	**Rb**	87	60	2	10	22	2	2	1	b.d.l.	5	15
2	**Sr**	167	118	186	485	504	364	319	257	329	200	400
2	**Mo**	b.d.l.	b.d.l.	b.d.l.	b.d.l.	b.d.l.	b.d.l.	b.d.l.	b.d.l.	4	b.d.l.	b.d.l.
0.3	**Ag**	b.d.l.	0.4	b.d.l.	b.d.l.	b.d.l.	b.d.l.	b.d.l.	b.d.l.	b.d.l.	b.d.l.	b.d.l.
1	**Sn**	2	1	1	1	2	1	3	1	b.d.l.	1	2
0.2	**Sb**	0.3	0.4	0.4	0.7	0.4	0.8	b.d.l.	0.6	2.1	b.d.l.	0.2
0.1	**Cs**	3.7	1.1	0.1	0.4	1.2	0.2	0.4	0.1	0.2	0.6	1.4
3	**Ba**	875	465	52	38	130	75	75	8	18	100	341
0.5	**W**	1.8	b.d.l.	b.d.l.	b.d.l.	1.7	b.d.l.	2.8	b.d.l.	0.8	b.d.l.	0.9
0.05	**Tl**	0.28	0.27	b.d.l.	0.06	0.11	b.d.l.	b.d.l.	b.d.l.	b.d.l.	b.d.l.	0.08
5	**Pb**	10	7	b.d.l.	b.d.l.	b.d.l.	13	b.d.l.	b.d.l.	b.d.l.	b.d.l.	b.d.l.
2	**Au**	77	b.d.l.	b.d.l.	b.d.l.	b.d.l.	b.d.l.	b.d.l.	b.d.l.	b.d.l.	b.d.l.	b.d.l.
0.1	**Sc**	17.4	15.7	37.8	46.7	47.4	37.4	37.3	37	39.6	41.3	24

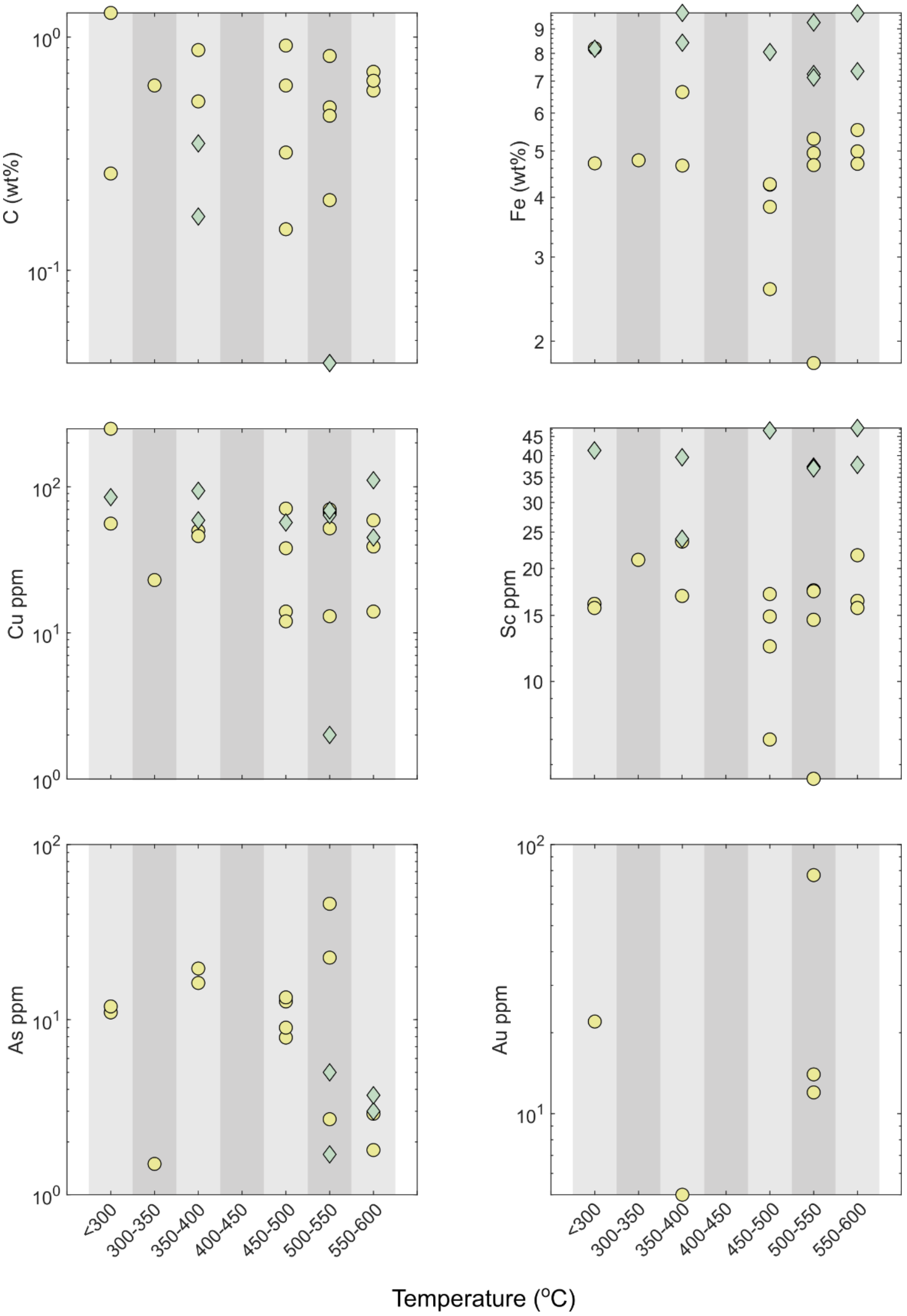

Figure 3.8 Select major and trace element data plotted against peak metamorphic temperature (°C) binned in 50 °C intervals. Circles correspond to metasedimentary samples, diamonds to metabasic samples. Note y-axis is logarithmic.

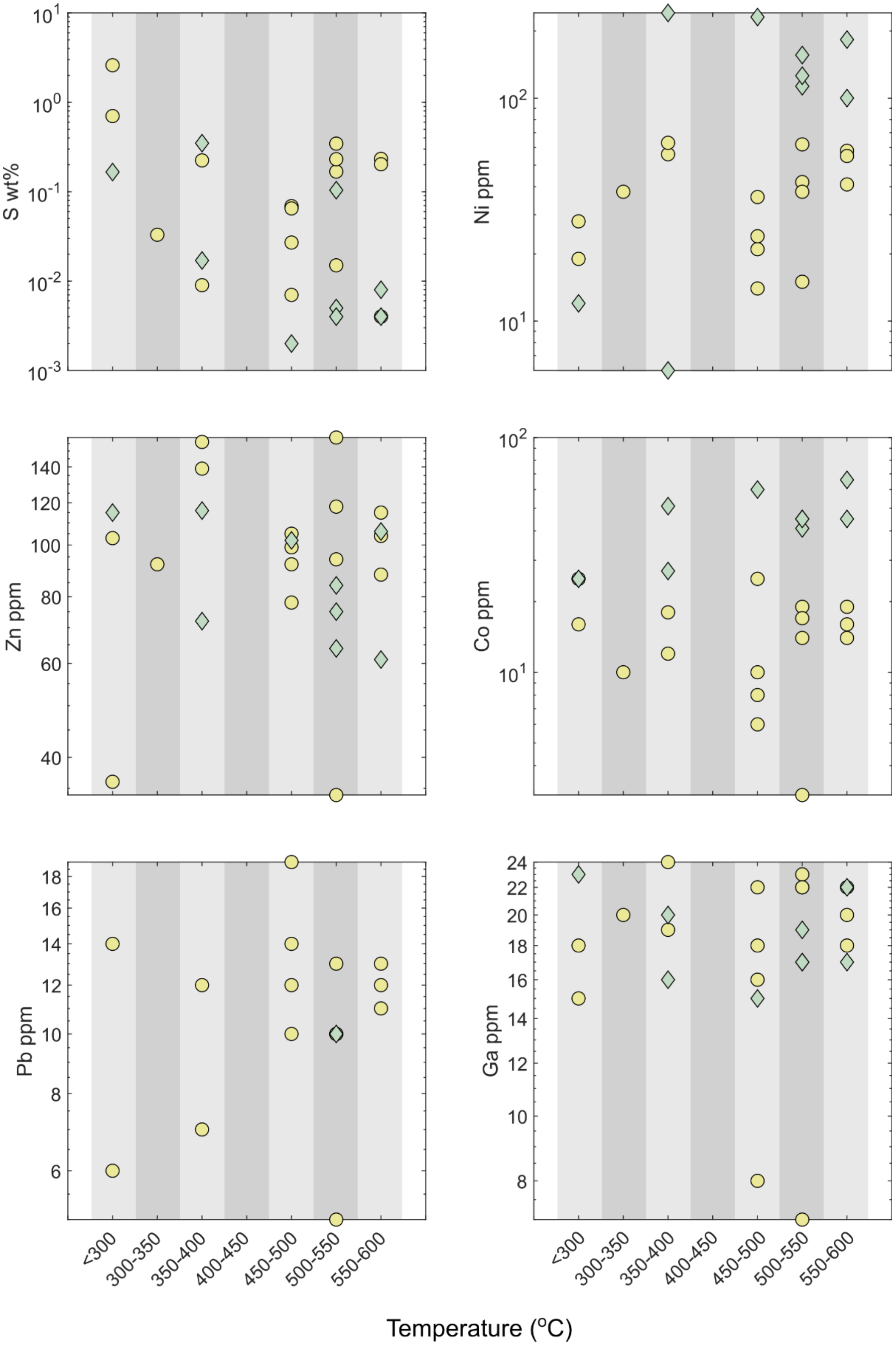

Figure 3.9 Continued from Figure *3.8*. Select chalcophile data plotted against peak metamorphic temperature. Note y-axis is logarithmic.

3.4.2 EPMA

EPMA and SEM surveys of samples identified only four main sulfide phases throughout the sample suite, with Py and Po being the most common, then Ccp, and only trace Sp. EPMA data (Table 3.3) show small subset of Py grains at low and high temperatures had detectable As, up to 0.05 wt %. Appreciable Cu was only measured in chalcopyrite grains or pyrite which hosts micro-inclusions of Ccp, and appreciable Ni was measured in Po (up to 0.75 wt% in metasedimentary samples, and up to 2.8 wt% in the metabasite sample analyzed). Sulfides in metasedimentary samples show Ni contents restricted to <0.25 wt%, except in sample AG042, wherein Po encapsulated in andalusite have Ni contents up to 0.75 wt%. Ni content in Py is more variable but is generally below detection limit for grains in the matrix but ranges up to 0.22 wt% among Py inclusions in andalusite. Molar Fe/S values in Po show significant variation among samples, ranging from ~0.83 to 0.93, with lowest values attained in the metabasite AG137 due to Ni substitution for Fe. Molar Metal/S values (Figure 3.10) show significant variability within samples, with some correlation to host phase. Matrix M/S values are consistently low except among the Po forming in the calcite lenses in AG010. Po hosted within staurolite shows the most significant variation, with M/S values ranging from ~0.87 to 0.92. Garnet-hosted Po have the highest M/S values at generally >0.9 M/S. Values retrieved from inclusions within a coarse andalusite porphyroblast exhibit a range from ~0.87 to 0.9 M/S, with the lowest values occurring among inclusions at the grain core and rim, while the highest values occur in the mid-rim.

Table 3.3 Grain averaged sulfide mineral chemistry determined by EPMA, where spot number corresponds to the first of the averaged series.

				wt%									°C
Sample	Spot	Min	Host	As	Zn	S	Mn	Fe	Cu	Ni	Total	Fe/S*	Est T
AG137	44	po	MX	0.00	0.03	39.43	0.00	58.19	0.00	1.76	99.40	0.85	511
AG137	48	po	MX	0.01	0.00	39.43	0.00	58.69	0.00	1.70	99.82	0.85	
AG137	49	ccp	MX	0.00	0.00	34.36	0.00	30.73	33.42	0.00	98.51	0.51	
AG137	50	po	MX	0.00	0.00	39.36	0.00	59.78	0.00	0.17	99.31	0.87	
AG137	52	ccp	MX	0.00	0.00	34.70	0.00	30.57	33.27	0.00	98.53	0.51	
AG137	54	py	MX	0.00	0.00	53.23	0.00	45.26	0.19	0.00	98.67	0.49	
AG137	56	ccp	MX	0.00	0.00	34.74	0.00	30.79	33.43	0.00	98.96	0.51	
AG137	59	po	AMP	0.01	0.00	39.52	0.00	57.60	0.00	2.60	99.73	0.84	
AG137	60	py	MX	0.00	0.06	53.34	0.00	45.36	0.41	0.00	99.17	0.49	
AG137	62	ccp	MX	0.00	0.00	34.77	0.00	30.71	32.92	0.03	98.42	0.51	
AG137	64	po	MX	0.00	0.00	39.53	0.00	58.25	0.07	1.77	99.62	0.85	
AG137	67	ccp	MX	0.00	0.00	34.82	0.00	30.70	33.54	0.01	99.06	0.51	
AG137	69	po	MX	0.02	0.00	39.52	0.00	58.39	0.00	1.79	99.72	0.85	
AG137	70	py	MX	0.00	0.00	53.13	0.00	44.20	0.03	0.00	97.36	0.48	
AG137	71	po	MX	0.00	0.00	39.47	0.00	58.90	0.00	1.21	99.58	0.86	
AG137	72	ccp	MX	0.00	0.00	34.99	0.00	30.67	33.19	0.00	98.85	0.50	
AG137	74	py	MX	0.00	0.00	52.82	0.00	44.75	0.00	0.00	97.56	0.49	
AG137	75	po	MX	0.03	0.00	39.73	0.00	59.84	0.00	1.11	100.71	0.86	
AG137	76	ccp	MX	0.00	0.00	34.80	0.00	30.35	33.41	0.00	98.56	0.50	
AG137	77	po	MX	0.03	0.00	39.66	0.00	59.58	0.00	1.19	100.46	0.86	
AG137	79	po	MX	0.02	0.00	39.43	0.00	57.27	0.00	2.81	99.51	0.83	
AG010	81	ccp	MX	0.00	0.00	34.78	0.00	30.60	33.59	0.00	98.97	0.51	306
AG010	84	po	MX	0.00	0.00	38.54	0.00	60.82	0.00	0.08	99.44	0.91	
AG010	86	sp	MX	0.00	58.07	33.92	0.00	7.96	0.85	0.00	100.80	0.13	
AG010	88	sp	MX	0.00	58.46	33.32	0.04	8.19	0.00	0.00	100.01	0.14	
AG010	90	po	MX	0.00	0.11	38.61	0.00	60.90	0.00	0.09	99.70	0.91	
AG010	91	ccp	MX	0.00	0.00	33.77	0.00	29.91	33.45	0.00	97.13	0.51	
AG010	92	ccp	MX	0.00	0.00	34.39	0.00	30.39	33.67	0.00	98.45	0.51	
AG010	93	po	MX	0.00	0.00	38.71	0.00	61.02	0.00	0.09	99.82	0.91	
AG010	94	po	MX	0.00	0.00	39.08	0.00	60.43	0.00	0.05	99.56	0.89	
AG010	96	po	MX	0.00	0.00	38.67	0.00	60.89	0.00	0.07	99.63	0.90	
AG010	98	po	MX	0.03	0.00	38.75	0.00	61.00	0.00	0.05	99.83	0.90	
AG010	101	po	MX	0.01	0.00	39.23	0.00	59.51	0.00	0.11	98.86	0.87	
AG049	104	po	GT	0.00	0.00	38.22	0.13	60.76	0.00	0.24	99.34	0.91	596
AG049	106	po	MX	0.02	0.00	39.15	0.00	59.93	0.02	0.23	99.36	0.88	
AG049	107	po	MX	0.00	0.00	39.33	0.00	59.56	0.00	0.22	99.11	0.87	
AG049	108	po	MX	0.03	0.00	38.43	0.00	59.04	0.00	0.23	97.73	0.88	
AG049	109	po	MX	0.00	0.00	39.55	0.00	59.64	0.00	0.25	99.44	0.87	
AG049	112	ccp	MX	0.00	0.00	34.82	0.00	30.61	33.62	0.00	99.04	0.50	
AG049	114	po	ILM	0.00	0.00	39.38	0.00	60.02	0.00	0.26	99.66	0.88	
AG049	116	po	ILM	0.02	0.00	39.48	0.00	60.05	0.00	0.25	99.80	0.87	
AG049	118	po	MX	0.00	0.00	39.22	0.00	59.78	0.00	0.26	99.26	0.88	
AG049	119	po	MX	0.00	0.00	39.00	0.00	59.34	0.00	0.28	98.62	0.87	
AG049	120	po	MX	0.00	0.00	39.26	0.00	59.74	0.00	0.34	99.34	0.87	
AG049	121	ccp	MX	0.00	0.00	34.55	0.00	30.97	32.61	0.00	98.13	0.51	
AG049	122	po	MX	0.00	0.00	39.05	0.00	59.40	0.00	0.30	98.75	0.87	
AG049	123	po	MX	0.00	0.00	39.34	0.00	59.14	0.00	0.29	98.77	0.86	
AG049	124	po	MX	0.00	0.00	39.60	0.00	59.80	0.00	0.24	99.64	0.87	
AG049	125	po	MX	0.00	0.00	39.31	0.00	59.72	0.00	0.24	99.27	0.87	
AG049	126	po	MX	0.00	0.00	39.32	0.00	59.71	0.00	0.25	99.28	0.87	

Sample	Spot	Min	Host	As	Zn	S	Mn	Fe	Cu	Ni	Total	Fe/S*	T
AG049	127	po	MX	0.00	0.00	39.25	0.00	59.72	0.00	0.27	99.24	0.87	596
AG049	129	po	MX	0.00	0.00	38.37	0.00	58.49	0.00	0.30	97.16	0.88	
AG049	131	po	GT	0.04	0.00	38.16	0.08	61.33	0.00	0.23	99.84	0.92	
AG049	133	po	ST	0.00	0.03	39.12	0.00	59.49	0.00	0.08	98.72	0.87	
AG049	134	po	ST	0.00	0.00	38.75	0.00	58.23	0.00	0.27	97.25	0.86	
AG109	135	po	GT	0.00	0.00	38.38	0.16	60.70	0.00	0.21	99.45	0.91	578
AG109	137	po	GT	0.02	0.00	38.40	0.00	60.21	0.00	0.33	98.96	0.90	
AG109	139	po	GT	0.00	0.00	37.95	0.02	60.04	0.00	0.33	98.32	0.91	
AG109	143	po	GT	0.00	0.00	37.90	0.09	59.59	0.00	0.23	97.81	0.90	
AG042	147	py	MX	0.04	0.03	52.76	0.00	46.65	0.00	0.00	99.48	0.51	563
AG042	148	py	MX	0.00	0.00	53.00	0.00	46.82	0.00	0.00	99.82	0.51	
AG042	149	py	MX	0.11	0.00	52.89	0.00	46.84	0.00	0.00	99.84	0.51	
AG042	150	py	MX	0.00	0.00	52.90	0.00	46.55	0.00	0.00	99.45	0.51	
AG042	152	po	ST	0.03	0.00	38.96	0.00	59.68	0.00	0.37	99.04	0.88	
AG042	153	po	ST	0.00	0.00	39.83	0.00	59.82	0.00	0.38	100.03	0.86	
AG042	155	po	ST	0.02	0.00	39.65	0.00	60.03	0.00	0.34	100.03	0.87	
AG042	157	po	AND	0.00	0.00	39.62	0.00	59.98	0.00	0.43	100.02	0.87	
AG042	158	ccp	AND	0.00	0.00	34.63	0.00	30.81	33.19	0.02	98.65	0.51	
AG042	160	po	AND	0.02	0.00	39.47	0.00	59.75	0.00	0.53	99.76	0.87	
AG042	163	po	AND	0.03	0.00	39.55	0.00	60.05	0.00	0.43	100.05	0.87	
AG042	164	py	AND	0.06	0.00	53.22	0.00	43.92	0.00	0.00	97.20	0.47	
AG042	165	py	AND	0.05	0.00	53.22	0.00	43.83	0.00	0.00	97.10	0.47	
AG042	167	po	AND	0.04	0.00	39.24	0.00	59.79	0.00	0.75	99.80	0.87	
AG042	168	ccp	AND	0.00	0.00	34.69	0.00	30.82	33.10	0.02	98.63	0.51	
AG042	169	po	AND	0.00	0.00	39.38	0.00	59.36	0.00	0.63	99.37	0.87	
AG042	171	py	AND	0.00	0.00	53.11	0.00	46.50	0.00	0.09	99.70	0.50	
AG042	174	po	AND	0.02	0.00	39.13	0.00	60.13	0.00	0.59	99.87	0.88	
AG042	176	po	AND	0.00	0.00	39.64	0.00	60.14	0.00	0.49	100.27	0.87	
AG042	177	ccp	AND	0.00	0.00	34.71	0.00	30.80	33.22	0.00	98.73	0.51	
AG042	179	po	AND	0.00	0.00	39.42	0.00	59.85	0.00	0.39	99.65	0.87	
AG042	181	py	AND	0.00	0.04	53.31	0.00	46.82	0.00	0.22	100.39	0.50	
AG042	183	py	AND	0.00	0.00	53.20	0.00	46.84	0.00	0.09	100.13	0.51	
AG042	186	po	AND	0.02	0.00	39.06	0.00	60.48	0.00	0.61	100.17	0.89	
AG042	187	ccp	AND	0.00	0.00	34.62	0.00	30.91	33.04	0.00	98.57	0.51	
AG042	189	po	AND	0.00	0.00	39.32	0.00	59.94	0.00	0.52	99.78	0.88	
AG042	190	po	AND	0.04	0.00	39.48	0.00	59.67	0.00	0.56	99.75	0.87	
AG042	191	po	AND	0.00	0.00	39.34	0.00	59.95	0.00	0.50	99.79	0.87	
AG042	193	po	AND	0.00	0.00	39.27	0.00	59.43	0.00	0.43	99.12	0.87	
AG042	195	po	AND	0.00	0.00	39.56	0.00	59.91	0.02	0.48	99.96	0.87	
AG042	196	ccp	AND	0.00	0.00	34.85	0.00	30.54	33.31	0.00	98.70	0.50	
AG042	198	po	AND	0.00	0.00	39.63	0.00	59.84	0.00	0.38	99.84	0.87	
AG042	199	po	GT	0.00	0.00	37.96	0.41	60.47	0.00	0.26	99.10	0.91	
AG042	200	po	GT	0.00	0.00	39.50	0.24	59.54	0.00	0.55	99.83	0.87	
AG042	201	po	GT	0.00	0.00	38.00	0.25	61.23	0.00	0.21	99.69	0.93	
AG042	203	po	AND	0.00	0.00	39.44	0.00	59.79	0.00	0.45	99.68	0.87	
AG042	205	po	ST	0.00	0.00	38.35	0.00	60.87	0.00	0.28	99.49	0.91	
AG042	206	po	ST	0.00	0.05	39.36	0.00	59.28	0.00	0.53	99.22	0.86	
AG042	209	po	ST	0.00	0.00	38.72	0.00	60.33	0.00	0.52	99.56	0.89	
AG042	210	po	ST	0.00	0.00	39.48	0.00	59.80	0.00	0.39	99.67	0.87	
AG042	212	po	MX	0.00	0.00	39.32	0.00	59.16	0.00	0.72	99.20	0.86	
AG042	213	po	MX	0.00	0.00	39.27	0.00	59.13	0.00	0.71	99.11	0.86	

*Molar Fe/S. Spot number corresponds to appendix figures

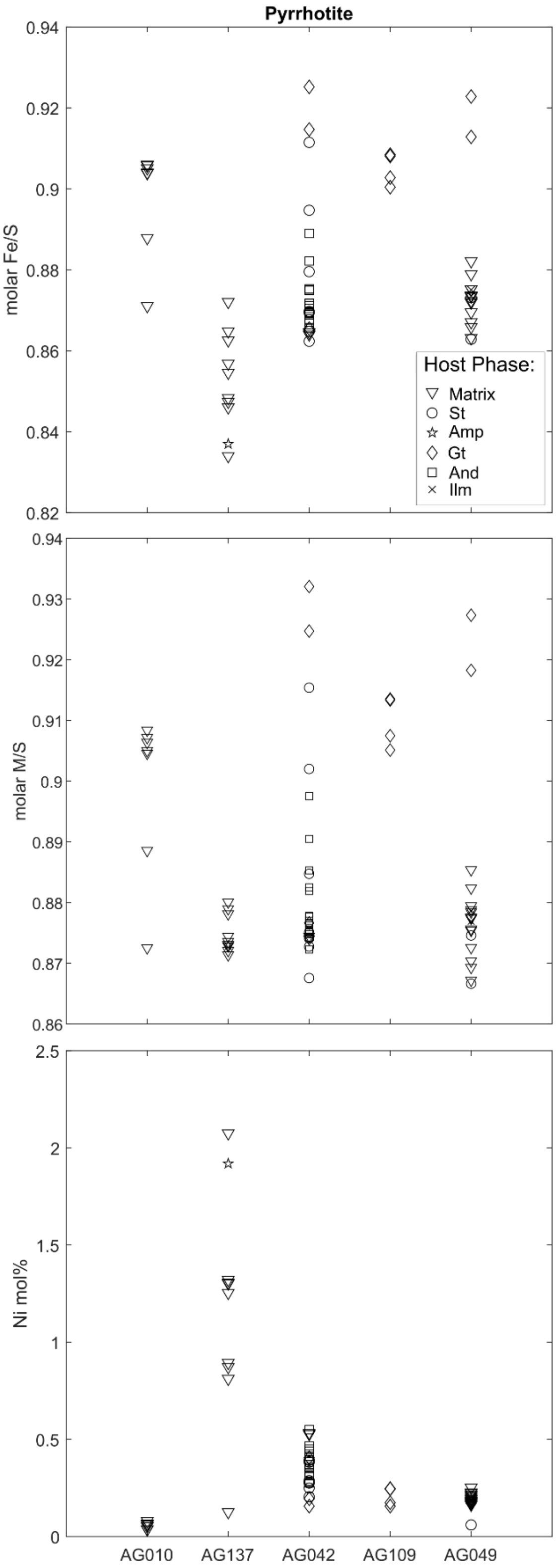

Figure 3.10 Strip charts showing molar Fe/S, molar M/S where M = (Fe + Ni + Zn), and Ni mol% in pyrrhotite (Po). Samples are arranged in order of increasing temperature from left to right. Note AG137 is a metabasic actinolite schist, whereas the other four samples are pelitic protoliths. Garnet-hosted pyrrhotite has the highest Fe/S and M/S, followed by staurolite, then andalusite.

3.5 Discussion

3.5.1 Thermodynamic Modelling

Pseudosections produced using the Perple_X suite of Gibbs free energy minimization routines (Connolly, 2005) were generated for a variety of compositions to delineate the conditions of the Py-Po transition (Tomkins, 2010; Zhong et al., 2015). To provide a benchmark for comparison, the bulk rock composition of the garnet-staurolite-sillimanite schist AG080 was selected as a reference composition (X1, Table 3.4) because the major element chemistry is representative of the modal composition of pelites in the terrane. However, since high grade schists in the LRC may have lost some total S, the AG080 bulk rock composition was normalized to 0.5 mol% S_2 (~0.65 wt% S_2). Metamorphism in the Pacific Rim Terrane is universally >200 °C, and therefore faithful recorder of post-diagenetic, pre-metamorphic S contents is unavailable. However, S content in siliciclastic marine sediments commonly ranges from 0 to 2.5 wt% S, and total S is positively correlated with total organic carbon at C/S 2.8 ± 0.8 (Goldhaber, 2003). Applying this relationship to the carbonaceous metapelites in the LRC and PPU gives total S contents of 0.25 – 1 wt% in the protolith. Thus, while the benchmark estimate of AG080 is higher than the mean value of the metasedimentary suite, it provides a reasonable protolith approximation for the S-bearing pelites that would contribute appreciable S via desulfidation.

Table 3.4 Pseudosection bulk rock compositions in mol percent and their naming for subsequent figures.

		Mol %											
Model		SiO_2	Al_2O_3	FeO	MnO	MgO	CaO	Na_2O	K_2O	TiO_2	H_2	O_2	S_2
AG080	X1	47.69	8.27	4.53	0.1	3.66	1.89	1.57	1.29	0.52	20.00	9.99	0.50
Psam.	X2	77.6	1.03	1.01	0.14	0.54	0.80	0.04	0.25	0.06	12.00	5.99	0.50
	X1	56.28	9.76	4.81	0.11	4.32	2.24	1.85	1.52	0.62	12.00	5.99	0.50
FeO	X3	57.80	10.03	2.75	0.11	4.43	2.30	1.90	1.56	0.63	12.00	5.99	0.50
	X4	50.94	8.84	12.10	0.10	3.91	2.02	1.68	1.37	0.56	12.00	5.99	0.50
CaO	X1	56.28	9.76	4.81	0.11	4.32	2.24	1.85	1.52	0.62	12.00	5.99	0.50
	X5	51.69	8.97	4.91	0.10	3.96	8.21	1.70	1.39	0.57	12.00	5.99	0.50
S_2	X6	56.19	9.75	5.34	0.11	4.31	2.23	1.85	1.52	0.62	12.00	5.99	0.10
	X7	52.83	9.17	5.02	0.10	4.05	2.10	1.74	1.43	0.58	12.00	5.99	5.00

Benchmark pelite

In the benchmark pseudosection X1, the Py-Po transition initiates at low temperatures within the model domain between 330 °C and 390 °C and concludes over an extremely narrow threshold (Figure 3.11). The field of coexisting Py and Po, and thus the desulfidation equilibria, only corresponds to a field width of a few degrees in the temperature domain, and therefore precedes the predicted conditions for growth of porphyroblasts (garnet, staurolite, andalusite) commonly seen in the Pacific Rim Terrane. Notably, garnet is part of the predicted low-T assemblage, but with very small total volumes (Figure 3.12a) and is substantially affected by specified MnO (see discussion, Chapter 2). Chlorite joins the predicted assemblage at temperatures greater than 340 °C at pressures greater than two kilobars, and the terminal chlorite-out reaction occurs over a narrow interval at between ~480 and 540 °C. Thus, the ‘desulfidation window’ (Tomkins, 2010) does not coincide with the fluid release associated with chlorite breakdown for a typical LRC pelite. Other studies have obtained similar results, wherein the Py-Po transition was identified to be at low temperature in P-T space, rather than a wide field which eclipses terminal chlorite breakdown (Zhong et al., 2015).

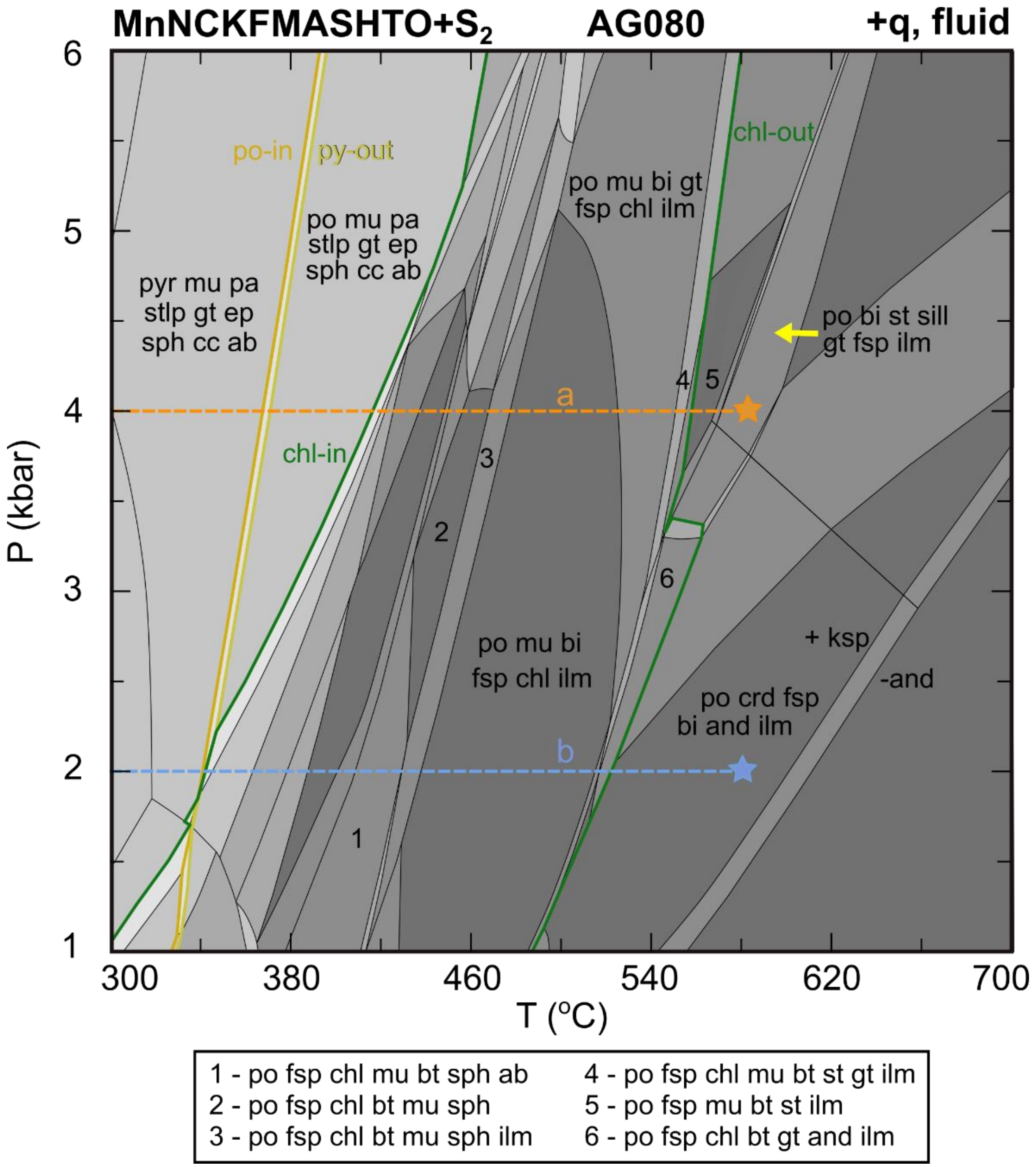

Figure 3.11 Pseudosection of bulk composition AG080 “X1”, the benchmark pelite. Field labels omitted for clarity. Key mineral -in and -out boundaries are highlighted, including Po-in, Py-out, Chl-in, and Chl-out. These lines represent the appearance or disappearance of mineral, either by a continuous reaction or discontinuous reaction. Lines (a) and (b) correspond to example isobaric heating paths (see text).

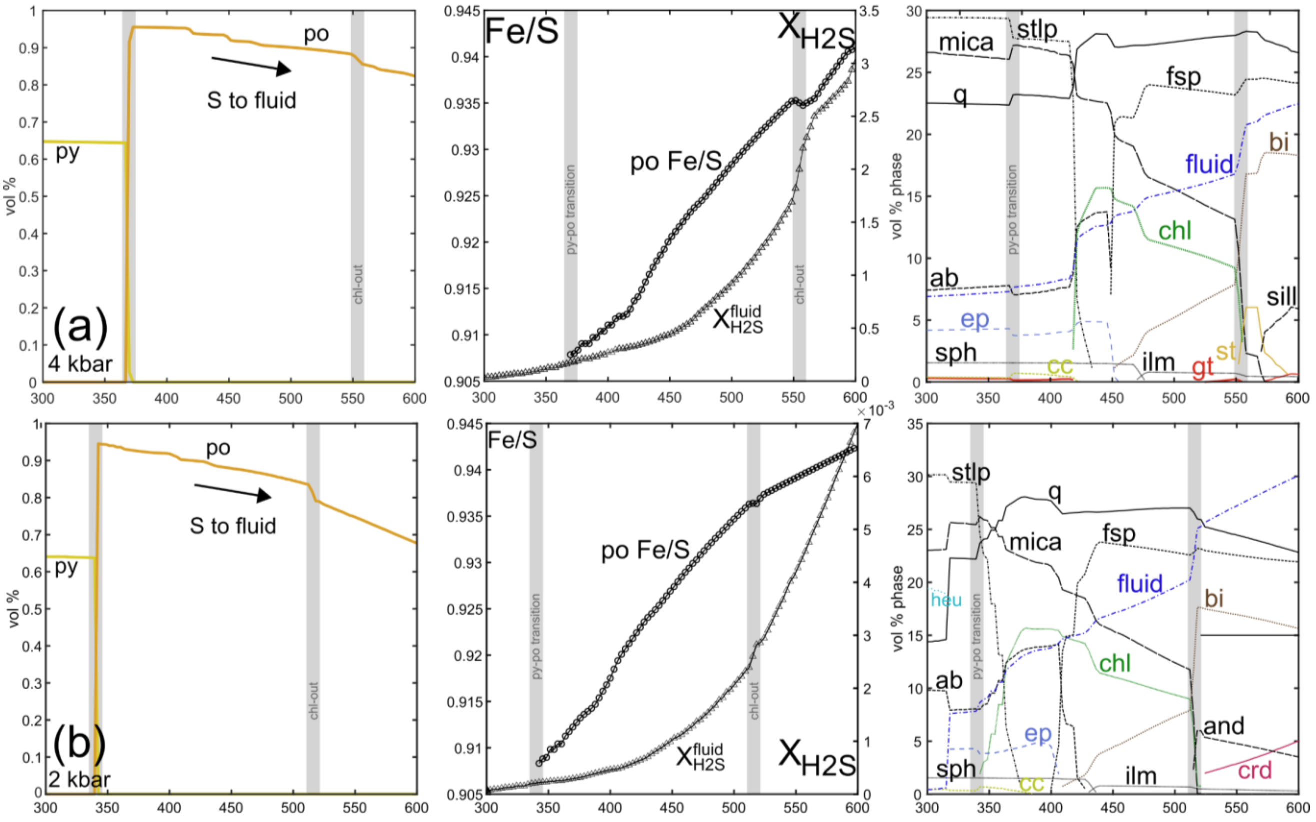

Figure 3.12 Panel plots showing changes to mineral volumes and chemistry along the isobaric heating paths in Figure 3.11 (a) and (b). From left to right: (i) Volume percent of Py and Po across the Py desulfidation threshold, and the terminal chlorite breakdown reaction boundary. (ii) Composition change in Po (Fe/S) recorded on left hand axis, Fluid X_{H2S} on the right ($\times 10^{-3}$). As Po breaks down, the released S is accommodated in the fluid. (iii) Tracking changes in mineral volume, and total fluid volume, with progressive isobaric thermal metamorphism.

Predicted phase abundances show that across the desulfidation threshold, an increase in the proportion of Po is accompanied by a concomitant decrease in the proportion of stilpnomelane, the dominant Fe-bearing phase at sub-chlorite conditions (Figure 3.12). Similarly, the proportions of quartz, fluid, and white mica increase across the desulfidation threshold. S liberated across the desulfidation threshold is not accommodated in the fluid as H_2S, as X_{H2S} remains low ($<1.0\times10^{-3}$) across the transition. Instead, the S released from the desulfidation reaction produces additional Po by reacting with Fe in stilpnomelane. Therefore, reaction [2] (after Ferry et al., 1981) is largely inapplicable since reactions with silicate phases sequester released S (Zhong et al., 2015). However, total Po content does not remain constant above the desulfidation threshold. Instead, Po is lost with progressive thermal metamorphism

(Figure 3.12), with total loss dependent on pressure conditions. Along an isobaric heating path at 4 kbar, ~0.13 vol% Po is lost between 370 °C and 600 °C. Total Po loss is a factor of two greater along an isobaric heating path at two kilobars with ~0.27 vol% expended over the same temperature interval, highlighting that Po desulfidation more efficiently liberates sulfur at low pressures. In both cases, there is a concomitant increase in fluid X_{H2S} content and the Fe/S ratio of remaining Po. From the initial Po formation T up to 600 °C, Fe/S ratios increase from ~0.91 to ~0.94 in both isobaric scenarios. However, the maximum fluid X_{H2S} reached in the 2 kbar scenario is 7×10^{-3}, a factor of 2.33 greater than the 4 kbar case. Thus, while the Py desulfidation reaction is not predicted to be the primary mechanism of S release, lower pressure conditions favour release of S to fluid via progressive metamorphism of Po.

The terminal chlorite breakdown reaction which occurs between 500 – 550 °C in the two isobaric heating paths produces an abrupt pulse of fluid, as well as biotite, and staurolite at high pressure (Figure 3.12). This threshold is indicative of the unbalanced reaction:

$$\mathrm{Chl + Mu + Pl = Bt + St + Pl + H_2O} \quad \textbf{[3]}$$

Across this interval, the significant Po is consumed over the narrow temperature interval, and thus there is a corresponding step increase in fluid X_{H2S}. Simultaneously, Po Fe/S ratios do not change in the 2 kbar case, and abruptly decrease in the 4 kbar scenario before resuming monotonic increase with progressive heating. Therefore, the devolatilization accompanying terminal chlorite breakdown in turn drives the breakdown of Po in response to a decrease in fluid X_{H2S} from adding water-rich fluid.

The X1 benchmark pseudosection reasonably replicates the petrography of the average metapelite in the Pacific Rim Terrane at high grades. Po is the dominant sulfide phase in high grade metapelites, including AG080. However, argillites and phyllites from the LRC do not show the predicted model assemblages at low grade, which is attributed to sluggish reaction rates in low greenschist facies conditions. For example, among carbonaceous phyllites collected from the northern LRC, small syn-deformation titanite grains are observed, but the small volumes of predicted garnet, paragonite and epidote are not. Nonetheless, above ~400 °C, there is reasonable agreement between predicted equilibrium assemblages and observations. Of note, however, the identification of pyrite as an inclusion within staurolite and andalusite is not readily explained in the topology of the benchmark pseudosection.

Given the X1 'typical pelite' benchmark pseudosection, the sensitivity of the Py-Po transition to changes in bulk rock composition can also be assessed. Because the LRC comprises numerous metasedimentary protoliths, sometimes interfoliated on the cm-scale, the sensitivity of the Py-Po transition threshold can be tested using temperature-composition (T-X) profiles. The compositional variables assessed are FeO, CaO, S_2, and a comparison between the benchmark composition X1 and the bulk rock composition of a psammitic lithology X2 from the LRC.

Psammitic Model

At 4 kbar, the change from pelitic to psammitic compositions (Figure 3.13) causes an expansion of Py stability to ~415 °C, but also a concomitant lowering of the temperature at which Po joins the assemblage to ~350 °C. The position of the chlorite breakdown reaction remains >540 °C for ~80 % of the compositional variation from pelite to psammite, but dramatically decreases in temperature at Fe-poor psammitic compositions. At 4 kbar and the psammitic composition X2, the terminal chlorite breakdown reaction is lowered to ~440 °C, and chlorite is not produced until ~420 °C, and predicted modal chlorite volumes never exceed 1%. In the 2 kbar isobaric section, the Py-Po transition is even narrower and restricted to <360 °C. Similarly, the chlorite terminal breakdown reaction is shifted to <540 °C, but any significant fluid generation via chlorite breakdown occurs at conditions above the modelled desulfidation reaction. Thus, psammitic lithologies do widen the Py desulfidation window, but not enough to coincide with the terminal chlorite breakdown reaction and that associated pulse of fluid (Tomkins, 2010).

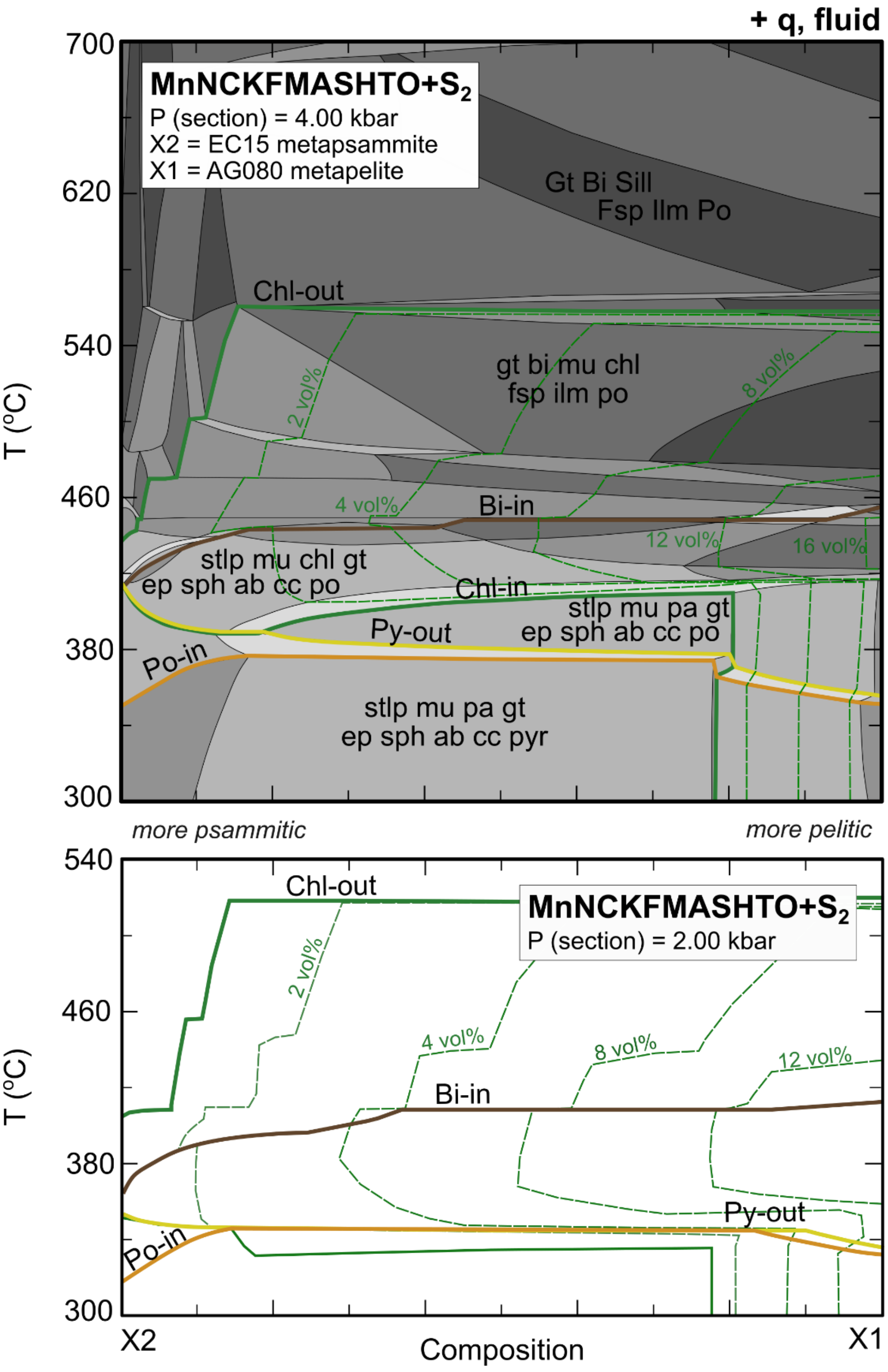

Figure 3.13 Temperature – Composition (T-X) pseudosection varying between X2 (psammitic sample EC15 from Canham (2000) BSc thesis, from Finlayson Arm) and the benchmark composition X1. Field labels omitted for clarity. Sections produced at 4 kbar (top) and 2 kbar (bottom). Chlorite volume percent contours computed show the rapid terminal chlorite breakdown reaction at high temperature, while the Py-Po transition remains <420 °C.

FeO Model

Adjustment of total molar FeO by ± 50% of the X1 benchmark composition (Figure 3.14) shows that FeO is a dominant control on desulfidation topology in the pelite-psammite model. Reduction of molar FeO by 50% produces a similar effect to variation towards a psammitic lithology, increasing the first appearance of pyrrhotite by ~40 °C. This effect has been established by previous workers (e.g., Zhong et al., 2015), wherein S liberated from the conversion of Py to Po reacts to form additional Po at the expense of Fe from phases such as chlorite. Therefore, in a bulk rock composition comprising significantly lower molar FeO, such as the psammitic composition X2 or the low-FeO case X4, the field of coexisting Py and Po expands (Zhong et al., 2015). Conversely, isobaric paths for profiles with up to 50% more molar FeO were characterized by narrowing the desulfidation threshold, and the conversion of Py to Po at conditions below the model temperature domain (<300 °C).

Among metasediments in the Pacific Rim Terrane there is substantial variation in bulk rock FeO, which is partly attributed to the cm- to m-scale layering of psammitic compositions within pelitic successions. Thus, most compositions fall between the Fe-poor composition X4 and the benchmark pelite X1 (Figure 3.14), whereas few metasediments are more ferrous than the benchmark case. Therefore, for sulfide-bearing metasediments, local variation in protolith Fe content could locally permit Py to persist up to ~400 °C. Petrographic evidence for this protolith contrast has been reported in the Otago Schist in New Zealand, where meter-scale layers can show displacement of the Po isograd (Pitcairn et al., 2010). However, the FeO variation model (Figure 3.14) was prescribed a constant 0.5 mol % S_2 to isolate the influence of changing FeO, which conflicts with the sulfide-poor nature of psammitic rocks in the Pacific Rim Terrane. The dearth of sulfides in psammitic rocks precludes conclusively testing the model predictions for the influence of FeO content in the Pacific Rim Terrane. Nevertheless, previous workers have contended that the displaced Po isograd in the Otago schist validates the influence of Fe on the desulfidation threshold (Zhong et al., 2015).

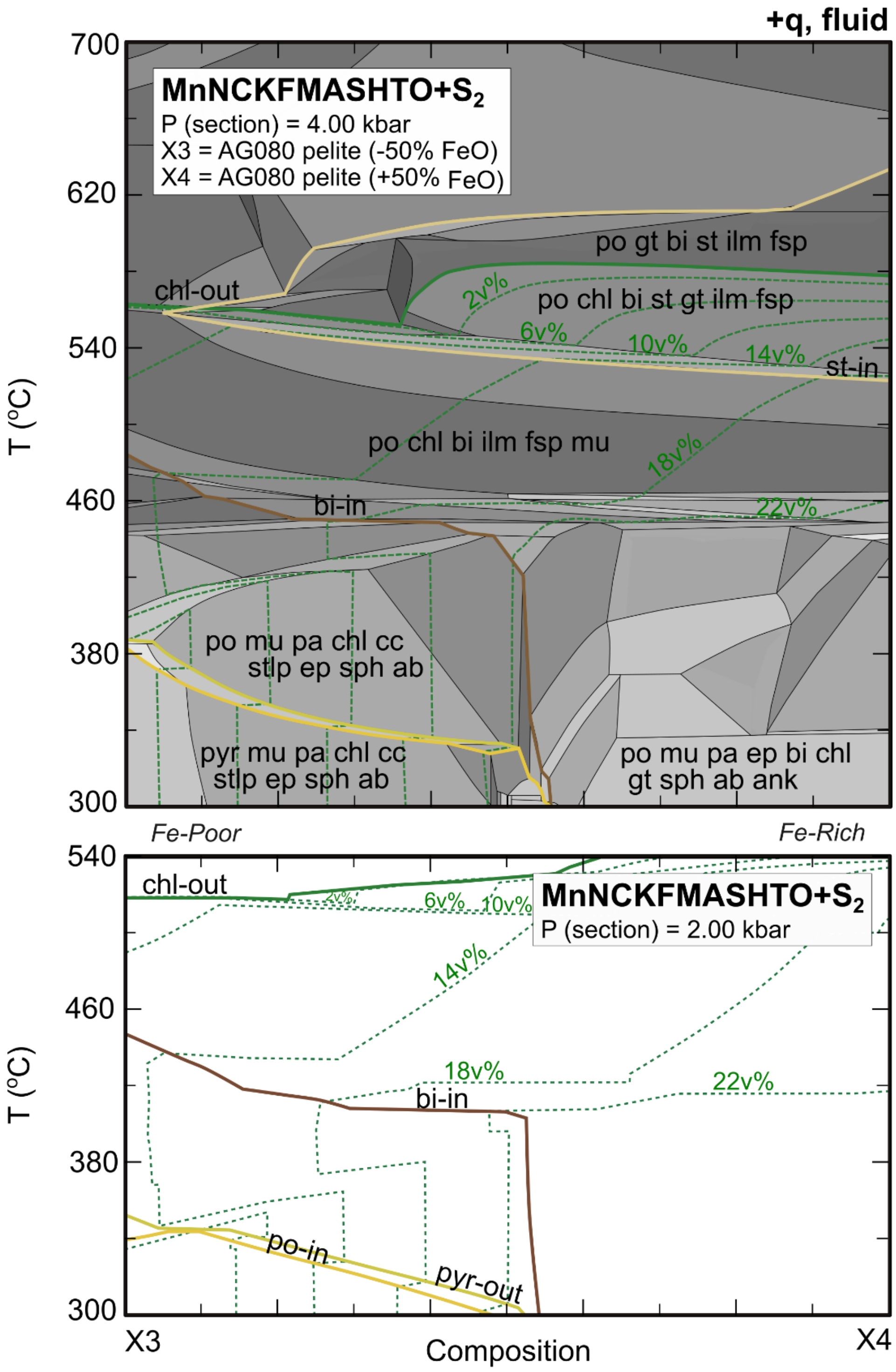

Figure 3.14 Temperature – Composition (T-X) pseudosection for the variable Fe model scenario. Composition X3 is X1 renormalized with 50% less FeO, where X4 is with renormalized to an additional 50% FeO, with fluid and S_2 content adjusted to be constant. Two sections at 4 kbar (top) and 2 kbar (bottom) are presented. Reducing FeO increases the maximum temperature of Py-stability, whereas even modest increases in FeO lead to Po-only conditions in the model domain.

CaO Model

While not represented in the sample suite in this study, previous workers have reported calcareous lithologies in the Pacific Rim Terrane (e.g., Rusmore & Cowan, 1985). Thus, the effect of bulk rock CaO content may also bear on the conditions of desulfidation. Since the preponderance of limestone in the terrane is minor, the constructed T-X plot is for an increase in molar CaO over benchmark compositions by a factor of four to simulate carbonate-bearing metasediments, which are somewhat more common in the PPU and LRC. At higher CaO contents, the first appearance of chlorite on a prograde path is raised to temperatures above the predicted Py-Po transition (Figure 3.15). Conversely, the first appearance of biotite is depressed to low greenschist temperatures (<400 °C) at high CaO contents. For the maximum CaO composition, chlorite is only stable over a <20 °C window with maximum chlorite volumes of less than 2%. Thus, for calcareous metasediments the prograde breakdown of chlorite contributes less fluid than other devolatilization reactions, but at slightly lower temperatures. The maximum stability of Py is approximately unchanged for CaO-rich compositions, remaining <350 °C at 4 kbar, and <340 °C at 2 kbar. However, the width of the transition is widened by the first appearance of Po at temperatures below the model domain towards the CaO-rich endmember.

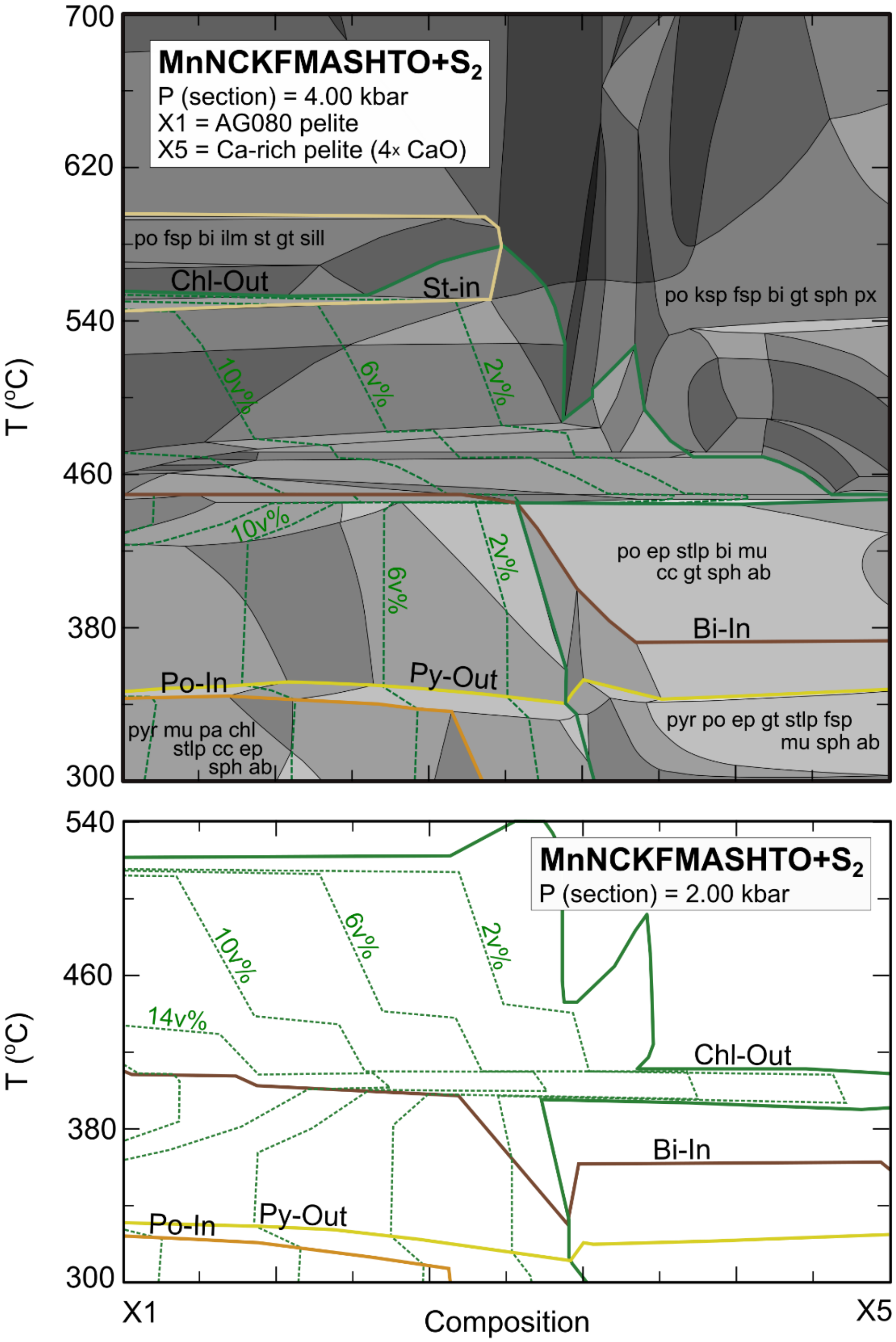

Figure 3.15 Temperature – Composition (T-X) pseudosection for the variable CaO model. Composition space varies between the benchmark case X1 and a Ca-rich pelite, analogous to the 'limey' sediments reported in the Pacific Rim Terrane. Higher CaO contents lead to a widening of the Py-Po transition to lower temperatures, below the model domain.

S_2 Model

The stability of Py and Po is notably dependent on the S content of the system (e.g., Tomkins, 2010; Evans et al., 2010), and greater proportions of Py versus Po are found in rocks with greater molar S/Fe (Ferry, 1981). Thus, the selected bulk S_2 content in model runs bears greatly on the Py desulfidation reaction. As previously discussed, 0.5 mol% S_2 was selected for benchmarking based on observed sulfide content in low grade samples, and from informed estimates for siliciclastic marine sediments. However, the absence of a faithful record of protolith S content introduces a degree of uncertainty when interpreting the thermodynamic models. Furthermore, analogous sedimentary lithologies and low-grade samples from the Pacific Rim Terrane have locally heterogeneous distributions of primary Py. Thus, the effect of variable S_2 content must be considered when evaluating the conditions of the Py-Po transition in prograde metamorphism.

This effect was investigated by varying specified S_2 content in the benchmark composition from 0.1 mol% to 5.0 mol% (Figure 3.16) at 4 kbar. Expectedly, at very high bulk sulfur contents Py remains stable to higher temperatures (e.g., Toulmin & Barton, 1964; Evans et al., 2010). Po appearance is also shifted to higher temperatures with increasing S content, but by a lesser degree except at S contents above 4.5 mol%. Conversely, at specified S contents less than the benchmark case, the transition is narrow and low until ~0.25 mol % S_2. Below this threshold, Po is stabilized and Py entirely destabilized at temperatures below the model domain. Over the range 0.25 – 1.6 mol % S_2, which encompasses most typical sulfidic pelite whole-rock compositions, the effect of bulk S_2 content is limited to a gradual widening of the Py-Po transition, since for small changes in total sulfur the Py-Po transition is effectively buffered (Evans et al., 2010). Above ~1.6 mol % S_2, Py is stabilized to drastically higher temperatures. At ~2.8 mol % S_2 the appearance of biotite coincides with Py-out, and at sulfur contents greater than 3 mol % S_2 the desulfidation reaction co-exists with chlorite breakdown. Thus, the ‘ideal’ case for simultaneous fluid production via chlorite breakdown and S release via the Py desulfidation reaction is predicted for samples containing greater than 3 mol % S_2, wherein both reactions occur in a narrow window at ~540

°C. Therefore, while S_2 content is the most influential parameter on the relative conditions of the Py-Po transition, only exceptional protoliths such as hydrothermal sulfide deposits or small, localized enrichments of Py could result in alignment of both the Py desulfidation and chlorite-breakdown reactions as predicted by the equilibrium thermodynamic model.

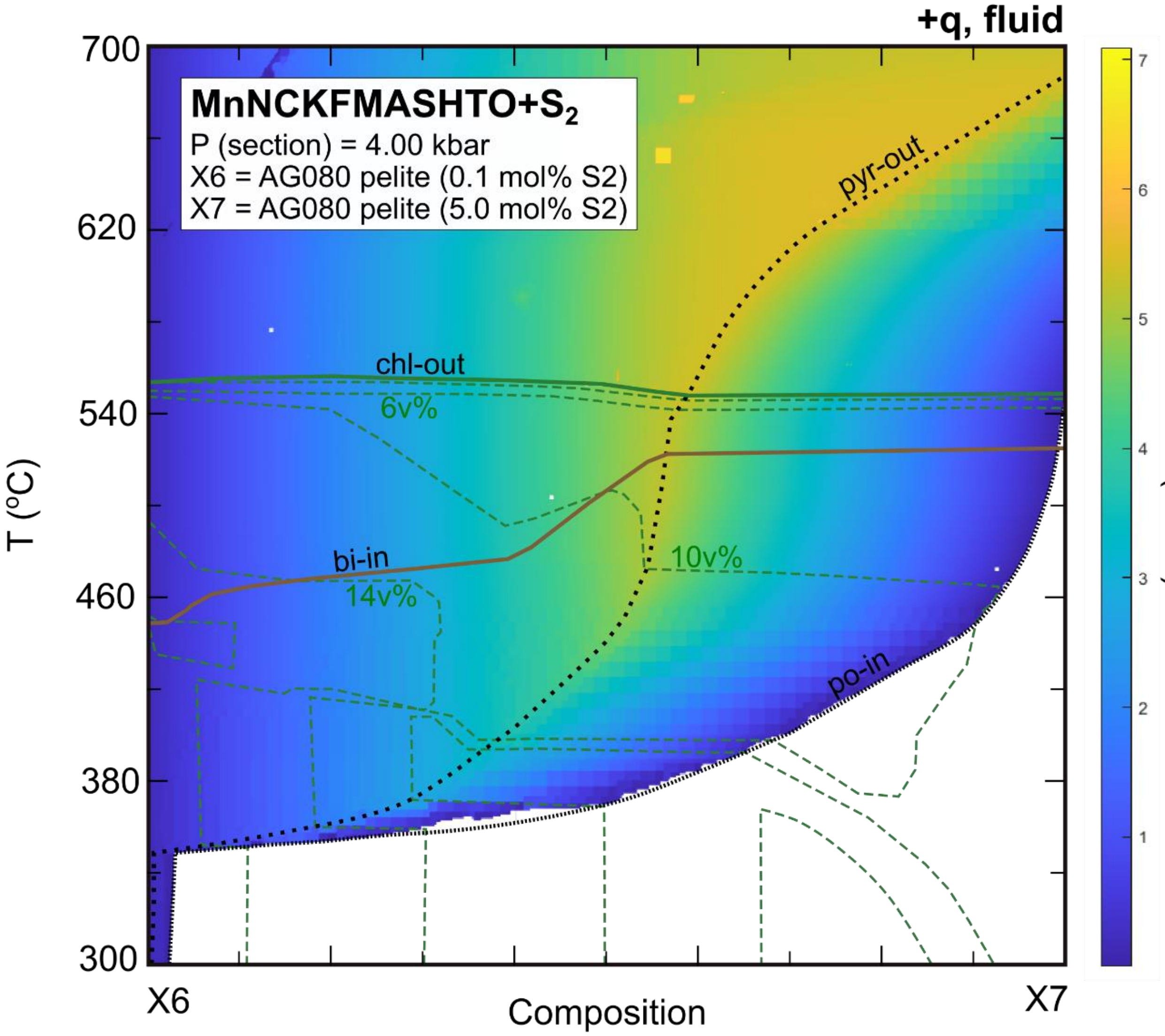

Figure 3.16 Temperature – Composition (T-X) section showing the effect of varying total S content between 0.1 and 5.0 mol% S_2. At very low S_2 conditions, Py is destabilized on Po is favoured. At very high S_2 conditions, Py and Po coexist over a large section of temperature space at 4 kbar, even exceeding the Chl-out window. At compositions nearing X7, fluid models predict fields of S-poor and S-rich fluid immiscibility.

3.5.2 Comparison with natural rocks

Low Grade

Only a few samples from the PPU attained peak temperatures <300 °C and therefore below the PerpleX model domain. The dominant sulfide in these samples is Py, locally rimmed by Fe-oxides or replaced by weathering products. Expectedly, these samples retain some primary and diagenetic textures. Thus, samples which correspond to temperatures less than the PerpleX model domain are consistent with pyrite being the dominant pre-metamorphic sulfide, and its retention to sub-greenschist conditions as observed in other thermodynamic models (e.g., Tomkins, 2010) and in natural rocks (e.g., Carpenter, 1974; Pitcairn et al., 2010; Large et al., 2011).

Samples with temperatures between 300 and 400 °C exhibit more variability. While Py is still the most common sulfide in this range, several samples from specifically the PPU comprise Po-dominated assemblages. Two such samples, AG010 and AG014, with peak temperatures of 306 and 301 °C respectively, correspond to the lowest temperatures in the model domain. AG010 is a carbonate-bearing tectonized pelite, and AG014 is a disrupted banded chert, and thus both firmly correspond to protoliths for which the predicted sulfide assemblage should include Py. Notably, these samples host considerably more sulfide than typical of other metasediments at equivalent temperatures. It is plausible that the Po-bearing low grade samples are a result S-addition by late metamorphic fluids, rather than in-situ desulfidation of pre-existing primary grains. The occurrence of Po in sub-greenschist facies is not unprecedented in comparable metamorphic terranes—in the Otago and Alpine schists, Po is the main sulfide among sub-greenschist facies rocks (Pitcairn et al., 2010). Conversely, the Barrovian-type Ocoee Series in the east south central USA has a distinct Po isograd that occurs slightly downgrade of the biotite isograd (Carpenter, 1974). Therefore, Po stability at temperatures of ~300 °C is inconsistent with PerpleX model predictions, but not unfeasible when compared to other terranes.

Typical samples in the Pacific Rim Terrane at low-greenschist facies conditions host small, discrete Py grains with spheroidal to anhedral habits. Surface texture varies from smooth and inclusion-free to entirely pitted, with the latter more common. In less deformed samples, small spherules in carbonaceous samples resemble framboids with small rim overgrowths of Py. The Py stringers from sample AG105-1 are interpreted as pre-metamorphic Py that formed *in-situ*, and were subject to concomitant deformation and metamorphism. The protolith composition is comparable to the benchmark case, and thus at a temperature of 399 °C and pressure of approximately 4 kbar, the predicted stable sulfide is Po (Figure 3.11). Furthermore, the sample AG105-1 abuts a large tonalitic sill with a ~1 m wide contact aureole. Since peak metamorphic temperature was estimated using RSCM geothermometry, and the method is prone to textural equilibration lag when contact metamorphism overprints a regional fabric (Beyssac et al., 2019) this temperature should be considered a minimum estimate. Therefore, Py persists above the predicted desulfidation threshold by at least ~40 °C. Other samples also indicate that Py regularly exceeds its predicted stability, including one sample exhibiting Py stringers in a biotitic schist which attained temperatures of ~500 °C.

High Grades

In upper greenschist and amphibolite facies rocks, Po is the most abundant sulfide in both matrix assemblages and in porphyroblast inclusions. Nonetheless, Py remains a prevalent matrix phase in the LRC schists. It is difficult to unequivocally assign matrix Py to prograde or retrograde parageneses to permit valid comparison with the PerpleX models. Textural clues, including narrow stringers of Py that trace the foliation around porphyroblasts (e.g., Figure 3.7d), and coarse cubic Py with porous to ‘vermicular’ pitting textures deformed in the foliation, suggest some primary Py may even persist to temperature above 550 °C. However, most matrix Py grains are ambiguous, anhedral, and are generally interpreted here as part of retrograde assemblages that are affected by late sulfidation.

For these reasons, inclusion assemblages among the common porphyroblasts garnet, staurolite and andalusite provide the least ambiguous record of sulfide stability during prograde metamorphism since they are isolated from ongoing equilibration with the matrix and metamorphic fluids (Brown et al., 2014). In the LRC, porphyroblasts of suitable size to encapsulate sulfides are not observed in metapelites below ~500 °C. This observation is consistent with the benchmark model, which does not predict appearance of the common porphyroblasts below 500 °C, and any significant modal abundances of garnet or staurolite until above 540 °C. One exception may be andalusite, which in Al_2O_3-rich compositions may stabilize it <500 °C in pseudosections, but no such samples were observed in the LRC.

The occurrence of Py inclusions in andalusite and staurolite porphyroblasts (Figure 3.6) as isolated and composite grains with Po suggests that Py persists above the idealized desulfidation threshold. Since staurolite is modelled as a product of chlorite and muscovite breakdown (Figure 3.12a), Py must persist to temperatures of at least 550 °C. Conversely, garnet porphyroblasts never host Py. The first appearance of garnet in each pseudosection model run is sensitive to bulk MnO content, with changes of ~0.01 mol% MnO capable of depressing the first appearance of garnet to low pressures and to sub-greenschist temperatures. In such circumstances, garnet modal volumes are vanishingly small and not reflected in the rocks. Garnet biotite thermometry (Chapter 2) indicates that in high grade rocks, garnet forms near peak temperature conditions and does not have a protracted period of growth, reflected in shallow to flat compositional zoning profiles. Direct comparison of the garnet-hosted sulfide assemblages with other porphyroblasts is hindered by a significant discrepancy in grain size: staurolite and andalusite locally form porphyroblasts in excess of 1 cm, while garnet porphyroblasts in most samples are <0.5 mm. Exceptional cases of coarse porphyroblastic garnet do occur among high grade paragneisses and schists, but are characteristically devoid of sulfide inclusions.

Barring preservation biases, the sulfide record in the LRC and PPU suggests that Py commonly exceeds the low, narrow threshold predicted by models for typical metapelites (Zhong et al., 2015; this study). The identification of primary Py at conditions above 500 °C has also been noted in other studies (e.g., Tracy & Robinson, 1988; Alirezaei & Cameron, 2001; Finch & Tomkins, 2017), suggesting the discrepancy between models and petrography isn’t an aberration for the Pacific Rim Terrane. The coexistence of Py and Po is recorded in both andalusite and staurolite inclusions, and possibly in the rock matrix. The contrasting prograde changes in the sulfide assemblage with models is further frustrated by the paucity of sulfides in upper greenschist facies phyllites in the LRC. Field observations suggest that this gap is not an artefact of sampling bias, and bulk rock sulfur data show a similar decrease in the temperature range 400 – 500 °C. While the exact mechanism is unclear, sulfur is seemingly mobilized across this range by either a syn- or post-metamorphic process, yielding phyllites with less visible sulfide than comparable composition rocks of higher and lower grade.

If S liberated from the sluggish desulfidation reaction does not react with Fe-silicates to produce additional Po, as predicted in the models, it is possible that X_{H2S}^{Fluid} is higher (e.g., Ferry, 1981), and there is less modal Po than predicted by the models. Additionally, if unlike the presented closed-system models, there is continual export of fluid with the liberated S and replenishment by new fluid from the breakdown of hydrous minerals, a net loss of S could be incurred (Ferry, 1981).

3.5.3 The equilibrium assumption

Pseudosections constructed in PerpleX intrinsically rely on the assumption of global equilibrium for a homogenous representative bulk composition (Connolly, 2005), and so careful selection of a representative bulk chemistry for the equilibration volume is critical (Lanari & Engi, 2017). A consequential limitation of applying the pseudosections to physical samples is unequivocally demonstrating attainment of equilibrium. Extensive recent work has shown that disequilibrium and the limitations of reaction rates must be considered when applying the results of thermodynamic equilibria calculations, especially during short-lived metamorphic events (e.g., in garnet zoning, Caddick et al., 2009; thermal overstepping, Pattison & Tinkham, 2009). Indeed, petrographic evidence among the lowest grade samples in both the LRC and PPU commonly imply limited local equilibrium (Rusmore & Cowan, 1985; Chapter 2) and the observed mineral assemblages for low- and sub-greenschist rocks are often not in agreement with predicted assemblages. More generally, workers have demonstrated that the equilibrium assumption may not necessarily be met throughout the greenschist facies (Carlson, 2002), and implementation of pseudosection modelling requires consideration of not only the ‘geologic uncertainty’ associated with selecting a representative bulk composition, but how that representative composition shifts with increasing metamorphic grade (Palin et al., 2016).

Thus, considering the effect of the equilibration or ‘reactive’ bulk composition (Lanari & Engi, 2017) among the LRC protoliths bears significantly on sulfide stability. As demonstrated, the width of the Py-Po transition is highly sensitive to specified bulk S_2, and to a lesser degree, FeO. Thus, while S_2 comprises generally <1 wt% of a typical LRC rock powder produced from a homogenized fist-sized metapelite sample, the reactive bulk composition in a low greenschist facies rock could be significantly different. In this theoretical case, the reactive bulk volume could comprise proportionally more sulfide at low metamorphic grades than tabulated for S distributed homogenously. For example, assuming the other components remain proportional to one another, increasing specified S_2 to 4 mol% of the bulk composition widens the desulfidation window to conditions higher than terminal chlorite breakdown (Figure 3.17). In this manner coexisting Py and Po could be a result of local equilibrium, until greater metamorphic temperatures or sufficient permeability to metamorphic fluid flow from progressive deformation permits a scale of equilibrium that is compatible with homogeneity in the specified bulk composition.

Figure 3.17 *(Next Page)*: Simplified P-T pseudosection using bulk composition X1 but renormalizing for various amounts of bulk S_2. The width and minimum temperatures of Py desulfidation increase with increasing bulk S_2 content, such that in the 4.0 mol% S_2 case the Py-Po transition eclipses the terminal chlorite breakdown reaction (shown schematically as the ‘chl-out’ field). The Py-Po transition widens to a greater degree at higher S_2 values. Note that pseudosection topology for other fields (not shown) also change significantly at higher S_2 contents.

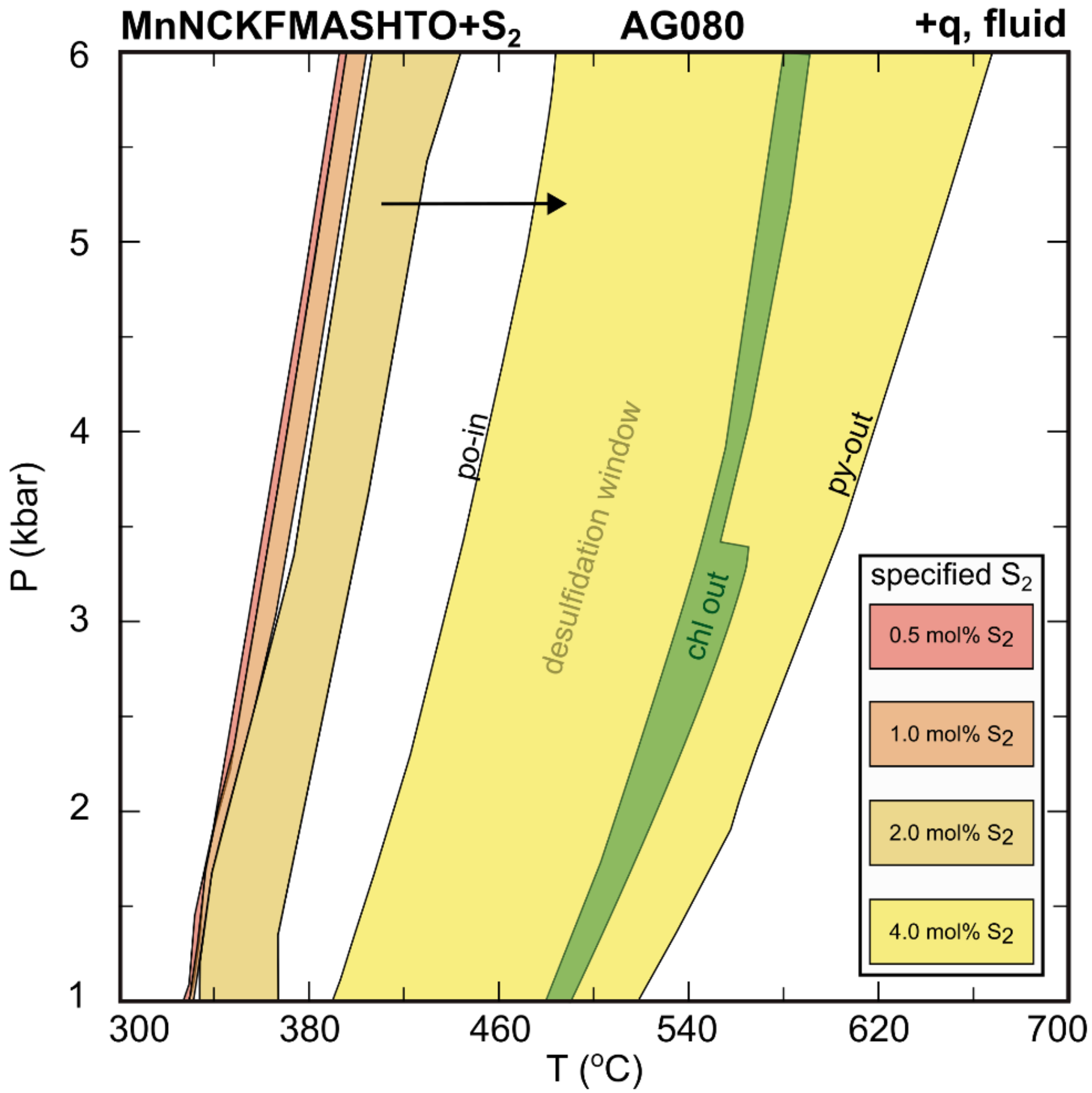

There is some evidence to support the notion of restrictive local equilibrium in sulfides among comparable graphitic metasediments. Strongly heterogeneous δ^{34}S values inherited from pre-metamorphic sulfide may persist on the scale of centimeters in moderate grade rocks, for which the scale of isotopic equilibrium is otherwise estimated at tens or hundreds of meters (Oliver et al., 1992). This is unexpected, given the longstanding view that sulfides equilibrate rapidly at even relatively low metamorphic temperatures (e.g., Barton, 1970). Other workers have also contested that the desulfidation reaction is not driven solely, or even principally by temperature, but rather fluid flux from devolatilization

(Ferry, 1981). Thus, perhaps in the deformed and tectonized metasediments of the Pacific Rim Terrane, it is plausible that permeabilities are heterogeneous and fluid flow is channelized, stymieing progression of the Py desulfidation reaction in impermeable sections, while driving the reaction to completion in others.

Lastly, the discrepancies between predicted mineral assemblages and those observed in sub- to low greenschist facies rocks could bear on reactions between silicates and sulfides. For example, while stilpnomelane is commonly predicted over the temperature domain ~300 to 400 °C, it is not observed among any of the argillites or phyllites. Similarly, predicted modal abundances of chlorite overestimate observed abundances, which range in typical LRC phyllites from negligible to a few modal percent. In turn, the modelled equilibria wherein S liberated during the production of Po reacts with Fe-silicates may not be strictly valid for low temperature samples if Fe is not available and reactive. However, if desulfidation effectively commences at higher temperatures, in the presence of chlorite or biotite, such equilibria could still be of consequence.

3.5.4 Relevance to regional orogenic gold genesis

High temperature, medium pressure metamorphism of metasedimentary lithologies are commonly associated with quartz-sulfide hosted Au ore deposits in forearc metapelites, such as in southeastern Alaska (Haeussler et al., 1995), and the Otago Schist in New Zealand (Pitcairn et al., 2006; Pitcarin et al., 2010). In the Pacific Rim Terrane, the LRC hosts the Valentine Mountain prospect, with indicated reserves of ~50 kton Au (Houle, 2011). Located centrally in the terrane (Figure 3.1), the ore presents mainly as auriferous quartz veins and is commonly associated with Py, Po, and Apy (Grove, 1984, Houle 2011). Ores are concentrated in the ‘arsenic window’ (after Houle, 2011) a region of elevated As concentrations that follows the shape of a large easterly plunging open fold, and the surface trace of a supra-meter scale amphibolite horizon. Furthermore, the Leech River catchment east of Valentine Mountain was historically exploited for placer gold, likely derived from eroded auriferous quartz veins (Grove, 1984).

Since Au efficiently forms complexes with sulfur ligands in metamorphic fluids (Pokrovski et al., 2009), previous workers have suggested that the desulfidation reaction is an effective mechanism to liberate sulfur from *in-situ* pre-metamorphic pyrite, and simultaneously scavenge trace concentrations of Au hosted in primary sulfides and throughout the rock volume (Tomkins, 2010; Finch & Tomkins, 2017). Thus, in the metamorphic orogenic Au paradigm, there must be a net transfer of S and Au during prograde metamorphism. Bulk rock data from the Pacific Rim Terrane do show a characteristic decrease in total S contents between 400 and 500 °C, consistent with the mobilization of S. Similarly, Au is only detected among very low- or high-grade samples, consistent with mobilization of Au at intermediate grades.

To delineate the influence of protolith from across-grade changes in major and trace element chemistry, the raw data were normalized against V (Figure 3.18), as values for both the metabasic and metasedimentary suites are conservative with metamorphic grade (Hammerli et al., 2016), and clearly distinguish protoliths. Notably, Cu/V shows a slight relative decrease with increasing temperature in both protolith suites. Sc/V also shows a disparate pattern compared to the raw values, with a relative decrease in Sc/V with grade for the metasedimentary suite, albeit with significant scatter. As and Ni are also mobilized and increase towards higher grades, except As exhibits a sharp decrease among the highest grade samples (550 – 600 °C). Cu shows a slight indistinct decrease with increasing grade, which is more clearly identifiable in V-normalized space. Most other elements, including Co, Zn, Ga, and Pb are not mobilized over these same conditions (Figure 3.18).

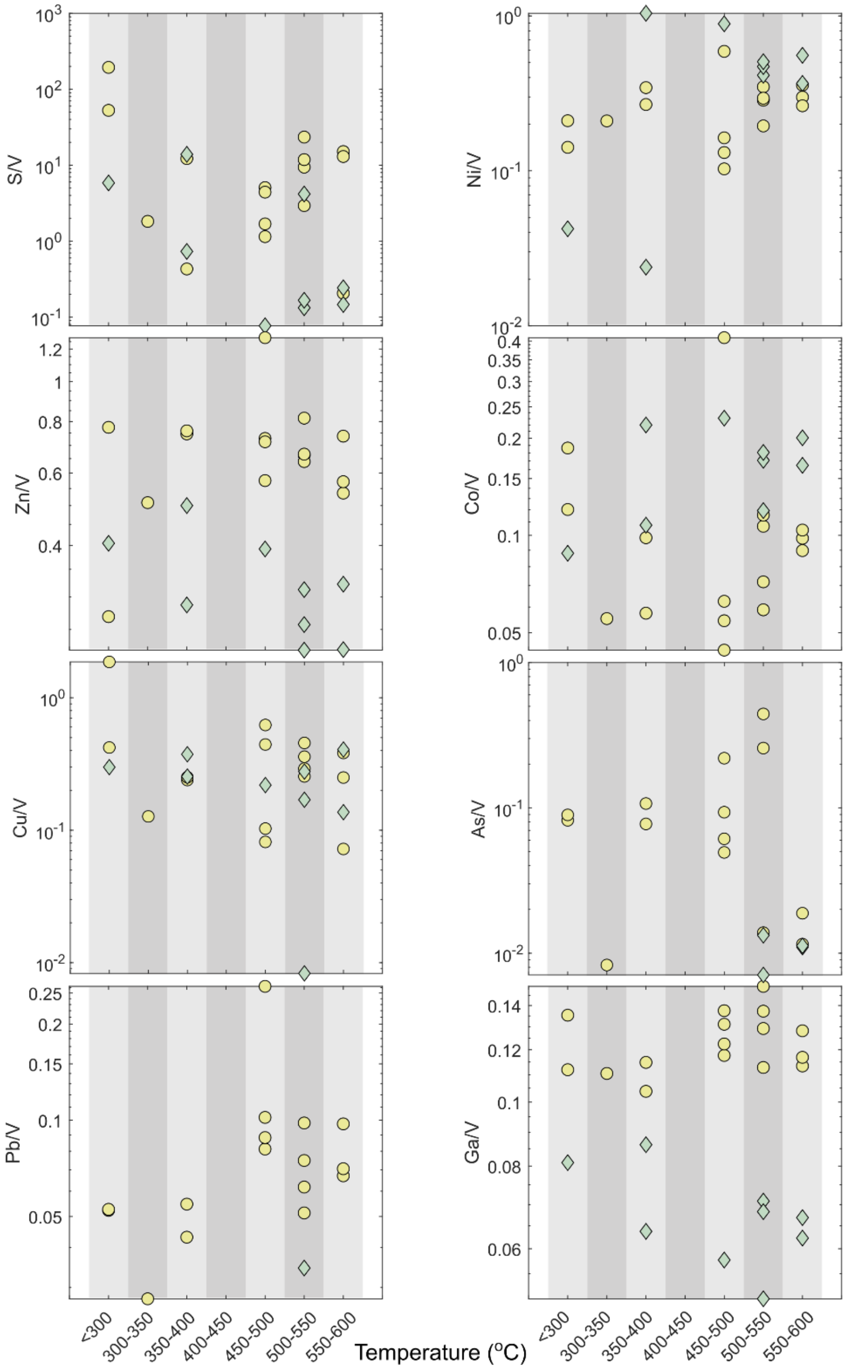

Figure 3.18 Vanadium-normalized bulk rock trends to delineate influence of local protolith effects and across grade changes. Vanadium is immobile across the same metamorphic conditions.

Large scale mobilization of chalcophile elements such as Cu, Zn, Pb, and Co is commonly not observed in metamorphic terranes (Hammerli et al., 2016; Stepanov, 2021). Nonetheless, the trends for S, Au, Ni, and As remain in V-normalized space, suggesting that despite a small *n*, trends with grade are not the result of differences in local bulk compositions. This is a reasonable indication that open-system desulfidation (e.g., Ferry, 1981) could have driven sulfur-mediated mobilization of Au, and to a lesser degree As, Ni, and Cu, but not other chalcophiles, yielding quartz-vein hosted Py, Po, Ccp, Apy, and free Au (Houle, 2011). Thus, the "orogenic Au" paradigm in which primarily Au, but not most base metals or chalcophiles, are mobilized and concentrated appears to be applicable in the Pacific Rim Terrane. Consequently, the Valentine Mountain deposit is best classified as a hypozonal (>12 km deep, >475 °C) class orogenic Au deposit (terminology after Groves et al., 1998).

A first order verification of this assessment can be made by estimating the amount of Au per km^3 of protolith, and order-of-magnitude estimates of metamorphosed Au 'fertile' metasediment. While the Pacific Rim Terrane lacks any faithful recorders of protolith Au content, compilation of carbonaceous shales suggest that ~6 ppb Au is representative (Large et al., 2011), although estimates for some terranes (e.g., the Otago Schist) are as low as 0.56 ppb (Pitcairn et al., 2010). The Py-Po conversion is particularly efficient at releasing Au, since it is not well accommodated in the structure of Po, and so >90% of 'invisible' Au in Py may be liberated (Large et al., 2011; Large et al., 2020). If this released Au efficiently complexes with bisulfide in a metamorphic fluid and mobilized on the scale of a few kilometers during peak metamorphism, then it becomes possible to generate an orebody of the scale of the Valentine Mountain deposit with intra-terrane sourced gold. Assuming a rock volume of 6000 km^3 (10 km × 10 km × 60 km) and a simple shale density of 2400 kg m^{-3}, the LRC pelitic protolith need only have ~3.9 ppb Au to produce an orebody of approximately 50 kton Au (Houle, 2011).

3.6 Summary

The forearc metasediments of the Pacific Rim Terrane underwent high temperature forearc metamorphism associated with the subcretion of young oceanic crust belonging to the Crescent terrane, and possibly interaction with a subducted mid-ocean ridge. The resultant thermal gradient caused up to amphibolite grade metamorphism among carbonaceous metasediments nearest the terrane boundary, to sub-greenschist facies at structurally higher levels. Equilibrium thermodynamic models suggest that during this thermal metamorphism, the Py desulfidation reaction would convert primary Py to Po over a narrow threshold at temperatures below 400 °C, and that the S liberated would likely react with Fe-bearing silicates rather than contributing to the fluid S budget. Instead, in the idealized models S release to the fluid phase is driven by the desulfidation of Po at higher grades.

However, petrographic evidence among similar protoliths at different grades indicates that Py locally survives past this threshold up to conditions up to 550 °C, as indicated by relict Py included within staurolite and andalusite porphyroblasts. Furthermore, evidence for co-existing Py and Po is found over a much wider window than suggested by the thermodynamic models. Samples from low greenschist facies conditions commonly show only partial or local equilibrium, and pseudosection models of the low temperature Py desulfidation reactions should be interpreted with caution. If the scale of equilibrium in greenschist facies metasediments is on the order of millimeters or centimeters, it is possible that S comprises a much greater proportion the reactive bulk composition than estimated for a homogenized metasedimentary sample. In this way, the desulfidation window could be widened extensively such that Py and Po could coexist throughout greenschist and lower amphibolite facies. Alternatively, limited or channelized metamorphic fluid flow could exert control on the progress of the desulfidation reaction (Ferry, 1981), allowing areas of fluid flow to drive the production of Po, while Py persists in adjacent impermeable horizons. The pervasive deformation that accompanied metamorphism in the LRC (Jakob et al., 2016), however, should have facilitated adequate fluid flow (e.g., Tomkins 2010).

Bulk rock data suggest that there is net mobilization of S and Au, as well as As, Cu, and Ni with increasing metamorphic grade. Whole-rock S contents show a depletion up to ~500 °C, coinciding with a window of minimal visible sulfide in samples between 400 and 500 °C. While most bulk rock analyses yield Au below detection limit (2 ppb), a subset of low- and high-grade samples which likely precede and succeed the true range of Py desulfidation suggest there is Au mobility on a terrane scale. More data are required to confirm this trend.

There are many unanswered questions that require additional attention. Phase texture and identity clues suggest that disequilibrium processes are governing the Py desulfidation reaction at low grades, but this should be tested more rigorously. For example, thin-section scale evaluation of δ^{34}S values in greenschist facies Py and Po could shed light on the scale of equilibration and homogenization. If the reactive bulk volumes are indeed small (cm-scale) in sub-amphibolite facies, future thermodynamic modelling should consider the prospects of S comprising a greater proportion of the reactive bulk chemistry. Finally, closed-system pseudosections do not adequately reflect realistic conditions of desulfidation in natural rocks, and thus future modelling should explicitly consider the effects of the net export of S via metamorphic fluid from the system during devolatilization of metapelites.

Chapter 4. Conclusions

4.1 Cause and magnitude of metamorphism in the Pacific Rim Terrane

The new thermometry and barometry results presented in this thesis resolve the metamorphic conditions in the southern contiguous Pacific Rim Terrane to be from 230 °C to ~600 °C at pressures of up to ~4.4 ± 1.8 kbar. RSCM thermometry, conventional garnet-biotite geothermobarometry and pseudosection models suggest that the LRC and PPU experienced a regional-scale thermal metamorphic event at shallow forearc depths. The distribution of exposed felsic sills does not bear on metamorphic grade, as evidenced by calculated RSCM isotherms and field observations. Furthermore, proposed Cretaceous felsic magmatism, and greenschist facies metamorphism therefrom, is contradicted by a new maximum depositional age from a detrital zircon in the PPU (72.5 ± 0.8 Ma). Volumetrically minor Eocene syn-deformation felsic sills are likely derived from supra-solidus conditions at depth during peak metamorphism at around ~51 Ma (after Groome et al., 2003). Intercalated metabasites in both the LRC and PPU lack contact aureoles and trace element data suggest the metabasites may locally host layers of metamorphosed hydrothermal or otherwise seafloor sediments that are Mn-rich and have negative Ce anomalies. Thus, the metabasites are likely not syn-metamorphic sills, and are instead interpreted here as tectonically interfoliated volcanic rocks. The LRC and PPU have discrepant geochemical provenances, with a greater felsic plutonic or recycled detritus signal among the LRC metasediments. Nevertheless, the two units were juxtaposed prior to Eocene thermal metamorphism such that the metamorphic gradient is continuous across their mutual boundary. Remnant lawsonite ± prehnite-pumpellyite sub-blueschist assemblages persist in the PPU and are locally overprinted to greenschist facies by thermal metamorphism. The subcretion of the then recently formed Crescent terrane beneath the LRC is the proposed cause of this forearc metamorphism, as well as possible proximity to the Kula- or Resurrection-Farallon ridge.

4.2 Consequences for sulfide metamorphism

Thermal metamorphism of sulfide-bearing carbonaceous metasediments at broadly low pressures (~4 kbar) in the Pacific Rim Terrane provides a suitable natural environment to test recent models of pyrite and pyrrhotite desulfidation. Results from this thesis show discrepant behavior between pseudosection models of the Py-Po transition, and the rock record. In the LRC, Py locally persists in the matrix and as inclusions within the common porphyroblasts andalusite and staurolite. Therefore, Py may locally persist to temperatures as high as ~550 °C. Po is the dominant sulfide above upper greenschist facies in both the matrix and inclusion assemblages. Garnet porphyroblasts host Po inclusions, but never host Py. Conversely, pseudosection models including S predict the Py-Po transition should occur in a narrow window initiating at low temperatures between 300 to 420 °C. Closed-system models predict Po desulfidation with prograde metamorphism as the mechanism to release S to the fluid. The results presented here suggest that disequilibrium governs the desulfidation reaction at low temperatures. In this manner, small reaction volumes derived from limited local equilibrium could explain the coexistence of Py and Po to greenschist facies conditions.

Bulk rock S contents show an overall decrease with increasing metamorphic grade up to ~500 °C, and an increase in S contents to ~550 °C. These data are consistent with the orogenic Au paradigm, in which S is mobilized in fluids produced by devolatilizing pelites. Detectable Au at very low and high grades are consistent with Au mobilization in rocks which attained peak metamorphic temperatures of between 400 and 500 °C. Other chalcophile elements like Cu, Zn, and Co do not show significant mobilization over the same temperature window. Therefore, the quartz-sulfide-Au veins comprising the Valentine Mountain orebody are best classified as a hypozonal orogenic Au deposit and likely formed via sluggish Py and Po desulfidation in devolatilizing pelites during the Eocene thermal metamorphic event.

4.3 Future work

Here, several avenues of study are recommended to provide further insight into the tectonic evolution of the Pacific Rim Terrane, and the metamorphism of sulfides therein. Given the geochemical indicators for differing provenance, further detrital zircon dating will help shed light on the paleo-position of the LRC prior to accretion, and how it relates to the cryptic PPU. Additionally, detrital zircon ages will help test 'mobilist' hypotheses about large scale margin-parallel translations among forearc units analogous to the Pacific Rim Terrane which are not tested by the results presented here.

Further study of the Survey Mountain metavolcanics, including petrography of purportedly preserved primary mineralogy, will help illuminate the nature of the Tripp Creek metabasites if they represent a continuous unit with the Survey Mountain metavolcanics, in gradational contact with the LRC. For example, the reported presence of stratiform Besshi-type volcanic-hosted massive sulfide deposits in the Survey Mountain metavolcanics, coupled with possible metamorphosed hydrothermal sediments in the Tripp Creek metabasites, are both consistent with a near-ridge seafloor environment. Therefore, future studies could establish if the Survey Mountain metavolcanics is a small, preserved section of oceanic crust subcreted between the LRC and Wrangellia. Reports of a dioritic plug at Survey Mountain (e.g., Malczak et al., 1982) could provide an opportunity to retrieve a crystallization age for those volcanics, further constraining their relationship to the Tripp Creek metabasites, the Crescent terrane, and the Eocene forearc evolution of the southern BC cordillera. Finally, several other recent *in-situ* techniques could vastly improve the pressure and temporal resolution of metamorphic events in the Pacific Rim Terrane. Namely, intra-garnet geochronology (e.g., Baxter et al., 2017) could especially be of use examining the coarse garnet porphyroblasts near the Leech River fault which exhibit zoning to better resolve the timing and duration of metamorphism. The prevalence of monazite and zircon inclusions in staurolite may present another opportunity to constrain the timing of metamorphism. Additionally, the advent of 'thermoba-Raman-try' (Kohn, 2014) could provide a barometer applicable to a wide number of rock types to examine the pressure conditions approaching the Leech River fault.

Future studies examining sulfide metamorphism in the Pacific Rim Terrane should seek to establish the degree of equilibrium attained among sulfides across metamorphic grade, to test the disequilibrium model invoked here. Furthermore, future implementations of the thermodynamic models used here should employ open-system conditions to reflect the environment of a devolatilizing pelite more accurately, as illustrated by bulk rock S mobility in this study. Fluid chemistry also bears greatly on ore genesis in the Pacific Rim Terrane, and zoned tourmaline grains could provide an avenue to examine fluid compositions during metamorphism (e.g., van Hinsberg et al., 2017). In this thesis, devolatilization of the pelitic rocks is invoked as the primary source of fluids. However, subcretion of oceanic crust could also contribute to the fluid budget by slab devolatilization down-dip, and therefore should be evaluated. This thesis constrained the likely mechanism for mobilizing Au but does not speculate on the ore deposition mechanism. Therefore, future work could examine possible structural and geochemical mechanisms to cause precipitation of quartz-sulfide-Au veins in the Valentine Mountain region, specifically within the large east-plunging Tripp Creek metabasite anticline. In-situ LA-ICP-MS analyses of Py and Po would provide an extremely useful parallel dataset to bulk rock trends, and trace element systematics therein (e.g., Co/Ni, Au, As) may be able to provide improved resolution on the conditions of Py desulfidation.

References

Alirezaei, S., & Cameron, E.M. (2001), Variations of sulfur isotopes in metamorphic rocks from Bamble Sector, southern Norway: a laser probe study. Cehmical Geology, 181, 23-45. https://doi.org/10.1016/S0009-2541(01)00266-2

Aoya, M., Kouketsu, Y., Endo, S., Shimizu, H., Mizukami, T., Nakamura, D. and Wallis, S. (2010), Extending the applicability of the Raman carbonaceous-material geothermometer using data from contact metamorphic rocks. Journal of Metamorphic Geology, 28, 895-914. https://doi.org/10.1111/j.1525-1314.2010.00896

Barnett, D. E., Bowman, J. R., Pavlis, T. L., Rubenstone, J. R., Snee, L. W., and Onstott, T. C. (1994). Metamorphism and near-trench plutonism during initial accretion of the Cretaceous Alaskan forearc, J. Geophys. Res., 99(B12), 24007– 24024, https://doi.org/10.1029/94JB02462

Barret, T.J., & Jarvis, I. (1988). Rare-earth element geochemistry of metalliferous sediments from DSDP Leg 92: The East Pacific Rise transect. Chemical Geology. 67(3-4), 243-259. https://doi.org/10.1016/0009-2541(88)90131-3

Barton, P.B. (1970). Sulfide Petrology. Mineral. Soc. Amer. Spec. Paper 3, 187-198. https://doi.org/10.1515/9781501508332-009

Baxter, E.F., Caddick, M.J., Dragovic, B. (2017). Garnet: A Rock-Forming Mineral Petrochronometer. Reviews in Mineralogy & Geochemistry. 83, 469-533. http://dx.doi.org/10.2138/rmg.2017.83.15

Beyssac, O., Goffé, B., Chopin, C., & Rouzaud, J. N. (2002). Raman spectra of carbonaceous material in metasediments: A new geothermometer. Journal of Metamorphic Geology, 20(9), 859–871. https://doi.org/10.1046/j.1525-1314.2002.00408.x

Beyssac, O., Pattison, D. R. M., & Bourdelle, F. (2019). Contrasting degrees of recrystallization of carbonaceous material in the Nelson aureole, British Columbia and Ballachulish aureole, Scotland, with implications for thermometry based on Raman spectroscopy of carbonaceous material. Journal of Metamorphic Geology, 37(1), 71–95. https://doi.org/10.1111/jmg.12449

Beyssac, Olivier, Goffé, B., Petitet, J.-P., Froigneux, E., Moreau, M., & Rouzaud, J.-N. (2003). On the characterization of disordered and heterogeneous carbonaceous materials by Raman spectroscopy. Spectrochimica Acta Part A: Molecular and Biomolecular Spectroscopy, 59(10), 2267–2276. https://doi.org/10.1016/S1386-1425(03)00070-2

Bhatia, M. R., & Crook, K. A. W. (1986). Trace element characteristics of graywackes and tectonic setting discrimination of sedimentary basins. Contr. Mineral. and Petrol. 92, 181–193 (1986). https://doi.org/10.1007/BF00375292

Bradley, D., Kusky, T., Haeussler, P., Goldfarb, R., Miller, M., Dumoulin, J., Nelson, S.W., Karl, S. (2003). Geologic signature of early Tertiary ridge subduction in Alaska. In V. B. Sisson, S. M. Roeske, & T. L. Pavlis, Geology of a transpressional orogen developed during ridge-trench interaction along the North Pacific margin: Boulder, Colorado, Geological Society of America Special Paper 371, 19-49. https://doi.org/10.1130/0-8137-2371-X.19

Brandon, M. T. (1989-a). Deformational styles in a sequence of olistostromal mélanges, Pacific Rim Complex, western Vancouver Island, Canada. Geological Society of America Bulletin. 101(12), 1520-1542. https://doi.org/10.1130/0016-7606(1989)101<1520:DSIASO>2.3.CO;2

Brandon, M. T. (1989-b). Origin of igneous rocks associated with Mélanges of the Pacific Rim Complex, western Vancouver Island, Canada. Tectonics, 8(6), 1115– 1136, doi:10.1029/TC008i006p01115.

Brown, J. L., Christy, A. G., Ellis, D. J., & Arculus, R. J. (2014). Prograde Sulfide Metamorphism in Blueschist and Eclogite, New Caledonia. Journal of Petrology, 55(3), 643–670. https://doi.org/10.1093/petrology/egu002

Caddick, M. J., Konopásek, J., & Thompson, A. B. (2010). Preservation of Garnet Growth Zoning and the Duration of Prograde Metamorphism. Journal of Petrology, 51(11), 2327–2347. https://doi.org/10.1093/petrology/egq059

Canil, D. (2017). Sulphide–sulphate stability and melting in subducted sediment and its role in arc mantle redox and chalcophile cycling in space and time. Earth and Planetary Science Letters, 470, 73-86. https://doi.org/10.1016/j.epsl.2017.04.028

Canham, E. (2000). Stratigraphy, structure and lithogeochemistry of the Finlayson Arm region of the Pacific Rim Terrane, Vancouver Island. (Unpublished Hons Thesis). University of Victoria, Canada.

Carlson, W. D. (2002). Scales of disequilibrium and rates of equilibration during metamorphism. American Mineralogist, 87(2–3), 185–204. https://doi.org/10.2138/am-2002-2-301

Carpenter, R. H. (1974). Pyrrhotite Isograd in Southeastern Tennessee and Southwestern North Carolina. GSA Bulletin 85 (3): 451–456. https://doi.org/10.1130/0016-7606(1974)85<451:PIISTA>2.0.CO;2

Cawood, P. A., Kusky, M., Mooney, W. D., & Windley, B. F. (2009). Accretionary orogens through Earth history. Geological Society, London, Special Publications, 318, 1-36. https://doi.org/10.1144/SP318.1

Clennett, E. J., Sigloch, K., Mihalynuk, M. G., Seton, M., Henderson, M. A., Hosseini, K., Mohammadzaheri, A., Johnston, S. T., & Müller, R. D. (2020). A Quantitative Tomotectonic Plate Reconstruction of Western North America and the Eastern Pacific Basin. Geochemistry, Geophysics, Geosystems, 21. https://doi.org/10.1029/2020GC009117

Clowes, R. M., Brandon, M. T., Green, A. G., Yorath, C. J., Brown, A. S., Kanasewich, E. R., & Spencer, C. (1987). LITHOPROBE—southern Vancouver Island: Cenozoic subduction complex imaged by deep seismic reflections. Canadian Journal of Earth Sciences, 24(1), 31–51. https://doi.org/10.1139/e87-004

Condie, K.C., (1993) Chemical composition and evolution of the upper continental crust: Contrasting results from surface samples and shales. Chemical Geology, 104(1-4), 1-37. https://doi.org/10.1016/0009-2541(93)90140-E

Connolly, J. A. D. (2005). Computation of phase equilibria by linear programming: A tool for geodynamic modeling and its application to subduction zone decarbonation. Earth and Planetary Science Letters, 236(1–2), 524–541. https://doi.org/10.1016/j.epsl.2005.04.033

Connolly, J.A.D., Cesare, B. (1993). C-O-H-S fluid composition and oxygen fugacity in graphitic metapelites. Journal of Metamorphic Geology, 11: 379-388. https://doi.org/10.1111/j.1525-1314.1993.tb00155.x

Cook, F.A., Percival, J.A., Clowes, R.M. (2012). Tectonic Styles in Canada: Lithoprobe Perspectives on the Evolution of the North American Continent. Chapter 8 *In* Tectonic Styles in Canada: The Lithoprobe Perspective. Edited by Percival, J.A., Clowes, R.M., Geological Association of Canada, Special Paper 49, 467-498.

Cowan, D.S. (1985). Structural styles in Mesozoic and Cenozoic mélanges in the western Cordillera of North America. GSA Bulletin, 96 (4), 451–462. https://doi.org/10.1130/0016-7606(1985)96<451:SSIMAC>2.0.CO;2

Cowan, D. S. (2003). Revisiting the Baranof-Leech River hypothesis for early Tertiary coastwise transport of the Chugach-Prince William terrane. Earth and Planetary Science Letters, 231(3-4), 463-475. https://doi.org/10.1016/S0012-821X(03)00300-5

Cui, Y., Miller, D., Schiarizza, P., and Diakow, L.J. (2017). British Columbia digital geology. British Columbia Ministry of Energy, Mines and Petroleum Resources, British Columbia Geological Survey Open File 2017-8, 9p. Data version 2019-12-19.

Davidson, C., Garver, J. I. (2018). The Time-Transgressive Sanak-Baranof Plutonic Belt, Alaska: A Tale Of Diachronous Timing Of Fore-Arc Burial And Pluton Emplacement. 89-12. 322269. https://doi.org/10.1130/abs/2018AM-322269

Dlugosz, J. P., Matthews, W.A., Geen, A., Canil, D. (2020). Stratigraphic Age and Provenance of the Leech River Schist on Vancouver Island, British Columbia from LA-ICP-MS Depth Profiling (Abstract). In: Geoconvention 2020 Virtual Conference.

Dumitru, T. A. (1991). Effects of subduction parameters on geothermal gradients in forearcs, with an application to Franciscan Subduction in California. Journal of Geophysical Research, 96(B1), 621. https://doi.org/10.1029/90JB01913

Eddy, M. P., Clark, K. P., & Polenz, M. (2017). Age and volcanic stratigraphy of the Eocene Siletzia oceanic plateau in Washington and on Vancouver Island. Lithosphere, 9 (4). 652–664. https://doi.org/10.1130/L650.1

Evans, K. A., Powell, R., & Holland, T. J. B. (2010). Internally consistent data for sulphur-bearing phases and application to the construction of pseudosections for mafic greenschist facies rocks in Na2O-CaO-K2O-FeO-MgO-Al2O3-SiO2-CO2-O-S-H2O: Internally consistent data for sulphur-bearing phases. Journal of Metamorphic Geology, 28(6), 667–687. https://doi.org/10.1111/j.1525-1314.2010.00890.x

Evans, K.A., & Tomkins, A.G., (2011) The relationship between subduction zone redox budget and arc magma fertility. Earth and Planetary Science Letters, 308(3-4), 401-409. https://doi.org/10.1016/j.epsl.2011.06.009

Fairchild, L. H., Cowan, D. S. (1982). Structure, petrology, and tectonic history of the Leech River complex northwest of Victoria, Vancouver Island. Canadian Journal of Earth Sciences, 19(9), 1817–1835. https://doi.org/10.1139/e82-161

Farris, D. W., & Paterson, S. R. (2009). Subduction of a segmented ridge along a curved continental margin: Variations between the western and eastern Sanak–Baranof belt, southern Alaska. Tectonophysics, 474(1-4), 100-117. https://doi.org/10.1016/j.tecto.2007.10.008

Ferry, J.M. (1981). Petrology of graphitic sulfide-rich schists from South-central Maine: an example of desulfidation during prograde regional metamorphism. American Mineralogist, 66(9-10): 908–930.

Ferry, J.M., Spear, F.S. (1978). Experimental calibration of the partitioning of Fe and Mg between biotite and garnet. Contr. Mineral. and Petrol. 66, 113–117. https://doi.org/10.1007/BF00372150

Festa, A., Ogata, K., Pini, G. A., Dilek, Y., & Alonso, J. L. (2016). Origin and significance of olistostromes in the evolution of orogenic belts: A global synthesis. Gondwana Research, 39, 180-203. https://doi.org/10.1016/j.gr.2016.08.002

Finch, E. G., & Tomkins, A. G. (2017). Pyrite-Pyrrhotite Stability in a Metamorphic Aureole: Implications for Orogenic Gold Genesis. Economic Geology, 112(3): 661–674. https://doi.org/10.2113/econgeo.112.3.661

Fuhrman, M.L., Lindsley, D.H., (1988) Ternary-feldspar modeling and thermometry. American Mineralogist, 73(3-4), 201–215.

Fuston, S., & Wu, J. (2020). Raising the Resurrection plate from an unfolded-slab plate tectonic reconstruction of northwestern North America since early Cenozoic time. GSA Bulletin. https://doi.org/10.1130/B35677.1

Goldhaber, M. B. (2003). Sulfur-rich Sediments. In Treatise on Geochemistry, Volume 7. Editors: Holland, H.D., Turekian, K.K. Pergamon. (7), 257–288. https://doi.org/10.1016/B0-08-043751-6/07139-5

Gregory, D.D., Large, R.R., Halpin, J.A., Lounejeva Baturina, E., Lyons, T.W., Wu, S., Danyushevsky, L., Sack, P.J., Chappaz, A., Maslennikov, V.V., Bull, S.W. (2015) Trace Element Content of Sedimentary Pyrite in Black Shales. Economic Geology,110 (6) 1389–1410. https://doi.org/10.2113/econgeo.110.6.1389

Groome, W. G., & Thorkelson, D. J. (2009). The three-dimensional thermo-mechanical signature of ridge subduction and slab window migration. Tectonophysics, 464(1–4), 70–83. https://doi.org/10.1016/j.tecto.2008.07.003

Groome, W. G., Thorkelson, D. J., Friedman, R. M., Mortensen, J. K., Massey, N. W. D., Marshall, D. D., & Layer, P. W. (2003). Magmatic and tectonic history of the Leech River Complex, Vancouver Island, British Columbia: Evidence for ridge-trench intersection and accretion of the Crescent Terrane. In V. B. Sisson, S. M. Roeske, & T. L. Pavlis, Geology of a transpressional orogen developed during ridge-trench interaction along the North Pacific margin. Geological Society of America. https://doi.org/10.1130/0-8137-2371-X.327

Grove, E.W. (1984). Geological Report and Work Proposal on the Valentine Mountain Property, Assessment Report 12642, NTS 92B/12W. Retrieved from: https://aris.empr.gov.bc.ca/search.asp?mode=repsum&rep_no=12642

Groves, David I, Goldfarb, R. J., & Robert, F. (2003). Gold Deposits in Metamorphic Belts: Overview of Current Understanding, Outstanding Problems, Future Research, and Exploration Significance. Economic Geology 98 (1), 1–29. https://doi.org/10.2113/gsecongeo.98.1.1

Groves, D.I, Goldfarb, R. J., Gebre-Mariam, M., Hagemann, S. G., & Robert, F. (1998). Orogenic gold deposits: A proposed classification in the context of their crustal distribution and relationship to other gold deposit types. Ore Geology Reviews, 13(1–5), 7–27. https://doi.org/10.1016/S0169-1368(97)00012-7

Groves, D.I, Goldfarb, R. J., Gebre-Mariam, M., Hagemann, S. G., & Robert, F. (1998b). Orogenic gold deposits: A proposed classification in the context of their crustal distribution and relationship to other gold deposit types. Ore Geology Reviews, 13(1–5), 7–27. https://doi.org/10.1016/S0169-1368(97)00012-7

Haeussler, P. J., & Bradley, D. C. (2003). Life and death of the Resurrection plate: Evidence for its existence and subduction in the northeastern Pacific in Paleocene–Eocene time. GSA Bulletin, 115 (7): 867–880. https://doi.org/10.1130/0016-7606(2003)115<0867:LADOTR>2.0.CO;2

Haeussler, P. J., Bradley, D., Goldfarb, R., Snee, L., & Taylor, C. (1995). Link between ridge subduction and gold mineralization in southern Alaska. Geology, 23 (11): 995–998. https://doi.org/10.1130/0091-7613(1995)023<0995:LBRSAG>2.3.CO;2

Hammerli, J., Spandler, C., & Oliver, N. H. S. (2016). Element redistribution and mobility during upper crustal metamorphism of metasedimentary rocks: An example from the eastern Mount Lofty Ranges, South Australia. Contributions to Mineralogy and Petrology, 171(4), 36. https://doi.org/10.1007/s00410-016-1239-7

Harris, R.N., Conder, J.A., Heuret, A. (2014). The thermal structure of the subduction thrust within accretionary and erosive margins. Tectonophysics, 633, 221-231. https://doi.org/10.1016/j.tecto.2014.07.009

Herron, M. M. (1988). Geochemical Classification of Terrigenous Sands and Shales from Core or Log Data. Journal of Sedimentary Research. 58 (5): 820–829. doi: https://doi.org/10.1306/212F8E77-2B24-11D7-8648000102C1865D

Holdaway, M.J., Mukhopadhyay, B., Dyar, M.D., Guidotti, C.V., Dutrow, B.L. (1997) Garnet-biotite geothermometry revised: New Margules parameters and a natural specimen data set from Maine. American Mineralogist, 82, 582-595. https://doi.org/10.2138/am-1997-5-618

Holdaway, M.J.. (2000). Application of new experimental and garnet Margules data to the garnet-biotite geothermometer. American Mineralogist, 85(7-8), 881-892. https://doi.org/10.2138/am-2000-0701

Houle, J. (2011). Technical Report on the Valentine Mountain Property, Assessment Report 32500, NTS 092B12W. Retrieved from: https://aris.empr.gov.bc.ca/search.asp?mode=repsum&rep_no=32500

Jakob, J., Johnston, S. T., Beyssac, O., & Corfu, F. (2016). The structural evolution of the Leech River Complex, Vancouver Island, Canada: in Geodynamic Significance of Regional Melange Units at Divergent and Convergent Plate Margins, Jakob, J. (Manuscript from Doctoral Dissertation). University of Oslo, Norway.

James, T. S., Hollister, L. S., & Morgan, W. J. (1989). Thermal modeling of the Chugach Metamorphic Complex. Journal of Geophysical Research: Solid Earth, 94(B4), 4411–4423. https://doi.org/10.1029/JB094iB04p04411

Johnston, S. (2000). Lithology, Structure and Geochemistry of the Southernmost Pacific Rim Terrane, Victoria, British Columbia. (Unpublished Hons. Thesis). University of Victoria, Canada.

Kant, L. B., Tepper, J. H., Eddy, M. P., & Nelson, B. K. (2018). Eocene Basalt of Summit Creek: Slab breakoff magmatism in the central Washington Cascades, USA. Lithosphere. 10(6). 792–805. https://doi.org/10.1130/L731.1

Kohn, M.J. (2014). “Thermoba-Raman-try”: Calibration of spectroscopic barometers and thermometer for mineral inclusions. Earth and Planetary Science Letters, 388, 187-196. https://doi.org/10.1016/j.epsl.2013.11.054

Kohn, M. J., Castro, A. E., Kerswell, B. C., Ranero, C. R., & Spear, F. S. (2018). Shear heating reconciles thermal models with the metamorphic rock record of subduction. Proceedings of the National Academy of Sciences, 115(46), 11706–11711. https://doi.org/10.1073/pnas.1809962115

Kouketsu, Y., Mizukami, T., Mori, H., Endo, S., Aoya, M., Hara, H., Nakamura, D., & Wallis, S. (2014). A new approach to develop the R aman carbonaceous material geothermometer for low-grade metamorphism using peak width. Island Arc, 23(1), 33–50. https://doi.org/10.1111/iar.12057

Laetsch T., & Downs R. (2006). Software for Identification and Refinement of Cell Parameters From Powder Diffraction Data of Minerals Using the RRUFF Project and American Mineralogist Crystal Structure Databases. Abstracts from the 19th General Meeting of the International Mineralogical Association, Kobe, Japan, 23-28 July 2006.

Lanari, P., & Engi, M. (2017). Local Bulk Composition Effects on Metamorphic Mineral Assemblages. Reviews in Mineralogy and Geochemistry. 83 (1): 55–102. doi: https://doi.org/10.2138/rmg.2017.83.3

Large, R. R., Bull, S. W., & Maslennikov, V. V. (2011). A Carbonaceous Sedimentary Source-Rock Model for Carlin-Type and Orogenic Gold Deposits. Economic Geology, 106(3), 331–358. https://doi.org/10.2113/econgeo.106.3.331

Large, R., Thomas, H., Craw, D., Henne, A., & Henderson, S. (2012). Diagenetic pyrite as a source for metals in orogenic gold deposits, Otago Schist, New Zealand. New Zealand Journal of Geology and Geophysics, 55(2), 137–149. https://doi.org/10.1080/00288306.2012.682282

Large, Ross R., & Maslennikov, V. V. (2020). Invisible Gold Paragenesis and Geochemistry in Pyrite from Orogenic and Sediment-Hosted Gold Deposits. Minerals, 10(4), 339. https://doi.org/10.3390/min10040339

Laursen, J., Scholl, D. W., & von Huene, R. (2002). Evolution of the late Cenozoic Valparaiso forearc basin in central Chile: Forearc basin response to ridge and seamount subduction. Tectonics, 21, 1-27. https://doi.org/10.1029/2001TC901023

Li, C., Arndt, N. T., Tang, Q., & Ripley, E. M. (2015). Trace element indiscrimination diagrams. Lithos, 232, 76–83. https://doi.org/10.1016/j.lithos.2015.06.022

Lünsdorf, N.K., Dunkl, I., Schmidt, B.C., Rantitsch, G. and von Eynatten, H. (2017), Towards a Higher Comparability of Geothermometric Data Obtained by Raman Spectroscopy of Carbonaceous Material. Part 2: A Revised Geothermometer. Geostand Geoanal Res, 41, 593-612. https://doi.org/10.1111/ggr.12178

Maekawa, H., Shozul, M., Ishll, T., Fryer P., Pearce, J.A. (1993). Blueschist metamorphism in an active subduction zone. Nature, 364(520–523) https://doi.org/10.1038/364520a0

Mahar, E. M., Baker, J. M., Powell, R., Holland, T. J. B., & Howell, N. (1997). The effect of Mn on mineral stability in metapelites. Journal of Metamorphic Geology, 15: 223-238. https://doi.org/10.1111/j.1525-1314.1997.00011.x

Malczak, J., Vergos, S., Dvorak, Z. (1982). A Combined Report on Geological, Geochemical and Airborne Geophysical Surveys on the Leech River Project, Assessment Report 10278, NTS M92B/12W. Retrieved from: https://aris.empr.gov.bc.ca/search.asp?mode=repsum&rep_no=10278

Maravelis, A. G., Boutelier, D., Catuneanu, O., Seymour, K. St., & Zelilidis, A. (2016). A review of tectonics and sedimentation in a forearc setting: Hellenic Thrace Basin, North Aegean Sea and Northern Greece. Tectonophysics, 674, 1–19. https://doi.org/10.1016/j.tecto.2016.02.003

Massey, N.W.D., MacIntyre, D.G., Desjardins, P.J., & Cooney, R.T. (2005) Geology of British Columbia Geoscience Map 2005 – 3. BC Geological Survey. Retrieved from BC MapPlace 2.

McCarron, T., McFarlane, C. R. M., & Gaidies, F. (2019). The significance of Mn-rich ilmenite and the determination of P–T paths from zoned garnet in metasedimentary rocks from the western Cape Breton Highlands, Nova Scotia. Journal of Metamorphic Geology, 37(9), 1171–1192. https://doi.org/10.1111/jmg.12507

McCrory, P. A., & Wilson, D. S. (2013). A kinematic model for the formation of the Siletz-Crescent forearc terrane by capture of coherent fragments of the Farallon and Resurrection plates: Kinematics of Siletz-Crescent terrane. Tectonics, 32(3), 718–736. https://doi.org/10.1002/tect.20045

McEwen, G. L. (2013). - Tectonic deformation of the Pandora Peak Unit inferred by folding at Harling Point, Victoria, BC: Implications for the Pacific Rim Terrane (Unpublished Hons. Thesis). University of Victoria, Canada

McIntyre, T.J., Wilson, R.G., (1989). Geological and Geochemical Report on the Wolf and Little Wolf Groups, Assessment Report 19381, NTS 092B12W. Retrieved from: https://aris.empr.gov.bc.ca/search.asp?mode=repsum&rep_no=19381

Molnar, P., England, P. (1995). Temperatures in zones of steady-state underthrusting of young oceanic lithosphere. Earth and Planetary Science Letters. 131(1-2), 57-70. https://doi.org/10.1016/0012-821X(94)00253-U

Monger, J., & Price, R. (2002) The Canadian Cordillera: Geology and Tectonic Evolution. CSEG Recorder. 17-36.

Muller, J.E. (1977). Evolution of the Pacific Margin, Vancouver Island, and adjacent regions. Canadian Journal of Earth Sciences. 14(9), 2062-2085. https://doi.org/10.1139/e77-176

Muller, J.E. (1983). Map 1553A, Geology of Victoria West of Sixth Meridian, British Columbia, 1:100 000. Geological Survey of Canada.

Nilsen, T. H., & Zuffa, G. G. (1982). The Chugach Terrane, a Cretaceous trench-fill deposit, southern Alaska Geological Society, London, Special Publications, 10, 213-227. https://doi.org/10.1144/GSL.SP.1982.010.01.14

Oliver, N.H.S., Hoering, T.C., Johnson, T.W., Rumble III, D., Shanks III, W.C. (1992) Sulfur isotopic disequilibrium and fluid-rock interaction during metamorphism of sulfidic black shales from the Waterville-Augusta area, Main, USA. Geochimica et Cosmochimica Acta, 56(12), 4257 – 4265. https://doi.org/10.1016/0016-7037(92)90266-L

Palin, R. M., Weller, O.M., Waters, D.J., & Dyck, B. (2016). Quantifying geological uncertainty in metamorphic phase equilibria modelling; a Monte Carlo assessment and implications for tectonic interpretations. Geoscience Frontiers, 7(4), 591-607. https://doi.org/10.1016/j.gsf.2015.08.005

Pasteris, J. D. (1989). In Situ Analysis in Geological Thin-Sections by Laser Raman Microprobe Spectroscopy: A Cautionary Note. Applied Spectroscopy, 43(3), 567–570. https://doi.org/10.1366/0003702894202878

Pattison, D.R.M. (1992). Stability of Andalusite and Sillimanite and the Al_2SiO_5 Triple Point: Constraints from the Ballachulish Aureole, Scotland. The Journal of Geology, 100(4), 423–446. https://doi.org/10.1086/629596

Pattison, D. R. M., & Tinkham, D. K. (2009). Interplay between equilibrium and kinetics in prograde metamorphism of pelites: An example from the Nelson aureole, British Columbia. Journal of Metamorphic Geology, 27(4), 249–279. https://doi.org/10.1111/j.1525-1314.2009.00816.x

Pavlis, T., Amato, J., Trop, J., Ridgway, K., Roeske, S., & Gehrels, G. (2019). Subduction Polarity in Ancient Arcs: A Call to Integrate Geology and Geophysics to Decipher the Mesozoic Tectonic History of the Northern Cordillera of North America. GSA Today, 29(11), 4–10. https://doi.org/10.1130/GSATG402A.1

Peacock, S. M. (2020). Advances in the thermal and petrologic modeling of subduction zones. Geosphere, 16(4), 936–952. https://doi.org/10.1130/GES02213.1

Pearce, J.A. (2008). Geochemical fingerprinting of oceanic basalts with applications to ophiolite classification and the search for Archean oceanic crust. Lithos, 100(1-4), 14-48. https://doi.org/10.1016/j.lithos.2007.06.016

Penniston-Dorland, S. C., Kohn, M. J., & Piccoli, P. M. (2018). A mélange of subduction temperatures: Evidence from Zr-in-rutile thermometry for strengthening of the subduction interface. Earth and Planetary Science Letters, 482, 525–535. https://doi.org/10.1016/j.epsl.2017.11.005

Phillips, B. A., Kerr, A. C., Mullen, E. K., & Weis, D. (2017). Oceanic mafic magmatism in the Siletz terrane, NW North America: Fragments of an Eocene oceanic plateau? Lithos, 274–275, 291–303. https://doi.org/10.1016/j.lithos.2017.01.005

Pitcairn, I.K., Olivo, G.R., Teagle, D.A.H., Craw, D. (2010) Sulfide evolution during prograde metamorphism of the Otago and Alpine Schists, New Zealand. The Canadian Mineralogist, 48 (5): 1267–1295. https://doi.org/10.3749/canmin.48.5.1267

Pitcairn I.K., Teagle, D.A.H., Craw, D., Olivo, G.R., Kerrich, R., Brewer, T.S. (2006). Sources of Metals and Fluids in Orogenic Gold Deposits: Insights from the Otago and Alpine Schists, New Zealand. Economic Geology, 101(8), 1525–1546. https://doi.org/10.2113/gsecongeo.101.8.1525

Pitcairn, I.K., Skelton, A. D. L., & Wohlgemuth-Ueberwasser, C. C. (2015). Mobility of gold during metamorphism of the Dalradian in Scotland. Lithos, 233, 69–88. https://doi.org/10.1016/j.lithos.2015.05.006

Plank, T. (2005). Constraints from Thorium/Lanthanum on Sediment Recycling at Subduction Zones and the Evolution of the Continents. Journal of Petrology, 46(5), 921–944. https://doi.org/10.1093/petrology/egi005

Plank, Terry, & Langmuir, C. H. (1993). Tracing trace elements from sediment input to volcanic output at subduction zones. Nature, 362(6422), 739–743. https://doi.org/10.1038/362739a0

Pokrovski, G. S., Tagirov, B. R., Schott, J., Hazemann, J.-L., & Proux, O. (2009). A new view on gold speciation in sulfur-bearing hydrothermal fluids from in situ X-ray absorption spectroscopy and quantum-chemical modeling. Geochimica et Cosmochimica Acta, 73(18), 5406–5427. https://doi.org/10.1016/j.gca.2009.06.007

Pope, M. D. (2006). Structure of the Wark-Colquitz Gneiss, Victoria: Implications for the Tectonic Evolution of Vancouver Island (Unpublished Hons. Thesis). University of Victoria, Canada.

Riel, N., Guillot, S., Jaillard, E., Martelat, J.-E., Paquette, J.-L., Schwartz, S., Goncalves, P., Duclaux, G., Thebaud, N., Lanari, P., Janots, E., & Yuquilema, J. (2013). Metamorphic and geochronogical study of the Triassic El Oro metamorphic complex, Ecuador: Implications for high-temperature metamorphism in a forearc zone. Lithos, 156–159, 41–68. https://doi.org/10.1016/j.lithos.2012.10.005

Roser, B. P., & Korsch, R. J. (1988). Provenance signatures of sandstone-mudstone suites determined using discriminant function analysis of major-element data. Chemical Geology, 67(1-2), 119-139. https://doi.org/10.1016/0009-2541(88)90010-1.

Ruh, J. B. (2020). Numerical modeling of tectonic underplating in accretionary wedge systems. Geosphere, 16(6), 1385–1407. https://doi.org/10.1130/GES02273.1

Rusmore, M. E., & Cowan, D. S. (1985). Jurassic–Cretaceous rock units along the southern edge of the Wrangellia terrane on Vancouver Island. Canadian Journal of Earth Sciences. 22(8): 1223-1232. https://doi.org/10.1139/e85-124

Ryan, K. M., & Williams, D. M. (2007). Testing the reliability of discrimination diagrams for determining the tectonic depositional environment of ancient sedimentary basins. Chemical Geology, 242(1-2), 103-125. https://doi.org/10.1016/j.chemgeo.2007.03.013.

Schmidt, W. L., & Platt, J. P. (2020). Metamorphic Temperatures and Pressures across the Eastern Franciscan: Implications for Underplating and Exhumation. Lithosphere, 2020(1), 8853351. https://doi.org/10.2113/2020/8853351

Seyler, C., Kirkpatrick, J., Licht, A., Silerova, D., Regalla, C. (2020). Evidence for subduction along the Leech River Fault and implications for Cordilleran tectonics (Abstract) Geological Society of America Abstracts with Programs. 52(6). https://doi.org/10.1130/abs/2020AM-355976

Sills, J. D., & Tarney, J. (1984). Petrogenesis and tectonic significance of amphibolites interlayered with metasedimentary gneisses in the Ivrea Zone, Southern Alps, northwest Italy. Tectonophysics, 107(3–4), 187–206. https://doi.org/10.1016/0040-1951(84)90251-8

Sisson, V. B., Pavlis, T. L., Roeske, S. M., & Thorkelson, D. J. (2003). Introduction: An overview of ridge-trench interactions in modern and ancient settings. In V. B. Sisson, S. M. Roeske, & T. L. Pavlis, Geology of a transpressional orogen developed during ridge-trench interaction along the North Pacific margin. Geological Society of America Special Paper. https://doi.org/10.1130/0-8137-2371-X.1

Spear, F. S., & Pattison, D. R. M. (2017). The implications of overstepping for metamorphic assemblage diagrams (MADs). Chemical Geology, 457, 38–46. https://doi.org/10.1016/j.chemgeo.2017.03.011

Stepanov, A. S. (2021). A review of the geochemical changes occurring during metamorphic devolatilization of metasedimentary rocks. Chemical Geology, 568, 120080. https://doi.org/10.1016/j.chemgeo.2021.120080

Stern, R.J., Dumitru, T.A. (2019). Eocene initiation of the Cascadia subduction zone: A second example of plume-induced subduction initiation? Geosphere 15(3), 659–681. https://doi.org/10.1130/GES02050.1

Sun, S.-s., McDonough, W.F. (1989). Chemical and isotopic systematic of oceanic basalts: implications for mantle composition and processes. Geological Society, London, Special Publications, 42, 313-345. https://doi.org/10.1144/GSL.SP.1989.042.01.19

Symmes, G. H., & Ferry, J. M. (1992). The effect of whole-rock MnO content on the stability of garnet in pelitic schists during metamorphism. Journal of Metamorphic Geology, 10(2), 221–237. https://doi.org/10.1111/j.1525-1314.1992.tb00080.x

Thomas, H. V., Large, R. R., Bull, S. W., Maslennikov, V., Berry, R. F., Fraser, R., Froud, S., & Moye, R. (2011). Pyrite and Pyrrhotite Textures and Composition in Sediments, Laminated Quartz Veins, and Reefs at Bendigo Gold Mine, Australia: Insights for Ore Genesis. Economic Geology, 106(1), 1–31. https://doi.org/10.2113/econgeo.106.1.1

Timpa, S., Gillis, K. M., & Canil, D. (2005). Accretion-related metamorphism of the Metchosin Igneous Complex, southern Vancouver Island, British Columbia. Canadian Journal of Earth Sciences. 42(8): 1467-1479. https://doi.org/10.1139/e05-043

Tomkins, A. G. (2010). Windows of metamorphic sulfur liberation in the crust: Implications for gold deposit genesis. Geochimica et Cosmochimica Acta, 74(11), 3246–3259. https://doi.org/10.1016/j.gca.2010.03.003

Tomkins, A.G., & Evans, K.A. (2015) Separate zones of sulfate and sulfide release from subducted mafic oceanic crust. Earth and Planetary Science Letters, 428, 73-83. https://doi.org/10.1016/j.epsl.2015.07.028

Toulmin, P., & Barton, P.B. (1964). A thermodynamic study of pyrite and pyrrhotite. Geochimica et Cosmochimica Acta, 23(5), 641-671. https://doi.org/10.1016/0016-7037(64)90083-3

Tracy, R.J., & Robinson, P. (1988). Silicate-sulfide-oxide-fluid reactions in granulite-grade pelitic rocks, central Massachusetts. American Journal of Science, 288-A, 45-74.

Tsukada, K., Nakane, Y., Yamamoto, K., Kurihara, T., Otoh, S., Kashiwagi, K., Chuluun, M., Gonchigdorj, S., Nuramkhaan, M., Niwa, M. & Tokiwa, T. (2013), Geological setting of basaltic rocks in an accretionary complex, Khangai-Khentei Belt, Mongolia. Island Arc, 22, 227-241. https://doi.org/10.1111/iar.12028

Usui, T., Nakamura, E., Kobayashi, K., Maruyama, S., Helmstaedt, H. (2003) Fate of the subducted Farallon plate inferred from eclogite xenoliths in the Colorado Plateau. Geology. 31(7), 589–592. https://doi.org/10.1130/0091-7613(2003)031<0589:FOTSFP>2.0.CO;2

Van Keken, P. E., Wada, I., Sime, N., & Abers, G. A. (2019). Thermal Structure of the Forearc in Subduction Zones: A Comparison of Methodologies. Geochemistry, Geophysics, Geosystems, 20, 3268– 3288. https://doi.org/10.1029/2019GC008334

Van Hinsberg, V.J., Franz, G., Wood, B.J. (2017). Determining subduction-zone fluid composition using a tourmaline mineral probe. Geochemical Perspectives Letters, 3(1), 160-169. https://doi.org/ 10.7185/geochemlet.1719

Von Huene, R., & Scholl, D.W. (1991). Observations at convergent margins concerning sediment subduction, subduction erosion, and the growth of continental crust. Rev. Geophys., 29(3), 279– 316, doi:10.1029/91RG00969

Wakabayashi, J. (2015) Anatomy of a subduction complex: architecture of the Franciscan Complex, California, at multiple length and time scales, International Geology Review, 57:5-8, 669-746. https://doi.org/10.1080/00206814.2014.998728

Walters, J.B., Cruz-Uribe, A.M., & Marschall, H.R. (2020) Sulfur loss from subducted altered oceanic crust and implications for mantle oxidation. Geochem. Persp. Let. 13, 36–41. https://doi.org/10.7185/geochemlet.2011

Wells, R., Bukry, D., Friedman, R., Pyle, D., Duncan, R., Haeussler, P., & Wooden, J. (2014). Geologic history of Siletzia, a large igneous province in the Oregon and Washington Coast Range: Correlation to the geomagnetic polarity time scale and implications for a long-lived Yellowstone hotspot. Geosphere, 10(4), 692–719. https://doi.org/10.1130/GES01018.1

White, R.W., Powell, R., Holland, T.J.B., Johnson, T.E. and Green, E.C.R. (2014), New mineral activity–composition relations for thermodynamic calculations in metapelitic systems. J. Meta. Geol., 32, 261-286. https://doi.org/10.1111/jmg.12071

Whitney, D.L., & Evans, B.W. (2010) Abbreviations for names of rock-forming minerals. American Mineralogist, 95(1), 185-187. https://doi.org/10.2138/am.2010.3371

Wojdyr, M. (2010). Fityk: A general-purpose peak fitting program. Journal of Applied Crystallography, 43(5), 1126–1128. https://doi.org/10.1107/S0021889810030499

Wu, C.-M. (2017). Calibration of the garnet–biotite–Al2SiO5–quartz geobarometer for metapelites. J Metamorph Geol. 35, 983– 998. https://doi.org/10.1111/jmg.12264

Wu, J. T.-J., & Wu, J. (2019). Izanagi-Pacific ridge subduction revealed by a 56 to 46 Ma magmatic gap along the northeast Asian margin. Geology, 47(10), 953–957. https://doi.org/10.1130/G46778.1

Zhong, R., Brugger, J., Tomkins, A. G., Chen, Y., & Li, W. (2015). Fate of gold and base metals during metamorphic devolatilization of a pelite. Geochimica et Cosmochimica Acta, 171, 338–352. https://doi.org/10.1016/j.gca.2015.09.013

Zumsteg, C.L., Himmelberg, G.R., Karl, S.M., Haeussler, P.J. (2003). Metamorphism within the Chugach accretionary complex on southern Baranof Island, southeastern Alaska. In V. B. Sisson, S. M. Roeske, & T. L. Pavlis, Geology of a transpressional orogen developed during ridge-trench interaction along the North Pacific margin. Geological Society of America. https://doi.org/10.1130/SPE371

Appendix A Sample Index and Glossary

Table A.1 List and description of all samples collected or acquired for study.

Sample	Lat (N)	Lon (W)	Loc ID	Rock Name	Protolith	Facies	Unit	Rock Description
AG002	48.408155	123.331567	Gonzalez Bay	Law meta-cataclasite	Clastic	<BS	PPU	Chl + Law + Ep (M'mic) Pl + Qz + Amp + Ttn (Clasts) Pale blue-grey rock. Low grade cataclasite, comprising large angular to rounded clasts of predominantly sericitized plagioclase, polymineralic quartz, and amphibole. Fine-grained qz-ep matrix with separate clots of chlorite and coarser lawsonite.
AG004	48.405647	123.322	Harling Pt	Metabasalt	Basalt	<GS	PPU	Pale-green, fine-grained, mylonitized sample. Cream-white anhedral grains interpreted as surviving plagioclase phenocrysts. Outcrops as boudins in argillite matrix.
AG005	48.405647	123.322	Harling Pt	Metabasalt	Basalt	<GS	PPU	Pale-green-grey mylonitized metabasalt with anhedral deformed plagioclase, calcite grains.
AG006-1	48.4057333	123.322267	Harling Pt	Argillite	Pelite	<GS	PPU	Black carbonaceous cataclasized argillite. Microcrystalline, strongly deformed, hosts deformed boudins of green metabasalt. Framboidal pyrite. Qz-cc pre- and post- deformation veining
AG006-2	48.4057333	123.322267	Harling Pt	Arg/Mbas	Pelite/Basalt	<GS	PPU	Interfoliated argillite (see AG006-1) and pale-green metabasalt (see AG005).
AG007	48.40615	123.3224	Harling Pt	Banded chert	Chert	<GS	PPU	Thinly banded green-white chert. Fine-grained. Euhedral pyrite cubes, variably replaced by hematite.
RD13	48.40615	123.3224	Harling Pt	Banded chert	Chert	<GS	PPU	Thinly laminated green-white chert.
AG010-1	48.4670333	123.533633	Bear Mtn	Chlorite Phyllite	Pelite	GS	PPU	CM + qz + cc + sph + ccp + py + po + mu ± chl Fine-grained carbonaceous phyllite, hosting large deformed patches of microcrystalline quartz and calcite intergrowths. Within calcite patches sulfides occur as large intergrowths of, in increasing abundance, sphalerite, chalcopyrite, pyrite and pyrrhotite.
LC12	48.495593	124.259104	Leech River	Chlorite Phyllite	Basite	GS	LRC	Strongly deformed mint-green chlorite phyllite. Fine grained. ± anhedral clasts of plagioclase.
AG011-1,2,3,4 DC1702	48.5102	124.286167	Sombrio Ck	Garnet Staurolite Schist	Pelite	LA	LRC	Gt + st + bt + mu + chl + qz + pl + gr ± tur Porphyroblastic gt st bt schist with qz-rich banding (inherited feature, not gneissic banding). Garnets euhedral. Staurolite variably poikiloblastic and subhedral, locally replaced by retrograde chl + mu + qz assemblage. Samples represent variability from pelitic to psammitic layering in station outcrop.

AG012 DC1703	48.5191	124.32785	McKay Ck	Garnet andalusite staurolite schist	Pelite	A	LRC	Gt + and + st + bt + mu + chl + qz + pl + gr + tur. Andalusite and staurolite are syn-kinematic. Garnet and biotite are syn- to post-kinematic (variable texture).
AG013	48.513460	123.529612	Holmes Peak	Meta-chert	Chert	LGS	PPU	Chl + qz + mu + cc + chert + prehnite + unknown mineral, pump (?) (high 2nd order interference colours, bladed habit, colourless in PPL – amphibole hypothesized). Radiolarian chert with large fractures and cavities infilled with predominantly chl, plus minor qz and the unknown mineral. See figure.
AG014	48.51626	123.53022	Holmes Peak	Disrupted chert	Chert	<GS	PPU	Blue-grey chert, cataclasized. Hosts numerous sulfides, including pyrite, pyrrhotite, chalcopyrite, and one grain of native Au was identified by SEM.
AG019-1,2	48.4729	123.5374	Bear Mtn	Cataclasite / Chert	Clastic sediments	LGS	PPU	Pl + qz + chert (Clasts) Mu + CM + qz (Mm'ic) Fine-grained cataclasized metasedimentary rock. Carbonaceous strands are deformed around bands (up to tens of cm) of a blue chert.
AG021-1,2	48.46765	123.53078	Bear Mtn	Banded Cherts	Chert	LGS	PPU	Banded cherts, locally folded and micro-faulted. Outcrop locally exhalative (sulfur-stained). Potentially silicified tuffaceous layers.
AG023	48.50942	123.53065	Holmes Pk	Cataclasite	Clastic sediments	LGS	PPU	Sericitized pl + ksp, qz, ep, lithic fragments (quartzite, plagioclase laths). Minor zircon. Matrix chl, mu Cataclasized metasediment, clast fragments are angular and all universally fine-grained.
AG027	48.447417	123.539955	Westshore Pkwy	Mudstone	Pelite	<GS	LRC?	Fine-grained pale green carbonaceous mudstone.
AG029-1	48.518430	123.56479	Goldstream Heights	Metapsammite	Psammite	GS	LRC	Well-sorted, mature quartz-rich metasandstone (non-foliated). Graded, fining up. Beds of metapsammite up to 1 – 2 m thick.
AG029-2	48.518430	123.56479	Goldstream Heights	Argillite/psammite	Pelite/Psammite	GS	LRC	Interbedded sandstone and pelite (contact).
AG029-3	48.518430	123.56479	Goldstream Heights	Argillite	Pelite	GS	LRC	Fine-grained, black argillite. Interbedded with the metasandstone, argillite beds range 0.5 m – 2 m. No obvious metamorphic mineral growth in hand sample.
AG029-4	48.518430	123.56479	Goldstream Heights	Argillite/psammite	Pelite/Psammite	GS	LRC	Rip-up clasts (oblong fragments of argillite) suspended in overlying quartz-rich metasandstones. Interpreted as original depositional texture.
AG029-5	48.518430	123.56479	Goldstream Heights	Meta-claystone	Pelite	GS	LRC	Grey-beige friable claystone, outcrops as a discontinuous layer between beds of argillite and psammite. Thickened in hinge of folds.

AG030-1,2	48.511950	123.568563	Goldstream Heights	Metapsammite	Psammite	GS	LRC	Immature, poorly sorted lithic arenite. Subangular grains ranging < 1 mm up to 1 cm in diameter. Annealed, like the other rocks.
AG031-1,2,3	48.506065	123.533547	Highlands	Argillite	Pelite	LGS	PPU	Outcrop as black, greasy lustre argillite. Sub-phyllitic foliation that deforms around ~10 cm diameter lenses of locally coarse white quartz.
AG032-1	48.523658	123.566288	Goldstream Heights	Metabasalt	Basalt	<GS	PPU	Green, fine-grained silicified metabasalt. No visible m’mic minerals in hand sample. Isotropic texture. Tension fractures infilled with qz ± chl
AG032-2	48.522255	123.565517	Goldstream Heights	Phyllite	Pelite	GS	PPU	Phyllite, greasy to waxy lustre foliation, fine-grained, foliation deflects around quartz lenses and blocks of banded blue-green cherts.
AG033-1	48.507137	123.570363	Goldstream Heights	Argillite	Pelite	GS	LRC	Compositionally homogeneous fine-grained black argillite from bedded argillite-psammite. Isotropic texture.
AG034-1	48.493083	123.569783	Goldstream Heights	Cataclasite	Pelite/Clastic sediment	<GS	PPU	Deformed argillite with lenses of lighter sandy to silty material. Locally laminae of porous, limey material. Angular lithic fragments of quartz and feldspar.
AG036	48.504084	124.28664	Sombrio Ck	Gt-St Schist	Pelite	LA	LRC	Gt + st + bt + mu + qz + pl + gr ± chl Banded psammitic and pelitic layers. Pelite layers are exceptionally staurolite-rich, with porphyroblasts up 2 cm long. Pink garnets are 1 mm or smaller diameter.
AG038	48.505983	124.288074	Sombrio Ck	Gt-St Schist	Pelite	LA	LRC	Gt + st + bt + mu + qz + pl + gr ± chl Carbonaceous, friable porphyroblastic schist. Less quartz than adjacent outcrops, thus more friable and cleaves along foliation planes.
AG039	48.530133	124.370015	Parkinson Ck	Gt-Bt Schist	Pelite	HGS	LRC	Gt + bt + mu + qz + pl + gr + chl Below staurolite isograd. Non-friable, annealed qz and bt rich schist. Gt porphyroblasts are small (< 1mm) and pink.
AG040	48.528058	124.355352	Hwy 14 Quarry	Metapsammite	Greywacke	A	LRC	Qz + pl + fsp + bt Quartz-rich, steel grey annealed massive metapsammite. Foliation identifiable by small, discontinuous biotite component. Locally heavily veined, with en echelon tension gashes (white qz).
AG041	48.529645	124.357833	Hwy 14	Sil-Gt-St Schist	Pelite	A	LRC	Fibrolite (Fi) + gt + st + bt + ilm + gr + qz + pl + mu + chl + tur + py + po High grade schist. ‘Milky’ appearance on biotite grains in hand sample are knots of fibrolite nucleation on grains and overprinting qz-pl matrix.
AG042	48.505130	123.926822	Butler M/L	Gt-St-And Schist	Pelite	A	LRC	Andalusite (And) + gt + st + bt + ilm + gr + qz + pl + mu + chl + tur + py + po + cp

								Coarse porphyroblastic andalusite (pink, *var* chiastolite) in non-friable, qz-banded graphitic schist. Large pressure shadows around andalusite (syn-kinematic) have qz + gr + chl + mu + gt paragenesis. Andalusite locally overgrows staurolite, garnet and biotite. Garnet is euhedral, staurolite is subhedral and poikiloblastic. Strong shear fabric, collected from Bear Creek Sheer Zone near Leech River Fault.
AG043	48.506878	123.937737	Butler M/L	Bt-Schist	Pelite/Psammite	LA	LRC	Qz + pl + bt Low-grade brown alteration replaces unknown mineral, outcrop is iron-stained / oxidized in appearance. No large porphyroblasts, more psammitic layer. No graphite.
AG044	48.50806503	123.944702	Walker M/L Quarry	Meta-tonalite	Tonalite	LA	WCI	Pl + qz + bt Sill of medium-grained, orange iron-stained tonalite on strike with larger outcrop of Walker Creek Intrusion sill. ~1m width at largest point in this quarry outcrop. Hosted in psammitic layers, no obvious increase in grade at margins identifiable (no p/blasts).
AG046-1	48.51343498	123.938898	Jordan M/L	Meta-tonalite	Tonalite	LA	WCI	Pl + qz + bt ± gt + xenoliths of foliated bt Sample of large grey-white sill >10 m wide, hosting fragments of foliated bt interpreted as xenoliths (after Groome et al., 2003). Locally, may be garnet-bearing but uncommon.
AG046-2, 3	48.51343498	123.938898	Jordan M/L	Gt-St-Bt Schist	Pelite/Psammite	LA	LRC	Gt + st + bt + mu + qz + pl + ilm + tur + py + po + cp Layered schist/psammite. Porphyroblasts of st restricted to pelitic layers. Gt occurs more commonly in pelitic layers but may also be observed in qz-rich bands. Sub-samples reflect pelite-psammite variability. Cohesive, non-friable schist. Porphyroblast size and abundance comparable with typical schists despite proximity to a large WCI sill.
AG047	48.51941999	123.938567	Jordan M/L	And-Gt-St Schist	Pelite	LA	LRC	And (retro. mu + chl + qz) + gt + st + bt + pl + qz + gr + mu + po Schist bears andalusite that is mostly retrogressed to a mu + chl + qz assemblage that pseudomorphs original grain shape. Staurolite is poikiloblastic at the rim but with few inclusions at the core. Staurolite rims show graphitic inclusion trails, like biotite typically does. Staurolite also hosts inclusion of pyrrhotite.
AG048	48.521983	123.939201	Jordan M/L	Gt-St Schist	Pelite	LA	LRC	Gt + st + bt + mu + qz + pl + gr ± chl Very similar to AG047, but slightly more quartz-rich and lacking andalusite. Difference between the two samples is interpreted as a change in protolith chemistry rather than change in metamorphic grade.

AG049-1	48.538678	123.950852	Jordan Riverbed	Spotted St-Gt-Bt Hornfels	Pelite	LA	LRC	Gt + st + bt + gr + qz + po + cp + ilm Spotted, non-foliated sample, retrieved from riverbed. Matrix is fine-grained quartz and graphite. Locally, crescent or irregular oblong-shaped areas of matrix comprise greater density of fine graphite particles. Porphyroblasts of garnet are euhedral, and rarely host inclusions of ilmenite and pyrrhotite. Poikiloblastic, porphyroblastic ilmenite laths also observed. Staurolite porphyroblasts are poikiloblastic, and subhedral to anhedral, with ragged rims suggesting dis'eqm. Pyrrhotite occurs as small, anhedral grains, and as peculiar groups of spherules hosted in biotite grains. Sub-linear cross-cutting quartz + biotite veins host most of the sulfide, but pyrrhotite also hosted in matrix biotite. Absence of foliation attributed to the qz-dominant matrix, but it is speculated there must be a nearby sill.
AG049-2	48.538678	123.950852	Jordan Riverbed	Meta-greywacke	Psammite	LA	LRC	Fine-to-medium-grained, non-foliated sample dominated by qz + feldspar + possibly lithic fragments? Small black grains interpreted as biotite but could possible be tourmaline. Present as layers within the AG049-1 lithology.
AG050	48.54194803	123.951492	Jordan M/L	Bt Schist	Pelite	GS	LRC	Bt + qz + pl + CM In < 0.5 km from AG049, sample is from below both garnet and staurolite isograd. Biotite is observable with hand lens and defines the foliation. Lack of p/blasts could also be attributed to composition differences? Small, oblong cavities in sample are lined with fine-grained brown mineral (oxide?).
AG051	48.55077803	123.945366	Jordan M/L	Bt Schist	Pelite	GS	LRC	Bt + qz + pl + CM + mu Very similar to AG050. Interpreted as below st & gt isograd. Biotite present, visible with hand lens, but fine-grained.
AG053	48.54221399	123.93296	Valentine Mtn	Bt Schist	Pelite	GS	LRC	Bt + qz + CM + mu Still classified as schist, though lustre and nature of foliation is verging phyllitic. Nonetheless, visible biotite grains distinguish sample from comparable phyllites.
AG054	48.56024698	123.935137	Jordan M/L	Bt Schist	Pelite	GS	LRC	Bt + qz + mu + CM Schistose foliation; biotite is fine-grained but visible in hand sample. No porphyroblasts. Layered carbonaceous pelite / psammite.
AG055-1 AG055-2	48.582914	123.939232	Williams M/L	Magnetite Chlorite Schist	Basite	GS	TCM	Mag + chl + ep-czo + pl + mu + qz Porphyroblastic euhedral magnetite, and locally porphyroblastic epidote. Matrix includes chlorite, epidote, quartz, plagioclase and muscovite. Chlorite defines the foliation. Magnetite p/blasts overprint the foliation (post-kinematic), and hosts inclusions of epidote and quartz. In outcrop, appears as a pale green schist

								with locally ‘facoidal’ appearance. Locally, multi-cm cavities are present partially infilled by epidote and an unidentified black mineral.
AG056	48.58234797	123.953458	Williams M/L	Carbonaceous phyllite	Pelite (+ sandy lenses)	GS	LRC	Carbonaceous phyllite. No visible micas. Phyllitic sheen. Small (< 2-3 cm) sandy lenses. Strands of carbon-rich material deform around the sandy lenses. Below the biotite isograd.
AG057	48.583519	123.964779	Williams M/L	Metapsammite	Psammite	GS	LRC	Sandier protolith than AG056. Locally CM-bearing in deformed tendrils. Lenses of ‘porous’ quartz (late-stage mineral dissolution leaving cavity?).
AG059	48.5086590	123.901792	Tripp Ck spur	Amphibolite	Basite	A	TCM	Amp (~hornblende) + pl + qz + bt + ilm + po + chl Medium-grained, foliated amphibolite. Amphibole is sub-aligned to foliation direction, locally zoned (actinolitic core, hornblende rim). Locally replaced by chlorite. Small ilmenite laths run parallel to the foliation and are included within most minerals (amphibole, biotite).
AG061	48.513344	123.852867	Valentine M/L	Gt-St-Bt Schist	Pelite	LA	LRC	Typical LRC schist, above st and gt isograd. Foliated, non-friable, qz-banding.
AG062	48.51755099	123.85749	Valentine M/L	Amphibolite	Basite	A	TCM	Foliated metabasite. Outcrops as a green-white amphibole schist.
AG063	48.521439	123.860597	Valentine M/L	Amphibolite	Basite	A	TCM	Same as AG063, but also hosts bands of very fine-grained pink garnet (grains not discernable by hand lens, but observable in thin section).
AG065	48.529602	123.88981	Valentine M/L	Gt-Bt Schist	Pelite	A	LRC	Gt + bt + mu + qz + pl Schistose foliation, verging gneissic texture.
AG066-1	48.53184097	123.895149	Valentine M/L	Gt-Bt Schist	Pelite	A	LRC	Gt + bt + mu + qz + pl Schistose foliation, verging gneissic texture.
AG066-2	48.53184097	123.895149	Valentine M/L	Amphibole Schist	Basite	A	TCM	Amp + pl + qz + chl + bt? Green, foliated amphibole schist. Outcrops as narrow (< 1 m) layers in successions of pelite/psammite.
AG067	48.532523	123.899356	Valentine M/L	Gt-St-Bt Schist	Pelite	A	LRC	Gt + st + bt + qz + pl + gr ± retrogressed and
AG068	48.531211	123.901679	Valentine M/L	Foliated Amphibolite	Basite	A	TCM	Amp + pl + qz + chl + bt ± gt Foliated/banded amphibolite (pl rich / amp rich layers)
AG069-1	48.53057999	123.903505	Valentine M/L	Metapsammite	Psammite	A	LRC	Foliated metapsammite. Bt + mu + qz. Metagraywacke.
AG069-2,3	48.53057999	123.903505	Valentine M/L	Gt Amphibolite	Basite	A	TCM	Amp + ep + qz + chl + bt + gt + pl + ilm + po + cp + cc

								Foliated amphibolite, locally with pink garnetite bands comprising very fine-grained garnets. Locally, zoned garnets occur outside of the banding as euhedral grains up to 0.5 mm in the interstices between amp laths. Modal plagioclase is significantly lower than typical amphibolites in TCM (less pl than qz, thus technically does not meet definition of true amphibolite).
AG070-1, 2	48.527609	123.889213	Valentine M/L	Foliated Metabasite	Basite	A	TCM	Amp + ep + qz + chl + ilm + po + cp Medium grained, foliated metabasite. No plagioclase, only quartz comprising matrix. Unclear if epidote is a retrograde replacement of plagioclase, or if epidote is prograde. Locally hosts garnetite banding, as observed in AG069. Outcrop is strongly exhalative, with sulfurous staining and porosity suggesting late-stage mineral dissolution.
AG071	48.51874701	123.864084	Valentine M/L	Amphibolite	Basite	A	TCM	Coarse, banded amphibolite. Similar to AG059.
AG072	48.507594	123.905999	Tripp Ck Spur	Gt-St-And Schist	Pelite	A	LRC	And + st + gt + bt + qz + pl + chl + ilm + ep + gr Another exception andalusite outcrop, exhibiting andalusite grains that have been extended into boudins in linear tracks that extend up to 50 cm – 1 m. Andalusite is variably retrogressed to mu + chl + qz. Where unaltered, andalusite is *var.* chiastolite, with a well-defined graphitic cross. Unlike AG042, there is very little sulfide in this outcrop, and unaltered andalusite hosts inclusions of epidote and ilmenite, but no sulfides.
AG073-1	48.50838597	123.93377	Butler M/L Spur	And-Gt-St Schist	Pelite	A	LRC	St + gt + and (retrogressed) + bt + mu + qz + pl + gr
AG073-2	48.50838597	123.93377	Butler M/L Spur	Bt-Schist	Psammite	A	LRC	Bt + qz + fsp Thin (< 2 mm) bands of planar biotite occur rhythmically (intervals of 0.5 – 1 cm) in a psammitic (fsp + qz) rich matrix. Could possibly be a meta-intrusive (tonalitic), but has greater modal biotite than any other observed sill. Collected in first roadside outcrop north of LRF.
AG074-1	48.50122799	124.069887	North M/L	Mylonitized Meta-Tuff	Tuff	A	LRC	Mylonitized (extreme shear fabric) silicified sample, interpreted as a tuff. Multi-colour green-blue-pink matrix. Small (< 1mm) diameter black mineral grains (hypothesize amp, or tur—no mineral habit to check).
AG074-2	48.50122799	124.069887	North M/L	St-Gt Schist	Pelite	A	LRC	Gt + bt + st + pl + qz + ilm + chl + gr Exceptional sample. Garnet porphyroblasts are largest recorded in terrane (up to 1cm diameter) and are a distinct orange-red colour. Garnets are subhedral and poikiloblastic (inclusions

								predominantly qz, ilm and chl). Foliation is chaotic and poorly developed, and there are large selvages of pl and qz. Minor graphite present, much less than a typical LRC schist. No aluminosilicate minerals.
AG075	48.50693598	124.077187	North M/L	Gt-St Schist	Pelite	A	LRC	Gt + st + bt + pl + qz + gr Typical LRC schist, similar to AG011.
AG077	48.50816402	124.086807	North M/L Quarry Pit	Gt-Bt Schist	Pelite	A	LRC	Gt + bt + qz + pl Particularly qz-rich schist with blocky, sulfidic-stained appearance in outcrop.
AG078-1,2	48.51473903	124.088874	San Juan M/L Bridge Int.	Gt-St Schist	Pelite/Psammite	A	LRC	Interfoliated metapsammite and metapelites. Pelitic layers have gt-st rich horizons.
AG079	48.51202003	124.097859	San Juan M/L	Amphibolite Schist	Basite	A	TCM	Amp + pl + chl (?) Foliated, dark green amphibole schist.
AG080	48.51258002	124.118506	San Juan M/L near gate	Sil-Gt-St Schist	Pelite	A	LRC	Sil (*var.* fib) + st + gt + bt + mu + qz + pl + ilm + po + gr Outcrop looks very similar to Sombrio (AG011) outcrop, but biotite is coarser and has a 'milky' appearance on flake surfaces—confirmed as fibrolite in thin section. Less sulfide present than comparable andalusite-bearing schists.
AG081	48.50469399	124.272412	Sombrio Spur	Gt-St Schist	Pelite	A	LRC	Gt + st + bt + qz + pl + mu + gr Typical LRC Schist, similar to AG011 (~ on strike with this outcrop)
AG082	48.58819703	124.344979	Pacific Marine Rd. (Fairy Lake)	Cataclasite (?)	Sediment	<GS	PPU	Fine-grained blue rock. Convoluted matrix, no penetrative deformation/foliation. Small clastic fragments, hence classification as cataclasite. Similar to AG002.
AG084	48.58866801	124.191478	Bear M/L	Phyllite	Pelite	GS	LRC	Interfoliated phyllitic/psammitic sample. Phyllitic sections are carbonaceous.
AG085-1,2,3	48.58366703	124.153852	Bear M/L	Phyllite / Metasandstone	Pelite/Psammite	GS	LRC	Layered carbonaceous phyllites and qz-rich psammites. Distinct black, variable thickness (max. < 30 cm) black horizon comprises friable organic material.
AG086	48.57840101	124.129893	Bear M/L	Phyllite	Pelite	GS	LRC	Fissile, carbonaceous, steel-grey phyllite. Locally hosts porous, 'limey' quartz lenses as observed on Williams M/L (AG056,57)
AG088	48.58249197	124.088932	Bear M/L	Phyllite	Pelite	GS	LRC	Grey carbonaceous phyllite, with lenticular sandier layers. Brown oxide (hematite?) hypothesized to replace sulfide grains in matrix.
AG089-1	48.589026	124.536036	Camper M/L	Metabasalt	Basalt	<GS	PPU	Grey-green silicified(?) metabasalt. Matrix alteration is too fine-grained to identify any minerals—possibly chl, or a sub-greenschist facies clay mineral. Grains of py and pl are visible

								in matrix. Outcrop similar to the metabasalt observed at Harling Point (AG006).
AG089-2	48.589026	124.536036	Camper M/L	Cataclasite	Carbonaceous sediments	<GS	PPU	Py + OM + chert + lithic fragments (pl/qz/variable) Carbonaceous cataclasite hosting significant modal percentage (>2%) pyrite as fine-grained subhedral to euhedral grains. Dark strands of CM deform around blocks of microcrystalline chert.
DC0514	48.5888399	124.554442	Camper M/L	Cataclasite	Carbonaceous sediments	<GS	PPU	See AG089-2, same lithology.
AG093-1	48.59536297	124.085323	Lens M/L	Meta-ultramafic	Ultramafic	GS	PPU	Large (several meter wide) dark green to black block hosted in metasedimentary matrix. Margins have a greasy, facoidal texture (likely chlorite?). Carbonate has pseudomorphed a pre-existing mineral (hypothesized to by orthopyroxene). Euhedral to subhedral spinel grains occur throughout, locally rimmed by the carbonate. Serpentinized.
AG093-2	48.59536297	124.085323	Lens M/L	Clastic Phyllite	Pelite / Clastic	GS	PPU	Grey, variably pelitic-sandy metasedimentary unit. Foliated, but not penetratively deformed as with LRC phyllites.
AG093-3	48.59536297	124.085323	Lens M/L	Metasomatized Margin (?)		GS	PPU	Soft, pale-white layer at the margin of the meta-ultramafic block. Not readily sampled since it is friable and crumbles when hit. Possibly a metasomatized margin around the ultramafic olistolith.
AG093-4	48.59536297	124.085323	Lens M/L	Meta-ultramafic	Ultramafic	GS	PPU	Another block (several meter wide) dark green-blue to black meta-ultramafic hosted in metasedimentary matrix. Margins have a greasy, facoidal texture (likely chlorite?). Sample is serpentinized. Less secondary carbonate than AG093-1. Possibly phlogopite, or similar magnesium mica.
AG094	48.5964520	124.07319	Lens M/L	Phyllite	Pelite	GS	PPU	Carbonaceous phyllite.
AG095-1	48.59877298	124.064628	Lens M/L	Phyllite	Pelite	GS	PPU	Carbonaceous phyllite with bands of qz-rich, sandier unit. Foliation is convoluted, locally disrupted.
AG095-2	48.59877298	124.064628	Lens M/L	Metabasalt	Basalt	GS	PPU	Chl + pl ± ep Fine-grained, homogenous block of pale-green metabasalt. Not ‘silicified’ as observed elsewhere in the PPU, and does not host any clasts of plagioclase or visible sulfide.
AG096	48.59864398	124.063487	Lens M/L	Exhalative Metasediment	Pelite	GS	PPU	Black sub-phyllitic metasediment with large (> 1cm wide) white quartz veins. Much of outcrop appears ‘exhalative’ verging gossan, with sulfidic and iron staining colouring weathered surfaces red, orange and brown. Locally, veining is extreme and a fine-grained red mineral appears alongside quartz in veining.

AG097-1	48.59555801	124.088323	Lens M/L	Meta-ultramafic	Ultramafic	GS	PPU	Serpentinized ultramafic. Euhedral to subhedral spinel. Unknown mineral (opx?) replaced fully by carbonate (possibly calcite or magnesite). Typical meshed web serpentine texture, with finer-grained spinels precipitating in fractures. Interpreted as an olistolith from overlying Wrangellia rocks.
AG097-2,3	48.59555801	124.088323	Lens M/L	Phyllite	Pelite	GS	PPU	Phyllite with lenses and lenticular layers of a sandier, coarser material present. Carbonaceous phyllitic foliation deforms around these blocks. Small, high-relief, colourless PPL clasts are rotated and deformed in the pelitic matrix (hyp. Titanite).
AG098	48.57659203	124.193481	Red Creek M/L	Phyllite	Pelite	GS	LRC	Carbonaceous phyllite hosting regular lenses of ‘porous’ quartz.
AG099	48.57282998	124.201225	Red Creek M/L	Phyllite	Pelite	GS	LRC	Phyllite, with a quartz-rich pelitic protolith. Less fissile than nearby phyllites. Still no m’mic minerals identifiable with hand lens. CM inferred by dark colour of rock.
AG100	48.57260501	124.214887	Mosquito M/L	Phyllite	Pelite	GS	LRC	Qz phyllite. Crenulated phyllitic foliation with thin quartz bands. Minor pyrite.
AG101-1,2	48.57912303	124.241639	Red Creek M/L	Phyllite / Metapsammite	Pelite / Psammite	GS	LRC	Layered pelitic and psammitic bands. Exceptionally carbonaceous phyllite. Crenulated phyllitic foliation. Psammitic bands are uniform, fine-grained, grey, quartz-rich.
AG103-1,2,3	48.57082704	124.137924	Alan M/L Quarry	Phyllite / Metapsammite	Pelite / Psammite	GS	LRC	Large meta-psammitic bluff (> 10 m wide exposed). Metapsammite is fine-grained, ‘steel-grey’ colour, similar to the Valentine Mountain meta-sandstone (see also AG040 metasandstone). Interpreted on the BC geologic map as a large continuous TTG sill, but adjacent carbonaceous phyllites show no development of contact metamorphism mineral assemblages. No indication of a change in grade near the margins.
AG104	48.574876	124.137293	Alan M/L	Phyllite	Pelite	GS	LRC	Carbonaceous phyllite. Comparable to AG086.
AG105-1	48.554828	124.411361	Port Renfrew	Phyllite	Pelite	GS	LRC	Dark black carbonaceous phyllite. Elongate ‘stringers’ of pyrite are deformed parallel to the foliation and stretch for up to 1 cm. Located > 2 meters away from the contact margin. No metamorphic minerals (contact metamorphism or otherwise) present. Further from the contact, lenticular layers of psammitic rock exhibit en echelon tension gashes.
AG105-2	48.554828	124.411361	Port Renfrew	Metasomatized zone	Pelite	GS	LRC	Spotted rock. Calcite has fully replaced an unknown mineral (hyp. Cordierite) in a contact zone within 2 meters of the tonalitic intrusion. Present assemblage is dominantly chlorite and calcite. Locally, veins hosting coarse calcite and siderite (?) occur. The metasomatized zone continues into the intrusion,

								characterized in hand sample by the brown, weathered iron carbonate.
AG105-3	48.554828	124.411361	Port Renfrew	Tonalite	Tonalite	GS	WCI	A plagioclase and quartz-dominated, medium to coarse grained rock. Occurs as two sills bracketing the central metamafic outcrop. Boundary with the metamafic is gradational.
AG105-4	48.554828	124.411361	Port Renfrew	Metabasite	Basite	GS	TCM	Fine-grained, pale to dark green metabasite. Hosts pyrrhotite and chalcopyrite as anhedral grains throughout matrix. Mineralogy not readily identifiable in hand sample, chl + ep inferred by colour.
AG106	48.518574	124.089944	North M/L spur	Gneiss	Psammite		LRC	Qz + bt + mu + pl Paragneiss exhibiting biotite & felsic segregations. Dominantly felsic minerals (biotite is subsidiary). Pegmatitic veins of quartz, muscovite, schorl (tur), and an unidentified pink mineral (lepidolite?) occur throughout.
AG108	48.52384304	124.085291	North M/L spur	Gt Bt Gneiss	Psammite	A	LRC	Gt + bt + qz + mu + pl + ilm + gr (minor) + zr (minor) Garnet (~1mm diameter) occur as subhedral grains, commonly with inclusions (mainly ilmenite and silicates like qz), though too few inclusions to be classified as ‘poikiloblastic’.
AG109-1,2	48.52372502	124.083864	North M/L spur near Kludahk trailhead	Gt Bt Schist	Pelite	A	LRC	Gt + bt + qz + pl + mu + ilm + gr + zr + tur Schist verging gneissic texture. Garnet porphyroblasts (up to ~1 mm) host ilmenite, silicates, and rarely pyrrhotite. Biotite shows graphitic inclusion trails generally parallel to foliation, although some have been rotated. Overgrowths on biotite without these inclusions suggest biotite continued to grow post-deformation.
AG110	48.52372502	124.083864	North M/L spur near Kludahk trailhead	Gt Bt Gneiss	Psammite	A	LRC	Similar to AG108. Psammitic protolith. Relatively few garnet porphyroblasts.
AG112	48.49940903	124.037388	Jordan M/L near Diversion Res.	Chl Amp Schist	Basite	A	TCM	Chl + pl + amp Fine-grained, foliated metabasite. Small black porphyroblasts in matrix are likely amphibole.
AG113	48.49834403	124.048472	Jordan M/L	Bt Schist	Pelite	HGS	LRC	Bt + qz + pl + CM ± gt (few p/blasts limited to thin horizons)
AG114-1	48.50897304	123.950696	Walker M/L	Gt-St Schist	Pelite	GS	LRC	Gt + st + bt + mu + pl + qz + ilm + gr + tur
AG114-2	48.50897304	123.950696	Walker M/L	Foliated Meta-Tonalite	Tonalite	A	WCI	Qz + pl + bt + mu Plagioclase-rich tonalite. Biotite defines foliation.

AG115	48.50873399	123.955574	Walker M/L	Gt-St Schist	Pelite	A	LRC	Gt + st + bt + qz + pl + mu + gr Fissile biotite schist. Less qz-rich than other LRC schists.
AG116-1	48.512232	123.96795	Walker M/L	Gt-Bt Schist	Pelite	A	LRC	Gt + st + bt + mu + qz + pl + gr + ilm Schist verging gneissic texture. Irregular felsic bands (pl + qz).
AG116-2	48.512232	123.967948	Walker M/L	Gt-Tur Schist	Pelite	A	LRC	Tur (schorl) + gt + mu + bt + qz Tourmaline-rich muscovite biotite schist. Layers range from fine-grained tur schists to coarse-grained pegmatitic tourmaline in selvages of plagioclase.
AG117	48.521123	123.96985	Walker M/L	Pegmatite		A	LRC	Qz + mu + coarse pink mineral (spodumene?) Pegmatitic vein run parallel to foliation. Generally hosted in schists, and proximal to outcrops of the Tripp Creek metabasite.
AG118	48.522488	123.97115	Walker M/L	Gt-St-Bt Schist	Pelite	A	LRC	Gt + st + bt + mu + qz + pl + gr. Tourmaline-rich horizons also present.
AG119	48.525034	123.970637	Walker M/L	Gt Amphibolite	Basite	A	TCM	Foliated fine-grained amphibolite. Locally, thin pink garnetite banding (as seen in AG069) occur.
AG120-1,2	48.53168498	123.993086	Walker M/L	Gt-St Gneiss	Pelite / Psammite	A	LRC	Gt + st + bt + mu + qz + pl + gr ± chl (retro) Interfoliated qz-rich psammitic gneiss and pelitic gt-st-bt gneiss.
AG120-3	48.53168498	123.993086	Walker M/L	Meta-quartzite	Quartzite	A	LRC	Extremely hard, white rock with subsidiary fine-grained black crystals (unidentified, too fine-grained). Interpreted as a metamorphosed quartzite, but could also be a quartz-rich meta-granitoid.
AG121-1	48.530995	123.98749	Walker M/L	Bt Gneiss	CM psammite	A	LRC	Bt + gr + qz + minor pl + mu + trace zr Biotite and graphite occur together in bands separated by quartz-rich bands with subsidiary feldspar. No garnet or staurolite porphyroblasts observed.
AG121-2	48.530995	123.98749	Walker M/L	Foliated Amphibolite	Basite	A	TCM	Fine-grained foliated amphibolite occurring as ~1 – 2 m wide layers within the Bt gneiss. Amphibolite is dark green, and shows relatively small proportion of plagioclase and quartz (amp-rich).
AG122	48.53168498	123.993086	Walker M/L	Bt Gneiss	Psammite	A	LRC	Simple qz-bt-fsp gneiss. No porphyroblasts observed w/ hand lens.
AG123	48.52707803	123.944291	Jordan M/L spur	Metagreywacke	Greywacke	A	LRC	Interpreted as part of the Valentine mountain metasandstone. Qz-rich, grey rock. Comparable to AG040.
AG127	48.51958101	123.883884	Valentine Mtn	Gt-St-And Schist	Pelite	LA	LRC	And + gt + st + bt + qz + gr + pl + mu + ilm + po Dark grey, blocky schist outcropping adjacent to a narrow (~1 m) sill of Walker Creek Intrusion (white tonalite). Andalusite mostly retrogressed to mu + qz ± chl. Staurolite may show

								graphitic trails in the rim, suggesting syn-kinematic growth. Garnets are subhedral, appearing to have been mechanically fractured during deformation, and may occasionally host inclusions of ilmenite.
AG128	48.51944799	123.886272	Valentine Mtn	Quartz vein		A	LRC	Large, coarsely crystalline quartz vein hosted in ~ AG127. Quartz has sulfidic staining and may host sulfide. Collected for bulk rock chalcophile analysis.
AG129-1, 2	48.50683297	123.820986	West Leech CRD gate	Mylonite	Psammite		LRC	Mylonitized metapsammite. Fine-grained, highly sheared qz + bt. Rafts of amphibole occur near margin with mylonitized metabasite. Taken from the Bear Creek shear zone area near the LRF.
AG129-3	48.50683297	123.820986	West Leech CRD gate	Mylonite	Basite	A	TCM	Sheared amp-rich metabasite. Amp is generally fine-grained, though a few significantly larger grains persist and are encapsulated in the deformed amp + qz matrix. Locally, cc + qz veins run parallel to direction of foliation.
AG130	48.53125398	123.886407	Valentine M/L spur	Gt Bt Schist	Pelite	A	LRC	Typical LRC gt-bt schist. Graphitic. Quartz layers here are highly continuous, not like the gneissic segregations observed to the west.
AG131	48.50777904	123.825193	Butler M/L spur	Bt Schist	Pelite	GS	LRC	Biotite schist. No other porphyroblasts observed, suggesting below gt and st isograds.
AG132	48.50812697	123.847576	Butler M/L	Gt-St-Bt Schist	Pelite	GS	LRC	Gt + st porphyroblasts present. Brackets the gt and st-in isograds with AG131 over relatively short distance.
AG133	48.50957704	123.865078	Butler M/L	Gt-Bt Schist	Pelite	High GS	LRC	Gt porphyroblasts, but no staurolite. Sample is qz-rich and has relatively few porphyroblasts. The absence of staurolite is interpreted as a compositional control rather than a change in grade.
AG134	48.551448	123.933719	Jordan M/L North	Amp Chl Schist	Basite	High GS	TCM	Fine-grained, foliated green metabasite. A few black, elongate minerals identified as ~ hornblende (amp).
AG135	48.54872698	123.923188	East Jordan M/L	Carbonaceous Phyllite	Pelite	GS	LRC	Grey-black carbonaceous phyllite. Pyrite (possibly oxidized / replaced) stringers occur as 0.1 cm to 1cm lineations parallel to the phyllitic foliation.
AG136-1,2,3	48.572061	123.889522	East Jordan M/L	Meta-tuff	Volcanic	GS	LRC	Fine-grained, green-orange-beige-red layered rock. Phyllitic foliation. Outcrop has clayey texture. Significant variability in outcrop (which is small, only a few meters exposed at the side of a roadcut). Collected for WR analysis, or possible future zircon work.
AG137	48.54880401	123.911461	Jordan M/L	Amp Schist	Basite	GS	TCM	Amp (actinolite) + pl + ep + ilm + po + cp + qz + chl Metabasite with a distinct schistose foliation. When viewing the foliation plane, elongate amp crystals are aligned with the plane.

								Locally, sections of extremely fine-grained foliated chlorite, amphibole, and epidote occur as sub-cm blocks within coarser matrix. Possibly xenoliths caught up in the protolith?
AG138	48.507647	123.56333	Goldstream Heights	Cataclasite	Clastic sediments	GS	PPU	Medium grain clastic rock. Fragments of quartz, plagioclase, and lithics (?) in a carbonaceous matrix. Sample collected near boundary between LRC segment at Goldstream heights (characterized by preserved bedding, sedimentary features) and PPU (chaotic rock matrix with poorly developed foliation).
AG139	48.5913315	124.153618	Lens M/L	Phyllite	Pelite	<GS	LRC	Carbonaceous phyllite collected for potential RSCM analysis.
AG140-1,2	48.5937373	124.127968	Lens M/L	Phyllite	Pelite	GS	LRC	Carbonaceous phyllite interfoliated with psammitic layers. Collected for potential RSCM analysis.
AG141	48.59434	124.122687	Lens M/L	Metapsammite	Psammite	GS	LRC?	Meta-sandstone, possible with lithic fragments (coarser, more immature protolith). Classified as LRC, although it is ambiguous and near the contact with PPU metasediments.
AG142	48.5900773	124.096930	Lens M/L	Metapsammite	Psammite	GS	LRC?	Psammitic layer interfoliated with carbonaceous phyllite.
AG143	48.59148833	124.074178	Lens M/L	Phyllite	Pelite	GS	LRC	Crenulated carbonaceous phyllite. RSCM sample candidate.
AG144	48.58731333	124.362652	Pacific Marine Rd	Pebbly Tectonite	Clastic sediment	GS	PPU	Clastic metasediment. Dark, carbonaceous matrix with pebbly fragments. For future geochron work.

Note: LRC = Leech Rive Complex; PPU = Pandora Peak Unit; TCM = Tripp Creek Metabasite; WCI = Walker Creek Intrusion
Sample IDs collected by AG = A. Geen; DC/LC = D. Canil; RD = R. D’Souza; MVDB = M. van den Berghes (Hons. Thesis)
Sample locations in decimal degrees (locally converted from northing / eastings UTM Zone 10, and from DD MM SS.xy where necessary)

Table A.2 Representative samples of sulfide texture and identity across metamorphic grade.

	°C					Sulfides					
Sample	Est T	Facies	Unit	Rock	Host	Py	Po	Cpy	Sph	Otr*	Texture
DC0514	229	<BS	PPU	Tectonite							
AG089-1	235	<BS	PPU	Metabasalt	mx	py	-	-	-	-	Subhedral cubic py Framboidal amalgamations (± py overgrowth)
AG006-1	290	<BS	PPU	Argillite	mx	py	po	-	-	-	Disseminated anhedral grains
AG007	290	<BS	PPU	Chert	mx	py	-	cpy	-	-	Framboidal py Anhedral elongate py with blebby cpy
AG014	301	BS*	PPU	Chert	mx	py	-	-	-	-	Euhedral/Anhedral py
AG010	306	GS	PPU	Argillite	mx	-	po	cpy	-	Au	Disseminated po in lithic fragments Large, anhedral, porous po with subsidiary cpy Discrete < 2 um native Au grain in po
AG030-2	319	GS	LRC	Argillite	mx	-	po	-	sph	-	Framboids and spheroidal porous po, locally intergrown with sph
					cc lens	-	po	cpy	sph	-	Coarse anhedral po with intergrown cpy and blebby sph 2 generations: irregular incl-rich, homogenous areas
AG105-1	399	GS	LRC	Phyllite	mx	py	-	cpy	-	-	Subrounded grains of porous py hosted in qz cobbles Small py spherules (possibly framboids) in argillite mx
AG105-4	399	GS	TCM	Metabasalt	mx	py	-	cpy	-	-	Deformed fol-parallel stringers of py with cpy blebs
AG100	500	GS	LRC	Bt Phyllite	mx	py	po	-	-	-	Disseminated py in f.g. matrix & veinlets of po
AG137	511	A	TCM	Amp Schist	mx	py	-	-	-	-	Fine grained elongate py, like AG105-1
AG069-3	544	A	TCM	Gt Amph	mx	py	po	cpy	-	-	Coarse, fractured po with marginal py intergrowth Py locally as unfractured grains within fractured po Round cpy grains at margin of po or locally intergrown
					amp	-	po	-	-	-	Small, discrete rounded grain in actinolitic core of amp

AG011	566	A	LRC	Schist	mx	-	po	cpy	-	bn	Med. grain po in interstices of amp & gt grains Oxidized rims with bornite (bn) margins
AG012	555	A	LRC	Schist	mx	py	-	cpy	-	Ni-Cu S	Ni-Cu-Co sulfide laths precipitated on cc cleavage Py and cpy occur as anhedral porous grains
					st	py	po	cpy	-	-	Small, round anhedral composite po-cpy grains Py as anhedral, rounded grains
					gt	-	po	-	-	-	Small, round anhedral po grains
AG042	563	A	LRC	Schist	mx	py	-	cpy	-	-	Thin stringers pyrite parallel foliation around p/blasts
					st	py	po	cpy	-	-	Anhedral py grain, sometimes encapsulated in ilm
					gt	-	po	-	-	-	Anhedral, irregular, and small po inclusions
					and	-	-	-	-	-	And strongly retrogressed
AG046-2	556	A	LRC	Schist	mx	py	po	cpy	-	-	Deformed py cubes within foliation
					st	-	po	cpy	-	-	Small anhedral inclusions
					gt	-	po	-	-	-	Small anhedral inclusions
					and	py	po	cpy	-	-	Angular, oxide rimmed po grains; smooth, rounded po grains, incl-rich and -poor py & po, and significant variation in size (<10um to 200um)
AG049-1	596	A	LRC	Hornfels	mx	py	po	cpy	-	-	Anhedral to rounded grains in interstices of qz and bt
					st	-	-	-	-	-	
					gt	-	po	cpy	-	-	Med. (up to 150 um) anhedral po and cpy intergrowths
					mx	-	po	cpy	-	-	Spheroidal & anhedral masses of po in qz veins Among anhedral masses at least 2 generations: incl-rich cores with silicate inclusions in rims, po overgrown.
					bt	-	po	cpy	-	-	Spheroidal po hosted in post-deformation bt grains
					st	-	-	-	-	-	St strongly retrogressed – no sulfides
					gt	-	po	cpy	-	-	Anhedral, irregularly shaped po ± cpy intergrowths
					ilm	-	po	-	-	-	Oblong anhedral laths of po in poikiloblastic ilm

*Other: includes rare sulfides and affiliated minerals of relevance. Abbrv: BS = Blueschist, GS = Greenschist, A = Amphibolite.

Table A.3 Glossary of mineral abbreviations used in-text, after Whitney & Evans (2010).

	Symbol Abb.	**Mineral Name**	**Ideal Formula**
Chapter 3 – Sulfides	Py	Pyrite	FeS_2
	Po	Pyrrhotite	$Fe_{1-x}S$
	Ccp	Chalcopyrite	$CuFeS_2$
	Sp	Sphalerite	ZnS
	Bn	Bornite	Cu_5FeS_4
	Apy	Arsenopyrite	FeAsS
Chapter 2 & 3 – Silicates, oxides and carbonates	Ms	Muscovite	Group
	Chl	Chlorite	Group
	Bt	Biotite	Group
	Ilm	Ilmenite	$FeTiO_3$
	Gt	Garnet	$(Mg,Fe,Mn,Ca)_3Al_2Si_3O_{12}$
	Fsp	Feldspar	Group
	Pl	Plagioclase feldspar	Group
	Ab	Albite	$NaAlSi_3O_8$
	Lws	Lawsonite	$CaAl_2Si_2O_7(OH)_2 \cdot H_2O$
	Prh	Prehnite	$Ca_2Al(AlSi_3O_{10})$
	Pmp	Pumpellyite	$Ca_2Al_2Si_3O_{10}(OH)_2$
	Ep	Epidote	Group
	Gr	Graphite	C
	CM*	Carbonaceous matter	Group
	And	Andalusite	Al_2SiO_5
	Sil	Sillimanite	Al_2SiO_5
	Crd	Cordierite	$(Mg,Fe,Mn)_2Al_3(AlSi_5O_{18})$
	Spn/Ttn	Sphene/Titanite	$CaTiSiO_5$
	Qz	Quartz	SiO_2
	St	Staurolite	$Fe_2Al_9Si_4O_{23}(OH)$
	Amp	Amphibole	Group
	Srp	Serpentinite	Group
	Spl	Spinel	Group
	Cal	Calcite	$CaCO_3$
	Zrn	Zircon	$ZrSiO_4$
	Tur	Tourmaline	Group

Appendix B Petrography, Geology and Related Figures

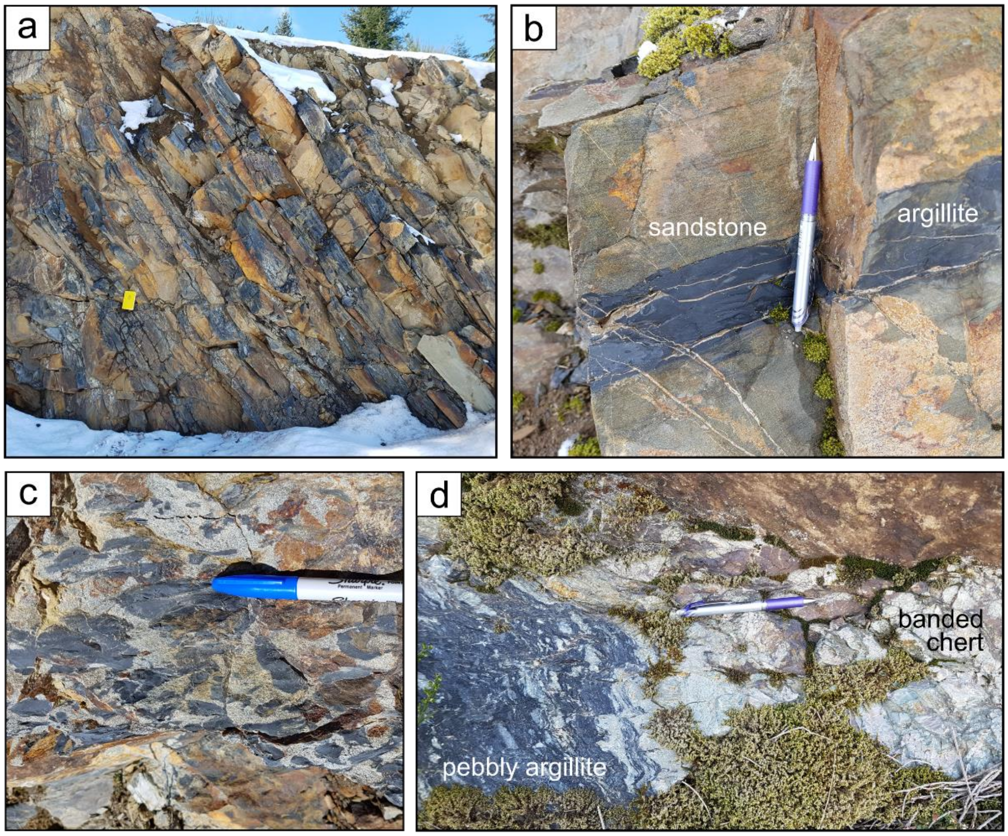

Figure B.1 Geology of the LRC fault-bound blocks at Finlayson Arm. (*a*) Flysch-like sequence of argillite and psammite ~N dipping beds. (*b*) Interbedded normally graded sandstone and argillite. *(c*) Rip up clasts of the argillite hosted in a coarse immature matrix of lithics + qz that has recrystallized (T ~300 C). (*d*) Pebbly argillite and banded cherts that comprise the PPU immediately surrounding the fault-bound LRC blocks in Finlayson Arm.

Figure B.2 Soft sediment deformation textures in the Gonzalez Bay PPU in an olistostromal outcrop.

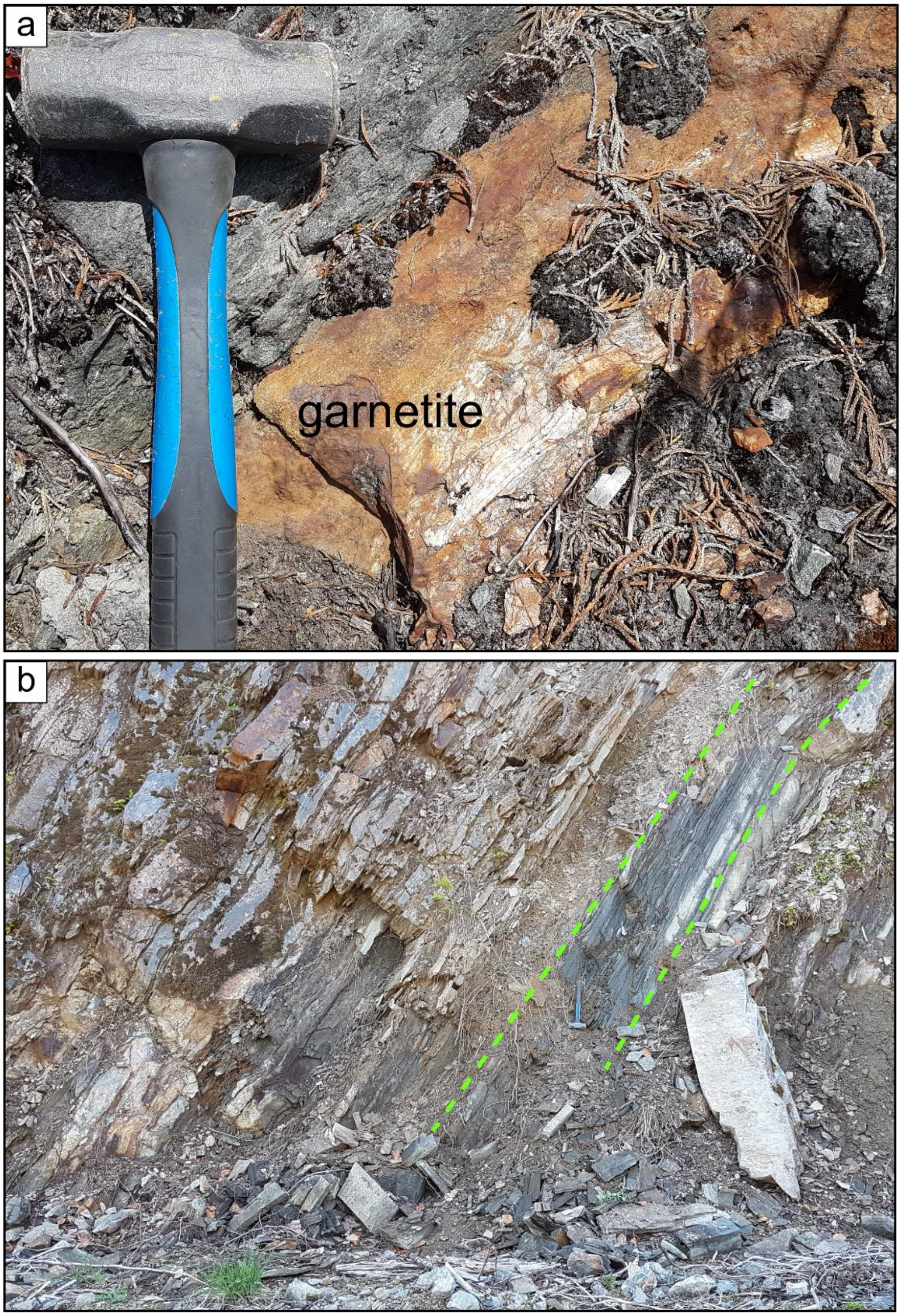

Figure B.3 Tripp Creek Metabasites in the Valentine Mountain region. (a) A thick, sulfidic section of garnetite banding interfoliated with a plagioclase-poor amphibolite (weathered). (b) Typical foliated metabasite intercalated with succession of pelitic and psammitic schists.

Figure B.4 Bt-foliated metapsammitic rock with *en echelon* veins (sillimanite zone). Highway 14, on strike with the large Valentine Mountain unit, re-interpreted here as a metapsammite, not an intrusion.

Figure B.5 Port Renfrew station AG105. From left to right: Carbonaceous Py phyllite; Spotted phyllite contact aureole at yellow notebook for scale (carbonate + chl); coarse ~tonalitic sill; green, fine-grained cryptic metabasite; felsic sill.

Figure B.6 Psammitic paragneiss from the central LRC with compositional banding. qz+pl+bt+gr.

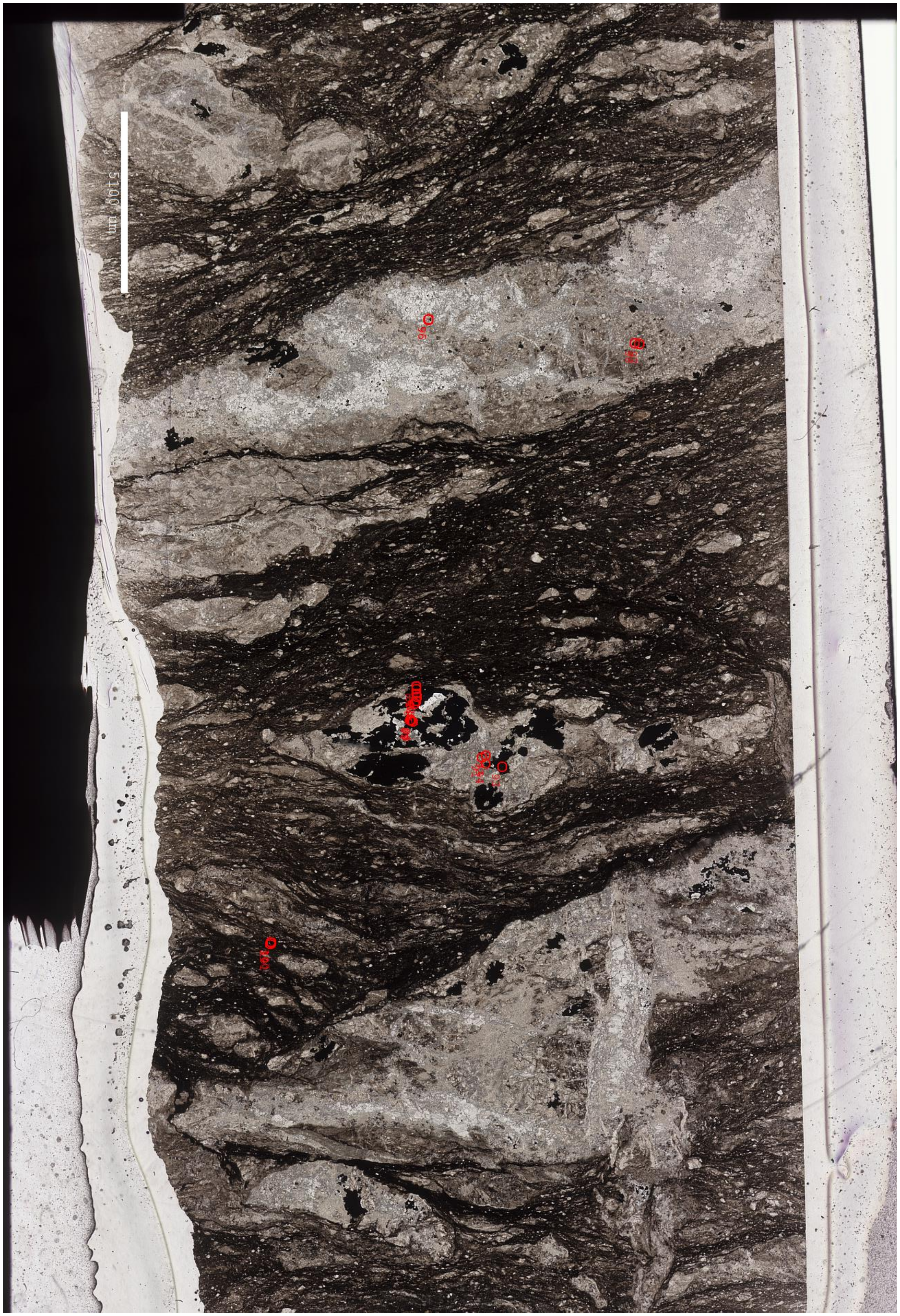

Figure B.7 AG010 (PPU) thin section with EPMA spots for sulfide analyses.

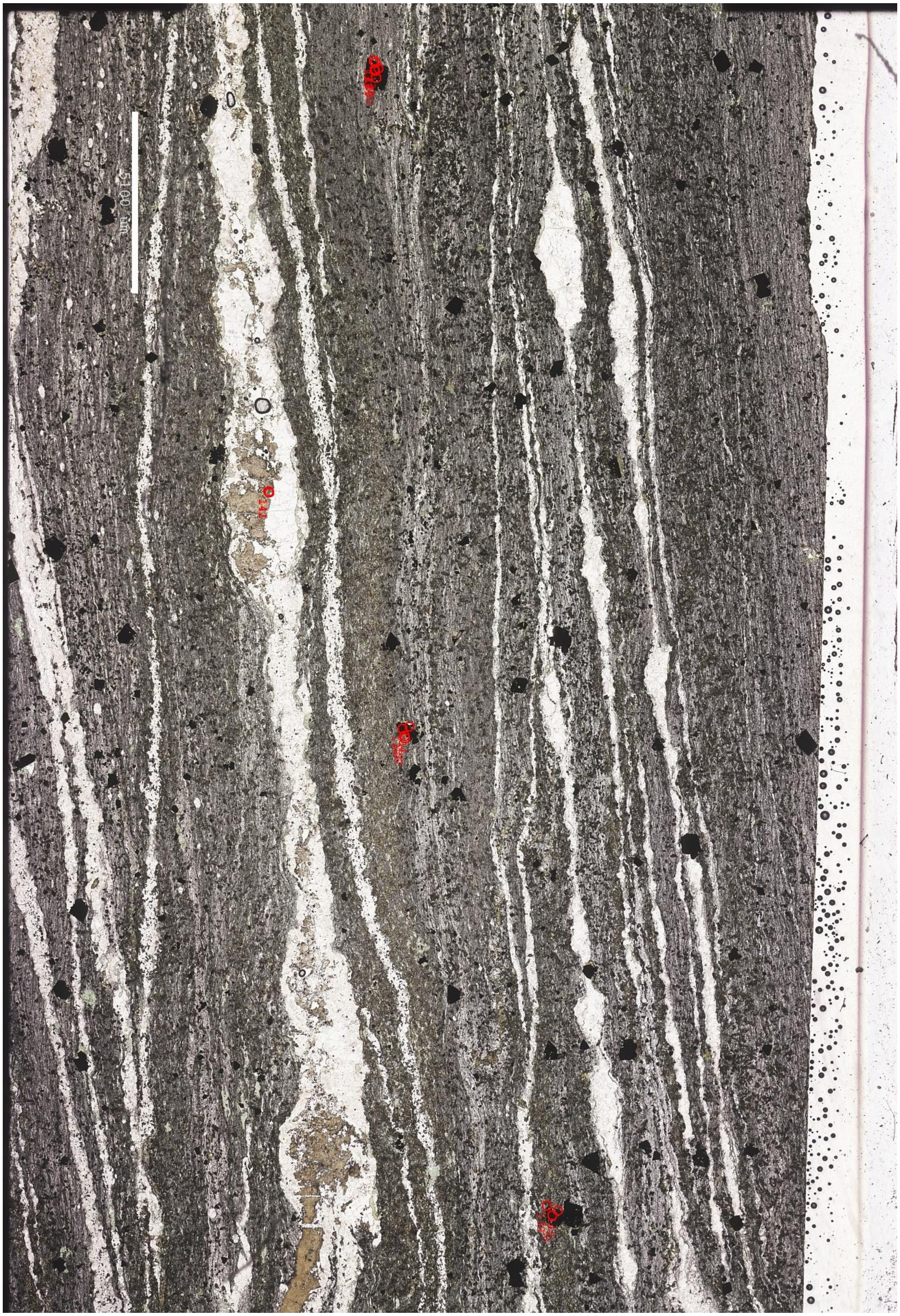

Figure B.8 AG055-1 thin section for EPMA with p/blastic magnetite in chl+ep mx.

Figure B.9 AG137 Actinolite schist for EPMA. Large xenolith (?) on right.

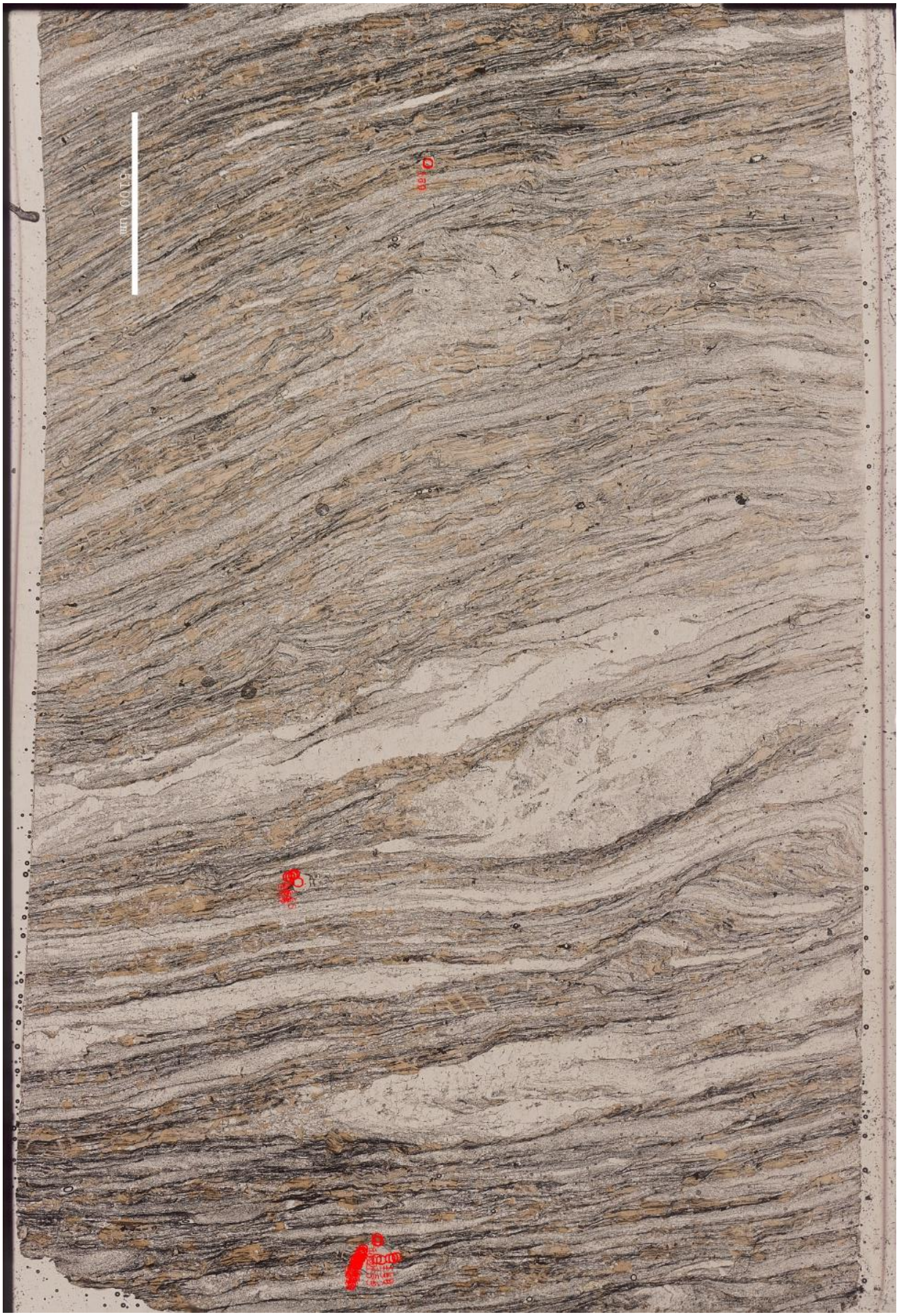

Figure B.10 AG067 thin section for EPMA gt-bt and RSCM.

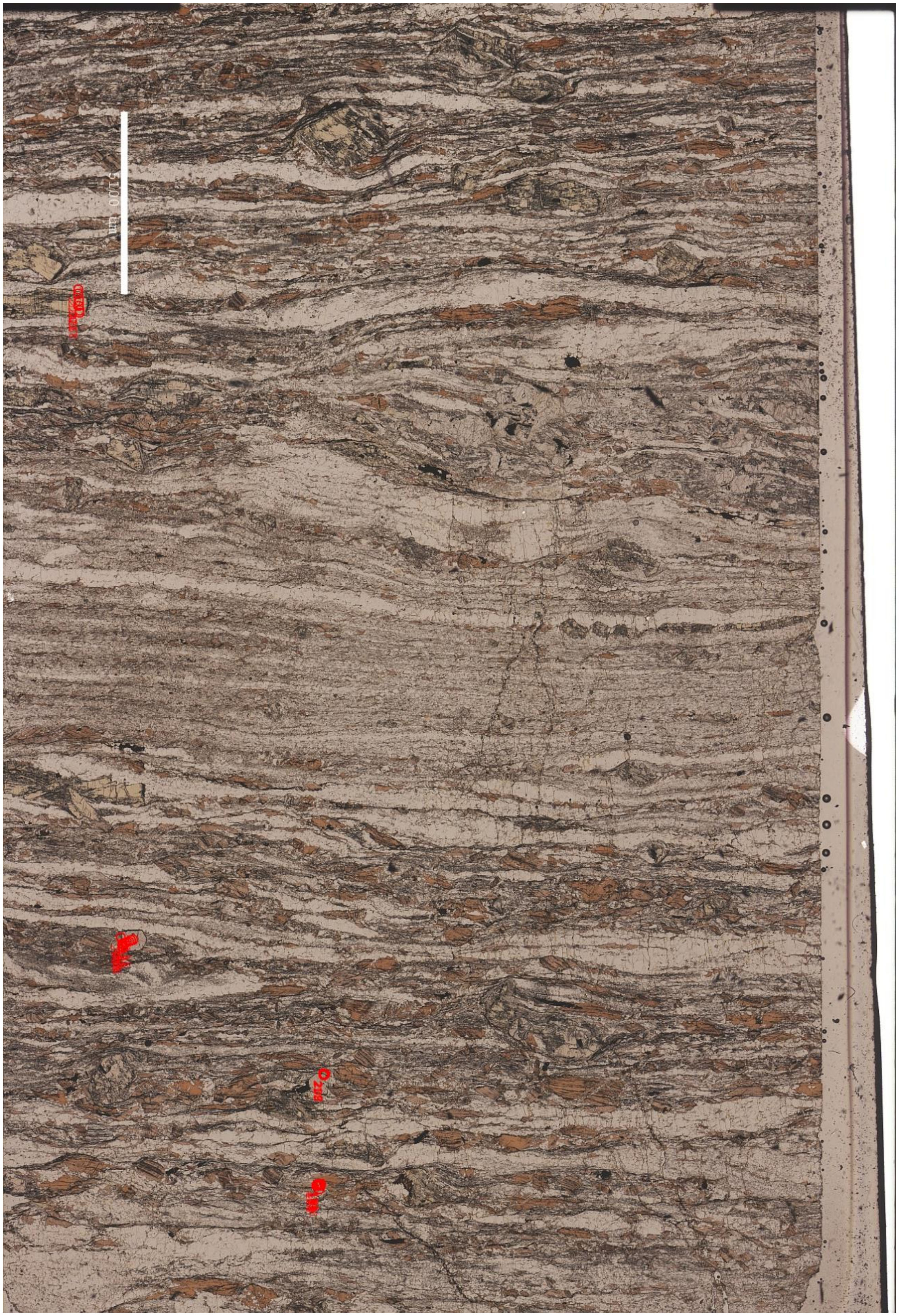

Figure B.11 AG047 thin section for gt-bt EPMA. Interfoliated pelite and psammite (middle).

Figure B.12 AG011-2 thin section (unused for EPMA), showing compositional layering.

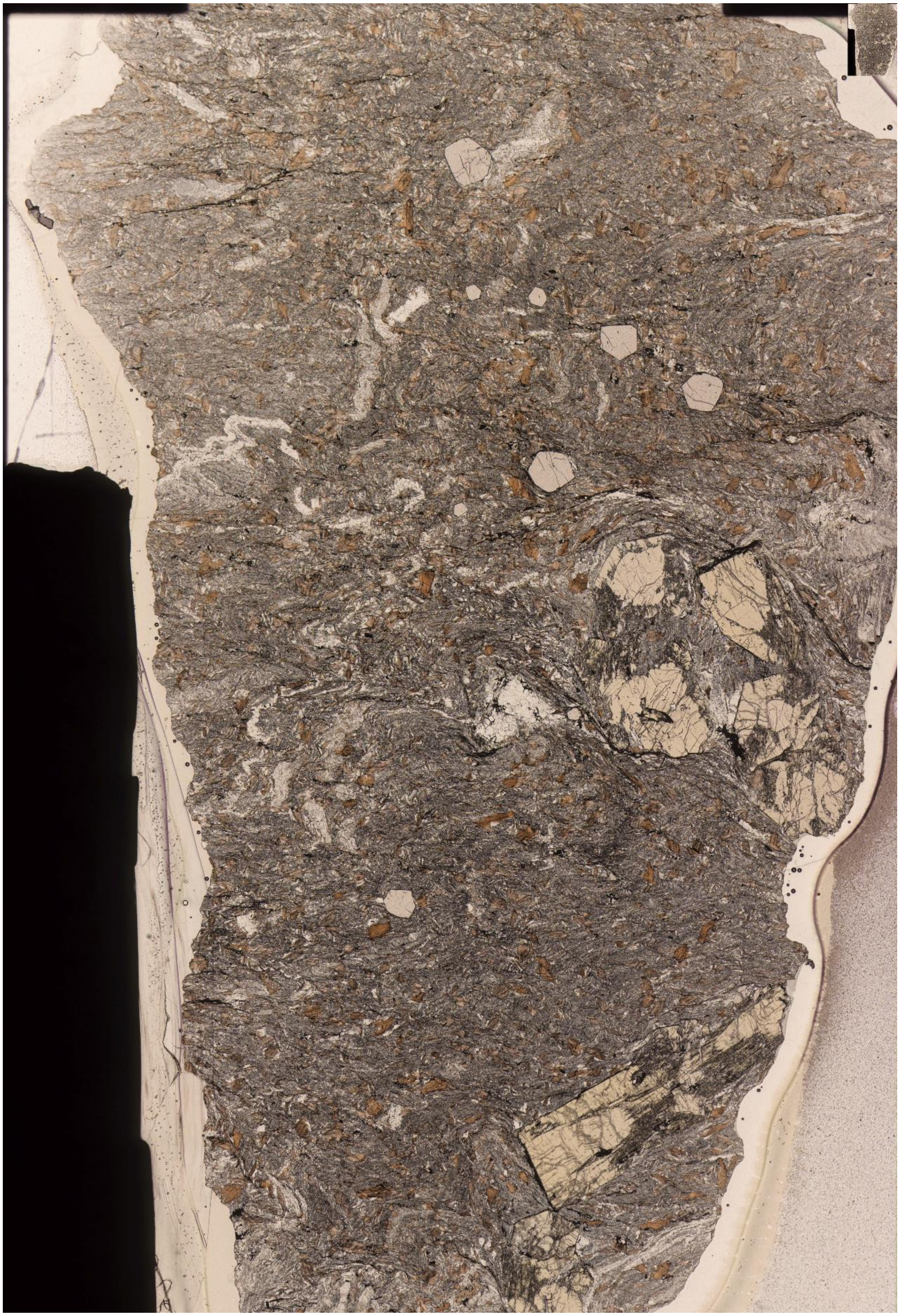

Figure B.13 AG012 thin section with coarse staurolite. Retrogressed andalusite on right.

Figure B.14 AG042 thin section for EPMA (gt-bt and sulfides) and RSCM. Gt + And + St.

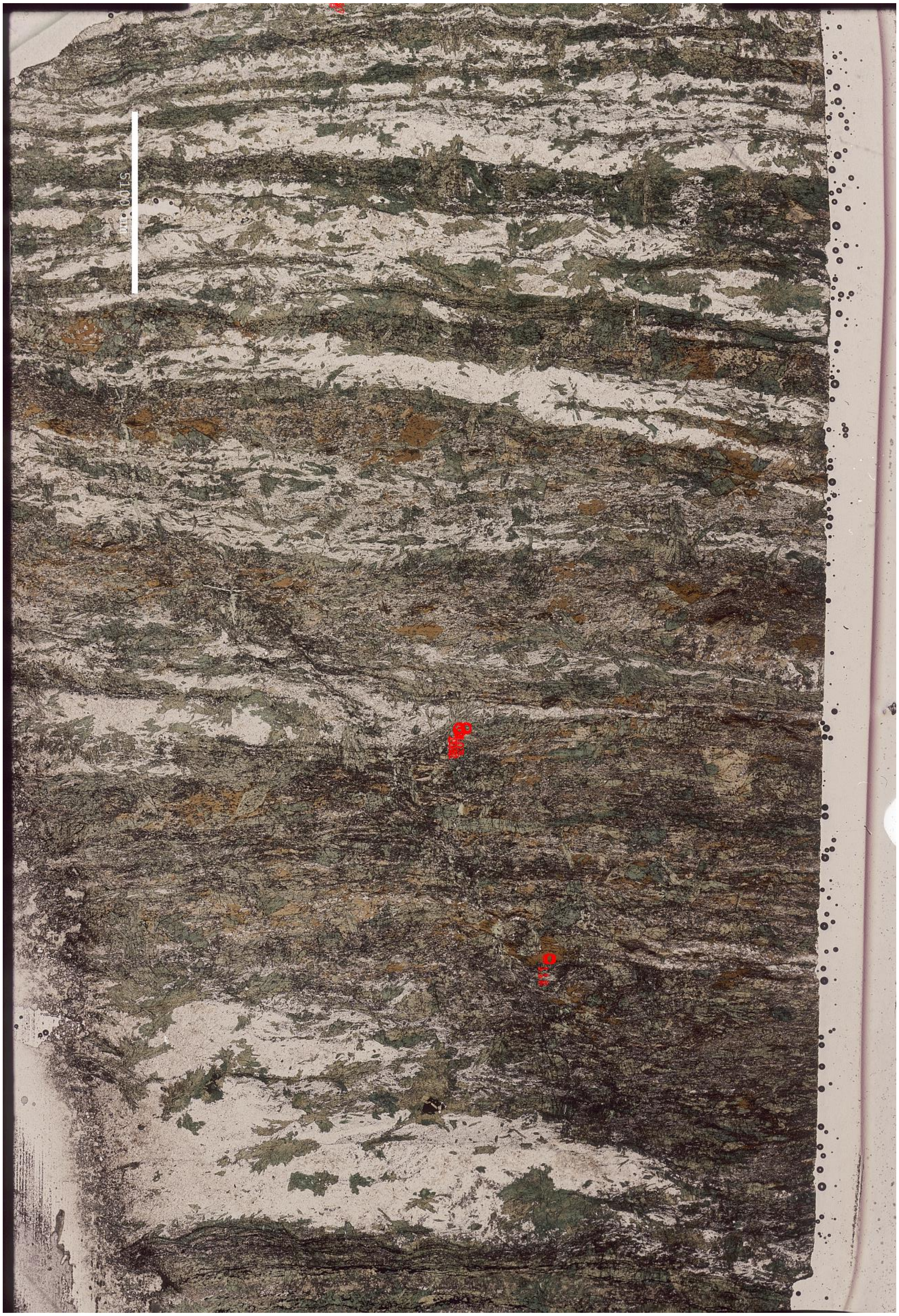

Figure B.15 AG059 banded amphibolite for EPMA amphibole identification

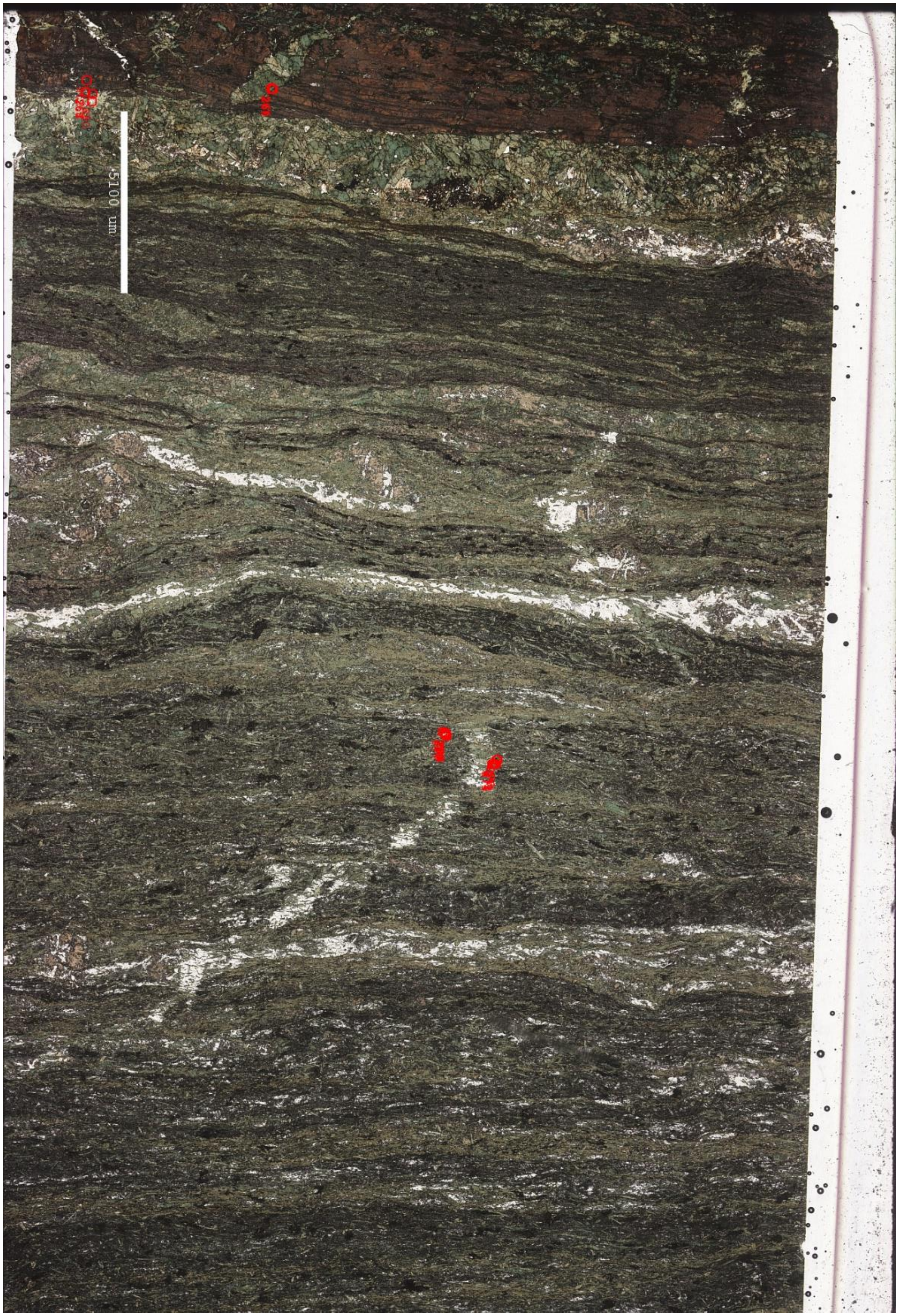

Figure B.16 AG069-2 foliated metabasite (plagioclase-poor) with garnetite banding for EPMA.

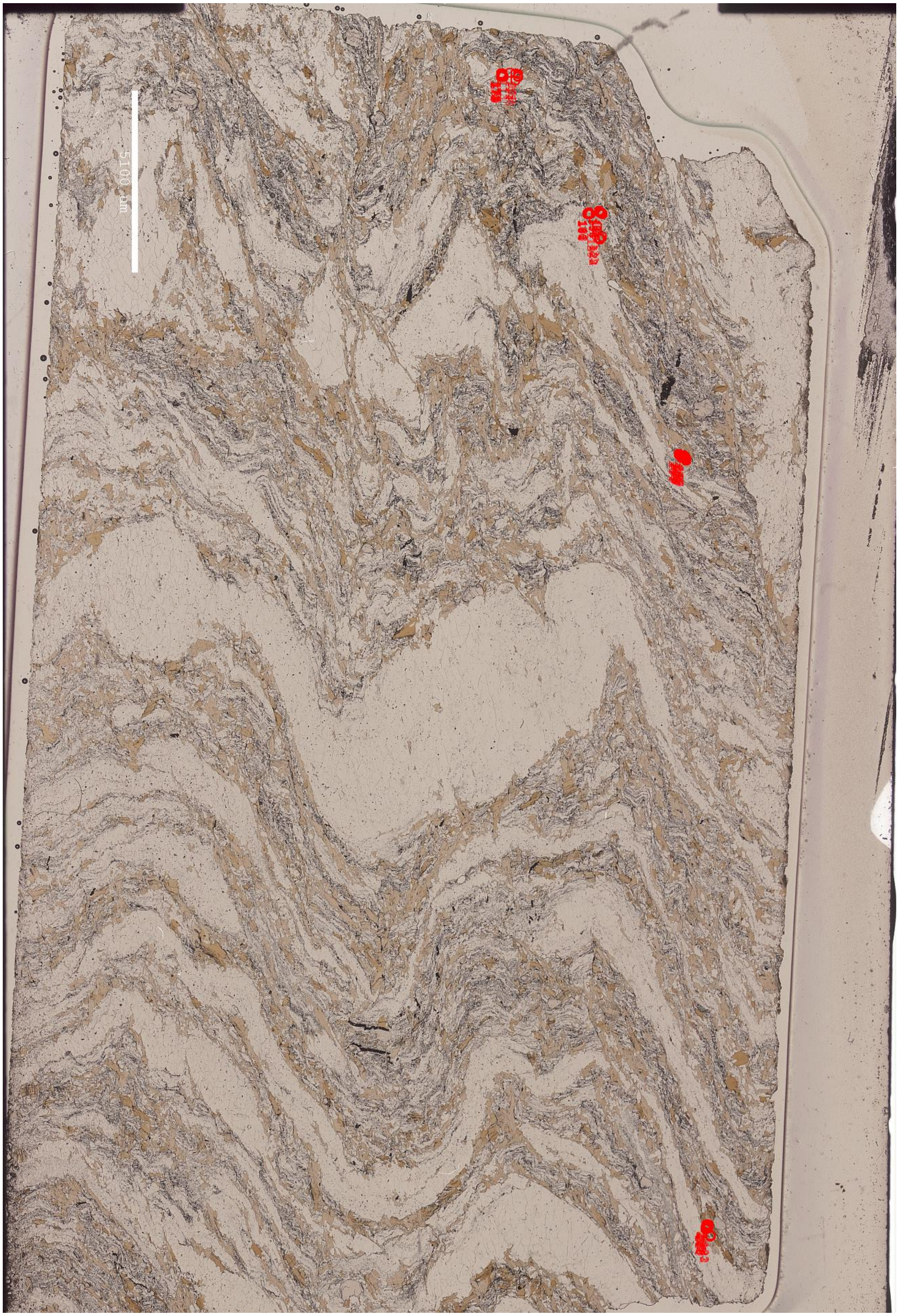

Figure B.17 AG116-1 for gt-bt EPMA and RSCM.

Figure B.18 AG041 sillimanite-bearing schist for gt-bt EPMA.

Figure B.19 AG119 thin section. Amphibolite with large ilmenite laths, from boudin in paragneiss.

Figure B.20 AG080 for gt-bt EPMA and RSCM. Sillimanite-bearing schist.

Figure B.21 AG109 thin section (EPMA for sulfide inclusions) Sillimanite zone.

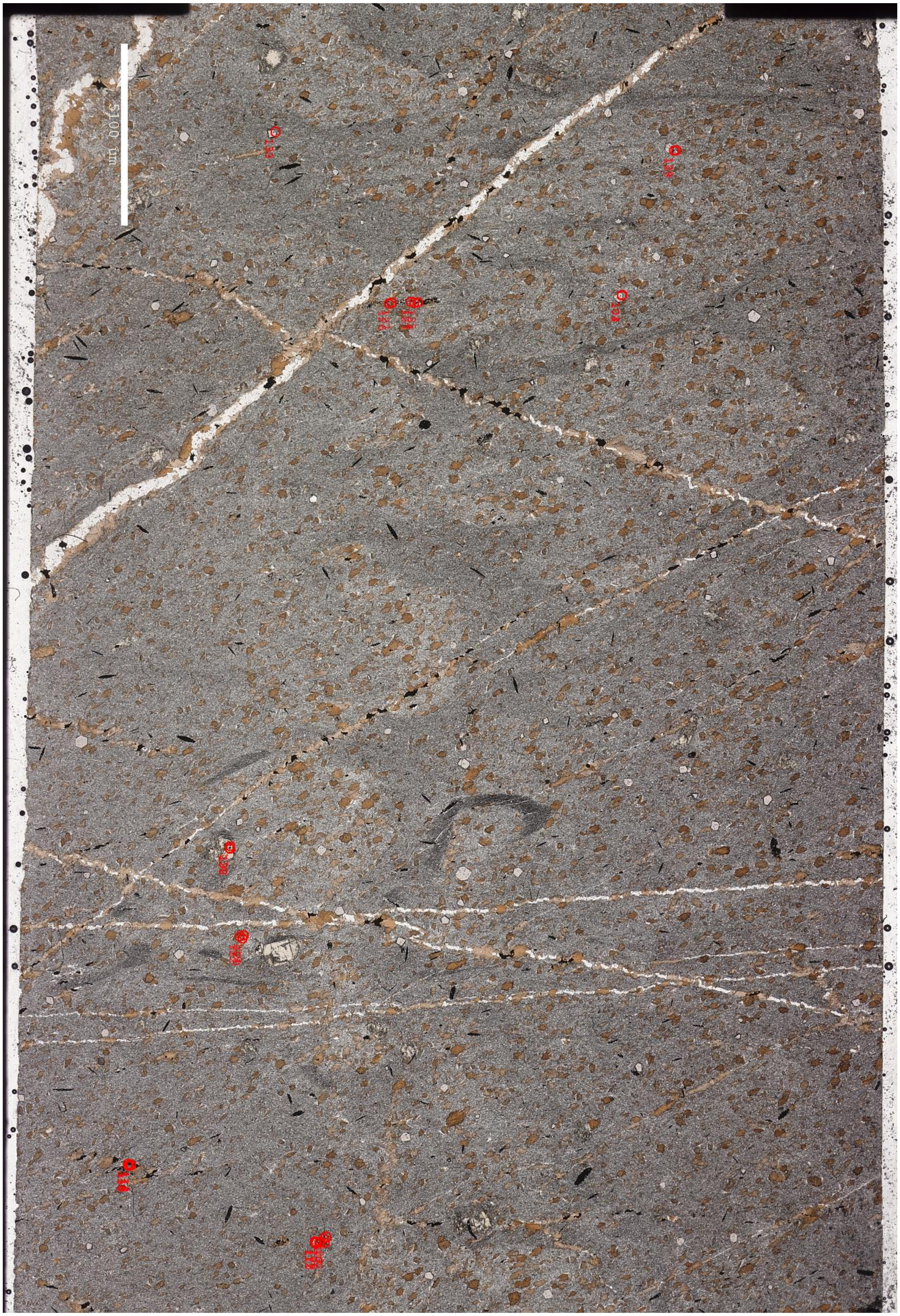

Figure B.22 AG049-1 for gt-bt and sulfide EPMA. Spotted gt-st-bt schist with coarse ilm.

Figure B.23 AG074-2 coarse gt for EPMA. From the LRF shear zone. Highest T sample in suite.

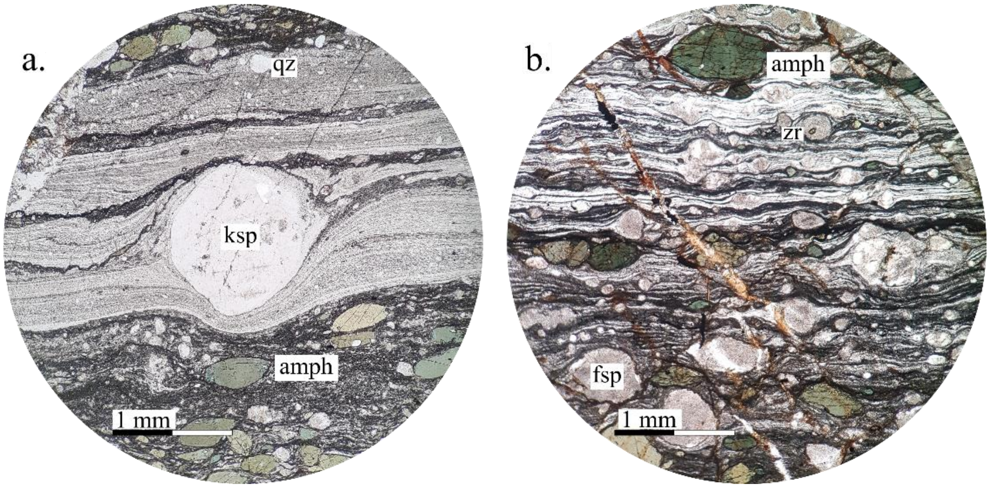

Figure B.24 PPL photomicrographs of MVDB09-33 from Gonzalez Bay. Mylonite with fragments of overlying WCC and the PPU from the fault zone juxtaposing the units.

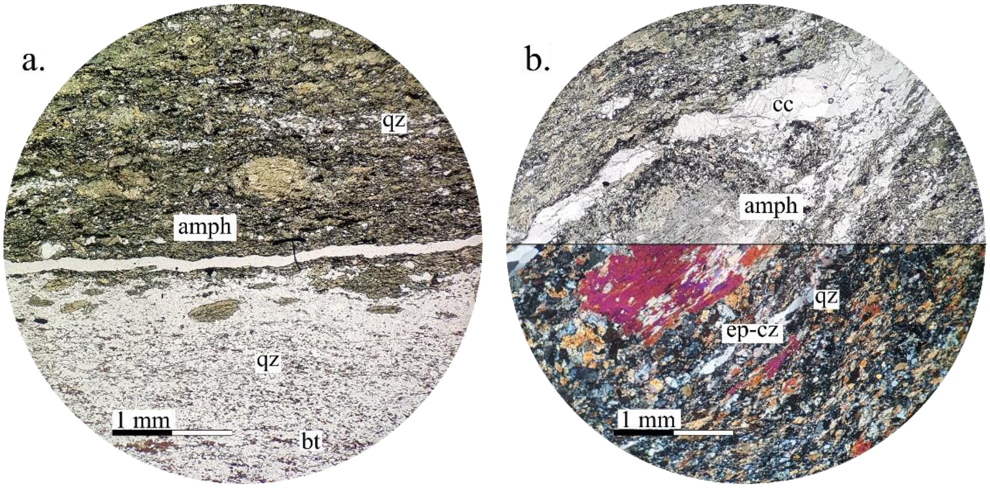

Figure B.25 PPL/XPL photomicrographs of mylonite AG129-2 from the Bear Creek Shear Zone.

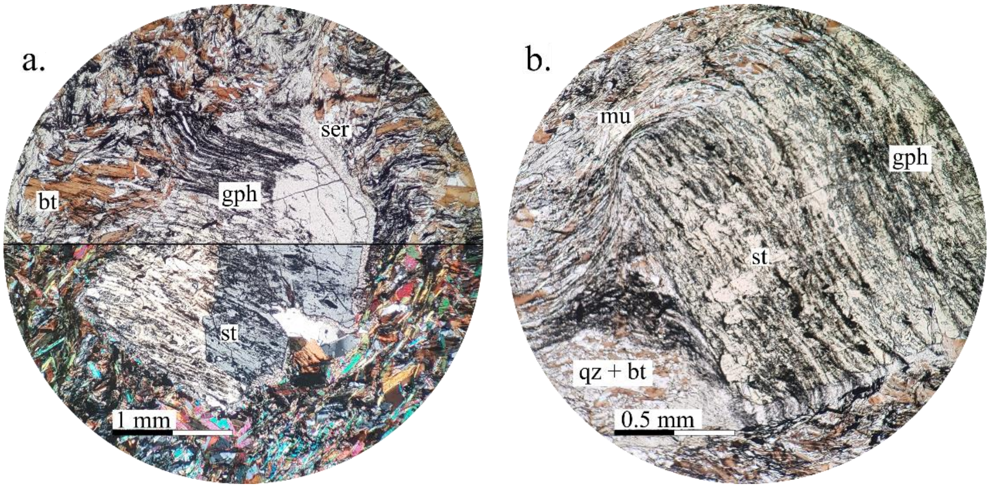

Figure B.26 PPL/XPL photomicrographs of syn-deformation St from AG127. (graphitic incl. trails)

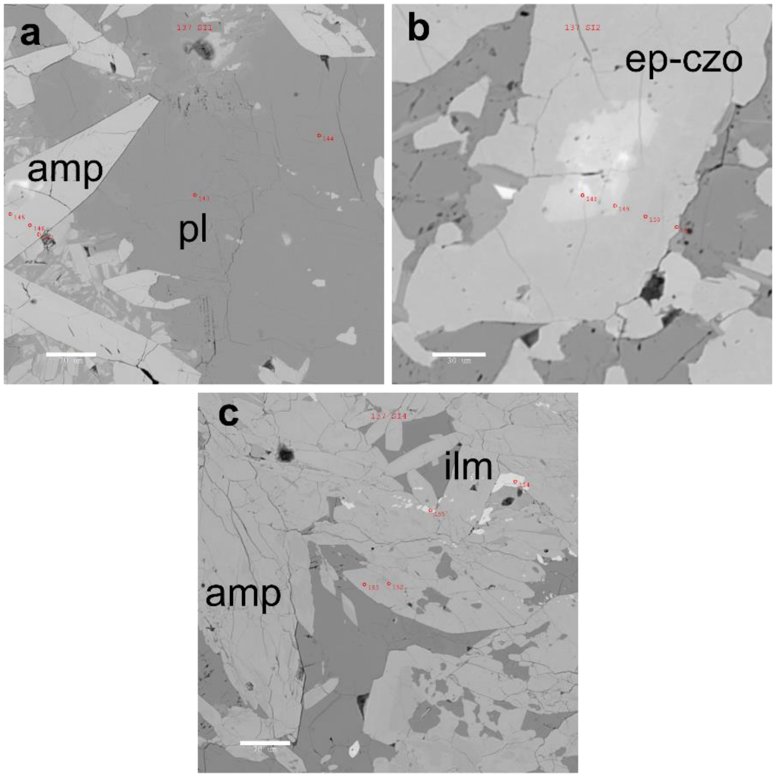

Figure B.27 BSE EPMA imagery (*U of A EML*). AG137. Amphibole schist, locally coarse zoned epidote.

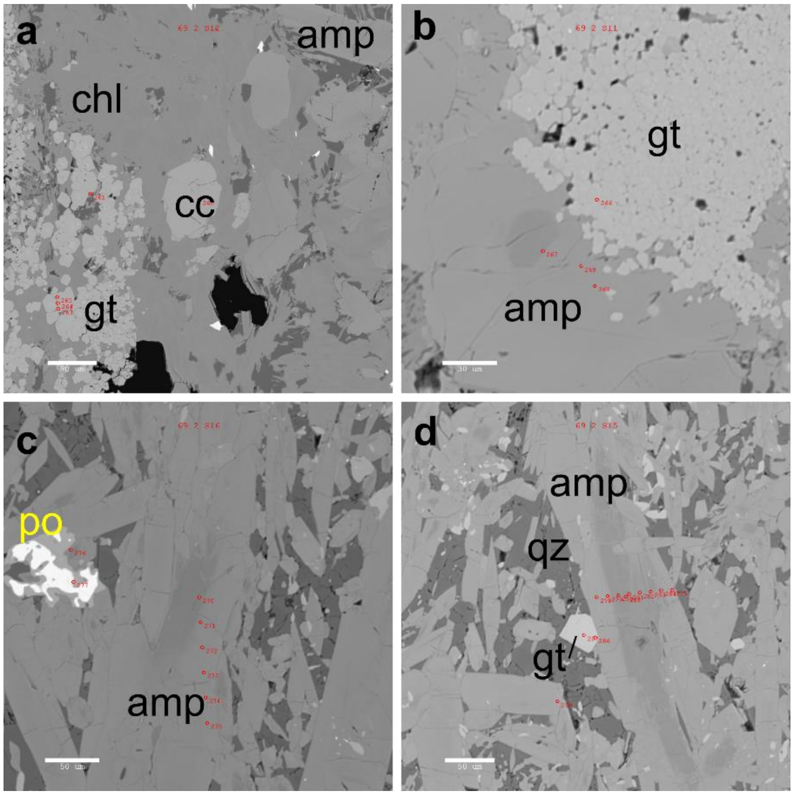

Figure B.28 BSE EPMA imagery (*U of A EML)*. AG069-2. Amphibolite and f.g. garnetite bands.

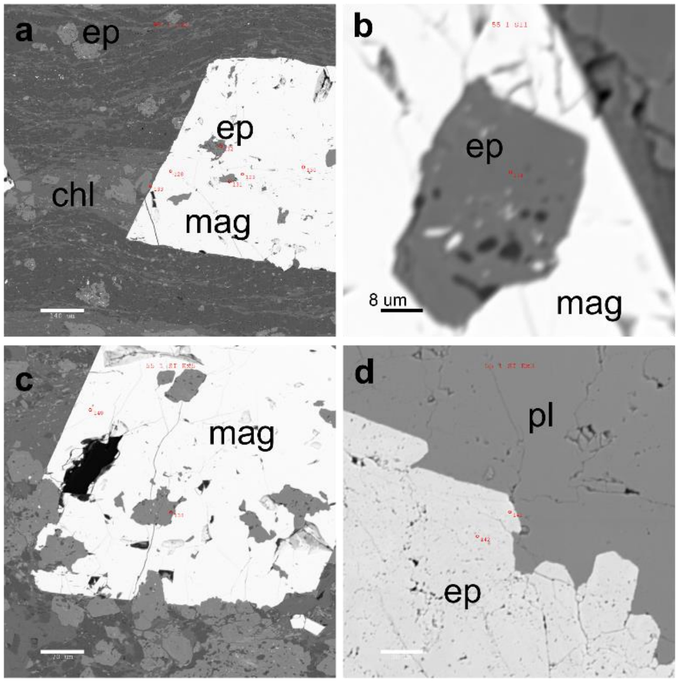

Figure B.29 BSE EPMA imagery (*UofA EML*). AG055-1. Post deformation magnetite p/blasts w/ ep incl. Interpreted as a mafic volcanic, possibly tuffaceous unit and hence lacks any remnant intrusive igneous textures (e.g., pseudomorphed cpx grains).

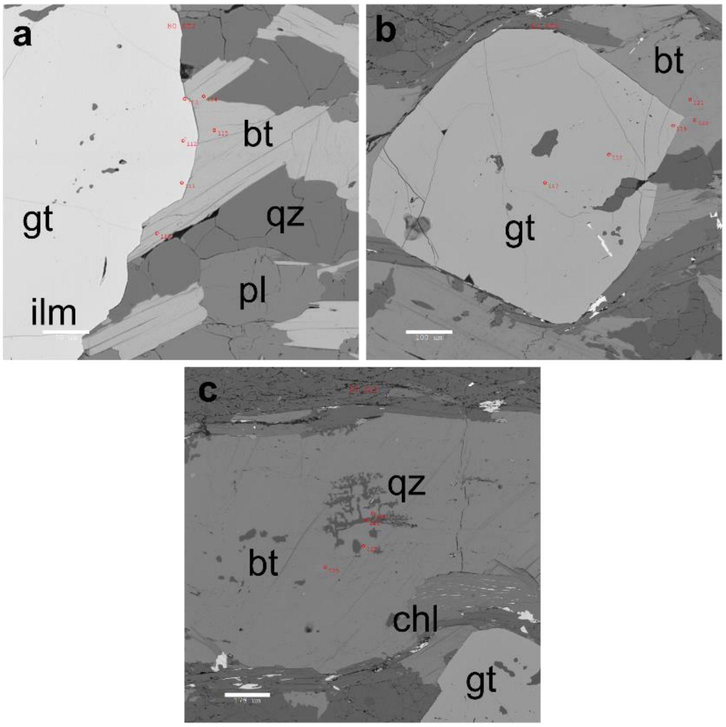

Figure B.30 BSE EPMA (*UofA EML)*. AG080. Gt-Bt thermometry. Bt dis-eq'm textures. Sil zone.

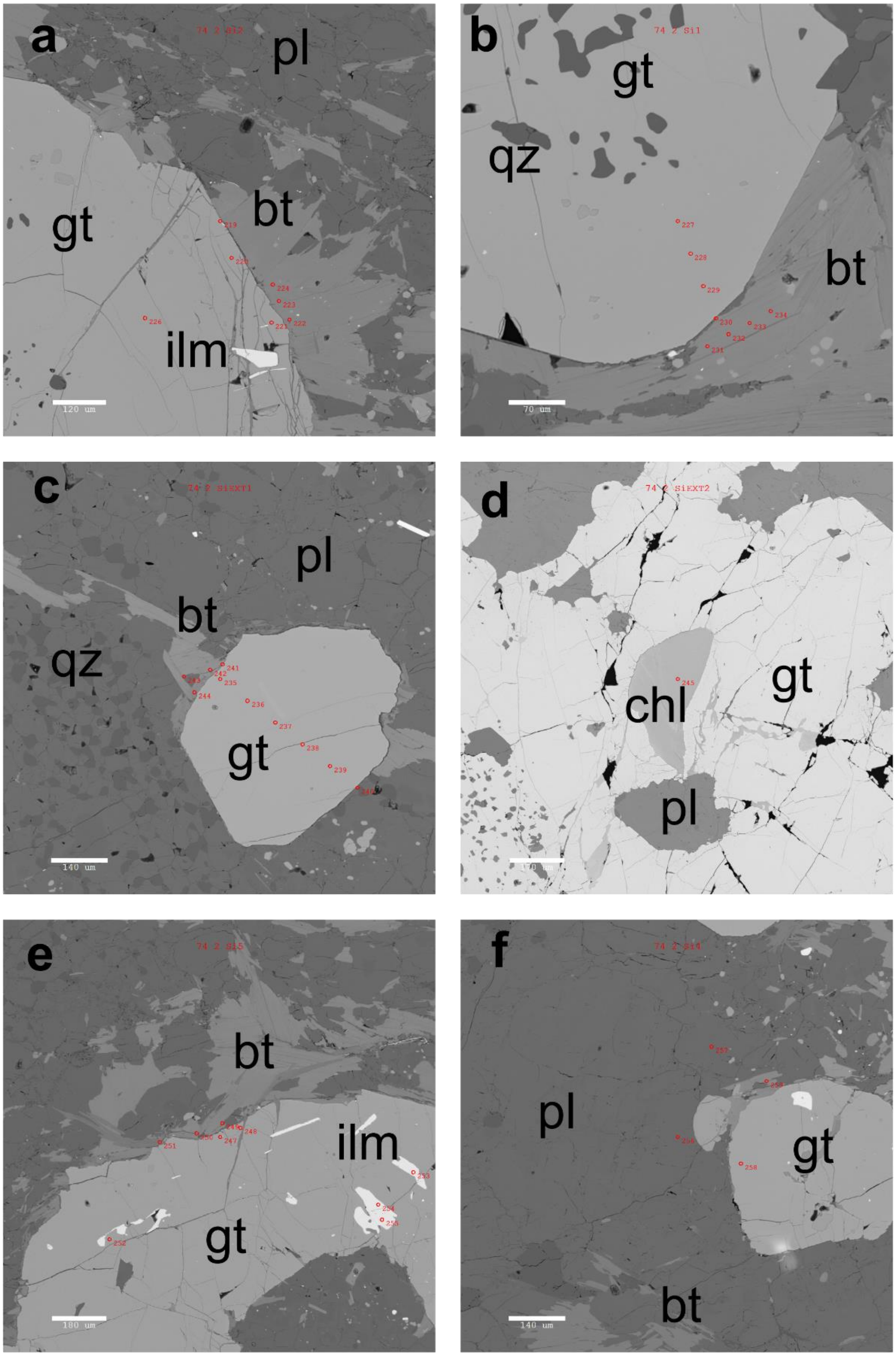

Figure B.31 BSE EPMA imagery (*UofA EML*). AG074-2. Coarse gt with inclusions of ilmenite, chlorite, quartz, and plagioclase. For Gt-Bt thermometry. Devoid of sulfides.

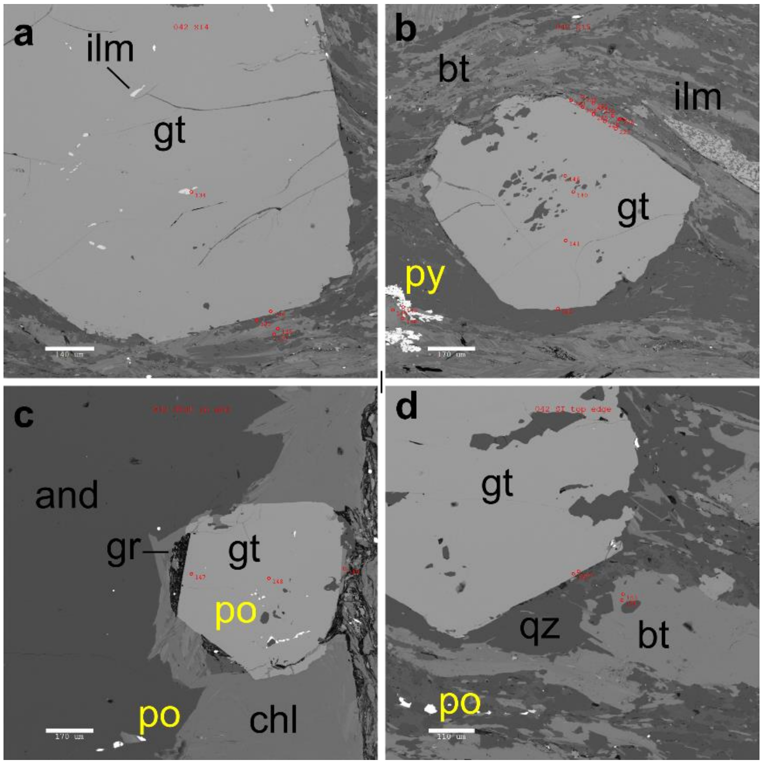

Figure B.32 BSE EPMA imagery (*UofA EML*). For gt-bt thermometry. Note garnet in rim of andalusite, wherein chlorite is replacing the margins.

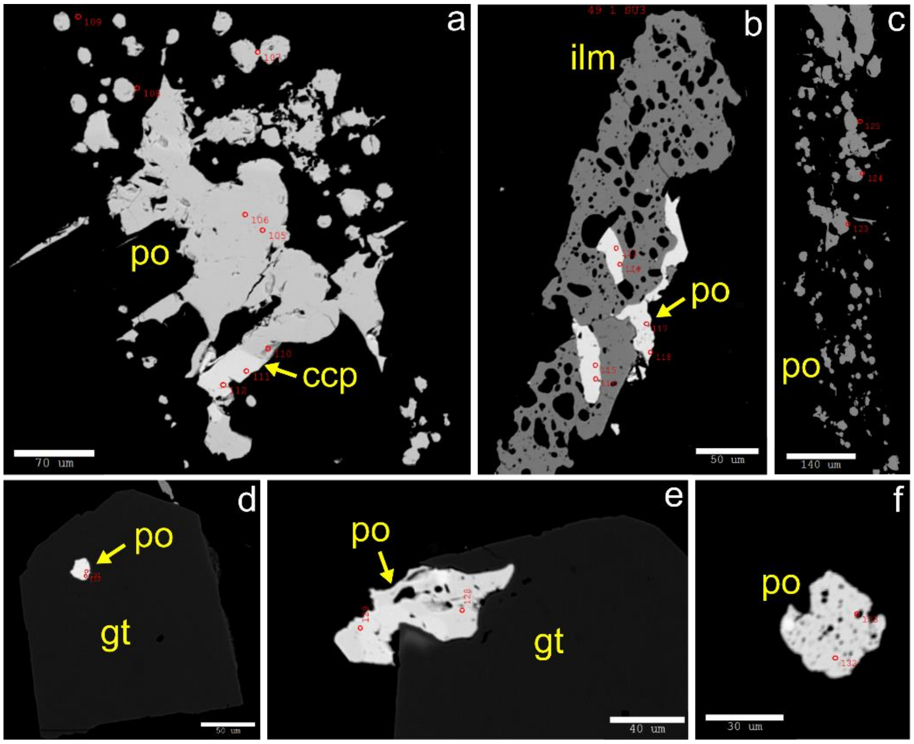

Figure B.33 BSE EPMA imagery (*UofA EML*). AG049-1. Blebby Po textures in biotite, veins, matrix and within garnet porphyroblasts. Vein blebs possibly indicate immiscible sulfide liquid?

Appendix C Supplementary Data and Data Plots

Table C.1 RSCM spectra fit results using the IFORS program and calibration curve (Lunsdorf et al., 2017).

						μ	σ	μ	σ	μ	σ	μ	σ	μ	σ	μ
Sample	ID	T [C]	Excl Est.	Exc Rsn	U*	D_STA	D_STA	G_STA	G_STA	G_shp	G_Shp	Dmax	Dmax	Gmax	Gmax	D/G
AG006_1	fit_n10_AG006_1_20191005	271			36	169.94	2.57	82.18	1.89	0.62	0.01	1329.61	0.00	1608.94	0.00	0.48
AG006_1	fit_n12_AG006_1_20191005	300			36	136.74	0.11	57.65	0.02	0.57	0.00	1328.34	0.00	1603.86	0.00	0.43
AG006_1	fit_n13_AG006_1_20191005	298			36	138.73	0.33	55.90	0.19	0.57	0.00	1329.61	0.00	1605.13	0.00	0.39
AG006_1	fit_n14_AG006_1_20191005	285			36	154.32	12.38	68.86	6.51	0.59	0.02	1328.34	0.00	1605.13	0.00	0.44
AG006_1	fit_n15_AG006_1_20191005	279			36	160.76	0.11	75.72	0.09	0.60	0.00	1333.42	0.00	1606.40	0.00	0.47
AG006_1	fit_n16_AG006_1_20191005	278			36	162.22	0.33	76.60	0.15	0.60	0.00	1333.42	0.00	1605.13	0.00	0.48
AG006_1	fit_n17_AG006_1_20191005	288			36	150.19	0.28	73.56	0.32	0.58	0.00	1332.15	0.00	1606.40	0.00	0.49
AG006_1	fit_n18_AG006_1_20191005	290			36	147.98	6.60	70.44	5.96	0.58	0.02	1329.61	0.00	1607.67	0.00	0.47
AG006_1	fit_n19_AG006_1_20191005	302			36	133.54	0.05	51.88	0.03	0.57	0.00	1330.88	0.00	1607.67	0.00	0.39
AG006_1	fit_n1_AG006_1_20191005	300			36	136.54	0.07	55.62	0.06	0.57	0.00	1333.42	0.00	1605.13	0.00	0.42
AG006_1	fit_n20_AG006_1_20191005	291			36	147.28	7.23	63.17	4.62	0.55	0.01	1332.15	0.00	1606.40	0.00	0.43
AG006_1	fit_n2_AG006_1_20191005	301			36	135.11	1.81	55.51	0.91	0.57	0.00	1330.88	0.00	1606.40	0.00	0.41
AG006_1	fit_n3_AG006_1_20191005	284			36	155.42	0.07	72.78	0.05	0.58	0.00	1330.88	0.00	1606.40	0.00	0.47
AG006_1	fit_n4_AG006_1_20191005	300			36	135.89	0.05	59.41	0.04	0.54	0.00	1329.61	0.00	1606.40	0.00	0.43
AG006_1	fit_n5_AG006_1_20191005	283			36	156.03	2.59	74.93	2.82	0.58	0.00	1329.61	0.00	1606.40	0.00	0.48
AG006_1	fit_n6_AG006_1_20191005	282			36	157.17	0.07	74.24	0.07	0.58	0.00	1333.42	0.00	1607.67	0.00	0.47
AG006_1	fit_n7_AG006_1_20191005	301			36	134.74	0.06	54.19	0.02	0.56	0.00	1335.96	0.00	1606.40	0.00	0.41
AG030_2	fit_n10_AG030_2_20201006	328			36	108.81	3.13	115.27	4.61	0.85	0.00	1347.39	0.00	1605.13	0.00	1.06
AG030_2	fit_n11_AG030_2_20201006	286			36	152.78	0.08	120.15	0.10	0.89	0.00	1346.12	0.00	1606.40	0.00	0.79
AG030_2	fit_n12_AG030_2_20201006		320	Phase Int	36	115.93	0.60	92.94	0.08	0.76	0.00	1347.39	0.00	1606.40	0.00	0.79
AG030_2	fit_n13_AG030_2_20201006	306			36	129.95	0.09	114.33	0.23	0.65	0.00	1327.07	0.00	1605.13	0.00	0.84
AG030_2	fit_n14_AG030_2_20201006	316			36	119.69	0.50	118.44	0.72	0.85	0.00	1346.12	0.00	1602.59	0.00	0.99
AG030_2	fit_n15_AG030_2_20201006		298	Phase Int	36	138.00	0.33	94.86	0.08	0.73	0.00	1337.23	0.00	1617.83	0.00	0.77
AG030_2	fit_n16_AG030_2_20201006	314			36	121.65	3.24	116.01	4.15	0.77	0.00	1351.19	0.00	1607.67	0.00	0.93
AG030_2	fit_n17_AG030_2_20201006	311			36	124.07	0.97	121.91	1.21	0.81	0.00	1342.31	0.00	1605.13	0.00	0.98
AG030_2	fit_n18_AG030_2_20201006	327			36	110.21	6.10	87.19	4.84	0.70	0.01	1344.85	0.00	1608.94	0.00	0.78
AG030_2	fit_n19_AG030_2_20201006	305			36	130.14	0.02	94.15	0.07	0.77	0.00	1342.31	0.00	1605.13	0.00	0.73
AG030_2	fit_n1_AG030_2_20201006	312			36	123.23	0.04	91.09	0.04	0.83	0.00	1347.39	0.00	1610.21	0.00	0.77
AG030_2	fit_n20_AG030_2_20201006	337			36	102.12	0.14	101.03	0.09	0.78	0.00	1344.85	0.00	1606.40	0.00	1.00
AG030_2	fit_n21_AG030_2_20201006	324			36	112.41	1.26	99.66	2.05	0.79	0.01	1341.04	0.00	1608.94	0.00	0.90
AG030_2	fit_n22_AG030_2_20201006	339			36	101.05	0.27	106.41	0.26	0.79	0.00	1343.58	0.00	1605.13	0.00	1.06
AG030_2	fit_n23_AG030_2_20201006	335			36	103.86	0.26	100.37	0.16	0.75	0.00	1338.50	0.00	1603.86	0.00	0.97
AG030_2	fit_n24_AG030_2_20201006	346			36	95.87	0.33	93.30	0.27	0.74	0.00	1344.85	0.00	1605.13	0.00	0.98

AG030_2	fit_n2_AG030_2_20201006	351			36	92.80	0.06	94.33	0.38	0.97	0.00	1343.58	0.00	1598.78	0.00	1.04
AG030_2	fit_n3_AG030_2_20201006		350	Phase Int	36	93.53	0.08	88.08	0.19	0.95	0.00	1349.93	0.00	1598.78	0.00	0.91
AG030_2	fit_n4_AG030_2_20201006	333			36	105.03	0.72	85.45	0.48	0.83	0.00	1348.66	0.00	1606.40	0.00	0.81
AG030_2	fit_n5_AG030_2_20201006	316			36	119.56	0.28	105.46	0.44	0.84	0.00	1348.66	0.00	1606.40	0.00	0.88
AG030_2	fit_n6_AG030_2_20201006	251			36	189.87	0.10	108.19	0.02	0.79	0.00	1351.19	0.00	1610.21	0.00	0.57
AG030_2	fit_n7_AG030_2_20201006	318			36	117.42	0.62	116.69	0.55	0.87	0.00	1346.12	0.00	1605.13	0.00	0.99
AG030_2	fit_n8_AG030_2_20201006	313			36	122.65	0.19	120.48	0.47	0.86	0.00	1347.39	0.00	1602.59	0.00	0.98
AG030_2	fit_n9_AG030_2_20201006	322			36	113.97	0.04	116.62	0.05	0.89	0.00	1347.39	0.00	1603.86	0.00	1.02
AG042	fit_no10_AG042_20201013	531			37	344.28	0.12	30.24	0.02	4.63	0.00	1324.53	0.00	1582.28	0.00	0.09
AG042	fit_no11_AG042_20201013	568			37	244.76	0.30	22.36	0.01	5.65	0.01	1319.45	0.00	1582.28	0.00	0.05
AG042	fit_no12_AG042_20201013	584			37	316.61	0.04	19.03	0.00	14.98	0.00	1360.08	0.00	1581.01	0.00	0.06
AG042	fit_no13_AG042_20201013	584			37	547.94	0.24	19.01	0.01	12.41	0.00	1360.08	0.00	1581.01	0.00	0.03
AG042	fit_no14_AG042_20201013	575			37	169.22	0.08	20.81	0.00	13.12	0.02	1352.46	0.00	1581.01	0.00	0.13
AG042	fit_no15_AG042_20201013	584			37	385.27	9.62	19.18	0.07	9.74	0.09	1349.93	0.00	1582.28	0.00	0.05
AG042	fit_no16_AG042_20201013	571			37	135.19	0.04	21.73	0.00	8.61	0.00	1363.89	0.00	1582.28	0.00	0.14
AG042	fit_no17_AG042_20201013	561			37	450.61	2.88	23.81	0.27	6.89	0.05	1431.18	0.00	1581.01	0.00	0.04
AG042	fit_no18_AG042_20201013	572			37	229.12	0.11	21.54	0.02	8.48	0.01	1356.27	0.00	1582.28	0.00	0.09
AG042	fit_no19_AG042_20201013	571			37	288.59	0.16	21.60	0.02	10.23	0.01	1363.89	0.00	1582.28	0.00	0.06
AG042	fit_no1_AG042_20201013	558			37	149.79	0.04	24.31	0.01	5.53	0.00	1360.08	0.00	1581.01	0.00	0.16
AG042	fit_no20_AG042_20201013	564			37	261.57	0.10	23.17	0.01	7.56	0.03	1361.35	0.00	1581.01	0.00	0.08
AG042	fit_no21_AG042_20201013	573			37	216.44	1.08	21.31	0.15	9.24	0.15	1358.81	0.00	1582.28	0.00	0.09
AG042	fit_no22_AG042_20201013	535			37	28.41	0.02	29.39	0.02	4.48	0.00	1376.59	0.00	1582.28	0.00	1.04
AG042	fit_no23_AG042_20201013	573			37	210.37	0.13	21.24	0.02	8.86	0.06	1361.35	0.00	1582.28	0.00	0.09
AG042	fit_no24_AG042_20201013	562			37	145.08	0.19	23.48	0.05	9.09	0.01	1360.08	0.00	1581.01	0.00	0.15
AG042	fit_no25_AG042_20201013	555			37	189.92	0.11	24.93	0.04	9.95	0.00	1358.81	0.00	1581.01	0.00	0.13
AG042	fit_no26_AG042_20201013	550			37	149.92	0.15	26.16	0.03	7.91	0.01	1360.08	0.00	1581.01	0.00	0.17
AG042	fit_no27_AG042_20201013	559			37	150.39	0.06	24.16	0.01	8.02	0.00	1363.94	0.00	1581.04	0.00	0.16
AG042	fit_no28_AG042_20201013	554			37	152.83	0.11	25.20	0.06	7.26	0.05	1357.59	0.00	1582.31	0.00	0.16
AG042	fit_no29_AG042_20201013	569			37	225.93	0.03	22.15	0.01	7.54	0.00	1357.59	0.00	1579.77	0.00	0.09
AG042	fit_no2_AG042_20201013	557			37	67.78	0.54	24.65	0.15	10.50	0.17	1332.15	0.00	1583.55	0.00	0.37
AG042	fit_no30_AG042_20201013		494	fluor	36	9.75	0.00	39.16	0.01	9.43	0.01	1332.15	0.00	1582.28	0.00	4.02
AG042	fit_no31_AG042_20201013	544			37	237.21	0.31	27.29	0.06	5.48	0.03	1349.93	0.00	1581.01	0.00	0.12
AG042	fit_no32_AG042_20201013	567			37	158.31	0.43	22.59	0.11	8.72	0.02	1356.27	0.00	1582.28	0.00	0.14
AG042	fit_no33_AG042_20201013	566			37	139.29	1.77	22.73	0.19	6.28	0.11	1349.93	0.00	1581.01	0.00	0.16
AG042	fit_no34_AG042_20201013	554			37	263.92	1.33	25.14	0.35	6.01	0.06	1362.62	0.00	1581.01	0.00	0.08
AG042	fit_no35_AG042_20201013		474	fluor	36	616.69	60.20	44.50	5.98	3.19	0.17	1349.93	0.00	1581.01	0.00	0.07
AG042	fit_no3_AG042_20201013	554			37	140.70	0.04	25.18	0.01	5.24	0.00	1361.35	0.00	1581.01	0.00	0.16
AG042	fit_no4_AG042_20201013	551			37	111.95	0.05	25.75	0.01	8.97	0.00	1361.40	0.00	1581.04	0.00	0.23
AG042	fit_no5_AG042_20201013	555			37	150.28	0.08	25.05	0.73	7.23	0.08	1361.40	0.00	1582.31	0.00	0.15
AG042	fit_no6_AG042_20201013		495	fluor	36	318.50	0.04	38.77	0.03	9.35	0.00	1330.93	0.00	1579.77	0.00	0.12
AG042	fit_no7_AG042_20201013	588			37	4152.18	4.19	18.23	0.01	13.72	0.03	1333.47	0.00	1581.04	0.00	0.00

AG042	fit_no8_AG042_20201013		428	fluor	36	200.77	8.44	58.63	8.13	3.82	0.28	1349.97	0.00	1581.04	0.00	0.28
AG042	fit_no9_AG042_20201013	556			37	174.00	0.08	24.76	0.01	7.00	0.00	1361.40	0.00	1579.77	0.00	0.12
AG116_1	fit_no10_AG116_20201013	559			37	139.46	0.25	24.23	0.21	5.99	0.01	1363.89	0.00	1581.01	0.00	0.15
AG116_1	fit_no11_AG116_20201013	528			37	126.21	0.05	31.02	0.03	4.82	0.01	1361.35	0.00	1581.01	0.00	0.22
AG116_1	fit_no12_AG116_20201013	579			37	199.80	0.13	20.11	0.01	9.51	0.01	1360.08	0.00	1581.01	0.00	0.09
AG116_1	fit_no13_AG116_20201013		500	fluor	36	250.44	0.59	37.66	0.23	4.13	0.03	1360.08	0.00	1583.55	0.00	0.14
AG116_1	fit_no14_AG116_20201013	568			37	171.22	4.06	22.20	0.10	6.01	0.19	1356.27	0.00	1581.01	0.00	0.13
AG116_1	fit_no15_AG116_20201013	568			37	163.02	0.01	22.35	0.00	9.64	0.00	1360.08	0.00	1581.01	0.00	0.13
AG116_1	fit_no16_AG116_20201013	576			37	169.19	4.93	20.72	0.05	7.74	0.01	1356.27	0.00	1579.74	0.00	0.10
AG116_1	fit_no17_AG116_20201013	558			37	181.88	0.02	24.45	0.01	4.88	0.00	1351.19	0.00	1582.28	0.00	0.13
AG116_1	fit_no18_AG116_20201013	561			37	216.12	0.32	23.77	0.04	5.06	0.01	1355.00	0.00	1581.01	0.00	0.10
AG116_1	fit_no19_AG116_20201013	579			37	199.20	0.02	20.17	0.01	14.70	0.01	1365.16	0.00	1579.74	0.00	0.08
AG116_1	fit_no1_AG116_20201013	554			37	173.74	1.28	25.17	0.27	5.84	0.08	1358.81	0.00	1582.28	0.00	0.14
AG116_1	fit_no20_AG116_20201013		580	bsl failure	37	4684.88	868.76	19.88	0.69	5.82	0.31	1361.35	0.00	1581.01	0.00	0.00
AG116_1	fit_no21_AG116_20201013		250	Phase Int	36	190.12	0.29	36.73	0.04	2.48	0.01	1361.35	0.00	1581.01	0.00	0.18
AG116_1	fit_no22_AG116_20201013	536			37	148.24	0.02	29.13	0.01	3.43	0.00	1363.89	0.00	1582.28	0.00	0.18
AG116_1	fit_no23_AG116_20201013	564			37	196.26	0.26	23.13	0.03	5.09	0.00	1362.62	0.00	1581.01	0.00	0.11
AG116_1	fit_no24_AG116_20201013	550			37	262.40	0.13	26.02	0.06	4.25	0.01	1362.62	0.00	1582.28	0.00	0.09
AG116_1	fit_no25_AG116_20201013	579			37	263.23	0.05	20.08	0.01	8.09	0.00	1364.61	0.00	1580.65	0.00	0.07
AG116_1	fit_no26_AG116_20201013	553			37	176.87	1.44	25.40	0.09	3.95	0.01	1360.08	0.00	1579.74	0.00	0.14
AG116_1	fit_no27_AG116_20201013	568			37	257.31	0.14	22.22	0.00	7.14	0.01	1362.62	0.00	1581.01	0.00	0.08
AG116_1	fit_no28_AG116_20201013	508			36	263.37	0.10	35.63	0.10	4.44	0.01	1351.19	0.00	1581.01	0.00	0.14
AG116_1	fit_no29_AG116_20201013	590			37	752.73	0.03	17.99	0.00	13.51	0.00	1346.12	0.00	1581.01	0.00	0.02
AG116_1	fit_no2_AG116_20201013	575			37	174.73	0.06	20.90	0.02	9.70	0.02	1360.08	0.00	1579.74	0.00	0.12
AG116_1	fit_no30_AG116_20201013	576			37	242.84	0.04	20.76	0.00	9.58	0.00	1357.54	0.00	1581.01	0.00	0.08
AG116_1	fit_no3_AG116_20201013	545			37	153.54	6.14	27.09	0.14	4.41	0.01	1361.35	0.00	1582.28	0.00	0.18
AG116_1	fit_no4_AG116_20201013	568			37	235.96	2.28	22.21	0.26	8.10	0.05	1349.93	0.00	1581.01	0.00	0.09
AG116_1	fit_no5_AG116_20201013	571			37	188.66	0.02	21.59	0.00	10.99	0.00	1358.81	0.00	1581.01	0.00	0.11
AG116_1	fit_no6_AG116_20201013	572			37	185.42	0.21	21.55	0.04	7.08	0.02	1360.08	0.00	1582.28	0.00	0.10
AG116_1	fit_no7_AG116_20201013	576			37	155.93	0.21	20.73	0.02	10.03	0.01	1356.27	0.00	1581.01	0.00	0.13
AG116_1	fit_no8_AG116_20201013	555			37	120.50	0.03	24.96	0.03	6.73	0.00	1352.46	0.00	1581.01	0.00	0.21
AG116_1	fit_no9_AG116_20201013	555			37	168.36	0.14	24.91	0.03	7.35	0.02	1362.62	0.00	1582.28	0.00	0.12
AG067	fit_no10_AG067_20201015		402	bsl failure	36	286.16	0.65	68.05	0.32	3.07	0.01	1365.21	0.00	1581.04	0.00	0.23
AG067	fit_no11_AG067_20201015	541			37	132.40	0.11	28.01	0.08	6.86	0.01	1355.05	0.00	1581.04	0.00	0.21
AG067	fit_no12_AG067_20201015	475			36	100.71	0.23	44.09	0.10	4.47	0.01	1349.97	0.00	1579.77	0.00	0.44
AG067	fit_no13_AG067_20201015	550			37	159.62	0.09	26.16	0.01	7.90	0.01	1353.78	0.00	1581.04	0.00	0.16
AG067	fit_no14_AG067_20201015	524			37	318.87	0.42	31.88	0.01	4.20	0.00	1423.61	0.00	1582.31	0.00	0.01
AG067	fit_no15_AG067_20201015	555			37	349.39	0.60	24.99	0.02	7.52	0.01	1362.67	0.00	1581.04	0.00	0.06
AG067	fit_no16_AG067_20201015	558			37	291.95	0.06	24.36	0.01	6.12	0.00	1328.39	0.00	1581.04	0.00	0.06
AG067	fit_no17_AG067_20201015	504			36	126.72	0.23	36.55	0.10	5.08	0.01	1353.78	0.00	1583.58	0.00	0.29
AG067	fit_no1_AG067_20201015	543			37	307.80	0.03	27.56	0.01	4.47	0.00	1349.97	0.00	1581.04	0.00	0.07

AG067	fit_no2_AG067_20201015	547			37	137.03	0.02	26.80	0.01	5.46	0.00	1352.51	0.00	1582.31	0.00	0.20
AG067	fit_no3_AG067_20201015	553			37	223.57	0.05	25.50	0.00	9.21	0.01	1355.05	0.00	1581.04	0.00	0.11
AG067	fit_no4_AG067_20201015	565			37	299.11	0.52	22.86	0.05	9.49	0.27	1351.24	0.00	1582.31	0.00	0.07
AG067	fit_no5_AG067_20201015	553			37	142.32	0.83	25.44	0.25	7.52	0.06	1355.05	0.00	1582.31	0.00	0.18
AG067	fit_no6_AG067_20201015	591			37	4093.37	0.85	17.83	0.00	14.36	0.00	1435.04	0.00	1581.04	0.00	0.00
AG067	fit_no7_AG067_20201015	582			37	335.76	0.07	19.58	0.00	10.92	0.00	1352.51	0.00	1581.04	0.00	0.06
AG067	fit_no8_AG067_20201015	526			37	131.24	0.25	31.28	0.07	4.83	0.00	1352.51	0.00	1583.58	0.00	0.24
AG067	fit_no9_AG067_20201015	541			37	246.84	0.20	28.04	0.03	7.40	0.01	1352.51	0.00	1581.04	0.00	0.11
DC0514	fit_no10_DC0514_20191218	233			37	202.75	0.29	88.45	0.28	0.78	0.00	1336.01	0.00	1606.43	0.00	0.44
DC0514	fit_no11_DC0514_20191218	225			37	207.88	0.02	90.99	0.01	0.78	0.00	1338.55	0.00	1606.43	0.00	0.44
DC0514	fit_no12_DC0514_20191218	261			36	180.55	0.01	64.86	0.01	0.75	0.00	1332.20	0.00	1605.16	0.00	0.35
DC0514	fit_no13_DC0514_20191218	227			37	206.73	0.16	91.19	0.13	0.79	0.00	1338.55	0.00	1605.16	0.00	0.44
DC0514	fit_no14_DC0514_20191218	229			37	205.65	0.69	91.77	0.61	0.79	0.00	1337.28	0.00	1605.16	0.00	0.45
DC0514	fit_no15_DC0514_20191218	226			37	207.57	0.23	91.21	0.03	0.78	0.00	1335.39	0.00	1604.79	0.00	0.44
DC0514	fit_no16_DC0514_20191218	241			37	197.34	12.57	81.87	9.98	0.75	0.02	1336.01	0.00	1605.16	0.00	0.41
DC0514	fit_no17_DC0514_20191218	224			37	208.77	0.23	89.63	0.39	0.80	0.00	1334.74	0.00	1605.16	0.00	0.43
DC0514	fit_no18_DC0514_20191218	226			37	207.40	0.10	90.51	0.13	0.78	0.00	1338.55	0.00	1606.43	0.00	0.44
DC0514	fit_no19_DC0514_20191218		293	fluor	36	143.87	10.60	59.94	6.94	0.66	0.02	1329.66	0.00	1606.43	0.00	0.41
DC0514	fit_no1_DC0514_20191218	227			37	207.13	0.37	89.84	0.15	0.81	0.00	1334.74	0.00	1605.16	0.00	0.43
DC0514	fit_no20_DC0514_20191218	228			37	206.17	0.56	87.83	0.47	0.77	0.00	1339.82	0.00	1606.43	0.00	0.42
DC0514	fit_no21_DC0514_20191218	225			37	207.97	0.36	89.50	0.36	0.78	0.00	1339.82	0.00	1605.16	0.00	0.43
DC0514	fit_no22_DC0514_20191218		302	fluor	36	133.89	8.12	56.92	4.83	0.61	0.02	1330.93	0.00	1606.43	0.00	0.42
DC0514	fit_no23_DC0514_20191218		289	bsl failure	36	149.25	13.71	64.58	8.34	0.65	0.03	1331.35	1.20	1606.43	0.00	0.43
DC0514	fit_no24_DC0514_20191218	227			37	206.75	0.04	91.78	0.03	0.79	0.00	1337.28	0.00	1605.16	0.00	0.44
DC0514	fit_no25_DC0514_20191218	233			37	203.00	2.56	87.77	2.04	0.79	0.00	1339.82	0.00	1606.43	0.00	0.43
DC0514	fit_no2_DC0514_20191218	227			37	206.97	0.15	88.73	0.13	0.79	0.00	1338.55	0.00	1605.16	0.00	0.43
DC0514	fit_no3_DC0514_20191218	224			37	208.53	0.80	87.34	0.77	0.79	0.00	1338.55	0.00	1605.16	0.00	0.42
DC0514	fit_no4_DC0514_20191218	224			37	208.46	0.62	92.05	0.10	0.80	0.00	1337.28	0.00	1605.16	0.00	0.44
DC0514	fit_no5_DC0514_20191218	223			37	209.43	0.32	91.57	0.21	0.81	0.00	1336.01	0.00	1605.16	0.00	0.44
DC0514	fit_no6_DC0514_20191218	221			37	210.68	0.11	91.53	0.08	0.80	0.00	1334.74	0.00	1605.16	0.00	0.43
DC0514	fit_no7_DC0514_20191218	221			37	210.41	0.23	92.79	0.16	0.82	0.00	1338.55	0.00	1603.89	0.00	0.44
DC0514	fit_no8_DC0514_20191218	227			37	206.98	0.43	91.13	0.44	0.80	0.00	1338.55	0.00	1605.16	0.00	0.44
DC0514	fit_no9_DC0514_20191218	234			37	202.24	2.25	88.79	1.32	0.77	0.00	1336.01	0.00	1605.16	0.00	0.44
AG080	fit_no10_AG080_20201015	599			37	4585.85	89.81	16.19	0.05	12.61	0.20	1426.11	0.00	1581.01	0.00	0.00
AG080	fit_no11_AG080_20201015	586			37	3719.12	2.89	18.77	0.01	12.16	0.01	1446.42	0.00	1581.01	0.00	0.01
AG080	fit_no12_AG080_20201015	566			37	1845.54	10.06	22.63	0.01	6.01	0.02	1443.88	0.00	1582.28	0.00	0.01
AG080	fit_no13_AG080_20201015	604			37	4591.38	17.85	15.33	0.01	16.61	0.09	1441.34	0.00	1581.01	0.00	0.00
AG080	fit_no14_AG080_20201015	594			37	4431.43	1.81	17.08	0.01	8.72	0.00	1442.61	0.00	1582.28	0.00	0.00
AG080	fit_no15_AG080_20201015	583			37	6181.38	168.41	19.32	0.05	7.64	0.01	1440.07	0.00	1583.55	0.00	0.00
AG080	fit_no16_AG080_20201015	593			37	4410.72	3.72	17.36	0.00	9.31	0.00	1442.61	0.00	1581.01	0.00	0.00
AG080	fit_no17_AG080_20201015	595			37	5081.96	300.65	16.94	0.11	9.13	0.06	1438.80	0.00	1582.28	0.00	0.00

AG080	fit_no18_AG080_20201015		482	bsl failure	36	339.35	0.47	42.29	0.68	4.01	0.06	1432.45	0.00	1581.01	0.00	0.05
AG080	fit_no19_AG080_20201015	537			37	1544.37	1.28	28.84	0.05	3.61	0.01	1442.61	0.00	1581.01	0.00	0.02
AG080	fit_no1_AG080_20201015	581			37	4464.57	4.27	19.61	0.01	5.44	0.00	1438.80	0.00	1581.01	0.00	0.00
AG080	fit_no20_AG080_20201015	589			37	318.15	0.12	18.17	0.00	12.73	0.00	1361.35	0.00	1581.01	0.00	0.05
AG080	fit_no21_AG080_20201015	589			37	3845.35	7.74	18.17	0.01	13.18	0.04	1442.61	0.00	1581.01	0.00	0.00
AG080	fit_no22_AG080_20201015	574			37	261.92	4.56	21.13	0.35	6.18	0.11	1352.46	0.00	1583.55	0.00	0.08
AG080	fit_no23_AG080_20201015	588			37	4245.61	4.26	18.35	0.01	8.09	0.00	1335.96	0.00	1582.28	0.00	0.00
AG080	fit_no24_AG080_20201015	587			37	370.51	0.06	18.58	0.00	12.14	0.00	1363.89	0.00	1581.01	0.00	0.04
AG080	fit_no25_AG080_20201015	591			37	4262.85	12.12	17.65	0.02	9.08	0.03	1438.80	0.00	1579.74	0.00	0.00
AG080	fit_no26_AG080_20201015	582			37	551.79	37.07	19.45	1.13	8.11	0.70	1356.27	0.00	1582.28	0.00	0.03
AG080	fit_no27_AG080_20201015	585			37	4113.82	2.57	18.84	0.01	6.29	0.00	1445.15	0.00	1583.55	0.00	0.00
AG080	fit_no28_AG080_20201015	516			37	342.84	1.96	33.77	1.16	4.80	0.12	1441.34	0.00	1582.28	0.00	0.03
AG080	fit_no29_AG080_20201015	610			37	4834.58	1.85	14.22	0.01	18.65	0.01	1440.07	0.00	1581.01	0.00	0.00
AG080	fit_no2_AG080_20201015	565			37	284.38	0.12	23.00	0.01	4.83	0.00	1351.19	0.00	1581.01	0.00	0.08
AG080	fit_no30_AG080_20201015	593			37	5755.62	54.07	17.44	0.01	7.13	0.00	1445.15	0.00	1581.01	0.00	0.00
AG080	fit_no3_AG080_20201015	597			37	4106.61	4.13	16.66	0.01	14.80	0.02	1318.18	0.00	1581.01	0.00	0.00
AG080	fit_no4_AG080_20201015	588			37	3743.82	7.54	18.35	0.04	12.60	0.04	1443.88	0.00	1581.01	0.00	0.01
AG080	fit_no5_AG080_20201015	576			37	7374.81	422.19	20.67	0.13	4.50	0.03	1306.76	0.00	1582.28	0.00	0.00
AG080	fit_no6_AG080_20201015	593			37	4048.40	10.29	17.44	0.00	13.27	0.05	1445.15	0.00	1581.01	0.00	0.00
AG080	fit_no7_AG080_20201015	593			37	4099.34	1.09	17.42	0.00	13.98	0.01	1448.96	0.00	1581.01	0.00	0.00
AG080	fit_no8_AG080_20201015	598			37	6187.05	49.34	16.47	0.03	9.10	0.08	1448.96	0.00	1582.28	0.00	0.00
AG080	fit_no9_AG080_20201015	587			37	3721.64	13.20	18.60	0.07	12.28	0.06	1431.18	0.00	1581.01	0.00	0.00
AG097_3	fit_no10_AG097_3_20191218	367			36	84.25	0.05	121.67	0.10	1.00	0.00	1351.24	0.00	1601.35	0.00	1.44
AG097_3	fit_no11_AG097_3_20191218	376			36	79.69	0.07	126.28	0.10	1.12	0.00	1349.97	0.00	1596.27	0.00	1.59
AG097_3	fit_no12_AG097_3_20191218	356			36	90.11	0.09	124.88	0.14	1.23	0.00	1353.78	0.00	1589.92	0.00	1.39
AG097_3	fit_no1_AG097_3_20191218	384			36	75.71	0.12	119.57	0.24	1.13	0.00	1349.97	0.00	1605.16	0.00	1.65
AG097_3	fit_no2_AG097_3_20191218	367			36	84.25	6.21	126.28	4.76	1.08	0.02	1352.51	0.00	1598.81	0.00	1.50
AG097_3	fit_no3_AG097_3_20191218	385			36	75.30	0.03	121.48	0.02	1.15	0.00	1348.70	0.00	1598.81	0.00	1.63
AG097_3	fit_no4_AG097_3_20191218	359			36	88.39	0.14	125.80	0.14	1.11	0.00	1349.97	0.00	1597.54	0.00	1.43
AG097_3	fit_no5_AG097_3_20191218	341			36	99.22	0.05	125.92	0.10	1.01	0.00	1352.51	0.00	1600.08	0.00	1.25
AG097_3	fit_no6_AG097_3_20191218	419			36	61.85	0.00	119.58	0.01	1.28	0.00	1348.70	0.00	1593.73	0.00	1.96
AG097_3	fit_no7_AG097_3_20191218	363			36	85.98	1.18	120.98	0.44	1.11	0.00	1353.78	0.00	1600.08	0.00	1.41
AG097_3	fit_no8_AG097_3_20191218	367			36	84.09	0.03	109.24	0.03	1.10	0.00	1352.51	0.00	1596.27	0.00	1.30
AG097_3	fit_no9_AG097_3_20191218	351			36	93.29	0.11	144.50	0.10	1.08	0.00	1349.97	0.00	1596.27	0.00	1.55
AG105_1	fit_no10_AG105_1_20201018	407			36	66.10	0.00	101.23	0.01	1.97	0.00	1349.97	0.00	1588.66	0.00	1.54
AG105_1	fit_no11_AG105_1_20201018	396			36	70.47	0.20	112.21	0.29	1.84	0.00	1348.70	0.00	1587.39	0.00	1.59
AG105_1	fit_no12_AG105_1_20201018	390			36	73.15	0.04	106.45	0.05	1.87	0.00	1382.98	0.00	1586.12	0.00	0.54
AG105_1	fit_no13_AG105_1_20201018	396			36	70.70	0.02	92.07	0.02	2.12	0.00	1349.97	0.00	1587.39	0.00	1.29
AG105_1	fit_no14_AG105_1_20201018	405			36	66.84	0.09	106.63	0.07	1.95	0.00	1348.70	0.00	1588.66	0.00	1.59
AG105_1	fit_no15_AG105_1_20201018	404			36	67.51	0.01	99.24	0.02	1.96	0.00	1348.70	0.00	1586.12	0.00	1.46
AG105_1	fit_no16_AG105_1_20201018	402			36	68.08	0.00	72.36	0.01	2.48	0.00	1351.21	0.00	1586.09	0.00	1.06

AG105_1	fit_no17_AG105_1_20201018	389	36	73.77	1.88	76.48	1.80	2.34	0.03	1352.48	0.00	1587.36	0.00	1.04
AG105_1	fit_no18_AG105_1_20201018	406	36	66.44	0.03	91.67	0.03	2.18	0.00	1351.21	0.00	1584.82	0.00	1.39
AG105_1	fit_no19_AG105_1_20201018	422	36	60.71	0.01	81.92	0.01	2.41	0.00	1351.21	0.00	1587.36	0.00	1.35
AG105_1	fit_no1_AG105_1_20201018	398	36	69.88	0.01	101.66	0.02	1.91	0.00	1352.51	0.00	1587.39	0.00	1.44
AG105_1	fit_no20_AG105_1_20201018	395	36	71.01	0.01	75.14	0.02	2.62	0.00	1352.48	0.00	1587.36	0.00	1.06
AG105_1	fit_no21_AG105_1_20201018	401	36	68.55	0.00	67.79	0.01	2.79	0.00	1351.21	0.00	1586.09	0.00	0.99
AG105_1	fit_no2_AG105_1_20201018	400	36	68.78	0.01	101.17	0.02	1.98	0.00	1352.51	0.00	1588.66	0.00	1.48
AG105_1	fit_no3_AG105_1_20201018	403	36	67.76	0.04	104.63	0.08	1.89	0.00	1349.97	0.00	1584.85	0.00	1.56
AG105_1	fit_no4_AG105_1_20201018	400	36	69.16	0.14	118.11	0.25	1.76	0.00	1353.78	0.00	1588.66	0.00	1.68
AG105_1	fit_no5_AG105_1_20201018	400	36	68.98	0.01	103.93	0.04	1.84	0.00	1349.97	0.00	1588.66	0.00	1.51
AG105_1	fit_no6_AG105_1_20201018	393	36	71.87	0.00	78.25	0.01	2.56	0.00	1349.97	0.00	1587.39	0.00	1.09
AG105_1	fit_no7_AG105_1_20201018	386	36	75.04	0.01	106.65	0.03	1.86	0.00	1348.70	0.00	1586.12	0.00	1.42
AG105_1	fit_no8_AG105_1_20201018	393	36	71.72	0.02	122.07	0.01	1.65	0.00	1351.24	0.00	1586.12	0.00	1.71
AG105_1	fit_no9_AG105_1_20201018	400	36	69.12	0.13	110.51	0.02	1.79	0.00	1351.24	0.00	1588.66	0.00	1.60
AG109_1	fit_no1_AG109_1_20201021	575	37	332.45	0.30	20.89	0.01	7.99	0.00	1341.09	0.00	1582.31	0.00	0.05
AG109_1	fit_no2_AG109_1_20201021	593	37	427.55	0.41	17.36	0.00	15.20	0.00	1355.05	0.00	1582.31	0.00	0.03
AG109_1	fit_no3_AG109_1_20201021	573	37	359.08	1.52	21.32	1.39	10.14	0.94	1361.40	0.00	1581.04	0.00	0.06
AG109_1	fit_no4_AG109_1_20201021	585	37	239.03	2.92	18.81	0.10	10.22	0.05	1352.51	0.00	1581.04	0.00	0.07
AG109_1	fit_no5_AG109_1_20201021	567	37	469.14	0.11	22.42	0.00	5.19	0.00	1446.46	0.00	1582.31	0.00	0.01
AG109_1	fit_no6_AG109_1_20201021	592	37	368.20	0.01	17.47	0.01	10.74	0.02	1361.40	0.00	1581.04	0.00	0.04
AG109_1	fit_no7_AG109_1_20201021	564	37	414.56	0.32	23.04	0.03	6.07	0.01	1342.36	0.00	1582.31	0.00	0.05
AG101_1	fit_no1_AG101_1_20191218	463	36	96.22	0.15	47.64	0.11	4.06	0.01	1351.24	0.00	1582.31	0.00	0.50
AG101_1	fit_no2_AG101_1_20191218	491	36	92.69	0.03	40.01	0.04	4.90	0.01	1352.51	0.00	1582.31	0.00	0.43
AG101_1	fit_no3_AG101_1_20191218	471	36	92.16	0.49	45.40	0.18	4.62	0.02	1351.24	0.00	1582.31	0.00	0.49
AG103_2	fit_no10_AG103_2_20201021	468	36	96.60	0.06	46.20	0.04	4.59	0.00	1351.21	0.00	1582.28	0.00	0.48
AG103_2	fit_no11_AG103_2_20201021	499	36	128.43	0.02	37.88	0.01	5.93	0.00	1352.48	0.00	1582.28	0.00	0.30
AG103_2	fit_no12_AG103_2_20201021	446	36	84.39	0.14	52.57	0.11	4.00	0.00	1351.21	0.00	1582.28	0.00	0.62
AG103_2	fit_no13_AG103_2_20201021	486	36	92.35	0.16	41.31	0.07	5.13	0.00	1353.75	0.00	1584.82	0.00	0.45
AG103_2	fit_no14_AG103_2_20201021	465	36	83.54	0.03	47.00	0.01	4.52	0.00	1349.94	0.00	1582.28	0.00	0.56
AG103_2	fit_no15_AG103_2_20201021	494	36	111.83	1.69	39.14	0.72	5.21	0.08	1352.48	0.00	1582.28	0.00	0.35
AG103_2	fit_no16_AG103_2_20201021	477	36	141.44	0.03	43.65	0.01	4.91	0.00	1353.75	0.00	1583.55	0.00	0.31
AG103_2	fit_no17_AG103_2_20201021	481	36	99.08	2.23	42.43	0.96	5.20	0.12	1351.21	0.00	1584.82	0.00	0.43
AG103_2	fit_no18_AG103_2_20201021	490	36	102.55	0.00	40.24	0.01	5.24	0.00	1351.21	0.00	1583.55	0.00	0.39
AG103_2	fit_no19_AG103_2_20201021	457	36	21.07	0.43	49.30	0.68	5.02	0.06	1379.14	0.00	1583.55	0.00	2.34
AG103_2	fit_no1_AG103_2_20201021	467	36	92.37	0.04	46.49	0.28	4.45	0.01	1349.94	0.00	1583.55	0.00	0.49
AG103_2	fit_no20_AG103_2_20201021	451	36	126.21	0.59	51.28	0.26	3.83	0.01	1351.21	0.00	1583.55	0.00	0.40
AG103_2	fit_no21_AG103_2_20201021	482	36	97.44	0.02	42.32	0.01	4.48	0.00	1351.24	0.00	1584.85	0.00	0.44
AG103_2	fit_no22_AG103_2_20201021	475	36	111.25	0.11	44.09	0.03	4.90	0.01	1355.05	0.00	1582.31	0.00	0.39
AG103_2	fit_no23_AG103_2_20201021	490	36	97.92	0.03	40.24	0.03	5.10	0.00	1351.24	0.00	1583.58	0.00	0.41
AG103_2	fit_no24_AG103_2_20201021	475	36	93.82	0.01	44.14	0.02	4.91	0.00	1352.51	0.00	1583.58	0.00	0.47
AG103_2	fit_no25_AG103_2_20201021	465	36	96.79	0.88	46.93	0.55	4.43	0.06	1349.97	0.00	1583.58	0.00	0.48

AG103_2	fit_no26_AG103_2_20201021		442	phase inter	36	166.09	0.48	53.88	0.04	5.17	0.00	1351.24	0.00	1583.58	0.00	0.32
AG103_2	fit_no2_AG103_2_20201021	478			36	101.95	0.03	43.28	0.00	4.79	0.00	1351.21	0.00	1583.55	0.00	0.42
AG103_2	fit_no3_AG103_2_20201021	445			36	122.72	1.53	53.10	0.61	4.51	0.03	1352.48	0.00	1584.82	0.00	0.43
AG103_2	fit_no4_AG103_2_20201021	480			36	90.82	3.62	42.91	2.27	4.75	0.21	1353.75	0.00	1583.55	0.00	0.47
AG103_2	fit_no5_AG103_2_20201021		417	bsl failure	36	115.61	0.50	62.56	0.38	4.02	0.01	1353.75	0.00	1584.82	0.00	0.54
AG103_2	fit_no6_AG103_2_20201021	481			36	98.74	0.02	42.45	0.00	4.79	0.00	1349.94	0.00	1583.55	0.00	0.42
AG103_2	fit_no7_AG103_2_20201021	467			36	100.25	0.21	46.52	0.08	4.74	0.00	1352.48	0.00	1584.82	0.00	0.46
AG103_2	fit_no8_AG103_2_20201021	464			36	101.53	0.04	47.41	0.02	4.48	0.00	1351.21	0.00	1584.82	0.00	0.47
AG103_2	fit_no9_AG103_2_20201021	486			36	111.71	0.01	41.34	0.00	5.03	0.00	1351.21	0.00	1583.55	0.00	0.37
AG027	fit_no10_AG027_20210211	301			36	134.53	3.71	72.41	1.96	0.65	0.01	1333.47	0.00	1606.01	1.20	0.54
AG027	fit_no11_AG027_20210211	305			36	130.86	0.19	72.59	0.15	0.65	0.00	1334.74	0.00	1607.70	0.00	0.56
AG027	fit_no12_AG027_20210211	305			36	130.76	0.07	71.65	0.03	0.65	0.00	1332.20	0.00	1606.43	0.00	0.55
AG027	fit_no13_AG027_20210211	310			36	125.02	0.27	74.82	0.29	0.69	0.00	1336.01	0.00	1605.16	0.00	0.60
AG027	fit_no14_AG027_20210211	294			36	143.78	2.13	83.73	1.24	0.67	0.00	1328.39	0.00	1606.43	0.00	0.57
AG027	fit_no15_AG027_20210211	314			36	121.47	0.69	68.50	0.82	0.65	0.00	1336.01	0.00	1605.16	0.00	0.56
AG027	fit_no16_AG027_20210211	280			36	160.37	0.10	93.80	0.07	0.70	0.00	1330.93	0.00	1606.43	0.00	0.58
AG027	fit_no17_AG027_20210211	305			36	130.77	1.49	72.98	1.50	0.66	0.00	1334.74	0.00	1605.16	0.00	0.56
AG027	fit_no18_AG027_20210211	292			36	145.05	1.65	86.63	1.13	0.68	0.00	1332.20	0.00	1606.43	0.00	0.60
AG027	fit_no1_AG027_20210211	304			36	132.08	0.11	67.08	0.09	0.65	0.00	1334.74	0.00	1605.16	0.00	0.51
AG027	fit_no2_AG027_20210211	316			36	119.15	0.12	66.85	0.11	0.66	0.00	1330.93	0.00	1605.16	0.00	0.56
AG027	fit_no3_AG027_20210211	322			36	113.82	0.08	63.13	0.01	0.63	0.00	1334.74	0.00	1605.16	0.00	0.56
AG027	fit_no4_AG027_20210211	283			36	156.59	0.75	95.89	0.74	0.74	0.00	1329.66	0.00	1606.43	0.00	0.61
AG027	fit_no5_AG027_20210211	304			36	132.21	0.08	75.18	0.06	0.65	0.00	1334.74	0.00	1607.70	0.00	0.57
AG027	fit_no6_AG027_20210211	299			36	137.26	0.95	75.70	1.11	0.62	0.00	1332.20	0.00	1607.70	0.00	0.55
AG027	fit_no7_AG027_20210211	305			36	130.59	0.87	65.89	0.26	0.65	0.00	1333.47	0.00	1606.43	0.00	0.50
AG027	fit_no8_AG027_20210211	289			36	149.49	0.34	88.24	0.26	0.65	0.00	1332.20	0.00	1606.43	0.00	0.59
AG027	fit_no9_AG027_20210211	317			36	118.58	0.03	57.03	0.03	0.63	0.00	1336.01	0.00	1605.16	0.00	0.48
AG056	fit_no10_AG056_20200131	461			36	82.75	0.03	48.07	0.01	4.20	0.00	1349.97	0.00	1582.31	0.00	0.58
AG056	fit_no11_AG056_20200131	434			36	81.44	0.01	56.39	0.01	3.50	0.00	1351.24	0.00	1584.85	0.00	0.70
AG056	fit_no12_AG056_20200131	439			36	93.09	0.02	54.80	0.02	3.61	0.00	1353.78	0.00	1583.58	0.00	0.59
AG056	fit_no13_AG056_20200131	429			36	91.71	0.01	58.16	0.02	3.45	0.00	1351.24	0.00	1582.31	0.00	0.64
AG056	fit_no14_AG056_20200131	447			36	91.10	0.07	52.52	0.05	3.79	0.00	1349.97	0.00	1581.04	0.00	0.59
AG056	fit_no15_AG056_20200131	447			36	90.30	0.01	52.50	0.01	3.58	0.00	1353.78	0.00	1583.58	0.00	0.58
AG056	fit_no16_AG056_20200131	469			36	96.16	0.02	45.97	0.01	4.22	0.00	1355.05	0.00	1584.85	0.00	0.47
AG056	fit_no17_AG056_20200131	471			36	94.15	0.05	45.26	0.07	3.76	0.00	1351.24	0.00	1582.31	0.00	0.48
AG056	fit_no18_AG056_20200131	462			36	92.35	0.91	47.81	0.33	3.73	0.03	1352.51	0.00	1584.85	0.00	0.52
AG056	fit_no19_AG056_20200131	455			36	126.47	0.03	49.83	0.05	4.17	0.00	1349.97	0.00	1584.85	0.00	0.39
AG056	fit_no1_AG056_20200131	475			36	90.90	0.01	44.17	0.01	3.59	0.00	1353.78	0.00	1582.31	0.00	0.49
AG056	fit_no20_AG056_20200131	452			36	121.85	0.02	50.73	0.00	4.09	0.00	1349.97	0.00	1582.31	0.00	0.41
AG056	fit_no21_AG056_20200131	491			36	118.75	0.04	39.93	0.01	4.20	0.00	1352.51	0.00	1583.58	0.00	0.34
AG056	fit_no22_AG056_20200131	454			36	83.09	0.05	50.12	0.04	4.21	0.00	1353.75	0.00	1583.55	0.00	0.60

AG056	fit_no23_AG056_20200131	468			36	103.44	0.03	46.20	0.04	3.84	0.00	1353.75	0.00	1584.82	0.00	0.45
AG056	fit_no24_AG056_20200131		384	fluor	36	75.62	0.14	56.30	0.08	2.99	0.00	1351.21	0.00	1586.09	0.00	0.75
AG056	fit_no25_AG056_20200131	474			36	125.03	0.02	44.57	0.01	4.45	0.00	1349.94	0.00	1583.55	0.00	0.35
AG056	fit_no26_AG056_20200131	430			36	109.59	0.03	57.88	0.03	3.33	0.00	1353.75	0.00	1582.28	0.00	0.54
AG056	fit_no27_AG056_20200131	429			36	115.47	0.02	58.11	0.01	3.69	0.00	1349.94	0.00	1582.28	0.00	0.50
AG056	fit_no28_AG056_20200131	452			36	117.30	0.56	50.95	0.32	3.85	0.02	1355.02	0.00	1584.82	0.00	0.43
AG056	fit_no2_AG056_20200131	464			36	92.87	0.00	47.26	0.00	3.94	0.00	1355.02	0.00	1582.28	0.00	0.51
AG056	fit_no3_AG056_20200131	478			36	83.69	0.02	43.25	0.01	3.96	0.00	1349.97	0.00	1583.58	0.00	0.51
AG056	fit_no4_AG056_20200131	451			36	82.39	0.02	51.27	0.02	3.24	0.00	1351.24	0.00	1582.31	0.00	0.62
AG056	fit_no5_AG056_20200131	497			36	113.51	0.33	38.29	0.16	5.15	0.01	1351.24	0.00	1583.58	0.00	0.34
AG056	fit_no6_AG056_20200131	467			36	79.60	0.02	46.41	0.01	3.99	0.00	1348.70	0.00	1583.58	0.00	0.57
AG056	fit_no7_AG056_20200131	471			36	84.67	0.01	45.33	0.01	3.95	0.00	1351.24	0.00	1583.58	0.00	0.54
AG056	fit_no8_AG056_20200131	473			36	89.57	0.01	44.68	0.02	3.94	0.00	1352.51	0.00	1582.31	0.00	0.50
AG056	fit_no9_AG056_20200131	439			36	99.21	0.04	54.85	0.02	3.56	0.00	1351.24	0.00	1584.85	0.00	0.56
AG138	fit_no1_AG138_20210212	325			36	111.74	0.03	106.77	0.02	0.82	0.00	1344.86	0.00	1602.60	0.00	0.96
AG138	fit_no2_AG138_20210212	312			36	123.17	0.48	123.13	0.46	0.89	0.00	1344.86	0.00	1606.41	0.00	1.01
AG138	fit_no3_AG138_20210212	293			36	144.43	0.38	135.61	0.25	0.87	0.00	1347.40	0.00	1605.14	0.00	0.94
AG138	fit_no4_AG138_20210212	312			36	123.27	0.05	125.79	0.16	0.91	0.00	1344.86	0.00	1602.60	0.00	1.02
AG138	fit_no5_AG138_20210212	319			36	116.32	0.70	109.08	0.49	0.82	0.00	1347.40	0.00	1606.41	0.00	0.94
AG138	fit_no6_AG138_20210212	297			36	139.25	1.38	126.52	1.79	0.85	0.00	1346.13	0.00	1605.14	0.00	0.91
AG138	fit_no7_AG138_20210212	302			36	134.27	0.07	135.42	0.06	0.84	0.00	1345.55	0.00	1603.52	0.00	1.01

ID: sequential sample number, sample, and date of processing (not collection). Any estimates excluded from calculation indicated with reasoning. All other data as means and 1std.
Raw data (Wave# and Intensity) for spectra may be obtained by writing to the author.

Table C.2 Example of standard inputs (IFORS_aux) for automated iterative fitting of RSCM spectra. Reported as per Lunsdorf et al. (2017) for replicability.

[Control]	**[Constraints]**	**[Readout_type]**	**[Ignored_peak_ranges]***	**[Estimate_temp]**
start_wn = 700	min_width = 1	Cm_readout = yes	range_1 = 1000, 1200	p1 = 0.95
stop_wn = 2000	max_width = 60	Peak_parameters = yes	range_2 = 1700, 1800	p2 = 0.9
seed = 0	min_dist = 5	Fitted_values = yes	range_3 = 0, 0	model = cubic
repetitions = 3	baseline_mode = polynom		range_4 = 0, 0	plot = yes
plotting = yes	polynom_order = 5	[Readout_opts]		
Gui = no	window_size = 0.2	mineral_phases = yes		
Cli = yes	alpha = 0.985	plot_results = yes		
smoothing = no	sigma_threshold = 0.01	print_mode = block		
smooth_win_size = 11	noise_intensity = 1	STA_range_start = 1000		
shuffle_peak_pos = No	max_peak_number = 100	STA_range_stop = 1800		
***Variable between sample trials. Specified ranges here as an example from AG042.**				

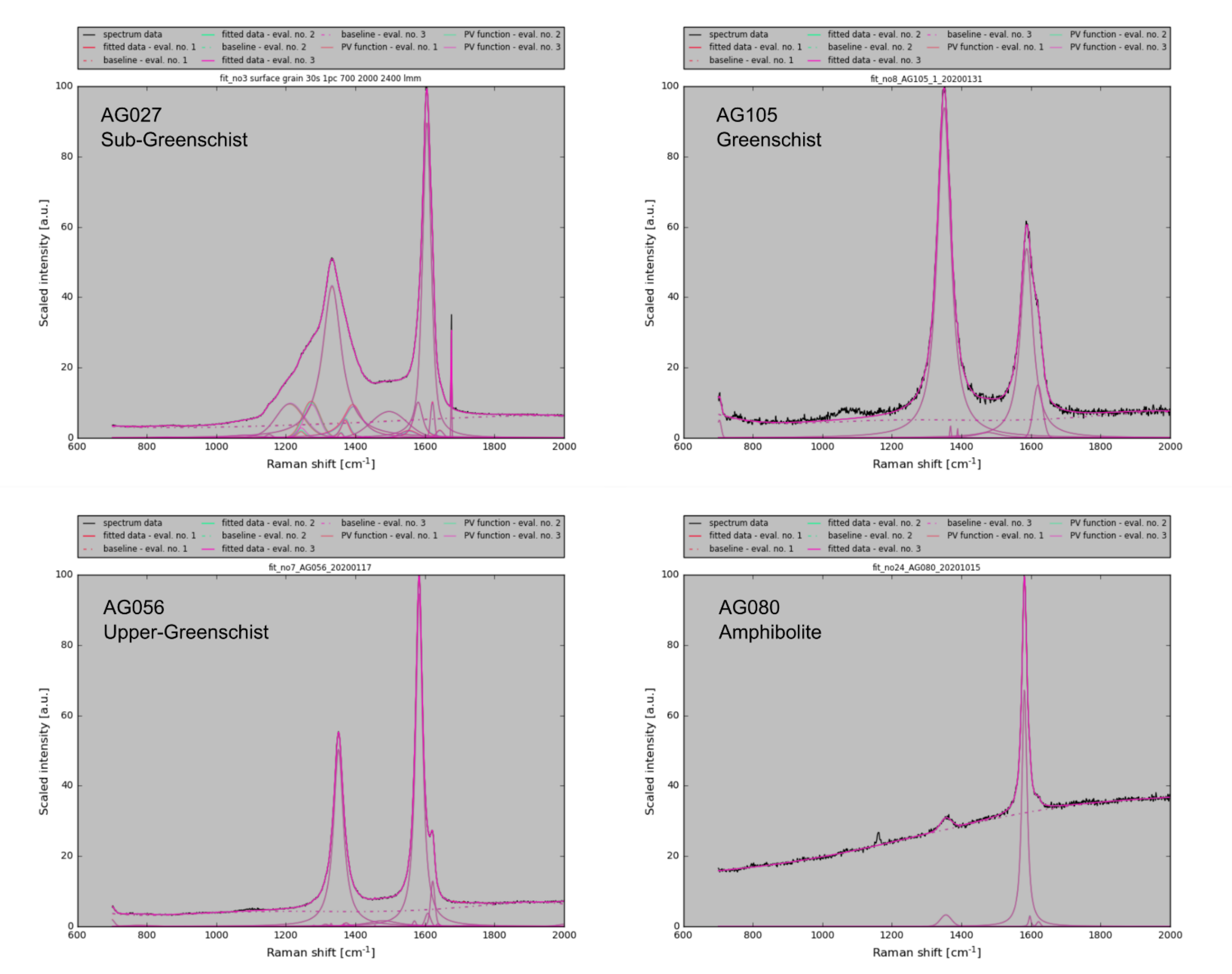

Figure C.1 Examples of Raman spectra from across grade (see facies label) using IFORS (Lunsdorf et al., 2017).

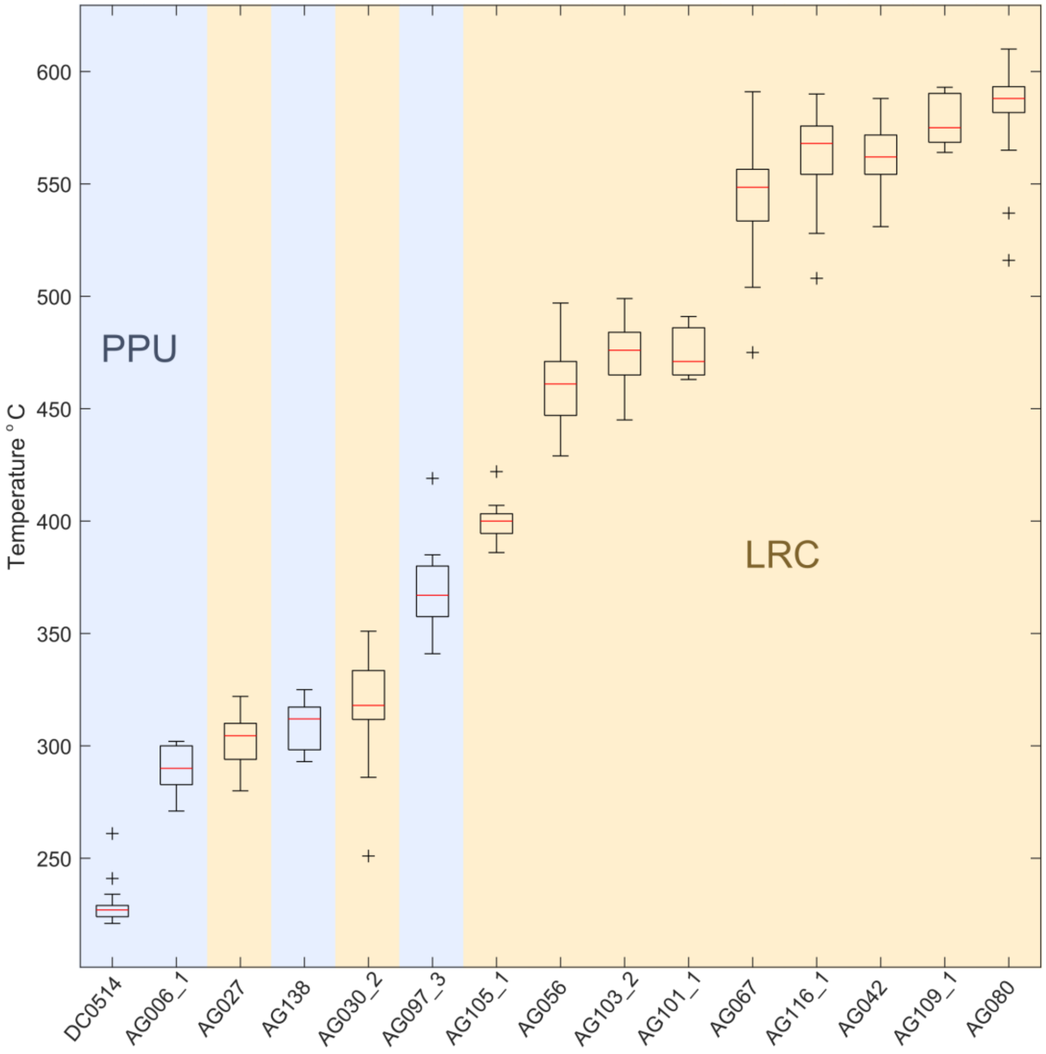

Figure C.2 Box plot showing peak metamorphic temperatures per sample as determined using the IFORS algorithm and calibration curve (Lunsdorf et al., 2017). Samples from the PPU are shaded blue, while samples from the LRC are shaded yellow. Center lines represent the median values, and whiskers correspond to the minimum and maximum values, excluding outliers (indicated by '+' symbol).

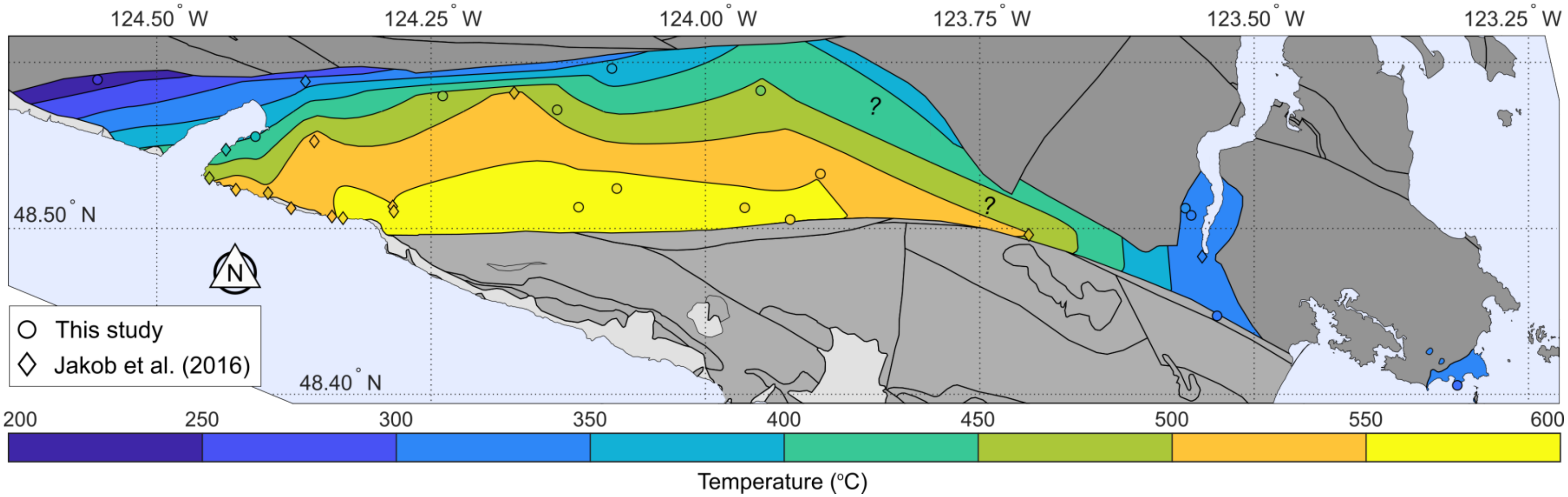

Figure C.3 Isotherms generated using natural neighbor interpolation and linear extrapolation in MATLAB. Minor non-physical features (including sharp points and bends) result from the 50 ºC binning procedure and minor method discrepancies between the Jakob et al. (2016) dataset and this study, and are not reflected by field observations.

Table C.3 Whole rock major element raw data (ICP-OES)

Analyte	SiO2	Al2O3	Fe2O3T	MnO	MgO	CaO	Na2O	K2O	TiO2	P2O5	LOI	Total
Unit Symbol	%	%	%	%	%	%	%	%	%	%	%	%
Detection Limit	0.01	0.01	0.01	0.001	0.01	0.01	0.01	0.01	0.001	0.01		0.01
Analysis Method	FUS-ICP	FUS-ICP	FUS-ICP	FUS-ICP	FUS-ICP	FUS-ICP	FUS-ICP	FUS-ICP	FUS-ICP	FUS-ICP	GRAV	FUS-ICP
AG 029-4	61.58	17.34	6.62	0.083	2.72	1.08	2.36	2.74	0.81	0.19	4.13	99.65
AG 101-1	61.49	17.68	5.71	0.069	2.36	3.01	1.83	2.87	0.828	0.16	4.03	100
AG 080	61.24	18.03	7.73	0.14	3.15	2.27	2.08	2.59	0.894	0.22	2.34	100.7
LC 12	49.06	16.01	10.35	0.17	7.61	11.31	2.52	0.13	1.109	0.09	2.46	100.8
AG 055-1	49.33	17.36	10.93	0.17	4.35	7.66	3.45	0.51	1.432	0.16	3.09	98.44
AG 059	45.83	18.98	13.09	0.20	4.07	9.39	3.52	0.69	2.511	0.39	0.77	99.44
AG 069-2	45.64	15.61	12.49	1.36	6.32	12.56	2.07	0.22	1.569	0.25	1.09	99.19
AG 069-3	49.74	15.2	10.3	0.33	8.22	10.55	3.04	0.53	1.578	0.15	1.03	100.7
AG 070-2	48.74	17.21	9.78	0.26	6.99	12.52	2.17	0.16	1.128	0.19	1	100.2
AG 121-2	47.68	15.88	12.11	0.27	6.6	13.51	1.49	0.32	1.632	0.15	0.95	100.6
AG 137	46.95	17.29	9.68	0.17	8.81	11.42	2.63	0.18	1.38	0.12	2.16	100.8
AG 136-2	61.25	16.54	6.82	0.23	2.72	2.05	6.2	0.04	0.751	0.34	2.59	99.53
AG 089-1	44.4	20.78	11.13	0.27	3.34	12.57	1.49	0.28	1.46	0.2	4.82	100.7
AG 105-4	49.34	18.61	11.57	0.21	4.34	9.34	3.1	< 0.01	0.832	0.13	3.32	100.8
AG 095-2	46.86	12.81	13.16	0.20	7.46	8.86	2.8	0.42	2.096	0.28	4.04	98.99
AG 093-1	37.02	0.58	7.96	0.12	37.68	0.17	< 0.01	< 0.01	0.011	< 0.01	16.63	100.2
AG 093-4	42.95	0.64	5.93	0.07	38.12	0.02	< 0.01	< 0.01	0.004	< 0.01	12.03	99.77
AG 097-1	43.27	0.19	4.84	0.058	38.7	0.38	< 0.01	< 0.01	0.003	< 0.01	12.76	100.2

Actlabs Report Number: A20-02286 Report Date: 13/3/2020

Table C.4 Quality control (standard, duplicate and method blank) data for whole rock major element data (Table C.3)

Analyte	**SiO2**	**Al2O3**	**Fe2O3T**	**MnO**	**MgO**	**CaO**	**Na2O**	**K2O**	**TiO2**	**P2O5**	**Total**
Unit Symbol	%	%	%	%	%	%	%	%	%	%	%
Detection Limit	0.01	0.01	0.01	0.001	0.01	0.01	0.01	0.01	0.001	0.01	0.01
Analysis Method	FUS-ICP	FUS-ICP	FUS-ICP	FUS-ICP	FUS-ICP	FUS-ICP	FUS-ICP	FUS-ICP	FUS-ICP	FUS-ICP	FUS-ICP
DNC-1 Meas	46.8	18.91	9.82	0.145	10.02	11.3	1.92	0.23	0.489	0.06	
DNC-1 Cert	47.15	18.34	9.97	0.15	10.13	11.49	1.89	0.234	0.48	0.07	
GBW 07113 Meas	73.04	12.97	3.2	0.142	0.14	0.58	2.49	5.38	0.285	0.04	
GBW 07113 Cert	72.8	13	3.21	0.14	0.16	0.59	2.57	5.43	0.3	0.05	
W-2a Meas	51.92	15.4	10.67	0.164	6.23	10.82	2.26	0.63	1.072	0.12	
W-2a Cert	52.4	15.4	10.7	0.163	6.37	10.9	2.14	0.626	1.06	0.14	
SY-4 Meas	50.02	20.54	6.18	0.11	0.51	8.12	6.94	1.64	0.29	0.13	
SY-4 Cert	49.9	20.69	6.21	0.108	0.54	8.05	7.1	1.66	0.287	0.131	
SY-4 Meas	50.41	20.84	6.2	0.109	0.5	8.08	6.99	1.68	0.29	0.13	
SY-4 Cert	49.9	20.69	6.21	0.108	0.54	8.05	7.1	1.66	0.287	0.131	
BIR-1a Meas	47.93	15.8	11.31	0.171	9.61	13.39	1.84	0.02	0.99	0.02	
BIR-1a Cert	47.96	15.5	11.3	0.175	9.7	13.3	1.82	0.03	0.96	0.021	
AG 095-2 Orig	46.56	12.93	13.22	0.198	7.45	8.82	2.79	0.42	2.09	0.28	98.78
AG 095-2 Dup	47.16	12.69	13.1	0.2	7.48	8.9	2.81	0.42	2.102	0.29	99.21
Method Blank	0.01	< 0.01	< 0.01	0.004	< 0.01	< 0.01	< 0.01	< 0.01	< 0.001	< 0.01	

Actlabs Report Number: A20-02286 Report Date: 13/3/2020

Table C.5 Trace element data (ICP-MS, ICP-OES, INAA, IR) tranche 1

Analyte Symbol	Cd	Cu	Ni	Zn	S	Ag	Pb	V	Cr	Co	Ni	Cu
Unit Symbol	ppm	ppm	ppm	ppm	%	ppm	ppm	ppm	ppm	ppm	ppm	ppm
Detection Limit	0.5	1	1	1	0.001	0.3	5	5	20	1	20	10
Analysis Method	TD-ICP	TD-ICP	TD-ICP	TD-ICP	TD-ICP	TD-ICP	TD-ICP	FUS-MS	FUS-MS	FUS-MS	FUS-MS	FUS-MS
AG029-4	< 0.5	23	38	92	0.033	< 0.3	< 5	181	100	10	40	30
AG055-1	< 0.5	57	231	102	0.002	< 0.3	< 5	260	570	60	270	60
AG059	< 0.5	45	183	106	0.008	< 0.3	< 5	329	400	66	230	60
AG069-2	0.6	64	156	84	0.005	< 0.3	10	377	350	45	180	70
AG070-2	< 0.5	2	113	75	0.004	< 0.3	< 5	240	230	41	130	< 10
AG080	< 0.5	14	58	104	0.004	< 0.3	11	194	120	19	60	20
AG089-1	< 0.5	85	12	115	0.166	< 0.3	< 5	284	20	25	< 20	90
AG095-2	< 0.5	59	241	116	0.017	< 0.3	< 5	232	390	51	270	60
AG101-1	< 0.5	71	21	92	0.027	< 0.3	10	160	80	10	20	70
AG105-4	< 0.5	94	6	72	0.349	< 0.3	< 5	251	< 20	27	< 20	100
AG136-2	< 0.5	110	22	94	0.005	< 0.3	< 5	141	120	9	20	110
AG137	< 0.5	69	126	64	0.104	< 0.3	< 5	249	330	45	140	70
LC12	< 0.5	111	100	61	0.004	< 0.3	< 5	273	330	45	120	120

Analyte Symbol	Zn	Ga	Ge	As	Rb	Sr	Y	Zr	Nb	Mo	Ag	In
Unit Symbol	ppm	ppm	ppm	ppm	ppm	ppm	ppm	ppm	ppm	ppm	ppm	ppm
Detection Limit	30	1	0.5	5	1	2	0.5	1	0.2	2	0.5	0.1
Analysis Method	FUS-MS	FUS-MS	FUS-MS	FUS-MS	FUS-MS	FUS-MS	FUS-MS	FUS-MS	FUS-MS	FUS-MS	FUS-MS	FUS-MS
AG029-4	90	20	1.3	< 5	80	185	23.9	113	7.3	< 2	< 0.5	0.1
AG055-1	120	15	2.2	< 5	10	485	30.8	98	1.2	< 2	< 0.5	0.1
AG059	130	22	2.7	< 5	22	504	38	211	14.3	< 2	0.5	0.1
AG069-2	100	19	2	< 5	2	364	34.7	109	4.7	< 2	< 0.5	0.1
AG070-2	80	17	2	< 5	2	319	23.6	62	1.5	< 2	< 0.5	0.1
AG080	150	22	1.8	< 5	89	263	23.1	145	8.8	< 2	< 0.5	0.1
AG089-1	140	23	3	< 5	5	200	42.1	113	4.4	< 2	< 0.5	0.1
AG095-2	130	20	1.9	< 5	15	400	29.1	161	13.5	< 2	< 0.5	0.1
AG101-1	80	22	1.9	5	83	607	19.6	113	8.5	< 2	< 0.5	0.1
AG105-4	80	16	2	< 5	< 1	329	19.3	24	0.3	4	< 0.5	0.1
AG136-2	90	15	0.7	< 5	< 1	226	34	167	9.2	15	0.5	0.1
AG137	70	17	1.4	< 5	1	257	25.3	73	1.6	< 2	< 0.5	0.1
LC12	70	17	1.7	< 5	2	186	20.1	57	2.5	< 2	< 0.5	0.1

Analyte Symbol	Sn	Sb	Cs	Ba	La	Ce	Pr	Nd	Sm	Eu	Gd	Tb
Unit Symbol	ppm	ppm	ppm	ppm	ppm	ppm	ppm	ppm	ppm	ppm	ppm	ppm
Detection Limit	1	0.2	0.1	3	0.05	0.05	0.01	0.05	0.01	0.005	0.01	0.01
Analysis Method	FUS-MS	FUS-MS	FUS-MS	FUS-MS	FUS-MS	FUS-MS	FUS-MS	FUS-MS	FUS-MS	FUS-MS	FUS-MS	FUS-MS

AG029-4	1	0.4	3.7	931	19.6	40.8	5.02	20.9	4.51	1.03	4.46	0.72
AG055-1	1	0.7	0.4	38	3.39	11.3	1.93	10.6	3.44	1.35	4.66	0.8
AG059	2	0.4	1.2	130	15.5	37.5	4.91	22.3	6.24	2.3	6.85	1.15
AG069-2	1	0.8	0.2	75	9.39	14.6	3.11	15.2	4.33	1.73	5.58	0.94
AG070-2	3	< 0.2	0.4	75	3	6.88	1.45	7.91	2.69	0.952	3.98	0.68
AG080	2	< 0.2	5	899	20.8	42.3	5.07	20.9	4.49	1.17	4.19	0.67
AG089-1	1	< 0.2	0.6	100	10.7	27.3	4.24	21.3	6.07	1.74	6.88	1.14
AG095-2	2	0.2	1.4	341	16.4	35.1	4.48	19.8	5.27	1.77	6.03	0.98
AG101-1	1	1.5	2.7	938	22.3	45.3	5.36	21.7	4.49	1.31	4.09	0.63
AG105-4	< 1	2.1	0.2	18	2.8	7.47	1.25	7.08	2.24	0.868	3.01	0.5
AG136-2	2	2.2	< 0.1	8	32.6	53	8.11	33.1	7.17	1.74	7.05	1.07
AG137	1	0.6	0.1	8	2.67	8.16	1.41	7.85	2.91	1.11	3.87	0.71
LC12	1	0.4	0.1	52	3.39	8.97	1.39	7.47	2.51	1.02	3.26	0.56
Analyte Symbol	Dy	Ho	Er	Tm	Yb	Lu	Hf	Ta	W	Tl	Pb	Mass
Unit Symbol	ppm	ppm	ppm	ppm	ppm	ppm	ppm	ppm	ppm	ppm	ppm	g
Detection Limit	0.01	0.01	0.01	0.005	0.01	0.002	0.1	0.01	0.5	0.05	5	
Analysis Method	FUS-MS	FUS-MS	FUS-MS	FUS-MS	FUS-MS	FUS-MS	FUS-MS	FUS-MS	FUS-MS	FUS-MS	FUS-MS	INAA
AG029-4	4.28	0.86	2.47	0.375	2.55	0.403	3	0.55	0.6	0.39	5	1.05
AG055-1	5.36	1.13	3.36	0.511	3.35	0.532	2.3	0.07	< 0.5	0.06	< 5	1.07
AG059	6.97	1.4	3.77	0.54	3.57	0.574	4.8	1.01	1.7	0.11	< 5	1.08
AG069-2	6.03	1.26	3.63	0.499	3.32	0.534	2.7	0.34	< 0.5	< 0.05	13	1.05
AG070-2	4.36	0.9	2.59	0.372	2.41	0.395	1.8	0.21	2.8	< 0.05	< 5	1.04
AG080	3.97	0.77	2.33	0.34	2.23	0.341	3.8	0.67	< 0.5	0.35	13	1.03
AG089-1	7.22	1.51	4.43	0.655	4.12	0.621	3.2	0.24	< 0.5	< 0.05	< 5	1.02
AG095-2	5.62	1.06	2.83	0.394	2.46	0.365	4	0.9	0.9	0.08	< 5	1.03
AG101-1	3.66	0.69	2.05	0.319	2	0.311	3.1	0.62	0.7	0.29	13	1.01
AG105-4	3.29	0.68	2.08	0.31	2.11	0.325	0.8	< 0.01	0.8	< 0.05	< 5	1.08
AG136-2	6.37	1.26	3.51	0.481	3.25	0.528	4.5	0.72	0.6	< 0.05	< 5	1.02
AG137	4.51	0.95	2.74	0.409	2.66	0.405	2.1	0.11	< 0.5	< 0.05	< 5	1.05
LC12	3.68	0.76	2.16	0.31	1.99	0.317	1.6	0.2	< 0.5	< 0.05	< 5	1.06
Analyte Symbol	Th	U	C-Total	Total S	Au	As	Br	Cr	Fe	Na	Sc	Sb
Unit Symbol	ppm	ppm	%	%	ppb	ppm	ppm	ppm	%	%	ppm	ppm
Detection Limit	0.05	0.01	0.01	0.01	2	0.5	0.5	5	0.01	0.01	0.1	0.2
Analysis Method	FUS-MS	FUS-MS	CS	CS	INAA	INAA	INAA	INAA	INAA	INAA	INAA	INAA
AG029-4	5.51	1.98	0.62	0.04	< 2	1.5	< 0.5	91	4.78	1.7	21.1	0.6
AG055-1	0.09	0.11	< 0.01	< 0.01	< 2	< 0.5	< 0.5	504	8.05	2.64	46.7	0.3
AG059	0.98	0.61	< 0.01	< 0.01	< 2	3.7	< 0.5	355	9.7	2.63	47.4	< 0.2
AG069-2	0.27	0.35	< 0.01	< 0.01	< 2	5	< 0.5	318	9.28	1.52	37.4	0.5
AG070-2	0.07	0.17	0.04	< 0.01	< 2	1.7	< 0.5	227	7.24	1.66	37.3	< 0.2
AG080	6.58	2.4	0.71	< 0.01	< 2	< 0.5	< 0.5	127	5.53	1.57	21.7	< 0.2
AG089-1	1.34	0.56	< 0.01	0.15	< 2	< 0.5	< 0.5	36	8.18	1.09	41.3	< 0.2
AG095-2	1.56	0.43	0.35	0.01	< 2	< 0.5	< 0.5	362	9.72	2.05	24	< 0.2

AG101-1	6.78	2.29	0.92	0.02	< 2	7.9	< 0.5	77	4.25	1.36	17.1	1.5
AG105-4	0.15	0.06	0.17	0.35	< 2	< 0.5	< 0.5	13	8.42	2.34	39.6	2
AG136-2	9	2.64	< 0.01	< 0.01	< 2	< 0.5	< 0.5	108	4.96	4.66	19	2
AG137	0.13	0.04	0.04	0.1	< 2	< 0.5	< 0.5	320	7.12	1.87	37	0.3
LC12	0.21	0.07	< 0.01	< 0.01	< 2	3	< 0.5	297	7.34	1.8	37.8	0.3
Report Number: A20-07062 Report Date: 21/7/2020												

Table C.6 Trace element data (ICP-MS, ICP-OES, INAA, IR) tranche 2

Analyte	Au	As	Br	Cr	Fe	S	Na	Sc	Sb	Se	Mass	Cd	Cu	Ni	Zn
Unit	ppb	ppm	ppm	ppm	%	%	%	ppm	ppm	ppm	g	ppm	ppm	ppm	ppm
Det Lim	2	0.5	0.5	5	0.01	0.001	0.01	0.1	0.2	3		0.5	1	1	1
Method	INAA	INAA	INAA	INAA	INAA	TD-ICP	INAA	INAA	INAA	INAA	INAA	TD-ICP	TD-ICP	TD-ICP	TD-ICP
AG140	< 2	16.2	< 0.5	116	6.64	0.009	1.22	23.6	2.4	< 3	23.9	< 0.5	50	56	156
AG046-3	< 2	2.9	< 0.5	96	4.99	0.233	1.84	16.4	1	< 3	31.7	< 0.5	59	55	88
AG127	14	45.9	< 0.5	111	4.95	0.168	1.39	17.5	< 0.2	< 3	33.2	< 0.5	52	62	118
AG118	< 2	1.8	< 0.5	96	4.7	0.203	1.67	15.7	0.5	< 3	32.9	< 0.5	39	41	115
AG049-1	< 2	< 0.5	< 0.5	68	4.67	0.345	1.83	14.6	0.3	< 3	33.4	< 0.5	67	42	94
AG054	< 2	12.7	< 0.5	71	3.82	0.069	1.72	12.4	0.7	< 3	29.6	< 0.5	14	14	99
AG128	12	22.6	< 0.5	30	1.8	0.015	0.79	5.5	< 0.2	< 3	34.1	< 0.5	13	15	34
AG089-2	22	11	< 0.5	18	8.2	2.6	1.08	16.1	0.9	< 3	33.9	< 0.5	250	19	36
AG105-1	5	19.6	< 0.5	104	4.66	0.224	1.42	16.9	1.5	< 3	27.4	< 0.5	46	63	139
AG103-2	< 2	9	< 0.5	98	4.26	0.065	1.73	14.9	0.5	< 3	28.4	< 0.5	12	24	105
AG056	< 2	13.4	< 0.5	48	2.57	0.007	2.82	7	0.4	< 3	30.7	< 0.5	38	36	78
AG135	77	2.7	< 0.5	103	5.3	0.231	1.56	17.4	0.7	< 3	27	< 0.5	70	38	159
AG006-1	< 2	11.9	< 0.5	44	4.71	0.702	2.61	15.7	0.6	< 3	30	< 0.5	56	28	103
Analyte	Ag	Pb	V	Nb	Co	Ni	Cu	Zn	Ga	Ge	As	Rb	Sr	Y	Zr
Unit	ppm	ppm	ppm	ppm	ppm	ppm	ppm	ppm	ppm	ppm	ppm	ppm	ppm	ppm	ppm
Det Lim	0.3	5	5	0.2	1	20	10	30	1	0.5	5	1	2	0.5	1
Method	TD-ICP	TD-ICP	FUSMS	FUSMS	FUSMS	FUSMS	FUSMS	FUSMS	FUSMS	FUSMS	FUSMS	FUSMS	FUSMS	FUSMS	FUSMS
AG140	< 0.3	7	209	6.7	12	60	50	140	24	1.8	12	75	134	34.8	122
AG046-3	< 0.3	12	154	7.3	16	50	50	90	18	1.4	< 5	86	297	21.3	120
AG127	< 0.3	10	178	8.5	19	60	40	120	23	1.1	26	82	218	26.3	147
AG118	< 0.3	13	156	7.5	14	50	40	110	20	1	< 5	79	250	21.1	117
AG049-1	< 0.3	10	147	8.3	17	40	60	100	22	1.2	< 5	96	407	23.2	118
AG054	< 0.3	12	136	5.8	6	20	20	90	16	1.2	10	89	377	13.5	89
AG128	< 0.3	5	51	1.8	3	< 20	10	30	7	0.8	14	21	114	8.4	31
AG089-2	< 0.3	14	134	1.4	25	20	220	30	15	0.9	6	2	145	25.6	71
AG105-1	< 0.3	12	183	6	18	60	40	120	19	0.8	15	84	247	20.9	99
AG103-2	< 0.3	14	147	6.1	8	30	10	100	18	1.4	9	63	272	18.1	118
AG056	< 0.3	19	61	3.6	25	30	40	70	8	1	9	19	114	11.7	67
AG135	< 0.3	13	195	9	14	50	60	130	22	1.1	< 5	87	167	28.2	117
AG006-1	0.4	6	133	4.8	16	30	50	90	18	0.8	7	60	118	19.5	106
Analyte	Mo	Ag	In	Sn	Sb	Cs	Ba	La	Ce	Pr	Nd	Sm	Eu	Gd	Tb
Unit	ppm	ppm	ppm	ppm	ppm	ppm	ppm	ppm	ppm	ppm	ppm	ppm	ppm	ppm	ppm

Det Lim	2	0.5	0.1	1	0.2	0.1	3	0.05	0.05	0.01	0.05	0.01	0.005	0.01	0.01
Method	FUSMS	FUSMS	FUSMS	FUSMS	FUSMS	FUSMS	FUSMS	FUSMS	FUSMS	FUSMS	FUSMS	FUSMS	FUSMS	FUSMS	FUSMS
AG140	< 2	< 0.5	0.1	5	2.1	3.4	770	32.8	43.5	8.33	37.5	8.91	2.28	8.51	1.18
AG046-3	< 2	< 0.5	0.1	5	0.7	4.2	877	21.2	41.5	5.1	20.9	4.46	1.1	4.16	0.69
AG127	< 2	< 0.5	0.1	4	0.2	3.8	1020	28.7	55.4	6.64	26.7	5.57	1.25	5.07	0.79
AG118	< 2	< 0.5	< 0.1	8	0.2	4.1	890	20	39.4	4.78	19.3	4.18	0.965	3.83	0.63
AG049-1	2	< 0.5	0.1	3	0.4	3.7	961	23.1	45.9	5.56	22.7	4.89	1.2	4.36	0.68
AG054	2	< 0.5	< 0.1	1	0.3	4.3	820	13.6	27.2	3.23	12.9	2.67	0.727	2.42	0.36
AG128	< 2	< 0.5	< 0.1	1	< 0.2	1.1	150	5.77	11.9	1.47	6.21	1.41	0.485	1.54	0.25
AG089-2	3	< 0.5	0.1	1	0.6	0.1	49	6.91	15.8	2.26	11.5	3.2	2.97	3.9	0.65
AG105-1	< 2	< 0.5	0.1	1	0.9	4.4	770	20.9	42	4.78	18.8	3.84	0.992	3.58	0.56
AG103-2	< 2	< 0.5	< 0.1	1	0.5	2	602	19.1	37.3	4.34	16.9	3.67	0.88	3.15	0.5
AG056	< 2	< 0.5	< 0.1	1	0.5	0.8	174	8.77	17.3	2.08	9.08	2.15	0.445	1.98	0.35
AG135	< 2	< 0.5	0.1	2	0.3	3.7	875	29.1	54.7	6.68	27.4	6.19	1.24	5.74	0.87
AG006-1	< 2	< 0.5	< 0.1	1	0.4	1.1	465	13.9	29.5	3.66	15.1	3.62	0.984	3.62	0.59

Analyte	Ho	Er	Tm	Yb	Lu	Hf	Ta	W	Tl	Pb	Dy	Th	U	C-Total	Total S
Unit	ppm	ppm	ppm	ppm	ppm	ppm	ppm	ppm	ppm	ppm	ppm	ppm	ppm	%	%
Det Lim	0.01	0.01	0.005	0.01	0.002	0.1	0.01	0.5	0.05	5	0.01	0.05	0.01	0.01	0.01
Method	FUSMS	FUSMS	FUSMS	FUSMS	FUSMS	FUSMS	FUSMS	FUSMS	FUSMS	FUSMS	FUSMS	FUSMS	FUSMS	CS	CS
AG140	1.18	3.22	0.484	3.12	0.51	3.3	0.43	< 0.5	0.31	9	6.28	4.61	1.79	0.53	< 0.01
AG046-3	0.73	2.05	0.308	2.08	0.313	3.2	0.53	< 0.5	0.41	15	3.65	6.83	2.08	0.59	0.23
AG127	0.9	2.53	0.387	2.52	0.388	3.9	0.64	< 0.5	0.32	11	4.38	7.92	2.7	0.5	0.16
AG118	0.75	2.06	0.31	1.96	0.357	3.1	0.56	< 0.5	0.32	11	3.58	6.3	2.1	0.65	0.2
AG049-1	0.79	2.24	0.346	2.31	0.332	3.3	0.59	0.8	0.4	11	3.87	6.99	2.72	0.46	0.34
AG054	0.45	1.31	0.211	1.41	0.235	2.3	0.43	1.5	0.41	12	2.17	5.47	1.78	0.32	0.06
AG128	0.29	0.75	0.119	0.8	0.12	0.8	0.14	< 0.5	0.09	5	1.41	1.7	0.6	0.2	< 0.01
AG089-2	0.85	2.48	0.38	2.61	0.413	1.9	0.09	0.5	< 0.05	7	3.83	1.21	0.72	1.27	2.54
AG105-1	0.73	2.13	0.318	2.18	0.36	2.7	0.54	0.9	0.33	10	3.42	7.84	2.66	0.88	0.22
AG103-2	0.6	1.85	0.303	2	0.316	2.9	0.5	< 0.5	0.27	15	2.88	6.2	2.08	0.62	0.05
AG056	0.39	1.06	0.167	1.08	0.171	1.7	0.31	< 0.5	0.06	16	1.91	3.65	1.21	0.15	< 0.01
AG135	1	2.77	0.414	2.63	0.406	3.3	0.65	1.8	0.28	10	4.88	8.88	3.13	0.83	0.3
AG006-1	0.7	2.02	0.286	1.86	0.315	2.8	0.3	< 0.5	0.27	7	3.29	3.25	1.46	0.26	0.63

Table C.7 Garnet-Biotite EPMA data (wt%).

			Gt (wt%)								Bt (wt%)*									
Sample	**Lin**	**Pos**	**SiO_2**	**TiO_2**	**Al_2O_3**	**FeO**	**MnO**	**MgO**	**CaO**	**Total**	**SiO_2**	**TiO_2**	**Al_2O_3**	**FeO**	**MnO**	**MgO**	**Na_2O**	**K_2O**	**H_2O**	**Total**
AG080	105	Rim	37.11	0.02	21.28	31.03	5.18	3.05	2.37	100.04	35.47	1.48	19.96	18.28	0.15	10.41	0.20	8.71	4.01	98.67
AG080	106	Rim	37.01	0.02	21.27	30.90	5.04	3.17	2.60	100.01	35.47	1.48	19.96	18.28	0.15	10.41	0.20	8.71	4.01	98.67
AG080	107	Rim	37.16	0.01	21.22	31.47	5.32	3.15	1.67	100.00	35.47	1.48	19.96	18.28	0.15	10.41	0.20	8.71	4.01	98.67
AG080	111	Rim	36.91	0.02	21.35	31.65	5.33	3.10	1.60	99.96	35.54	2.20	19.78	17.75	0.11	10.03	0.23	8.87	4.02	98.51
AG080	112	Rim	37.02	0.03	21.23	30.68	5.21	3.20	2.59	99.96	35.54	2.20	19.78	17.75	0.11	10.03	0.23	8.87	4.02	98.51
AG080	113	Rim	36.89	0.00	21.36	31.51	5.52	3.07	1.61	99.96	35.54	2.20	19.78	17.75	0.11	10.03	0.23	8.87	4.02	98.51
AG080	117	Core	36.28	0.95	21.03	27.59	7.60	2.43	3.99	99.87	35.77	1.57	20.32	17.54	0.11	10.35	0.28	8.72	4.03	98.70
AG080	118	Mid	37.05	0.04	21.26	29.38	6.03	3.12	3.29	100.17	35.77	1.57	20.32	17.54	0.11	10.35	0.28	8.72	4.03	98.70
AG080	119	Rim	36.96	0.00	21.61	31.82	5.25	3.24	1.57	100.45	35.77	1.57	20.32	17.54	0.11	10.35	0.28	8.72	4.03	98.70
AG041	156	Rim	36.69	0.06	21.27	29.69	8.35	2.31	1.77	100.14	35.13	1.16	20.18	18.84	0.21	9.73	0.18	9.09	3.99	98.52
AG041	157	Mid	36.74	0.03	21.13	29.16	9.03	2.23	1.77	100.09	35.13	1.16	20.18	18.84	0.21	9.73	0.18	9.09	3.99	98.52
AG041	158	Mid	36.84	0.05	21.21	28.75	9.45	2.11	1.78	100.19	35.13	1.16	20.18	18.84	0.21	9.73	0.18	9.09	3.99	98.52
AG041	159	Core	36.64	0.02	21.07	28.38	9.65	2.06	1.90	99.72	35.13	1.16	20.18	18.84	0.21	9.73	0.18	9.09	3.99	98.52
AG041	160	Core	36.70	0.02	21.11	28.48	9.72	2.02	1.83	99.88	35.13	1.16	20.18	18.84	0.21	9.73	0.18	9.09	3.99	98.52
AG041	161	Mid	36.71	0.04	21.21	28.78	9.41	2.21	1.70	100.06	35.13	1.16	20.18	18.84	0.21	9.73	0.18	9.09	3.99	98.52
AG041	162	Rim	36.69	0.10	21.25	28.96	8.97	2.21	1.81	99.99	35.13	1.16	20.18	18.84	0.21	9.73	0.18	9.09	3.99	98.52
AG041	163	Edge	36.49	0.03	21.04	29.58	8.39	2.17	1.72	99.42	35.13	1.16	20.18	18.84	0.21	9.73	0.18	9.09	3.99	98.52
AG041	169	Mid	36.84	0.02	21.11	29.30	8.86	2.29	1.75	100.17	35.13	1.16	20.18	18.84	0.21	9.73	0.18	9.09	3.99	98.52
AG041	170	Rim	37.20	0.00	21.21	29.49	8.63	2.36	1.72	100.61	35.13	1.16	20.18	18.84	0.21	9.73	0.18	9.09	3.99	98.52
AG041	171	Rim	36.98	0.05	21.18	29.67	8.63	2.26	1.63	100.40	35.13	1.16	20.18	18.84	0.21	9.73	0.18	9.09	3.99	98.52
AG041	175	Core	36.88	0.03	21.08	28.82	8.79	2.24	1.96	99.80	34.31	1.54	19.19	19.39	0.25	9.63	0.09	8.68	3.98	97.05
AG041	176	Mid	36.69	0.03	20.97	29.19	8.72	2.33	1.65	99.58	34.31	1.54	19.19	19.39	0.25	9.63	0.09	8.68	3.98	97.05
AG041	177	Rim	36.57	0.03	20.74	29.55	8.40	2.26	1.65	99.20	34.31	1.54	19.19	19.39	0.25	9.63	0.09	8.68	3.98	97.05
AG042	135	Rim	36.92	0.02	21.05	29.37	8.32	2.13	2.26	100.07	34.61	1.37	20.17	19.22	0.18	9.73	0.24	7.88	4.01	97.41
AG042	136	Rim	36.95	0.03	21.17	29.48	8.74	2.23	1.79	100.39	34.61	1.37	20.17	19.22	0.18	9.73	0.24	7.88	4.01	97.41
AG042	215	Rim	37.26	0.02	21.08	29.44	8.50	2.19	2.18	100.67	34.61	1.37	20.17	19.22	0.18	9.73	0.24	7.88	4.01	97.41
AG042	216	Rim	36.67	0.06	20.97	29.37	8.46	2.12	2.11	99.76	34.61	1.37	20.17	19.22	0.18	9.73	0.24	7.88	4.01	97.41
AG042	217	Rim	36.81	0.05	21.23	29.37	8.57	2.19	2.10	100.32	34.61	1.37	20.17	19.22	0.18	9.73	0.24	7.88	4.01	97.41
AG042	222	Rim	36.92	0.03	21.05	29.31	8.58	2.09	2.06	100.04	34.61	1.37	20.17	19.22	0.18	9.73	0.24	7.88	4.01	97.41
AG042	140	Core	36.71	0.05	21.22	27.71	10.65	1.92	1.96	100.22	35.45	1.66	19.92	18.08	0.18	9.68	0.22	8.44	4.02	97.66
AG042	141	Mid	36.66	0.06	21.22	27.75	10.46	1.98	1.92	100.05	35.45	1.66	19.92	18.08	0.18	9.68	0.22	8.44	4.02	97.66
AG042	142	Rim	36.94	0.01	21.29	28.93	8.50	2.23	1.93	99.83	35.45	1.66	19.92	18.08	0.18	9.68	0.22	8.44	4.02	97.66
AG042	223	Rim	36.56	0.04	21.15	29.14	8.46	2.15	2.14	99.64	35.45	1.66	19.92	18.08	0.18	9.68	0.22	8.44	4.02	97.66
AG042	224	Rim	36.94	0.10	21.13	29.16	8.43	2.19	2.14	100.09	35.45	1.66	19.92	18.08	0.18	9.68	0.22	8.44	4.02	97.66
AG042	225	Rim	36.84	0.06	21.26	29.06	8.44	2.14	2.19	99.99	35.45	1.66	19.92	18.08	0.18	9.68	0.22	8.44	4.02	97.66
AG042	226	Rim	36.54	0.06	21.04	29.11	8.50	2.15	2.16	99.56	35.45	1.66	19.92	18.08	0.18	9.68	0.22	8.44	4.02	97.66
AG042	227	Rim	36.90	0.08	21.20	29.33	8.57	2.19	2.07	100.34	35.45	1.66	19.92	18.08	0.18	9.68	0.22	8.44	4.02	97.66
AG042	147	Rim	37.56	0.02	21.08	29.44	8.61	2.12	2.25	101.08	35.15	1.55	20.02	19.29	0.16	9.57	0.20	8.61	3.99	98.54
AG042	148	Core	36.98	0.04	21.24	27.83	10.55	1.95	1.89	100.48	35.15	1.55	20.02	19.29	0.16	9.57	0.20	8.61	3.99	98.54
AG042	149	Edge	36.26	0.05	21.74	29.23	8.81	1.94	2.11	100.14	35.15	1.55	20.02	19.29	0.16	9.57	0.20	8.61	3.99	98.54
AG042	151	Edge	36.84	0.01	21.32	29.11	8.81	2.18	2.10	100.37	35.56	1.37	20.36	18.76	0.19	9.53	0.30	8.78	4.00	98.86

AG042	152	Edge	36.61	0.02	21.41	29.13	8.74	2.21	2.11	100.23	35.56	1.37	20.36	18.76	0.19	9.53	0.30	8.78	4.00	98.86
AG042	233	Rim	36.87	0.03	21.13	29.30	8.39	2.16	2.09	99.97	35.56	1.37	20.36	18.76	0.19	9.53	0.30	8.78	4.00	98.86
AG042	234	Rim	36.66	0.02	21.11	29.45	8.49	2.18	2.18	100.09	35.56	1.37	20.36	18.76	0.19	9.53	0.30	8.78	4.00	98.86
AG042	235	Rim	37.11	0.03	21.10	29.17	8.42	2.14	2.22	100.19	35.56	1.37	20.36	18.76	0.19	9.53	0.30	8.78	4.00	98.86
AG042	236	Rim	36.89	0.05	21.18	29.51	8.34	2.15	2.17	100.29	35.56	1.37	20.36	18.76	0.19	9.53	0.30	8.78	4.00	98.86
AG042	237	Rim	36.91	0.03	21.15	29.08	8.46	2.13	2.27	100.03	35.56	1.37	20.36	18.76	0.19	9.53	0.30	8.78	4.00	98.86
AG067	155	Core	36.85	0.05	21.07	26.49	12.16	1.85	1.87	100.34	35.63	1.63	20.16	18.22	0.24	9.47	0.13	8.93	4.01	98.43
AG067	156	Core	36.51	0.08	21.02	26.20	12.03	1.90	1.94	99.68	35.63	1.63	20.16	18.22	0.24	9.47	0.13	8.93	4.01	98.43
AG067	157	Mid	36.82	0.05	21.07	27.13	11.15	2.02	1.96	100.20	35.63	1.63	20.16	18.22	0.24	9.47	0.13	8.93	4.01	98.43
AG067	158	Rim	36.93	0.05	20.98	27.57	10.76	2.02	1.92	100.23	35.63	1.63	20.16	18.22	0.24	9.47	0.13	8.93	4.01	98.43
AG067	159	Edge	37.08	0.03	21.21	27.21	10.89	1.78	2.30	100.50	35.63	1.63	20.16	18.22	0.24	9.47	0.13	8.93	4.01	98.43
AG067	243	Edge	36.94	0.03	20.91	27.58	10.83	1.99	1.86	100.14	35.63	1.63	20.16	18.22	0.24	9.47	0.13	8.93	4.01	98.43
AG067	244	Rim	36.67	0.02	20.89	27.65	10.80	2.00	1.81	99.84	35.63	1.63	20.16	18.22	0.24	9.47	0.13	8.93	4.01	98.43
AG067	245	Rim	36.76	0.02	20.96	27.66	10.86	1.88	1.85	99.99	35.63	1.63	20.16	18.22	0.24	9.47	0.13	8.93	4.01	98.43
AG067	246	Rim	36.68	0.05	20.84	27.77	10.97	1.99	1.78	100.08	35.63	1.63	20.16	18.22	0.24	9.47	0.13	8.93	4.01	98.43
AG067	247	Rim	36.71	0.10	20.98	27.63	10.94	2.06	1.81	100.23	35.63	1.63	20.16	18.22	0.24	9.47	0.13	8.93	4.01	98.43
AG067	248	Rim	36.61	0.07	21.07	27.67	10.76	1.90	1.89	99.97	35.63	1.63	20.16	18.22	0.24	9.47	0.13	8.93	4.01	98.43
AG067	249	Rim	36.78	0.03	20.76	27.52	10.71	1.88	2.01	99.69	35.63	1.63	20.16	18.22	0.24	9.47	0.13	8.93	4.01	98.43
AG067	250	Rim	36.90	0.01	21.01	27.81	10.79	1.98	1.80	100.30	35.63	1.63	20.16	18.22	0.24	9.47	0.13	8.93	4.01	98.43
AG067	163	Rim	36.62	0.04	20.90	27.41	10.98	1.89	1.75	99.59	35.38	1.53	19.48	18.72	0.26	9.44	0.15	8.77	4.00	97.73
AG067	164	Rim	36.66	0.03	21.00	27.39	10.77	1.97	1.79	99.61	35.38	1.53	19.48	18.72	0.26	9.44	0.15	8.77	4.00	97.73
AG067	165	Core	36.60	0.05	20.88	26.59	12.06	1.82	1.57	99.57	35.38	1.53	19.48	18.72	0.26	9.44	0.15	8.77	4.00	97.73
AG067	169	Edge	36.58	0.07	21.13	27.17	11.57	1.61	1.85	99.98	36.72	1.51	19.12	18.62	0.24	9.94	0.13	8.76	4.01	99.06
AG047	188	Rim	36.40	0.02	21.08	30.01	7.51	2.71	1.59	99.32	35.46	1.77	19.64	18.39	0.17	9.97	0.15	9.23	4.00	98.77
AG047	189	Rim	36.75	0.01	21.12	29.72	7.65	2.68	1.66	99.59	35.46	1.77	19.64	18.39	0.17	9.97	0.15	9.23	4.00	98.77
AG047	190	Rim	36.47	0.02	21.08	29.58	7.62	2.69	1.69	99.15	35.46	1.77	19.64	18.39	0.17	9.97	0.15	9.23	4.00	98.77
AG047	191	Rim	36.94	0.01	21.04	30.09	7.71	2.58	1.58	99.95	35.46	1.77	19.64	18.39	0.17	9.97	0.15	9.23	4.00	98.77
AG047	197	Core	36.83	0.03	21.05	28.05	9.74	2.26	2.03	99.99	34.96	1.57	20.11	18.23	0.19	10.04	0.09	9.18	4.00	98.38
AG047	198	Mid	36.49	0.02	21.04	28.14	9.70	2.26	1.97	99.62	34.96	1.57	20.11	18.23	0.19	10.04	0.09	9.18	4.00	98.38
AG047	199	Mid	36.71	0.04	21.01	28.40	9.22	2.37	1.99	99.74	34.96	1.57	20.11	18.23	0.19	10.04	0.09	9.18	4.00	98.38
AG047	200	Mid	36.58	0.02	20.98	28.95	8.84	2.41	1.80	99.58	34.96	1.57	20.11	18.23	0.19	10.04	0.09	9.18	4.00	98.38
AG047	201	Rim	36.59	0.00	21.00	30.01	7.86	2.73	1.52	99.71	34.96	1.57	20.11	18.23	0.19	10.04	0.09	9.18	4.00	98.38
AG047	202	Rim	36.38	0.02	21.00	30.30	7.72	2.39	1.66	99.47	34.96	1.57	20.11	18.23	0.19	10.04	0.09	9.18	4.00	98.38
AG047	207	Rim	37.08	0.02	21.20	30.12	7.99	2.61	1.57	100.59	35.35	1.50	19.82	18.48	0.24	9.74	0.09	9.48	3.99	98.69
AG047	208	Rim	36.82	0.02	21.32	30.36	7.80	2.67	1.52	100.51	35.35	1.50	19.82	18.48	0.24	9.74	0.09	9.48	3.99	98.69
AG047	209	Edge	36.92	0.02	21.22	30.10	7.84	2.45	1.75	100.30	35.35	1.50	19.82	18.48	0.24	9.74	0.09	9.48	3.99	98.69
AG1161	113	Core	36.88	0.14	20.97	26.60	9.69	2.06	3.22	99.56	35.80	1.80	19.45	19.00	0.19	9.65	0.15	8.82	4.00	98.85
AG1161	114	Mid	37.13	0.01	21.23	28.56	8.45	2.46	2.80	100.64	35.80	1.80	19.45	19.00	0.19	9.65	0.15	8.82	4.00	98.85
AG1161	115	Rim	37.35	0.02	21.16	30.39	7.19	2.63	2.07	100.81	35.80	1.80	19.45	19.00	0.19	9.65	0.15	8.82	4.00	98.85
AG1161	171	Rim	37.09	0.00	21.40	30.73	7.13	2.64	1.87	100.86	35.80	1.80	19.45	19.00	0.19	9.65	0.15	8.82	4.00	98.85
AG1161	172	Rim	37.05	0.02	21.15	30.58	7.25	2.49	1.90	100.44	35.80	1.80	19.45	19.00	0.19	9.65	0.15	8.82	4.00	98.85
AG1161	173	Rim	37.03	0.00	21.27	30.54	7.06	2.64	1.94	100.48	35.80	1.80	19.45	19.00	0.19	9.65	0.15	8.82	4.00	98.85
AG1161	174	Rim	37.05	0.05	21.30	30.53	7.11	2.64	1.95	100.63	35.80	1.80	19.45	19.00	0.19	9.65	0.15	8.82	4.00	98.85
AG1161	175	Rim	37.11	0.01	21.16	30.54	7.10	2.67	1.95	100.54	35.80	1.80	19.45	19.00	0.19	9.65	0.15	8.82	4.00	98.85
AG1161	119	Core	36.72	0.05	21.09	25.59	10.59	1.87	3.57	99.48	35.24	1.34	19.37	19.31	0.20	10.15	0.19	8.47	3.99	98.26

AG1161	120	Mid	36.91	0.03	21.25	27.38	10.09	2.05	2.70	100.41	35.24	1.34	19.37	19.31	0.20	10.15	0.19	8.47	3.99	98.26
AG1161	121	Rim	37.08	0.02	21.38	30.58	6.95	2.60	1.95	100.56	35.24	1.34	19.37	19.31	0.20	10.15	0.19	8.47	3.99	98.26
AG1161	181	Rim	36.70	0.03	21.32	30.39	7.03	2.54	1.95	99.96	35.24	1.34	19.37	19.31	0.20	10.15	0.19	8.47	3.99	98.26
AG1161	182	Rim	36.86	0.00	21.18	30.46	7.16	2.54	1.88	100.08	35.24	1.34	19.37	19.31	0.20	10.15	0.19	8.47	3.99	98.26
AG1161	183	Mid	36.86	0.00	21.16	30.63	7.31	2.46	1.99	100.41	35.24	1.34	19.37	19.31	0.20	10.15	0.19	8.47	3.99	98.26
AG1161	187	Rim	36.94	0.00	21.14	30.65	6.99	2.60	2.01	100.33	35.24	1.34	19.37	19.31	0.20	10.15	0.19	8.47	3.99	98.26
AG1161	188	Rim	37.08	0.03	21.17	30.54	7.23	2.51	2.05	100.61	35.24	1.34	19.37	19.31	0.20	10.15	0.19	8.47	3.99	98.26
AG1161	189	Rim	36.52	0.03	21.11	30.09	7.21	2.51	1.95	99.42	35.24	1.34	19.37	19.31	0.20	10.15	0.19	8.47	3.99	98.26
AG1161	190	Rim	37.22	0.03	21.18	30.40	7.16	2.60	1.97	100.56	35.24	1.34	19.37	19.31	0.20	10.15	0.19	8.47	3.99	98.26
AG1161	125	Rim	37.19	0.01	21.46	30.00	7.35	2.68	2.01	100.70	35.09	1.75	19.28	18.61	0.19	9.91	0.21	8.42	4.00	97.46
AG1161	126	Edge	37.16	0.02	21.25	30.54	7.06	2.61	1.83	100.47	35.09	1.75	19.28	18.61	0.19	9.91	0.21	8.42	4.00	97.46
AG1161	127	Edge	37.04	0.02	21.34	30.37	7.60	2.22	1.83	100.42	35.09	1.75	19.28	18.61	0.19	9.91	0.21	8.42	4.00	97.46
AG1161	195	Rim	37.09	0.04	21.25	30.58	6.83	2.69	1.90	100.38	35.09	1.75	19.28	18.61	0.19	9.91	0.21	8.42	4.00	97.46
AG1161	196	Rim	37.24	0.04	21.26	30.36	6.90	2.72	1.90	100.42	35.09	1.75	19.28	18.61	0.19	9.91	0.21	8.42	4.00	97.46
AG1161	197	Rim	37.25	0.02	21.06	30.35	6.93	2.67	1.88	100.16	35.09	1.75	19.28	18.61	0.19	9.91	0.21	8.42	4.00	97.46
AG1161	198	Rim	37.04	0.00	21.19	30.44	6.95	2.69	1.95	100.26	35.09	1.75	19.28	18.61	0.19	9.91	0.21	8.42	4.00	97.46
AG1161	199	Rim	36.96	0.02	21.29	30.58	6.98	2.68	1.88	100.39	35.09	1.75	19.28	18.61	0.19	9.91	0.21	8.42	4.00	97.46
AG1161	131	Edge	36.92	0.02	21.05	29.37	8.32	2.13	2.26	100.07	35.73	1.75	19.65	18.21	0.18	9.65	0.25	8.98	4.01	98.40
AG1161	132	Edge	36.95	0.03	21.17	29.48	8.74	2.23	1.79	100.39	35.73	1.75	19.65	18.21	0.18	9.65	0.25	8.98	4.01	98.40
AG1161	205	Rim	36.95	0.00	21.09	30.24	7.45	2.56	1.79	100.08	35.73	1.75	19.65	18.21	0.18	9.65	0.25	8.98	4.01	98.40
AG1161	206	Rim	37.04	0.02	21.05	30.17	7.39	2.67	1.83	100.17	35.73	1.75	19.65	18.21	0.18	9.65	0.25	8.98	4.01	98.40
AG1161	207	Rim	37.03	0.03	21.10	30.02	7.47	2.58	1.85	100.08	35.73	1.75	19.65	18.21	0.18	9.65	0.25	8.98	4.01	98.40
AG1161	208	Rim	37.14	0.00	21.16	30.11	7.35	2.65	1.85	100.26	35.73	1.75	19.65	18.21	0.18	9.65	0.25	8.98	4.01	98.40
AG1161	209	Rim	36.95	0.00	21.12	30.31	7.27	2.72	1.84	100.21	35.73	1.75	19.65	18.21	0.18	9.65	0.25	8.98	4.01	98.40
AG049	85	Core	36.49	0.05	21.14	28.58	9.35	2.31	1.92	99.84	34.45	1.92	19.89	18.66	0.18	10.03	0.17	8.55	4.00	97.84
AG049	86	Mid	36.53	0.05	20.98	29.02	8.95	2.40	1.84	99.77	34.45	1.92	19.89	18.66	0.18	10.03	0.17	8.55	4.00	97.84
AG049	87	Rim	36.30	0.01	21.38	30.62	7.55	2.45	1.62	99.93	34.45	1.92	19.89	18.66	0.18	10.03	0.17	8.55	4.00	97.84
AG049	91	Rim	36.81	0.04	21.24	30.43	7.42	2.62	1.66	100.22	34.81	1.75	20.09	18.74	0.16	9.80	0.13	9.17	3.99	98.65
AG049	92	Rim	36.71	0.02	21.11	30.83	7.35	2.41	1.58	100.01	34.81	1.75	20.09	18.74	0.16	9.80	0.13	9.17	3.99	98.65
AG049	95	Core	36.30	0.03	21.01	29.23	8.39	2.40	1.91	99.27	34.09	1.92	19.85	19.28	0.19	9.94	0.09	8.65	3.98	97.98
AG049	96	Mid	36.17	0.05	21.00	29.71	8.20	2.52	1.77	99.42	34.09	1.92	19.85	19.28	0.19	9.94	0.09	8.65	3.98	97.98
AG049	97	Rim	36.10	0.03	21.01	30.62	7.27	2.52	1.63	99.18	34.09	1.92	19.85	19.28	0.19	9.94	0.09	8.65	3.98	97.98
AG0742	219	Edge	37.38	0.00	21.33	34.69	0.47	4.10	2.22	100.19	35.90	1.31	18.64	17.58	0.03	11.42	0.12	8.85	4.02	97.88
AG0742	220	Rim	37.54	0.02	21.36	34.43	0.31	4.28	2.27	100.21	35.90	1.31	18.64	17.58	0.03	11.42	0.12	8.85	4.02	97.88
AG0742	221	Rim	37.45	0.04	21.48	34.23	0.39	4.31	2.22	100.12	35.90	1.31	18.64	17.58	0.03	11.42	0.12	8.85	4.02	97.88
AG0742	226	Mid	37.53	0.03	21.48	34.79	0.62	3.59	2.61	100.65	35.90	1.31	18.64	17.58	0.03	11.42	0.12	8.85	4.02	97.88
AG0742	227	Mid	37.60	0.05	21.35	34.51	0.24	4.16	2.34	100.25	36.26	1.31	18.69	17.03	0.02	11.74	0.17	8.89	4.04	98.13
AG0742	228	Rim	37.38	0.05	21.45	33.98	0.23	4.28	2.68	100.05	36.26	1.31	18.69	17.03	0.02	11.74	0.17	8.89	4.04	98.13
AG0742	229	Rim	37.47	0.00	21.43	34.24	0.30	4.36	2.25	100.05	36.26	1.31	18.69	17.03	0.02	11.74	0.17	8.89	4.04	98.13
AG0742	230	Edge	37.10	0.00	21.54	34.42	0.57	3.91	2.15	99.69	36.26	1.31	18.69	17.03	0.02	11.74	0.17	8.89	4.04	98.13
AG0742	235	Rim	37.67	0.03	21.35	34.24	0.39	4.12	2.28	100.08	34.91	1.23	18.46	19.13	0.03	10.56	0.13	8.52	3.99	96.95
AG0742	236	Mid	37.69	0.03	21.46	34.56	0.25	4.16	2.59	100.74	34.91	1.23	18.46	19.13	0.03	10.56	0.13	8.52	3.99	96.95
AG0742	237	Core	38.24	0.04	21.39	34.95	0.29	4.23	2.19	101.33	34.91	1.23	18.46	19.13	0.03	10.56	0.13	8.52	3.99	96.95
AG0742	238	Core	37.54	0.06	21.47	34.51	0.25	4.06	2.58	100.47	34.91	1.23	18.46	19.13	0.03	10.56	0.13	8.52	3.99	96.95
AG0742	239	Mid	37.31	0.03	21.36	34.67	0.26	4.21	2.33	100.17	34.91	1.23	18.46	19.13	0.03	10.56	0.13	8.52	3.99	96.95

AG0742	240	Rim	37.32	0.03	21.36	34.76	0.55	3.71	2.19	99.92	34.91	1.23	18.46	19.13	0.03	10.56	0.13	8.52	3.99	96.95
AG0742	246	Rim	36.95	0.01	21.28	33.60	1.15	3.94	2.77	99.70	36.27	1.49	18.61	17.19	0.02	11.69	0.15	8.85	4.03	98.30
AG0742	247	Edge	37.84	0.02	21.37	34.63	0.52	4.08	2.15	100.61	36.27	1.49	18.61	17.19	0.02	11.69	0.15	8.85	4.03	98.30
AG0742	248	Edge	37.66	0.00	21.65	34.59	0.42	4.14	2.23	100.69	36.27	1.49	18.61	17.19	0.02	11.69	0.15	8.85	4.03	98.30
*Biotite analyses with low totals were not selected for Gt-Bt Thermometry and thus are excluded here (multiple biotite analyses taken at each gt-bt pair).																				

Table C.8 EPMA sulfide data (wt%).

SAMPLE	LINE	As WT%	Zn WT%	S WT%	Mn WT%	Fe WT%	Cu WT%	Ni WT%	TOTAL	Mineral
137 SUEXT1	43	0.00	0.00	39.41	0.00	58.17	0.00	1.76	99.34	po
137 SUEXT1	44	0.00	0.05	39.44	0.00	58.20	0.00	1.76	99.45	po
137 SUEXT1	45	0.03	0.00	39.48	0.00	58.65	0.00	1.72	99.88	po
137 SUEXT1	46	0.00	0.00	39.41	0.00	58.67	0.00	1.70	99.78	po
137 SUEXT1	47	0.00	0.00	39.48	0.00	58.71	0.00	1.74	99.93	po
137 SUEXT1	48	0.00	0.00	39.35	0.00	58.71	0.00	1.64	99.70	po
137 SUEXT1	49	0.00	0.00	34.36	0.00	30.73	33.42	0.00	98.51	ccp
137 SUEXT1	50	0.00	0.00	39.36	0.00	59.78	0.00	0.17	99.31	po
137 SUEXT1	51	0.00	0.00	34.66	0.00	30.52	33.34	0.00	98.52	ccp
137 SUEXT1	52	0.00	0.00	34.73	0.00	30.61	33.19	0.00	98.53	ccp
137 SUEXT1	53	0.00	0.00	53.20	0.00	44.79	0.21	0.00	98.20	py
137 SUEXT1	54	0.00	0.00	53.25	0.00	45.72	0.16	0.00	99.13	py
137 SUEXT1	55	0.00	0.00	34.76	0.00	30.83	33.34	0.00	98.93	ccp
137 SUEXT1	56	0.00	0.00	34.71	0.00	30.75	33.52	0.00	98.98	ccp
137 SU1	57	0.00	0.00	39.55	0.00	57.53	0.00	2.61	99.69	po
137 SU1	58	0.00	0.00	39.59	0.00	57.73	0.00	2.57	99.89	po
137 SU1	59	0.03	0.00	39.41	0.00	57.55	0.00	2.62	99.61	po
137 SU2	60	0.00	0.06	53.34	0.00	45.36	0.41	0.00	99.17	py
137 SU2	61	0.00	0.00	34.71	0.00	30.56	32.92	0.02	98.21	ccp
137 SU2	62	0.00	0.00	34.83	0.00	30.86	32.91	0.03	98.63	ccp
137 SU2	63	0.00	0.00	39.59	0.00	58.16	0.14	1.74	99.63	po
137 SU2	64	0.00	0.00	39.47	0.00	58.33	0.00	1.80	99.60	po
137 SU2	65	0.00	0.00	34.74	0.00	30.58	33.56	0.00	98.88	ccp
137 SU2	66	0.00	0.00	34.79	0.00	30.60	33.61	0.00	99.00	ccp
137 SU2	67	0.00	0.00	34.92	0.00	30.91	33.46	0.02	99.31	ccp
137 SU2	68	0.00	0.00	39.53	0.00	58.38	0.00	1.82	99.73	po
137 SU2	69	0.04	0.00	39.51	0.00	58.40	0.00	1.76	99.71	po
137 SU2	70	0.00	0.00	53.13	0.00	44.20	0.03	0.00	97.36	py
137 SU2	71	0.00	0.00	39.47	0.00	58.90	0.00	1.21	99.58	po
137 SUEXT2	72	0.00	0.00	34.99	0.00	30.67	33.19	0.00	98.85	ccp
137 SUEXT2	73	0.00	0.00	52.97	0.00	44.38	0.00	0.00	97.35	py

137 SUEXT2	74	0.00	0.00	52.66	0.00	45.11	0.00	0.00	97.77	py
137 SU3	75	0.03	0.00	39.73	0.00	59.84	0.00	1.11	100.71	po
137 SU3	76	0.00	0.00	34.80	0.00	30.35	33.41	0.00	98.56	ccp
137 SU3	77	0.03	0.00	39.66	0.00	59.58	0.00	1.19	100.46	po
137 SUEXT3	78	0.03	0.00	39.40	0.00	57.14	0.00	2.88	99.45	po
137 SUEXT3	79	0.00	0.00	39.45	0.00	57.39	0.00	2.73	99.57	po
010 SU1	80	0.00	0.00	34.86	0.00	30.66	33.63	0.00	99.15	ccp
010 SU1	81	0.00	0.00	34.69	0.00	30.54	33.55	0.00	98.78	ccp
010 SU1	82	0.00	0.00	38.63	0.00	61.28	0.00	0.08	99.99	po
010 SU1	83	0.00	0.00	38.24	0.00	60.37	0.00	0.08	98.69	po
010 SU1	84	0.00	0.00	38.76	0.00	60.80	0.00	0.09	99.65	po
010 SU1	85	0.00	58.31	33.97	0.00	7.88	0.78	0.00	100.94	sph
010 SU1	86	0.00	57.82	33.87	0.00	8.04	0.92	0.00	100.65	sph
010 SUEXT1	87	0.00	58.54	33.37	0.04	8.12	0.00	0.00	100.07	sph
010 SUEXT1	88	0.00	58.38	33.27	0.04	8.26	0.00	0.00	99.95	sph
010 SUEXT1	89	0.00	0.22	38.57	0.00	60.85	0.00	0.08	99.72	po
010 SUEXT1	90	0.00	0.00	38.64	0.00	60.95	0.00	0.09	99.68	po
010 SU2	91	0.00	0.00	33.77	0.00	29.91	33.45	0.00	97.13	ccp
010 SU2	92	0.00	0.00	34.39	0.00	30.39	33.67	0.00	98.45	ccp
010 SU2	93	0.00	0.00	38.71	0.00	61.02	0.00	0.09	99.82	po
010 SU2	94	0.00	0.00	39.08	0.00	60.43	0.00	0.05	99.56	po
010 SU4	95	0.00	0.00	38.63	0.00	60.89	0.00	0.07	99.59	po
010 SU4	96	0.00	0.00	38.71	0.00	60.88	0.00	0.07	99.66	po
010 SU6	97	0.03	0.00	38.73	0.00	60.89	0.00	0.04	99.69	po
010 SU6	98	0.03	0.00	38.77	0.00	61.11	0.00	0.06	99.97	po
010 SU5	99	0.00	0.00	39.15	0.00	59.64	0.00	0.08	98.87	po
010 SU5	100	0.00	0.00	39.38	0.00	59.61	0.00	0.15	99.14	po
010 SU5	101	0.04	0.00	39.16	0.00	59.29	0.00	0.09	98.58	po
49 1 SU1	102	0.00	0.00	38.47	0.14	61.02	0.00	0.24	99.87	po
49 1 SU1	103	0.00	0.00	38.44	0.11	61.17	0.00	0.23	99.95	po
49 1 SU1	104	0.00	0.00	37.74	0.15	60.08	0.00	0.24	98.21	po
49 1 SU2	105	0.00	0.00	39.26	0.00	59.84	0.00	0.21	99.31	po
49 1 SU2	106	0.03	0.00	39.35	0.00	60.07	0.00	0.24	99.69	po
49 1 SU2	107	0.00	0.00	39.33	0.00	59.56	0.00	0.22	99.11	po
49 1 SU2	108	0.03	0.00	38.43	0.00	59.04	0.00	0.23	97.73	po
49 1 SU2	109	0.00	0.00	39.55	0.00	59.64	0.00	0.25	99.44	po
49 1 SU2	110	0.03	0.00	38.85	0.00	59.89	0.07	0.23	99.07	po
49 1 SU2	111	0.00	0.00	34.48	0.00	30.69	33.55	0.00	98.72	ccp
49 1 SU2	112	0.00	0.00	35.15	0.00	30.53	33.68	0.00	99.36	ccp
49 1 SU3	113	0.00	0.00	39.32	0.00	60.05	0.00	0.27	99.64	po

49 1 SU3	114	0.00	0.00	39.44	0.00	59.98	0.00	0.25	99.67	po
49 1 SU3	115	0.04	0.00	39.57	0.00	60.17	0.00	0.24	100.02	po
49 1 SU3	116	0.00	0.00	39.38	0.00	59.93	0.00	0.26	99.57	po
49 1 SU3	117	0.00	0.00	39.19	0.00	59.86	0.00	0.26	99.31	po
49 1 SU3	118	0.00	0.00	39.25	0.00	59.70	0.00	0.26	99.21	po
49 1 SU4	119	0.00	0.00	39.00	0.00	59.34	0.00	0.28	98.62	po
49 1 SU4	120	0.00	0.00	39.26	0.00	59.74	0.00	0.34	99.34	po
49 1 SU4	121	0.00	0.00	34.55	0.00	30.97	32.61	0.00	98.13	ccp
49 1 SU4	122	0.00	0.00	39.05	0.00	59.40	0.00	0.30	98.75	po
49 1 SU5	123	0.00	0.00	39.34	0.00	59.14	0.00	0.29	98.77	po
49 1 SU5	124	0.00	0.00	39.60	0.00	59.80	0.00	0.24	99.64	po
49 1 SU5	125	0.00	0.00	39.31	0.00	59.72	0.00	0.24	99.27	po
49 1 SU5	126	0.00	0.00	39.32	0.00	59.71	0.00	0.25	99.28	po
49 1 SU5	127	0.00	0.00	39.25	0.00	59.72	0.00	0.27	99.24	po
49 1 SU6	128	0.00	0.00	39.48	0.00	59.78	0.00	0.30	99.56	po
49 1 SU6	129	0.00	0.00	37.26	0.00	57.19	0.00	0.30	94.75	po
49 1 SU7	130	0.03	0.00	38.28	0.08	61.28	0.00	0.25	99.92	po
49 1 SU7	131	0.04	0.00	38.04	0.08	61.38	0.00	0.21	99.75	po
49 1 SUEXT1	132	0.00	0.05	39.06	0.00	59.26	0.00	0.06	98.43	po
49 1 SUEXT1	133	0.00	0.00	39.18	0.00	59.72	0.00	0.10	99.00	po
49 1 SUEXT1	134	0.00	0.00	38.75	0.00	58.23	0.00	0.27	97.25	po
109 1 SU1	135	0.00	0.00	38.38	0.16	60.70	0.00	0.21	99.45	po
109 1 SU2	136	0.04	0.00	38.46	0.00	60.30	0.00	0.34	99.14	po
109 1 SU2	137	0.00	0.00	38.33	0.00	60.12	0.00	0.32	98.77	po
109 1 SU2	138	0.00	0.00	37.80	0.00	60.00	0.00	0.33	98.13	po
109 1 SU2	139	0.00	0.00	38.09	0.03	60.07	0.00	0.32	98.51	po
109 1 SU7	142	0.00	0.00	38.02	0.11	59.73	0.00	0.22	98.08	po
109 1 SU7	143	0.00	0.00	37.78	0.07	59.45	0.00	0.24	97.54	po
042 SUEXT1	146	0.07	0.06	52.98	0.00	46.85	0.00	0.00	99.96	py
042 SUEXT1	147	0.00	0.00	52.54	0.00	46.45	0.00	0.00	98.99	py
042 SUEXT1	148	0.00	0.00	53.00	0.00	46.82	0.00	0.00	99.82	py
042 SUEXT1	149	0.11	0.00	52.89	0.00	46.84	0.00	0.00	99.84	py
042 SUEXT1	150	0.00	0.00	52.90	0.00	46.55	0.00	0.00	99.45	py
042 SU14	151	0.00	0.00	39.64	0.00	59.68	0.00	0.40	99.72	po
042 SU14	152	0.03	0.00	38.96	0.00	59.68	0.00	0.37	99.04	po
042 SU14	153	0.00	0.00	40.02	0.00	59.96	0.00	0.36	100.34	po
042 SU14	154	0.00	0.00	39.19	0.00	60.06	0.00	0.40	99.65	po
042 SU14	155	0.03	0.00	40.10	0.00	60.00	0.00	0.28	100.41	po
042 SU5	156	0.00	0.00	39.57	0.00	60.16	0.00	0.44	100.17	po
042 SU5	157	0.00	0.00	39.66	0.00	59.80	0.00	0.41	99.87	po

042 SU5	158	0.00	0.00	34.63	0.00	30.81	33.19	0.02	98.65	ccp
042 SU5	159	0.00	0.00	39.40	0.00	59.78	0.00	0.54	99.72	po
042 SU5	160	0.03	0.00	39.53	0.00	59.71	0.00	0.52	99.79	po
042 SUEXT2	161	0.00	0.00	39.57	0.00	60.11	0.00	0.42	100.10	po
042 SUEXT2	162	0.05	0.00	39.48	0.00	60.05	0.00	0.44	100.02	po
042 SUEXT2	163	0.03	0.00	39.60	0.00	59.99	0.00	0.42	100.04	po
042 SUEXT2	164	0.06	0.00	53.22	0.00	43.92	0.00	0.00	97.20	py
042 SUEXT2	165	0.05	0.00	53.22	0.00	43.83	0.00	0.00	97.10	py
042 SU6	166	0.04	0.00	39.30	0.00	59.87	0.00	0.69	99.90	po
042 SU6	167	0.03	0.00	39.17	0.00	59.70	0.00	0.80	99.70	po
042 SU6	168	0.00	0.00	34.69	0.00	30.82	33.10	0.02	98.63	ccp
042 SU6	169	0.00	0.00	39.38	0.00	59.36	0.00	0.63	99.37	po
042 SU7	170	0.00	0.00	53.14	0.00	46.54	0.00	0.10	99.78	py
042 SU7	171	0.00	0.00	53.07	0.00	46.46	0.00	0.08	99.61	py
042 SU8	172	0.03	0.00	39.42	0.00	60.09	0.00	0.37	99.91	po
042 SU8	173	0.00	0.00	39.07	0.00	60.19	0.00	0.63	99.89	po
042 SU8	174	0.03	0.00	38.91	0.00	60.10	0.00	0.78	99.82	po
042 SU8	175	0.00	0.00	39.53	0.00	60.42	0.00	0.63	100.58	po
042 SU8	176	0.00	0.00	39.75	0.00	59.86	0.00	0.34	99.95	po
042 SU8	177	0.00	0.00	34.71	0.00	30.80	33.22	0.00	98.73	ccp
042 SUEXT3	178	0.00	0.00	39.40	0.00	59.81	0.00	0.40	99.61	po
042 SUEXT3	179	0.00	0.00	39.44	0.00	59.88	0.00	0.37	99.69	po
042 SUEXT3	180	0.00	0.00	47.98	0.00	43.72	0.00	0.79	92.49	py
042 SUEXT4	181	0.00	0.04	53.31	0.00	46.82	0.00	0.22	100.39	py
042 SUEXT4	182	0.00	0.00	53.28	0.00	46.73	0.00	0.13	100.14	py
042 SUEXT4	183	0.00	0.00	53.12	0.00	46.95	0.00	0.05	100.12	py
042 SUEXT4	184	0.00	0.00	39.20	0.00	60.51	0.00	0.38	100.09	po
042 SUEXT4	185	0.00	0.00	38.87	0.00	60.52	0.00	0.80	100.19	po
042 SUEXT4	186	0.05	0.00	39.12	0.00	60.41	0.00	0.65	100.23	po
042 SUEXT4	187	0.00	0.00	34.62	0.00	30.91	33.04	0.00	98.57	ccp
042 SU9	188	0.00	0.00	39.35	0.00	59.87	0.00	0.52	99.74	po
042 SU9	189	0.00	0.00	39.29	0.00	60.01	0.00	0.52	99.82	po
042 SU9	190	0.04	0.00	39.48	0.00	59.67	0.00	0.56	99.75	po
042 SU9	191	0.00	0.00	39.34	0.00	59.95	0.00	0.50	99.79	po
042 SU9	192	0.00	0.00	39.07	0.00	59.04	0.00	0.41	98.52	po
042 SU9	193	0.00	0.00	39.47	0.00	59.81	0.00	0.44	99.72	po
042 SUEXT5	194	0.00	0.00	39.47	0.00	59.82	0.00	0.50	99.79	po
042 SUEXT5	195	0.00	0.00	39.65	0.00	59.99	0.03	0.45	100.12	po
042 SUEXT5	196	0.00	0.00	34.85	0.00	30.54	33.31	0.00	98.70	ccp
042 SUEXT6	197	0.00	0.00	39.55	0.00	59.88	0.00	0.37	99.80	po

042 SUEXT6	198	0.00	0.00	39.70	0.00	59.80	0.00	0.38	99.88	po
042 SU12	199	0.00	0.00	37.96	0.41	60.47	0.00	0.26	99.10	po
042 SU12	200	0.00	0.00	39.50	0.24	59.54	0.00	0.55	99.83	po
042 SU12	201	0.00	0.00	38.00	0.25	61.23	0.00	0.21	99.69	po
042 SU10	202	0.00	0.00	39.45	0.00	59.78	0.00	0.48	99.71	po
042 SU10	203	0.00	0.00	39.43	0.00	59.80	0.00	0.41	99.64	po
042 SUEXT7	204	0.00	0.00	38.29	0.00	60.88	0.00	0.26	99.43	po
042 SUEXT7	205	0.00	0.00	38.40	0.00	60.86	0.00	0.29	99.55	po
042 SUEXT7	206	0.00	0.05	39.36	0.00	59.28	0.00	0.53	99.22	po
042 SUEXT8	207	0.00	0.00	38.82	0.00	60.26	0.00	0.45	99.53	po
042 SUEXT8	208	0.00	0.00	38.68	0.00	60.38	0.00	0.52	99.58	po
042 SUEXT8	209	0.00	0.00	38.65	0.00	60.35	0.00	0.58	99.58	po
042 SUEXT8	210	0.00	0.00	39.48	0.00	59.80	0.00	0.39	99.67	po
042 SUEXT9	211	0.00	0.00	39.42	0.00	59.24	0.00	0.77	99.43	po
042 SUEXT9	212	0.00	0.00	39.21	0.00	59.08	0.00	0.67	98.96	po
042 SUEXT9	213	0.00	0.00	39.27	0.00	59.13	0.00	0.71	99.11	po

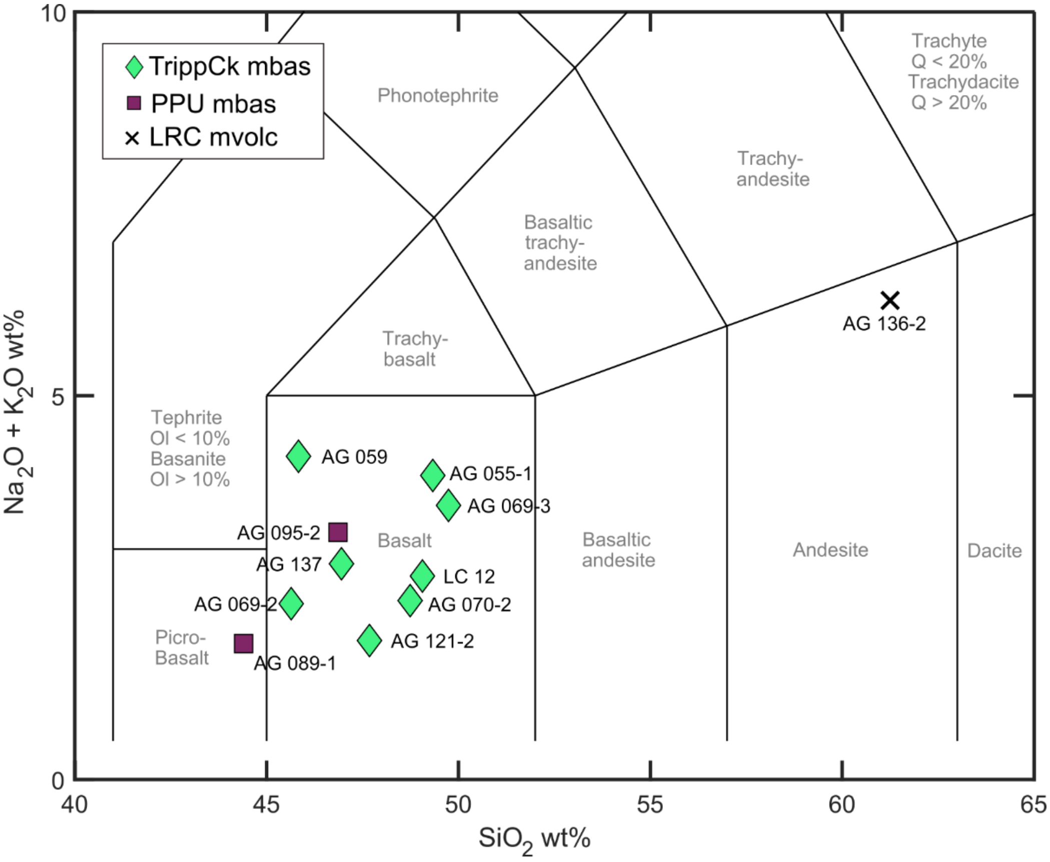

Figure C.4 Total Alkali – Silica (TAS) Diagram for metaigneous rocks from the LRC and PPU.

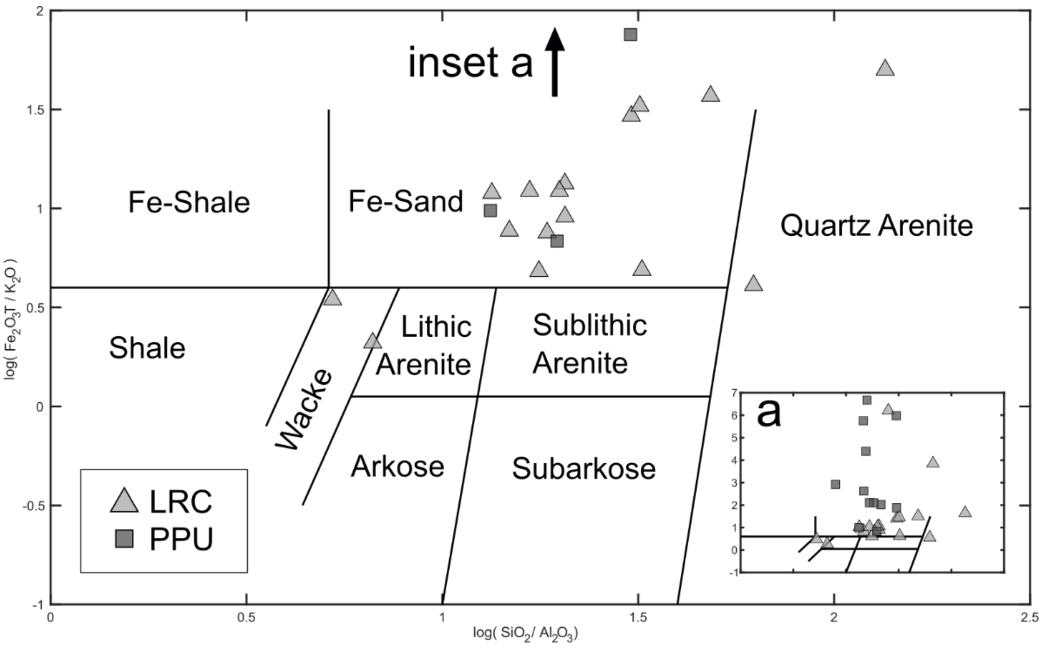

Figure C.5 Sediment classification diagram after Herron (1988) for LRC and PPU metasediments. Protolith mixing shifts compositions in the LRC to higher ‘Fe-sand’ classification.

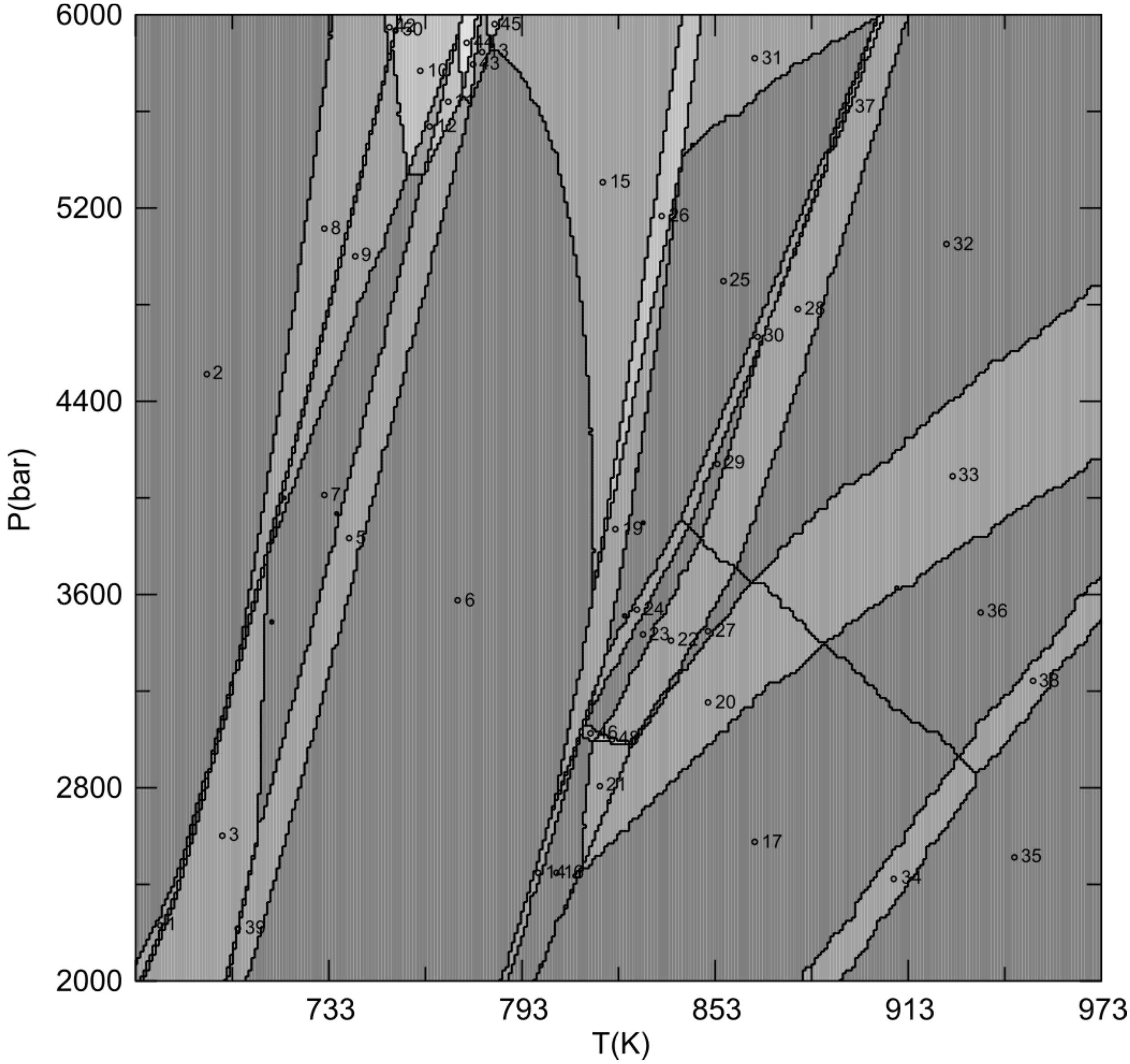

Figure C.6 Raw version of pseudosection 'Average Pelite' from Chapter 2, generated using PerpleX (Connolly, 2005).

Average Pelite Pseudosection (Chapter 2) Full Assemblage*:

1 - COH-Fluid Chl(W) feldspar Mica(W) Ep(HP11) sph ab q
2 - Ep(HP11) COH-Fluid Mica(W) Chl(W) sph ab q
3 - feldspar Chl(W) COH-Fluid Mica(W) Bi(W) sph ab q
4 - feldspar Chl(W) COH-Fluid Ep(HP11) Mica(W) Bi(W) sph ab q
5 - feldspar Ilm(WPH) Chl(W) COH-Fluid Mica(W) Bi(W) sph q
6 - Mica(W) Bi(W) COH-Fluid feldspar Chl(W) Ilm(WPH) q

7 - Chl(W) feldspar COH-Fluid Mica(W) Bi(W) sph q
8 - Chl(W) COH-Fluid Bi(W) Ep(HP11) Mica(W) sph ab q
9 - Bi(W) Chl(W) feldspar COH-Fluid Mica(W) Ep(HP11) sph q
10 - feldspar COH-Fluid Chl(W) Mica(W) Bi(W) Gt(W) Ep(HP11) sph q
11 - COH-Fluid Ilm(WPH) Chl(W) Mica(W) Bi(W) feldspar Gt(W) sph q
12 - feldspar Mica(W) COH-Fluid Bi(W) Chl(W) Gt(W) sph q
13 - COH-Fluid feldspar Ilm(WPH) Chl(W) Mica(W) Bi(W) Ep(HP11) q
14 - feldspar COH-Fluid Ilm(WPH) Mica(W) Bi(W) Chl(W) and q
15 - COH-Fluid feldspar Bi(W) Chl(W) Ilm(WPH) Mica(W) Gt(W) q
16 - feldspar COH-Fluid Bi(W) Ilm(WPH) Chl(W) and q
17 - COH-Fluid Bi(W) feldspar Ilm(WPH) Crd(W) and q
18 - feldspar COH-Fluid Bi(W) Mica(W) Chl(W) St(W) Ilm(WPH) and q
19 - COH-Fluid Ilm(WPH) Mica(W) feldspar St(W) Chl(W) Bi(W) q
20 - feldspar COH-Fluid Ilm(WPH) Bi(W) Gt(W) Crd(W) and q
21 - COH-Fluid Chl(W) feldspar Bi(W) Gt(W) Ilm(WPH) and q
22 - feldspar COH-Fluid Bi(W) Ilm(WPH) Gt(W) St(W) and q
23 - COH-Fluid feldspar Ilm(WPH) Bi(W) St(W) and q
24 - COH-Fluid Bi(W) St(W) Mica(W) feldspar Ilm(WPH) and q
25 - COH-Fluid Bi(W) feldspar St(W) Ilm(WPH) Mica(W) q
26 - Mica(W) COH-Fluid feldspar Chl(W) Bi(W) Gt(W) Ilm(WPH) St(W) q
27 - Gt(W) feldspar Ilm(WPH) COH-Fluid Bi(W) and q
28 - Bi(W) St(W) feldspar Ilm(WPH) COH-Fluid Gt(W) sill q
29 - Ilm(WPH) feldspar COH-Fluid Bi(W) St(W) sill q
30 - St(W) Bi(W) feldspar Mica(W) COH-Fluid Ilm(WPH) sill q
31 - COH-Fluid Bi(W) Mica(W) feldspar Gt(W) Ilm(WPH) St(W) q
32 - COH-Fluid Gt(W) Ilm(WPH) Bi(W) feldspar sill q
33 - feldspar Crd(W) COH-Fluid Bi(W) Ilm(WPH) Gt(W) sill q
34 - Crd(W) Bi(W) feldspar feldspar Ilm(WPH) COH-Fluid and q
35 - feldspar feldspar Crd(W) Bi(W) Ilm(WPH) COH-Fluid q
36 - Ilm(WPH) Crd(W) Bi(W) COH-Fluid feldspar sill q
37 - Ilm(WPH) COH-Fluid St(W) feldspar Bi(W) Mica(W) Gt(W) sill q
38 - COH-Fluid feldspar feldspar Crd(W) Bi(W) Ilm(WPH) sill q
39 - feldspar COH-Fluid Chl(W) Ilm(WPH) Bi(W) Mica(W) sph ab q
40 - Mica(W) COH-Fluid Chl(W) feldspar sph q
41 - Ep(HP11) Mica(W) COH-Fluid Chl(W) feldspar sph q
42 - Ep(HP11) COH-Fluid Bi(W) Mica(W) Chl(W) Gt(W) sph ab q
43 - Ilm(WPH) COH-Fluid feldspar Mica(W) Bi(W) Ep(HP11) Chl(W) sph q
44 - Mica(W) feldspar COH-Fluid Ilm(WPH) Gt(W) Bi(W) Chl(W) Ep(HP11) sph q
45 - Chl(W) Bi(W) COH-Fluid Ep(HP11) Ilm(WPH) feldspar Gt(W) Mica(W) q
46 - COH-Fluid feldspar Bi(W) Ilm(WPH) St(W) Chl(W) and q
47 - COH-Fluid Bi(W) Mica(W) feldspar Ilm(WPH) q
48 - feldspar COH-Fluid Chl(W) Gt(W) Ilm(WPH) Bi(W) St(W) and q
49 - Bi(W) COH-Fluid feldspar Gt(W)
50 - feldspar Bi(W) Mica(W) Chl(W) COH-Fluid Ep(HP11) Gt(W) sph ab q
51 - COH-Fluid Crd(W) Bi(W) Ilm(WPH) Chl(W) feldspar and q
52 - COH-Fluid feldspar Ilm(WPH) Crd(W) Bi(W) Chl(W) Gt(W) and q
53 - feldspar Bi(W) COH-Fluid Gt(W) Crd(W) sill q

*Mineral abbreviations in PerpleX jargon, see solution files. Duplicate minerals (e.g. Mica(W), Mica(W)) indicate coexisting phases (e.g., muscovite and paragonite).

Appendix D Preliminary LA-ICP-MS data for in-situ sulfide analyses

Preliminary data were collected to evaluate in-situ variations in sulfide trace element content with progressive metamorphism in the Pacific Rim Terrane. This section is included in support of the proposed future work to investigate terrane-wide trends with this technique. Extenuating circumstances precluded acquiring a matrix-matched sulfide standard (MASS-1, USGS) during the time of study. However, as a test of concept, the following data was collected to evaluate relative trends.

Methods

Matrix and inclusion sulfide grains were analyzed for a suite of chalcophile and trace elements at the University of Victoria ICP-MS lab using a Thermo X-Series II (X7) quadrupole ICP-MS. Analyses were performed in linear transects with a spot size of 20 µm and approximate scan rate of 10 µm s^{-1} over ~100 µm segments with six repetitions at a rate of 10 Hz. Smaller inclusions were analyzed separately using spot analyses with the same beam diameter and repetition rates. Laser energy was set at 30% and fluence maintained at 6.12 J cm^{-2}. Because some sulfide grains analyzed were only slightly larger than the spot size, care was taken to isolate sections of time resolved spectra contaminated by matrix, which was identifiable by elevated Si, Ti, and Mn content depending on the grain host. Raw counts per second (cps) were taken as ratios to evaluate relative trends among the sulfides.

Preliminary Results

Preliminary findings show encouraging relative trends that invite future work pursuing in-situ sulfide analyses for Py and Po. Pb counts show generally no trends with metamorphic grade, and thus in Figure D.1, Pb was taken as the denominator in ratios for comparing other relative trends. Cu/Pb ratios show no significant change in Py or Po, suggest Cu is not mobilized over the desulfidation window, consistent with ‘Au-only’ ores in the Valentine Mountain orebody (Houle, 2011). As/Pb shows indications of a decrease between 300 and 400 °C, but more data are required to confidently identify this change. Co/Ni shows the most robust trends, with Py Co/Ni decreasing several orders of magnitude from very low grade to 400 °C. Co/Ni has been historically used in classifying different kinds of pyrite (e.g., sedimentary, diagenetic, and hydrothermal) with some limited success (Gregory et al., 2015). The data presented here at low grade far exceed the domain for 'sedimentary' Py and would be classed as 'hydrothermal' in this paradigm. However, the homogenization of within-sample values and overall decrease in Co/Ni with increasing grade over a window ascribed to desulfidation suggests the ratio might have some utility in tracking changes to the sulfide assemblage with grade in future work.

Figure D.1 Preliminary results (cps and ratios thereof) for in-situ sulfide analyses. Yellow squares correspond to Py analyses. Orange circles correspond to Po analyses.

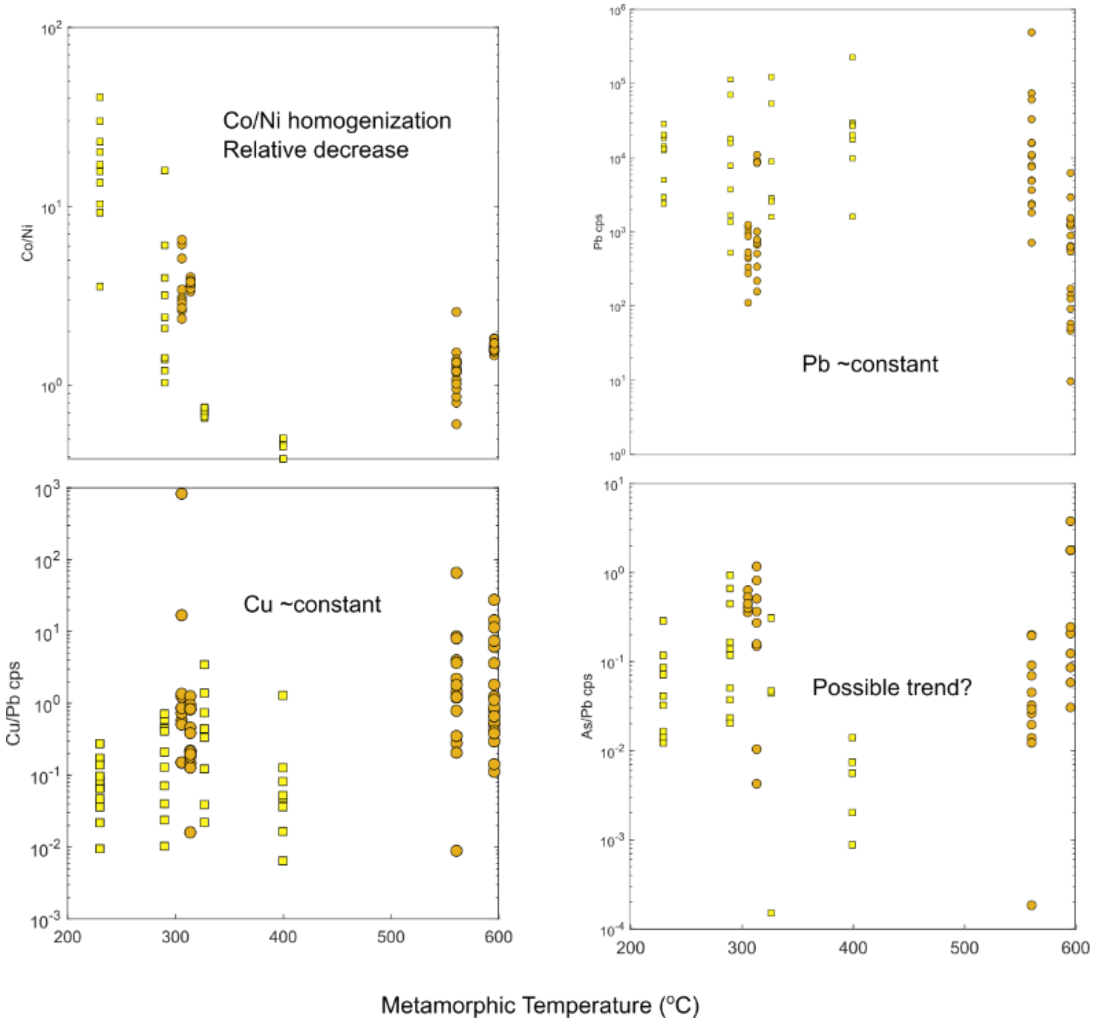

Table D.1 Background-subtracted and signal-averaged raw LA-ICP-MS in-situ sulfide data.

ID		29Si	34S	43Ca	47Ti	55Mn	57Fe	59Co	60Ni	65Cu	66Zn	75As	95Mo	107Ag	111Cd	Pb*	T
AG006-A1	Py	0	81110	17.2	6.1	38669	799312	103542	32480	1176.6	16566.5	4265.6	310.6	673.6	121.2	114312	290
AG006-B1	Py	1887	49259	0.0	30.5	3577	579581	28341	23435	418.2	7567.1	410.6	41.9	177.5	0.6	17597	290
AG006-B3	ccp	28137	77205	510.6	2742.9	74066	3001283	349913	103942	204098.7	38839.8	7779.8	1530.4	3062.9	93.8	181060	290
AG006-C1	Py	26900	51379	216.2	2992.9	31434	456651	15533	981	9387.1	8100.5	14816.0	80.1	85.6	15.3	15859	290
AG006-C2	Py	507	50604	0.0	0.0	2422	600154	21181	15235	68.3	22.9	348.0	0.6	4.7	0.8	527	290
AG006-C3	Py	2767	43589	66.5	1541.7	1400	490476	23706	22902	607.9	126.4	224.7	8.4	30.3	1.5	1356	290
AG006D2	Py	2906	90483	21.7	17.6	30822	876069	69220	28865	2858.1	541.7	9827.3	363.4	517.7	2.3	71007	290
AG006D3	Py	2458	53625	0.2	12.3	17936	586858	21338	14995	561.2	522.2	159.7	23.9	88.7	0.0	7855	290
AG006D4	Py	0	44875	1128.4	6.1	1284	559461	16976	2804	355.0	30.1	85.1	0.0	23.5	0.0	1684	290
AG006D5	Py	0	90891	51.2	86.4	48369	743578	3484	875	2679.6	251.9	1680.2	199.7	32.4	0.0	3759	290
AG006-E2	Py	713	72572	41.9	310.6	147051	626662	39267	18860	7420.6	601.5	2140.8	299.4	204.5	0.0	18070	290
AG010-1A	Po	348	52769	36.3	148.2	1904	648364	35364	13346	146.8	14.5	347.2	0.0	36.3	0.0	977	306
AG010-1B	Po	139	49204	2.7	0.0	1949	576012	30971	11781	548.1	33.8	280.6	0.0	13.9	0.6	443	306
AG010-1C	Po	2675	44855	393.0	15.2	6391	548320	30435	8886	20519.1	53.0	0.0	575.0	48.3	0.0	1213	306
AG010-2C	Po	1559	48186	76.9	48.3	9780	589359	35144	11437	132.0	98.6	0.0	0.0	16.3	0.0	874	306
AG010-3A	Po	13537	29247	1868.5	445.0	50066	378029	20691	8792	667.4	71.4	0.0	9.1	38.5	0.0	1150	306
AG010-3C	Po	1186	43153	19.9	0.0	722	528362	28046	9423	399.2	9.8	0.0	1.6	18.0	0.0	466	306
AG010-4A	Po	1445	40128	27.7	528.0	3216	482838	25903	9021	244.2	23.2	0.0	0.0	34.0	0.0	334	306
AG010-5A	Po	1107	38447	954.1	6.1	11942	457649	24323	3970	270.0	78.1	280.8	4.4	27.3	0.0	531	306
AG010-6B	Po	0	43828	6.0	0.0	114	538875	30009	4617	150.4	5.0	0.0	0.0	5.7	1.4	111	306
AG010-7A	Po	29	36641	958.5	6.0	8985	450710	23866	4666	238.9	0.0	110.4	0.0	8.3	0.0	276	306
AG010-8A	ccp	1423	16571	0.0	0.0	609	94570	83	45	989166.7	747.2	0.0	0.0	66.7	7.6	59	306
AG010-8C	ccp	0	18847	40.1	0.0	860	106729	152	56	1032134.1	996.8	552.6	0.0	81.6	5.8	1246	306
AG089-A1	Py	1871	74022	11.5	12.1	6921	580665	3186	893	402.0	65.7	257.7	12.7	12.7	0.0	18471	230
AG089-A3	ccp	5434	18043	472.9	18.4	13781	110575	62	8	980002.8	470.3	0.0	1.2	22.2	6.7	1088	230
AG089-A4	Py	848	75324	24.4	240.8	4653	592719	5650	359	1374.5	36.8	821.9	3.0	13.9	0.8	19962	230
AG089-C2	Py	658	82062	0.0	113.8	4503	630030	1949	85	1209.1	26.9	0.0	1.3	10.1	0.0	14382	230
AG089-C1	Py	4025	73016	507.7	12241.4	14218	545462	1949	212	746.0	311.8	250.7	56.1	26.1	2.9	20553	230
AG089D2	Py	1257	83209	16.9	71.9	5416	647901	4541	226	597.1	36.1	410.4	5.2	12.6	0.7	12634	230
AG089D3	Py	2678	79428	101.8	6.0	9540	599551	1480	144	124.3	80.2	0.0	0.0	3.8	1.5	13123	230
AG089-E1	Py	7697	71497	453.5	9847.3	31534	560829	6896	509	2258.6	233.4	1117.7	54.7	58.4	0.0	13030	230
AG089-E2	Py	1222	80844	135.3	571.5	2452	592192	4063	440	487.8	56.7	592.6	9.8	24.0	0.8	5041	230
AG089-E3	Py	21515	50259	11.3	552.0	2349	376584	4788	160	666.8	87.2	691.9	1.4	9.1	2.3	2417	230
AG089-F2	Py	443	96060	5.5	46.7	1177	702515	2836	166	1846.0	9.4	468.6	4.5	12.6	1.3	28504	230

AG089-F3	Py	2185	73717	6.2	158.5	362	558783	3645	90	407.7	5.5	209.7	53.4	9.1	0.0	2947	230
49M1-1A	Po	0	38494	0.0	0.0	0	449482	22564	14488	990.2	1.0	0.0	357.4	21.9	0.8	1225	596
49M1-1E	Po	8	34974	21.1	1062.6	73	399837	22874	14327	99.9	6.1	109.8	0.8	59.6	0.0	891	596
49M1-2A	Po	0	40451	4.1	0.0	0	460343	24025	15128	125.7	1.1	0.0	0.8	12.2	1.5	142	596
49M1-3B	ccp	3957	20561	8.5	55.6	22	122040	1251	616	994221.6	2032.9	130.3	0.8	777.1	201.7	519	596
49M1-3A	Po	21	40233	3.2	6.1	323	469017	25301	15379	766.7	2.6	221.6	3.0	3.4	0.0	125	596
49M1-4A	Po	128	46615	5.9	18.3	206	549082	30152	18022	744.2	1.3	298.7	0.8	57.2	0.0	1448	596
49M1-4B	ccp	666	29943	23.3	12.1	107	267421	11351	6071	651996.5	547.4	102.3	0.0	990.4	26.2	2653	596
49M1-4C	Po	0	44090	0.0	6.1	0	503882	29435	17939	57.5	2.3	0.0	2.3	6.1	0.0	46	596
49M1-6A	Po	671	45709	0.0	115.2	354	530815	28598	17649	355.3	2.1	103.0	1.5	52.8	0.6	1203	596
49M1-6C	Po	1571	47050	9.7	865.4	1407	536228	26468	14461	320.5	50.8	0.0	2.3	39.1	0.0	584	596
49M1-7A	Po	0	43268	14.2	41.9	56	500370	28827	18729	1940.6	27.4	89.5	2.9	159.3	0.5	2932	596
49M1-7B	Po	160	40395	0.0	18.0	0	444503	25156	15345	184.3	2.1	0.0	3.0	291.0	0.0	1293	596
49M2-1A	Po	0	54154	0.0	0.0	0	612829	30192	20514	268.6	2.0	0.0	2.3	346.8	0.0	646	596
49M2-1B	Po	966	56676	4.7	0.0	41	634107	33120	21157	14983.2	76.9	0.0	1.8	84.9	10.2	543	596
49M2-1E	Po	382	54410	13.5	0.0	30	628124	31548	17389	167.0	6.3	0.0	0.0	9.8	1.5	91	596
49M2-1G	Po	5094	53097	0.0	30.9	354	630096	31448	18167	593.3	22.1	378.4	0.0	99.2	1.7	1546	596
49M2-2A	Po	11	48801	0.0	43.2	36	553199	29977	19373	829.6	0.0	217.5	0.0	9.1	0.8	58	596
49M2-2B	Po	0	48907	15.8	0.0	0	568167	28953	18558	184.2	1.1	90.4	3.7	5.2	0.8	51	596
49M2-2C	Po	17	43867	13.6	6.1	0	537115	27910	18018	109.8	3.8	0.0	2.3	3.5	2.3	10	596
49M2-2D	ccp	0	21733	4.8	6.0	0	126715	93	78	1294386.4	1414.1	0.0	0.7	218.5	138.2	16	596
49M2-3C	ccp	0	24335	0.0	0.0	0	177869	4193	2088	1009784.7	1445.2	0.0	1.5	257.2	104.3	371	596
49M2-3D	Po	171	43955	11.4	6.0	6	504390	28590	18022	192.8	5.7	0.0	2.1	16.6	0.0	172	596
492-3E	Po	152	43607	7.5	59.9	64	489669	27567	17436	419.6	4.6	36.9	3.0	135.9	0.0	633	596
49M2-4	Po	0	41108	2.5	170.4	288	453545	26561	15452	46205.0	171.9	0.0	2.7	131.0	6.1	6238	596
AG014-A1	Po	0	48121	0.0	6.1	18	546921	35235	9126	2004.8	0.2	0.0	2.3	77.3	2.2	9093	314
AG014-A2	Po	1456	41512	157.3	3267.8	6217	509086	31518	8237	235.2	20.7	139.0	0.0	21.9	0.0	509	314
AG014-B1	Po	1039	41939	0.0	0.0	1917	496809	31798	8449	84.7	14.4	32.7	0.0	11.1	0.0	219	314
AG014-B2	Po	47	39529	0.0	0.0	380	472422	29530	8117	136.8	5.1	0.0	14.1	64.6	1.5	8544	314
AG014-B3	ccp	1351	40916	0.5	4.0	14926	492758	29365	7545	60357.2	155.5	405.6	13.9	95.6	2.0	9108	314
AG014-C5	Po	2852	47373	180.5	4557.2	13777	579154	35903	9435	150.1	66.8	513.6	0.0	31.4	3.6	1013	314
AG014-C1	Po	509	38772	9.2	35.9	1674	476899	29336	8207	99.4	22.2	0.0	0.7	12.7	0.0	778	314
AG014D1	ccp	3242	40089	246.4	3866.1	8267	472804	28853	7606	18203.2	149.8	0.0	0.0	45.2	1.4	1162	314
AG014-E2	Po	12437	25138	32.6	1241.7	121333	382959	19048	5154	1553.2	829.2	36.7	3.0	75.0	0.0	8614	314
AG014-E4	Po	16127	26750	1549.6	13633.8	46021	335038	19959	5962	143.7	398.4	780.9	3.0	40.2	1.4	668	314
AG014-F1	Po	4513	101332	593.5	13791.2	19350	852208	88301	25385	2153.4	152.3	114.2	26.8	119.6	2.8	10966	314
AG014G1	Po	6622	32631	676.9	21409.9	24229	390563	23648	6398	898.5	152.5	260.3	1.5	41.3	0.7	712	314
AG014G5	Po	367	38219	13.3	18.3	670	452361	28323	7048	149.5	2.4	0.0	0.0	14.5	0.0	157	314
AG014H3	Po	2135	33440	165.0	4736.2	15969	408763	24734	6405	647.5	103.5	123.5	2.3	23.8	0.0	786	314

Ag014-H4	Po	18805	27060	779.7	10260.2	41450	350911	20943	5538	283.4	169.4	275.8	3.8	10.2	0.0	339	314
AG105-1A	Py	1969	100670	3.6	111887.6	1526	1169785	35178	73693	1444.9	103.8	26.4	0.7	489.5	2.2	30038	400
AG105-1B	ccp	6055	84260	0.5	3018.3	2058	839873	20622	30475	1786975.0	6902.9	200.4	4.2	690.9	43.9	57569	400
AG105-2A	Py	41	124948	6.9	-9.8	464	1460267	36080	92752	2075.7	31.5	-92.7	7.4	57.2	0.0	1607	400
AG105-2B	Py	926	149715	85.0	34.6	2507	1683367	41726	107484	1460.9	90.5	458.7	5.0	937.2	-0.5	227143	400
AG105-3A	Py	824	114285	2.9	1512.3	216	1317557	42155	89525	1473.0	14.7	207.6	-4.8	367.3	-3.1	27947	400
AG105-3B	Py	34	115761	17.9	3073.4	143	1327530	43474	91290	1450.7	12.8	98.9	20.2	397.1	-0.2	17664	400
AG105-4B	Py	1058	122041	8.5	158.5	394	1389479	39454	77962	2597.4	26.9	286.4	3.1	75.8	-1.8	20432	400
AG105-4A	Py	3027	118099	9.6	392.9	502	1310438	37409	74046	162.2	33.0	-233.8	-1.2	124.7	-0.9	9835	400
AG105-5A	Py	1089	159720	9.1	1103.1	698	1572431	55758	122864	978.0	64.0	-1.8	3.8	99.3	-1.5	26782	400
AG030-1A	Py	1172	114306	187.4	1.4	3910	1271135	88255	125669	1093.3	35.7	398.1	2.0	101.0	0.7	8914	327
AG030-2A	Py	1326	120620	5.2	8.5	2645	1319170	92869	141950	1155.7	43.6	-138.2	3.7	78.5	0.0	2641	327
AG030-2B	Py	-218	141264	101.9	-7.4	5917	1499944	101755	148232	4804.7	5.5	18.6	1013.8	1059.4	-0.9	123171	327
AG030-2C	Py	1562	114377	24.5	1823.6	7220	1240277	86528	129121	9892.5	237.5	134.6	-0.9	69.0	0.0	2866	327
AG030-3A	Py	1194	106626	27.6	611.5	4889	1185451	77759	106567	942.8	46.0	-380.1	7.6	91.8	0.5	2803	327
AG030-3B	Py	443	106220	452.4	13.0	3139	1147226	76074	104105	1252.3	54.6	-282.1	0.3	38.8	0.0	2823	327
AG030-4A	Py	1096	115932	0.6	37.2	2357	1265969	85237	113208	1891.1	43.0	788.4	1.1	65.3	1.1	2555	327
AG030-4B	Py	5056	123161	3.3	38.1	7828	1331833	90826	126693	1189.4	125.2	-160.9	2.5	189.6	-0.9	53979	327
AG030-5A	Py	1705	114272	2.7	196.6	4103	1246337	85444	113540	2208.9	65.5	-297.1	4.6	56.4	2.3	1591	327
AG046-1A	Py	81868	130323	218.0	621.4	7817	1097649	127169	83332	95174.1	2421.9	1035.4	359.9	18502.1	54.9	74144	561
AG046-1B	Po	26929	80899	317.1	539.5	906913	1015648	22062	36364	1905.4	43.3	166.9	2.6	110.9	9.4	2409	561
AG046-2A	Po	1337	133368	7.1	35.9	59217	1417361	89741	83503	62320.8	240.2	411.4	13.4	681.3	24.3	15664	561
AG046-2C	Po	967	97230	1.1	3113.0	5965	1070291	59443	74364	4371.9	13.0	90.6	-1.5	614.3	13.5	491424	561
AG0462D	Po	21848	77476	353.8	27.4	1292897	955244	46478	53877	46993.2	18.9	-486.3	2.0	66.4	25.5	716	561
AG046-2E	Po	13562	88929	214.3	-14.6	941965	1000933	60977	63799	4400.9	51.6	-341.2	5.2	288.5	22.6	3660	561
AG046-2F	Po	2239	119580	22.4	170.6	15592	1303967	72871	71430	67300.3	143.6	1566.1	-2.2	274.7	29.8	7874	561
AG0462H	ccp	768	106671	0.4	76.7	9453	903906	77738	56963	1403660.4	1925.0	389.9	5.7	1051.5	227.2	25217	561
AG046-2I	ccp	2386	135253	20.4	198.1	11483	1098421	79470	58215	1107284.2	1242.1	-325.2	-1.0	4642.2	134.6	17874	561
AG0463D	Po	28000	77033	1153.0	6106.1	33658	956987	38851	15109	84768.0	373.6	-936.0	59.1	499.1	12.7	10537	561
AG046-3B	Po	16606	88959	16.0	210619.3	300551	1468795	70723	60206	88493.8	1035.9	-9.3	45.3	1383.9	26.6	61093	561
AG0465D	Po	291	125634	6.2	180.8	581	1326398	93175	70721	10937.5	101.0	97.1	9.8	177.3	34.6	4969	561
AG046-5A	Po	-126	130927	-3.2	-2.4	34	1410943	86571	69110	1372.0	23.3	158.0	1.8	305.1	2.8	4884	561
AG046-5B	ccp	7088	55136	1.7	1544.4	5315	377911	6064	4143	2595960.9	2274.9	-522.4	1.2	1270.6	214.5	1371	561
AG046-5E	Po	-31	142550	-3.5	20.4	417	1507244	97237	79931	6663.0	67.6	-477.3	3.2	76.5	16.3	1819	561
AG046-6B	Po	2141	127108	7.0	2.1	914	1211137	84093	60546	3294.4	122.4	196.1	3.0	233.6	28.2	15983	561
AG046-7A	Po	35	168415	5.5	7.3	116	1561947	113450	84517	2839.6	42.1	452.4	2.4	47.6	6.7	2316	561
AG046-7B	Po	626	325181	15.8	397.3	2536	2298489	260664	194118	11658.5	226.5	970.9	15.2	451.4	117.5	33091	561
AG046-8A	Po	4994	125234	7.6	2128.0	4272	1418452	75068	62755	13586.1	162.2	684.7	-2.8	197.3	-0.9	7525	561